Medizinische Fakultät
der
Universität Duisburg-Essen

Aus dem Erwin L. Hahn Institute for Magnetic Resonance Imaging
sowie dem Fachbereich Informatik der Fachhochschule Dortmund

Time-frequency analysis of optical and electrical cardiac signals with applications in ultra-high-field MRI

Inaugural-Dissertation
zur
Erlangung des Doktorgrades
der Naturwissenschaften in der Medizin
durch die Medizinische Fakultät
der Universität Duisburg-Essen

vorgelegt von
Nicolai Spicher
aus Bochum
2020

DOI: 10.17185/duepublico/72858
URN: urn:nbn:de:hbz:464-20201103-094130-8

Dekan: Herr Univ.-Prof. Dr. med. J. Buer
1. Gutachter: Herr Prof. Dr. sc. techn. M. E. Ladd
2. Gutachter: Herr Priv.-Doz. Dr. med. K. Naßenstein
3. Gutachter: Herr Prof. Dr. rer. nat. U. Flögel

Tag der mündlichen Prüfung: 16. September 2020

This page intentionally left blank.

Publications

Results of this thesis have been submitted to peer-reviewed journals and conferences.

Journal paper

3. Spicher, N., Kukuk, M. (2020): Delineation of electrocardiograms using multiscale parameter estimation. IEEE Journal of Biomedical and Health Informatics, 24(8), 2216–2229. *Impact Factor (2019):* 5.2
2. Kukuk, M., Spicher, N. (2019): Parameter estimation based on scale-dependent algebraic expressions and scale-space fitting. IEEE Transactions on Signal Processing, 67(6), 1431–1446. *Impact Factor (2019):* 5.0
1. Spicher, N., Kukuk, M., Maderwald, S., Ladd, M. E. (2016): Initial evaluation of prospective cardiac triggering using photoplethysmography signals recorded with a video camera compared to pulse oximetry and electrocardiography at 7T MRI. BioMedical Engineering OnLine, 15(1), 126. *Impact Factor (2019):* 2.0

Conference paper

5. Spicher, N., Kukuk, M., Maderwald, S., Ladd, M. E. (2019): Multiscale parameter estimation (msPE) of QRS complexes distorted by magnetohydrodynamic effects at 7 Tesla. Current Directions in Biomedical Engineering, 5(1), 365–368.
4. Spicher, N., Kukuk, M. (2019): ECG delineation using a piecewise Gaussian derivative model with parameters estimated from scale-dependent algebraic expressions In: Proceedings of the 41st Annual International Conference of the IEEE Engineering in Medicine and Biology Society, Berlin, Germany.
3. Spicher, N., Lovelace, T., Kukuk, M. (2018): Feasibility of photoplethysmography imaging of the sole of the foot In: Proceedings of the 13th IEEE International Symposium on Medical Measurements & Applications, Rome, Italy.
2. Spicher, N. (2016): Cardiac activity measurement from video signals of the human skin in ultra-high-field magnetic resonance imaging In: Proceedings of the 46th Annual Meeting of the German Informatics Society, Klagenfurt, Austria.
1. Spicher, N., Maderwald, S., Ladd, M. E., Kukuk, M. (2015): Heart rate monitoring in ultra-high-field MRI using frequency information obtained from video signals of the human skin compared to electrocardiography and pulse oximetry. Current Directions in Biomedical Engineering, 1(1), 69–72.

Conference abstracts

7. Spicher, N., Orzada, S., Maderwald, S., Ladd, M. E., Kukuk, M. (2018): A novel method for video-based cardiac gating in 7T MR angiography using a video of the foot In: Proceedings of the 26th Annual Meeting of the International Society for Magnetic Resonance in Medicine, Paris, France.
6. Spicher, N., Orzada, S., Maderwald, S., Kukuk, M., Ladd, M. E. (2017): On the importance of skin color phase variations for video measurement of cardiac activity in MRI In: Proceedings of the 25th Annual Meeting of the International Society for Magnetic Resonance in Medicine, Honolulu, USA.
5. Spicher, N., Orzada, S., Maderwald, S., Kukuk, M., Ladd, M. E. (2017): An open-source hardware and software system for video-gated MRI In: Proceedings of the 25th Annual Meeting of the International Society for Magnetic Resonance in Medicine, Honolulu, USA.
4. Spicher, N., Tanriverdi, F., Thiem, J., Kukuk, M. (2017): PPG imaging: Investigating skin inhomogeneity using hyperspectral imaging and principal component analysis In: Proceedings of the 51st Annual Conference of the German Society of Biomedical Engineering, Dresden, Germany.
3. Spicher, N., Maderwald, S., Ladd, M. E., Kukuk, M. (2016): High-speed, contact-free measurement of the photoplethysmography waveform for MRI triggering In: Proceedings of the 24th Annual Meeting of the International Society for Magnetic Resonance in Medicine, Singapore.
2. Spicher, N., Kukuk, M., Ladd, M. E., Maderwald, S. (2015): In vivo 7T MR imaging triggered by phase information obtained from video signals of the human skin In: Proceedings of the 23rd Annual Meeting of the International Society for Magnetic Resonance in Medicine, Toronto, Canada.
1. Spicher, N., Brumann, C., Kukuk, M., Ladd, M. E., Maderwald, S. (2014): Eulerian video magnification for heart pulse measurement in MRI Scanners In: Proceedings of the 22nd Annual Meeting of the International Society for Magnetic Resonance in Medicine, Milan, Italy.

Contents

1 Introduction **8**

2 Background **11**

2.1 Magnetic Resonance Imaging (MRI) 11

2.2 Time-frequency analysis 18

2.2.1 Fourier Transform 20

2.2.2 Windowed Fourier Transform 23

2.2.3 Wavelet Transform 26

2.3 Cardiac assessment 30

2.3.1 Cardiovascular physiology 30

2.3.2 Electrocardiography (ECG) 36

2.3.3 Photoplethysmography (PPG) 43

2.3.4 Photoplethysmography imaging (PPGi) 46

2.4 Challenges of cardiac assessment in UHF MRI and related work 48

3 Material and methods **52**

3.1 Material 52

3.1.1 Dataset acquired within UHF MRI (ECG, PPG, PPGi) 53

3.1.2 Dataset acquired outside UHF MRI (PPG, PPGi) 56

3.1.3 A setup for PPGi-based cardiac triggering in UHF MRI 58

3.2 PPGi-based methods . . . 61
3.2.1 Cardiac monitoring during UHF MRI . . . 61
3.2.2 Cardiac triggering during UHF MRI . . . 64
3.2.3 Investigation of PPGi signal characteristics . . . 69
3.3 ECG-based methods . . . 75
3.3.1 A novel framework for multiscale parameter estimation (msPE) . . . 75
3.3.2 msPE of synthetic signals . . . 89
3.3.3 msPE of ECG signals from a standard database . . . 95
3.3.4 msPE of QRS complexes acquired within UHF MRI . . . 107

4 Results **109**

4.1 PPGi-based methods . . . 109
4.1.1 Cardiac monitoring during UHF MRI . . . 110
4.1.2 Cardiac triggering during UHF MRI . . . 112
4.1.3 Investigation on PPGi signal characteristics . . . 119
4.2 ECG-based methods . . . 126
4.2.1 msPE of synthetic signals . . . 126
4.2.2 msPE of ECG signals from a standard database . . . 133
4.2.3 msPE of QRS complexes acquired during UHF MRI . . . 139

5 Discussion **142**

5.1 PPGi-based methods . . . 142
5.2 ECG-based methods . . . 146

6 Summary **149**

7 References **150**

1 Introduction

Quest towards higher magnetic fields Within a few decades after acquisition of the first blurry images from brave volunteers in the 1970s, magnetic resonance imaging (MRI) has become the method of choice for radiological examinations of many parts of the human body with particular value in soft tissues. The advent of clinical MRI in the 1980s was accompanied by a trend towards higher magnetic fields which has continued until the present day. The reason lies in the positive relationship between magnetic field strength and signal-to-noise ratio (SNR).

Increasing SNR allows acquiring images with higher spatial resolution and/or higher temporal resolution. The first aspect allows revealing details in the images that are not visible at lower field strengths, while the latter allows enhancing application within clinical practice where examination time is crucial. Furthermore, higher field strengths enable new methodologies, for example by increasing the number of metabolites that can be detected by MR spectroscopy or by opening new scales of the brain for analysis by functional MRI.

Challenges at high magnetic fields Currently there are more than 70 MRI sites worldwide with magnetic field strengths $\geq 7\,\mathrm{T}$ (Tesla (T), which are termed ”ultra-high-fields" (UHF) (Ladd et al. 2018). Recently, the first UHF MRI system with $7\,\mathrm{T}$ entered clinical routine and research systems with $10.5\,\mathrm{T}$ are already available for human use. Research on humans with even higher field strengths on a large scale can be expected in the near future as research on single applications has already been initiated, including brain (Budinger, Bird 2018), body (Ertürk et al. 2016), and non-proton imaging applications (Nagel et al. 2016).

However, higher magnetic fields come at the cost of several biological and technical challenges: Biological challenges include unpleasant effects such as dizziness, nausea, or a metallic taste. Moreover, tissue heating from the electric field induced by radio-frequency pulses becomes a more serious risk due to increased local variability and requires careful consideration. Technical challenges limit the potential of UHF MRI during image acquisition, such as inhomogeneity of the magnetic field (Truong et al. 2006) or an increased susceptibility to artifacts (Birkholz et al. 2004).

Magnetohydrodynamic interactions MRI has always been susceptible to motion artifacts due to its rather long acquisition time, resulting in blurring and ghosting within the acquired MR images which can compromise diagnosis (McRobbie 2006). At low field strengths, a technique called cardiac "triggering" or "gating", can mitigate the negative effects of cardiac activity by synchronizing image acquisition to the heart cycle (Lanzer et al. 1984). Usually, this is done by using electrocardiography (ECG) for measuring the electrical activity of the heart from skin electrodes.

However, this technique cannot be applied in UHF MRI without difficulties as ECG acquisition is distorted, next to other noise sources of minor importance, by the magnetohydrodynamic (MHD) effect. It results from the influence of the magnetic field on the blood flow, leading to voltages on the human body surface that superimpose the ECG signal and increase with magnetic field strength (Gaffey, Tenforde 1981). This distorts the synchronization between image acquisition and the heart cycle, resulting in image artifacts. Furthermore, if ECG is used for cardiac monitoring, MHD interactions might lead to false or missed alarms due to inaccurate heart rate (HR) values.

Alternative methods for cardiac assessment Photoplethysmography (PPG) is an optical measurement of volume changes, which is used by means of pulse oximetry in the context of UHF MRI and has the advantage of not being affected by the magnetic field. However, it has limitations unrelated to MRI, such as signal loss and motion artifacts in clinical practice (Hanning, Alexander-Williams 1995). Furthermore, it is only of limited value for MRI cardiac triggering as there is a delay between cardiac systole and measurement of volume change at the location of the pulse oximeter, such as the finger or the toe (Scott et al. 2009).

Contributions This thesis explores novel approaches for overcoming the described limitations of cardiac assessment in UHF MRI. The main contributions are computer algorithms based on the principles of time-frequency analysis which are evaluated using synthetic data, data from publicly-available reference databases, and data from two studies on human subjects. Two approaches are pursued:

i) Optical cardiac signals: The first approach aims for evaluating to what extent the principle of photoplethysmography imaging (PPGi) can be used as alternative to contact-based ECG and PPG. PPGi constitutes a contact-free measurement of the cardiac activity from skin color changes which are captured by a video camera. The presented contributions are an investigation of PPGi signal characteristics within the UHF MRI setting and the development and evaluation of hardware and software for PPGi-based cardiac monitoring and triggering.

ii) Electrical cardiac signals: The second approach aims for increasing the usefulness of existing ECG hardware by novel algorithms. At most MRI sites, a physiological measurement unit (PMU) is available, providing a basic ECG measurement. However, due to the described constraints, the acquired signal is not comparable to clinical ECG in terms of validity and reliability which requires robust algorithms for obtaining useful information. Therefore, a novel framework for multiscale parameter estimation (msPE) is proposed which is evaluated using synthetic data and various noise models. In order to gain insight into the feasibility of the framework in processing real signals with a high intersubject variability, it is firstly customized for the delineation of (non-MR) ECG signals from a reference database. Building upon the results obtained, the framework is customized for QRS detection in signals acquired using a PMU in UHF MRI, which eventually may serve as a PMU ECG triggering method.

Thesis outline In Chapter 2 the principles of MRI and the measurement of the heart's activity by means of electrical (ECG) and optical (PPG, PPGi) signals are given. Furthermore, an introduction in time-frequency analysis is presented as the proposed algorithms stem from this field. The study data collected in this thesis as well as the developed methods are layed out in detail in Chapter 3 and results are given in Chapter 4. A discussion of obtained results and avenues for future work are given in Chapter 5. The contributions of this thesis are summarized in Chapter 6.

2 Background

This chapter contains brief introductions into MRI (McRobbie 2006), time-frequency analysis (Mallat 2008), the cardiovascular system (Hall 2010) and its assessment using optical and electrical signals (Sörnmo, Laguna 2005). In-depth information can be found in the given standard references.

2.1 Magnetic Resonance Imaging (MRI)[1]

In this section, physical concepts required for a basic understanding of nuclear magnetic resonance and its application in medical imaging are introduced.

Quantum mechanical spin Elementary particles are the building blocks of reality and each carries an intrinsic quantum mechanical property termed spin which describes a quantized angular momentum. Quarks and leptons are two types of elementary particles and, as such, both are assigned a spin quantum number s which describes the spin angular momentum $\vec{S} = (S_x, S_y, S_z)^T$ and its norm

$$\|\vec{S}\| = \frac{h}{2\pi}\sqrt{s(s+1)} \tag{2.1}$$

with $h \approx 6.6 \cdot 10^{-34}$ J·s being the Planck constant. While $\vec{S}$ is defined here as a vector in a Cartesian coordinate frame, usually described by a continuous length/norm and direction, its projection along a direction in space is quantized: s can only take non-negative integers or half-integers and there are $(2s+1)$ associated quantization

[1] Please note that variables introduced in the current chapter may be reassigned in other contexts in the following chapters to conform to the nomenclature of the corresponding field of research.

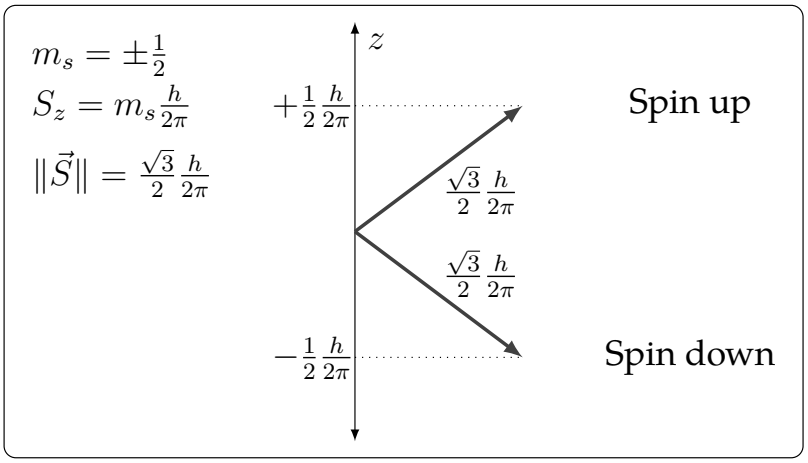

Figure 2.1: Spatial quantization of spin angular momentum for a $s = \frac{1}{2}$ particle.

levels, i.e., states. s equals $\frac{1}{2}$ for quarks and leptons, therefore there are two states (spin "up"/"down") representing the orientation of $\vec{S}$ described by the magnetic quantum number $m_s = \pm\frac{1}{2}$. $\vec{S}$ can only be measured along a single axis and Fig. 2.1 shows the quantization of S_z. In the absence of an external magnetic field, both states have the same energy and therefore the same probability of occurring.

Nuclear spin Ordinary matter is composed of atoms which are composed of electrons bound to a dense nucleus made out of nucleons, i.e., protons and neutrons. Electrons belong to the group of leptons while the nucleons are compositions of quarks. Quarks, leptons, and composites with half-integer spins $s \in \left\{ \frac{1}{2}, \frac{3}{2}, \frac{5}{2}, \cdots \right\}$ are called fermions. A composite fermion that contains an odd number of fermions is a fermion itself, i.e it will have a half-integer spin. For example, a neutron consists of two down- and one up-quark and a proton consists of two up- and one down-quark. Both neutrons and protons have a spin quantum number of $s = \frac{1}{2}$.

The spin of the proton is not carried by only "adding" the spins of the quarks – under the assumption that one of the up-quarks must carry spin up and the other spin down due to the Pauli exclusion principle $\left(\frac{1}{2} - \frac{1}{2} + \frac{1}{2}\right)$. Apparently, gluons, another group of elementary particles, which are massless and carry the force between the quarks, and other interactions contribute as well. To date, the question how the spin of the proton is carried exactly from its constituents is an unsolved problem.

The nucleons carry the spin of the nucleus they constitute. Nuclei with an even number of nucleons do not have spin as they cancel each other out. But, for an odd

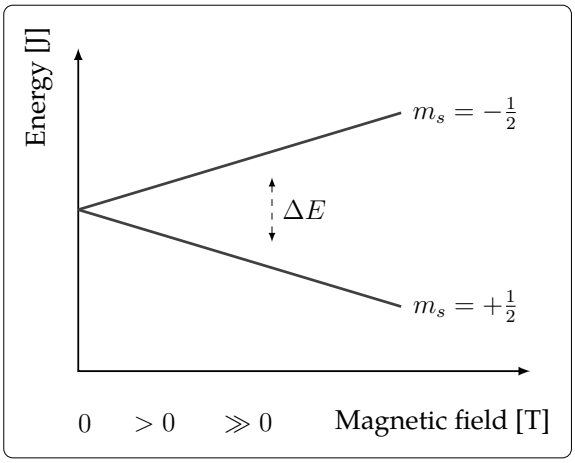

Figure 2.2: Splitting of nuclei spin energies as a function of magnetic field strength.

number of nucleons, the spin angular momentum $\vec{S}$ leads to a circulating electric current and an associated magnetic moment

$$\vec{\mu} = \gamma \vec{S}\,\mathrm{J/T} \tag{2.2}$$

where γ is called gyromagnetic ratio and depends on the type of nucleus. Hence, hydrogen ^{1}H nuclei ($\gamma = 2\pi 42.576\,\mathrm{MHz/T}$) which are the most abundant nuclei in the human body, have a magnetic moment which can be measured when considering them on a macroscopic scale by averaging of large numbers of nuclei.

Properties of ^{1}H nuclear spin When a single ^{1}H nucleus is brought into a static magnetic field $\overrightarrow{B0} = (0, 0, B0_z)^T$, aligned with the z-axis by convention, the spin aligns parallel ($m_s = +\frac{1}{2}$) or antiparallel ($m_s = -\frac{1}{2}$). Due to the interaction with the magnetic field, the energy E of both spin states becomes

$$E = -\gamma\, m_s\, B0_z\, \frac{h}{2\pi}\,\mathrm{J} \tag{2.3}$$

resulting in an energy difference

$$\Delta E = -\gamma\, B0_z\, \frac{h}{2\pi}\,\mathrm{J} \tag{2.4}$$

between both states as depicted in Fig. 2.2. There is a slightly higher probability that the spin of an individual nucleus aligns parallel, and is therefore associated with the lower energy state, than antiparallel and associated with the higher energy state.

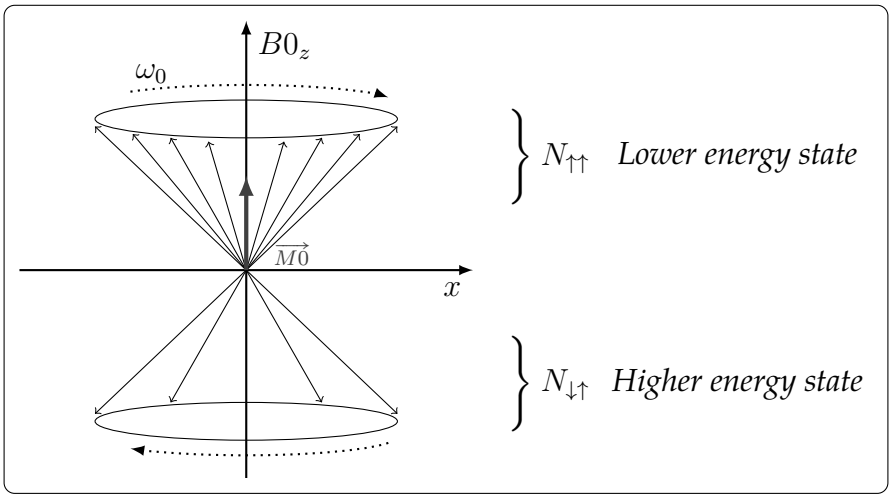

Figure 2.3: Schematic representation (y-axis suppressed) of individual nuclear spins (thin arrows), aligning parallel or antiparallel to the z-axis within a static magnetic field $\overrightarrow{B0}$. As $N_{\uparrow\uparrow} > N_{\downarrow\uparrow}$, $\overrightarrow{M0}$ (bold arrow) precesses around $\overrightarrow{B0}$ with frequency ω_0.

In thermal equilibrium, the ratio between the number of parallel ($N_{\uparrow\uparrow}$) to the number of antiparallel states ($N_{\downarrow\uparrow}$) can be described by Boltzmann statistics

$$\frac{N_{\uparrow\uparrow}}{N_{\downarrow\uparrow}} = e^{-\frac{\Delta E}{kT}} \tag{2.5}$$

where k equals $1.38 \cdot 10^{-23}$ J/K (Boltzmann constant) and T is temperature measured in degrees K, resulting in a slightly higher value of $N_{\uparrow\uparrow}$ at room temperature.

Without an external magnetic field, the equilibrium magnetization which represents the average of all spins on a macroscopic scale, $\overrightarrow{M0} = (M0_x, M0_y, M0_z)$, equals 0 as each spin is equally likely to occupy either energy state. Within the presence of an external magnetic field $\overrightarrow{B0} = (0, 0, B0_z)^T$, the behavior of individual proton spins changes as is illustrated in Fig. 2.3: As the majority of spins is in parallel to $\overrightarrow{B0}$, $\overrightarrow{M0}$ is as well. Considering the proton spin density ρ, representing a given number of proton spins per unit volume, the equilibrium magnetization can be estimated by

$$\overrightarrow{M0} \approx \frac{\rho\, \gamma^2 \left(\frac{h}{2\pi}\right)^2 \overrightarrow{B0}}{4\, k\, T} \text{J/T}. \tag{2.6}$$

As can be seen, by increasing the magnetic field strength, the measurable signal increases proportionally which explains the trend towards higher magnetic field strengths in MRI. By manipulating the magnetization $\overrightarrow{M0}$ with time-dependent magnetic fields, the MRI signal is formed as will be explained in the next section.

Manipulation of the equilibrium magnetization Next to alignment to the z-axis within a magnetic field $\overrightarrow{B0}$, the nuclei spins start to precess, as depicted in Fig. 2.3 as a dotted arrow, with a frequency ω_0 proportional $\overrightarrow{B0}$, which is called the Larmor frequency

$$\omega_0 = \gamma \|\overrightarrow{B0}\| \,\text{MHz}. \tag{2.7}$$

In this case, although the nuclei spins precess with the same frequency, they are not in phase, i.e., they have a random orientation in x- and y-direction. Within a static magnetic field $\overrightarrow{B0}$, the motion of magnetization $\overrightarrow{M}(t)$, which is now assumed to be time-dependent, can be described by

$$\frac{\mathrm{d}\overrightarrow{M}(t)}{\mathrm{d}t} = \gamma \left(\overrightarrow{B0} \times \overrightarrow{M}(t)\right) \tag{2.8}$$

with $\times$ denoting the vector cross product. Considering $\overrightarrow{B}(t) = \overrightarrow{B0} + \overrightarrow{B1}(t)$ where $\overrightarrow{B1}(t) = (\cos(\omega_0 t), \sin(\omega_0 t), 0)^T$ is a time-dependent, perpendicular magnetic field realized by applying a radio-frequency pulse with $\|\overrightarrow{B0}\| \gg \|\overrightarrow{B1}\|$, the motion changes towards

$$\frac{\mathrm{d}\overrightarrow{M}(t)}{\mathrm{d}t} = \gamma \left((\overrightarrow{B0} + \overrightarrow{B1}(t)) \times \overrightarrow{M}(t)\right). \tag{2.9}$$

As a result, a so-called "flip angle" is induced by means of two parallel processes: First, due to the fact that the transmitted radio-frequency field consists of photons with an energy that equals the energy difference between spin states ΔE, a transitions from the parallel to the antiparallel state is induced in the individual spins, reducing $\|\overrightarrow{M}_z\|$. Second, the phases of the spins in x- and y-direction are aligned, which increases the transverse magnetization $\|\overrightarrow{M}(t)_{xy}\|$. The combination of both processes is called "excitation" which can be described by

$$M_x(t) = \sin(\omega_1 t)\sin(\omega_0 t) \tag{2.10}$$

$$M_y(t) = \sin(\omega_1 t)\cos(\omega_0 t) \tag{2.11}$$

$$M_z(t) = \cos(\omega_1 t) \tag{2.12}$$

with $\omega_1 = \gamma \|\overrightarrow{B1}\|\,\text{MHz}$ and therefore $\omega_0 \gg \omega_1$. Fig. 2.4 shows an illustration of hydrogen excitation ($\gamma = 2\pi 42.576\,\text{MHz/T}$) with each point representing a terminal point of the magnetization vector $\overrightarrow{M}(t)$ connected with the origin $(0,0,0)^T$.

As can be seen, magnetization $\overrightarrow{M}(t)$ spirals away from the z- to the xy-axes due to the radio-frequency pulse applied. The longer the time t_{B1} during that $\overrightarrow{B1}$ is applied, the greater the induced flip angle between $\overrightarrow{M}(t)$ and the z-axis which can be computed by $\alpha = \omega_1 t_{B1}$.

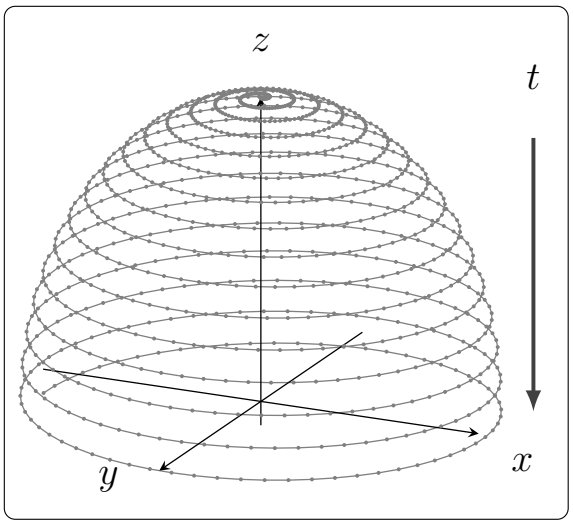

Figure 2.4: Excitation of $\overrightarrow{M}(t)$ with $\|\overrightarrow{B0}\| = 3\,\mathrm{T}$, and $\|\overrightarrow{B1}\| = 50\,\mathrm{mT}$.

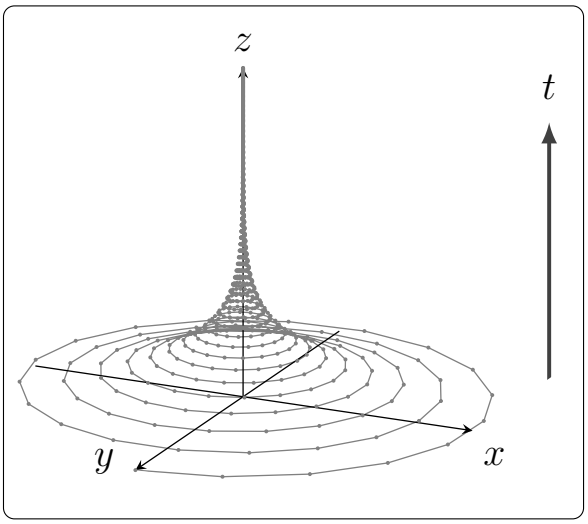

Figure 2.5: Relaxation of $\overrightarrow{M}(t)$ with $\mathrm{T}_1 = 1607\,\mathrm{ms}$ and $\mathrm{T}_2 = 85\,\mathrm{ms}$.

Return to equilibrium state When the radio-frequency radiation is discontinued, $\overrightarrow{B1}$ decays and therefore $\vec{B}(t) = \overrightarrow{B0}$ again. Immediately, the thermal equilibrium is restored during the so-called "relaxation" of the nuclei spins which is described by the phenomenological Bloch equations

$$\frac{\mathrm{d}M(t)_x}{\mathrm{d}t} = \gamma \left(\vec{B}(t) \times \overrightarrow{M}(t)\right)_x - \frac{M_x(t)}{\mathrm{T}_2} \tag{2.13}$$

$$\frac{\mathrm{d}M(t)_y}{\mathrm{d}t} = \gamma \left(\vec{B}(t) \times \overrightarrow{M}(t)\right)_y - \frac{M_y(t)}{\mathrm{T}_2} \tag{2.14}$$

$$\frac{\mathrm{d}M(t)_z}{\mathrm{d}t} = \gamma \left(\vec{B}(t) \times \overrightarrow{M}(t)\right)_z - \frac{M_z - M_0(t)}{\mathrm{T}_1}. \tag{2.15}$$

T_1 describes the longitudinal relaxation time until $M0_z(t)$ is restored to equilibrium magnetization due to spins realigning with $\overrightarrow{B0}$. T_2 describes the loss in transverse magnetization $\overrightarrow{M_{xy}}(t)$ due to reduction of phase coherence of the spins over time. Assuming the radio-frequency pulse was applied so long such that $\overrightarrow{M_z}(t) = 0$, i.e. a $90°$ flip angle was applied, the subsequent relaxation can be described by

$$M_x(t) = M_{0x}\, e^{-t/\mathrm{T}_2}\, \sin(\omega_0 t) \tag{2.16}$$

$$M_y(t) = M_{0y}\, e^{-t/\mathrm{T}_2}\, \cos(\omega_0 t) \tag{2.17}$$

$$M_z(t) = M_{0z} \left(1 - e^{-t/\mathrm{T}_1}\right). \tag{2.18}$$

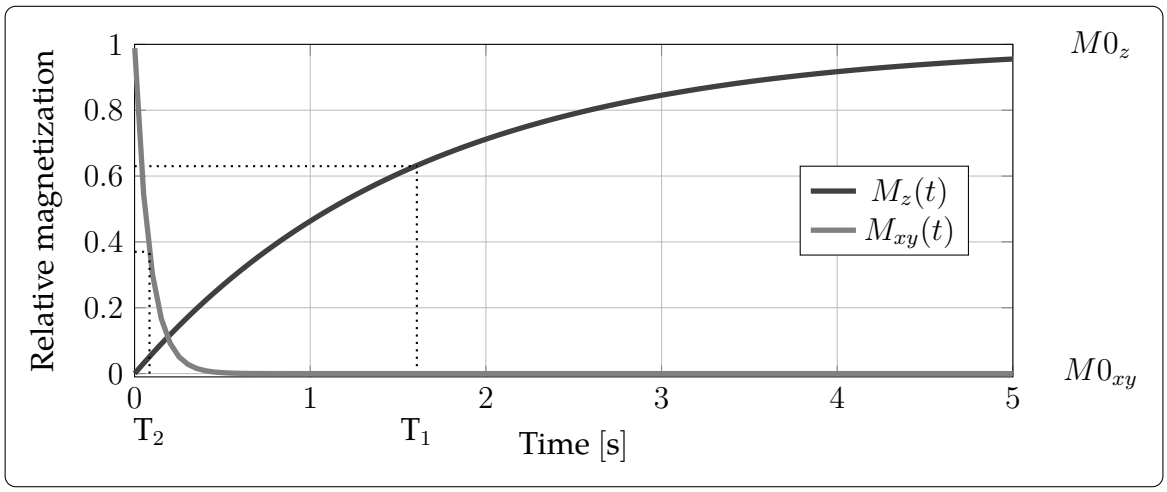

Figure 2.6: Relaxation using the T_1, T_2 values from Fig. 2.5 and $\|\overrightarrow{B0}\| = 3\,\mathrm{T}$.

Fig. 2.5 shows the course of the net magnetization vector $\vec{M}(t)$ over time in z- and xy-direction: While the magnetization is decaying, an oscillating magnetic field appears which induces a small current in a radio-frequency receive coil which constitutes the MRI signal. Fig. 2.6 displays the exemplary course of relaxation in two dimensions: T_1 represents the duration until $M_z(t)$ reaches approximately 63% of the equilibrium magnetization, and T_2 represents the duration until the transverse magnetization is reduced to approximately 37%.

As can be seen in Table 2.1, T_1 and T_2 are both tissue-dependent and T_2 is significantly shorter than T_1. These properties allow for the differentiation of biological tissue based on contrast in MRI images. To obtain the position in space of a portion of tissue, the magnetic field $\vec{B}(t)$ is superposed by linearly increasing variations in x-, y-, and z-direction, called gradients, which subtly change the Larmor frequency and thereby allow to localize the MRI signal.

Table 2.1: Relaxation times [ms] for different tissues, taken from (McRobbie 2006).

▼ Tissue	T1 (0.5 T)	T1 (1.5 T)	T1 (3.0 T)	T2 (0.5 T)	T2 (1.5 T)	T2 (3.0 T)
White matter	520	560	832	107	82	110
Gray matter	780	1100	1331	110	92	80
Fat	192	200	382	108	-	68
Muscle	560	1075	898	34	33	29
Liver	395	570	809	96	-	34

2.2 Time-frequency analysis

In the following, fundamental properties of linear time-invariant operators are introduced as they are indispensable for an understanding of time-frequency analysis. Subsequently, two popular tools of time-frequency analysis, namely the windowed Fourier Transform and the Wavelet Transform, are introduced.

Impulse response Assuming a continuous signal x, one can make use of the sifting property of the Dirac delta function $\delta(t)$ to acquire a value at position in time t by

$$x(t) = \int_{-\infty}^{+\infty} x(u)\ \delta(u-t)\ \mathrm{d}u \tag{2.19}$$

due to the fact that $\delta(t)$ is zero except at $t = 0$. Accordingly, a linear and time-invariant operator L can be used to transform an input signal $x(t)$ to an output signal $y(t)$:

$$y(t) = Lx(t) = \int_{-\infty}^{+\infty} x(u)\ L\delta(u-t)\ \mathrm{d}u \tag{2.20}$$

with operator L being characterized by its impulse response

$$h(t) = L\delta(t). \tag{2.21}$$

Eq. (2.20) can be reformulated such that

$$y(t) = Lx(t) = \int_{-\infty}^{+\infty} x(u)\ h(t-u)\ \mathrm{d}u = \int_{-\infty}^{+\infty} h(u)\ x(t-u)\ \mathrm{d}u = h(t) \star x(t) \tag{2.22}$$

with $\star$ denoting the convolution of $h(t)$ and $x(t)$. Thereby, the output signal $y(t)$ is defined solely by the convolution of input signal $x(t)$ with the impulse response $h(t)$.

Transfer functions If the equation $Dz = \lambda z$ holds for a linear operator D, function z, and scalar λ, z is called the eigenfunction and λ the eigenvalue of D. By applying an exponential wave $e^{j\omega t} \in \mathbb{C}$ with j denoting the imaginary unit and ω the angular frequency, it can be shown that complex exponentials are eigenfunctions of L

$$Le^{j\omega t} = \int_{-\infty}^{+\infty} h(u)\ e^{j\omega(t-u)}\,\mathrm{d}u = e^{j\omega t} \int_{-\infty}^{+\infty} h(u)\ e^{-j\omega u}\,\mathrm{d}u = \underbrace{e^{j\omega t}}_{z}\ \underbrace{\hat{h}(\omega)}_{\lambda} \tag{2.23}$$

with

$$\hat{h}(\omega) = \int_{-\infty}^{+\infty} h(u)\ e^{-j\omega u}\ \mathrm{d}u \tag{2.24}$$

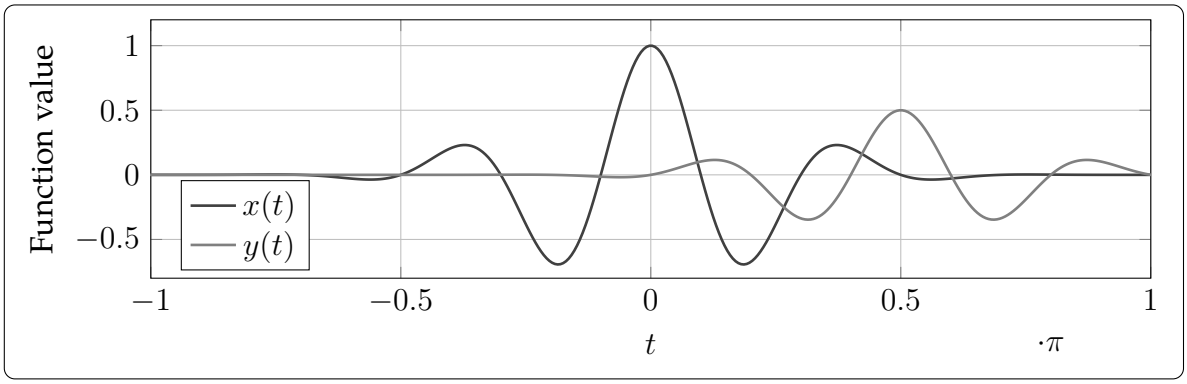

Figure 2.7: $Lx(t) = \alpha x(\alpha\pi - t)$ with $\alpha = 0.5$ is applied to a signal $x(t) = e^{-t^2}\cos(5t)$.

being called the transfer function. Thereby, an output function $y(t)$ has the same frequencies ω as the input signal $x(t)$ with each frequency being scaled by $\hat{h}(\omega)$. Operator L cannot introduce new frequency components to $y(t)$.

Linearity and time invariance The above stated properties of impulse response and transfer function only hold for a linear and time-invariant L. The first requires that the effect of L on the sum of two input signals $x_1 + x_2$ must be equal to the effect on both individual signals

$$L\big(c_1x_1(t) + c_2x_2(t)\big) = Lc_1x_1(t) + Lc_2x_2(t) \tag{2.25}$$

with $c_{\{1,2\}}$ being scalar constants. The second requires that the properties of L do not change over time, i.e., if the input signal in eq. (2.20) is delayed by a certain amount of time τ, the output signal must be delayed by the same amount

$$y(t - \tau) = Lx(t - \tau). \tag{2.26}$$

Fig. 2.7 shows a burst signal $x(t) \in \mathbb{R}$ being processed by an operator L which is basically an amplitude attenuation and time shift using parameter α. As the Dirac delta function is the neutral element of convolution, the filters impulse response can be derived from eq. (2.19) effortlessly: $h(t) = \alpha\delta(\alpha\pi + t)$.

In the given example, the input signal is based on a cosine wave and α results in a $\frac{\pi}{2}$ phase shift, hence the filtered signal equals $y(t) = 0.5e^{-(0.5\pi - t)^2}\sin(5t)$. It is obvious that eq. (2.25) as well as eq. (2.26) hold. The proposed operator is a typical linear and time-invariant filter operator.

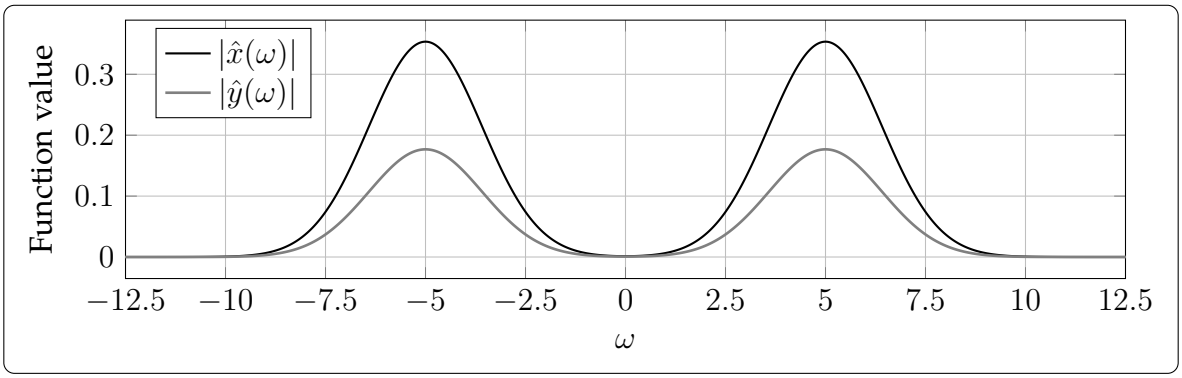

Figure 2.8: Magnitudes $\hat{x}(\omega)$ and $\hat{y}(\omega)$ corresponding to the signals shown in Fig. 2.7.

2.2.1 Fourier Transform

As complex exponentials are eigenfunctions of L, it would be beneficial to represent $x(t)$ using the same basis because then processing of $x(t)$ (eq.(2.22)) would not require the convolution operator anymore. In fact, this can be accomplished using the so-called Fourier Transform that has already been used in eq. (2.24)

$$\hat{x}(\omega) = \int_{-\infty}^{+\infty} x(t)\, e^{-j\omega t}\, \mathrm{d}t = \int_{-\infty}^{+\infty} x(t)\, \big(\cos(\omega t) - j\sin(\omega t)\big)\, \mathrm{d}t \tag{2.27}$$

where the latter is due to Eulers formula $e^{ja} = \cos(a) + j\sin(a)$. As can be seen, the Fourier Transform $\hat{x}(\omega) \in \mathbb{C}$ decomposes the signal $x(t)$ into complex exponentials, respectively trigonometric functions with respect to (w.r.t.) frequency ω.

Magnitude and phase The Fourier Transform can be represented using polar coordinates by magnitude

$$|\hat{x}(\omega)| = \sqrt{\big(\mathrm{Re}(\hat{x}(\omega))^2 + \mathrm{Im}(\hat{x}(\omega))^2\big)} \tag{2.28}$$

and phase

$$\angle\hat{x}(\omega) = \arctan\big(\mathrm{Im}(\hat{x}(\omega))/\,\mathrm{Re}(\hat{x}(\omega))\big) \tag{2.29}$$

where $\mathrm{Re}(\cdot)$ and $\mathrm{Im}(\cdot)$ retrieve the real and imaginary part, respectively. The magnitude gives a measure of the presence of a certain frequency ω in $x(t)$ relative to other frequencies while the phase represents a time shift relative to a complex exponential with the same ω but $\angle z = 0$. It can be seen from Fig. 2.8 that a phase shift has no influence on the magnitude's shape and that the amplitude attenuation can be observed in the magnitudes due to energy conservation of the Fourier Transform.

Hermitian symmetry A corollary of Eulers formula is $\cos(a) = 0.5(e^{ja} + e^{-ja})$, thereby $\hat{x}(\omega)$ is defined for $\pm\omega$. If $x(t) \in \mathbb{R}$ the property of Hermitian symmetry holds and in that case $\hat{x}(\omega)$ is a Hermitian function such that $\hat{x}^*(\omega) = \hat{x}(-\omega)$ with * indicating complex conjugation. This can be seen in Fig. 2.8 as $x(t), y(t) \in \mathbb{R}$.

Inverse Fourier Transform The inverse of the Fourier Transform (eq. (2.27)) is given by

$$x(t) = \frac{1}{2\pi} \int_{-\infty}^{+\infty} \hat{x}(\omega)\, e^{j\omega t}\, \mathrm{d}\omega. \tag{2.30}$$

By applying this to an operation $Lx(t)$ as introduced in eq. (2.20), the usefulness of the Fourier Transform can be demonstrated. It allows obtaining a filtered signal

$$y(t) = Lx(t) = \frac{1}{2\pi} \int_{-\infty}^{+\infty} \hat{h}(\omega)\, \hat{x}(\omega)\, e^{j\omega t}\, \mathrm{d}\omega \tag{2.31}$$

with the amount of a given ω in $x(t)$ amplified or attenuated by the filter's transfer function $\hat{h}(\omega)$. This is depicted in Fig. 2.9 where the relationship between $x(t)$ and its Fourier Transform $\hat{x}(\omega)$ is shown. As can be seen, the value of $\hat{x}(\omega)$ at a certain frequency represents the amount of complex exponentials with this frequency in $x(t)$. Thereby, the removal of a certain frequency component (dashed line) can be realized effortlessly by applying the Fourier Transform eq. (2.27), attenuation of the value using $\hat{h}(\omega)$, and applying the inverse Fourier Transform eq. (2.30).

Convolution theorem Combining eq. (2.22) and eq. (2.31), results in the equality

$$h(t) \star x(t) = \hat{h}(\omega)\, \hat{x}(\omega) \tag{2.32}$$

demonstrating that multiplication is equivalent to convolution after applying the Fourier Transform.

Fourier Transform pairs As can be seen in eq. (2.19), each value of $x(t)$ can be assumed as the weight of a delta impulse $\delta(t)$. Vice versa, as can be seen in eq. (2.27), each value of $\hat{x}(\omega)$ can be assumed as the weight of $e^{-j\omega t}$. As both contain the same information but only in a different representation, it is customary to write $x(t) \rightleftharpoons \hat{x}(\omega)$. It is customary to call the representation of a signal as a function w.r.t. t as being in time domain and w.r.t. ω as being in frequency domain.

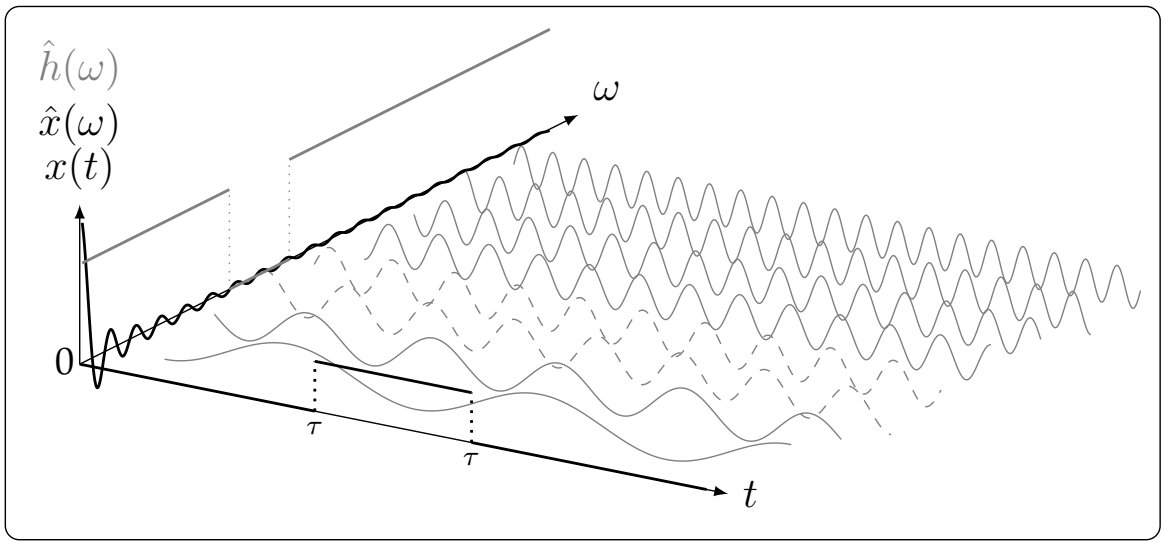

Figure 2.9: Visualization of $x(t) \rightleftharpoons \hat{x}(\omega)$ which is here $1_{[-\tau,\tau]} \rightleftharpoons \frac{\sin(\tau\omega)}{\omega}$. The complex exponentials $e^{-j\omega t}$ as eigenfunctions of the Fourier Transform are visualized as sine waves in the surface spanned between ω- and t-axis. The transfer function $\hat{h}(\omega)$ of L allow to attenuate certain frequencies (dashed lines). $x(t)$ is discontinuous at $t = \pm\tau$ requiring to modify the integral limits of eq. (2.27) but concepts remain identical.

Typical pairs of $x(t) \rightleftharpoons \hat{x}(\omega)$ are:

- $\delta(t) \rightleftharpoons 1$
- $\delta(t-\tau) \rightleftharpoons e^{-j\omega\tau}$
- $\cos(\omega_0 t) \rightleftharpoons \pi(\delta(\omega-\omega_0) + \delta(\omega+\omega_0))$
- $\sin(\omega_0 t) \rightleftharpoons j\pi(\delta(\omega+\omega_0) - \delta(\omega-\omega_0))$

(Bronstein et al. 2016)

Resolution in time and frequency In the next section, joint representations covering the time and frequency domain simultaneously are introduced. However, the pair $\delta(t-\tau) \rightleftharpoons e^{-j\omega\tau}$ has crucial consequences: The Fourier Transform of the Dirac delta function, which is only non-zero at $t = \tau$, is spread over all frequencies and has a constant value of 1 in the case of $\tau = 0$. This trade-off between accuracy in time domain (maximal for $\delta(t)$) and frequency domain (minimal for $\hat{\delta}(\omega)$) is inevitable and holds for window functions in joint time-frequency analysis as well.

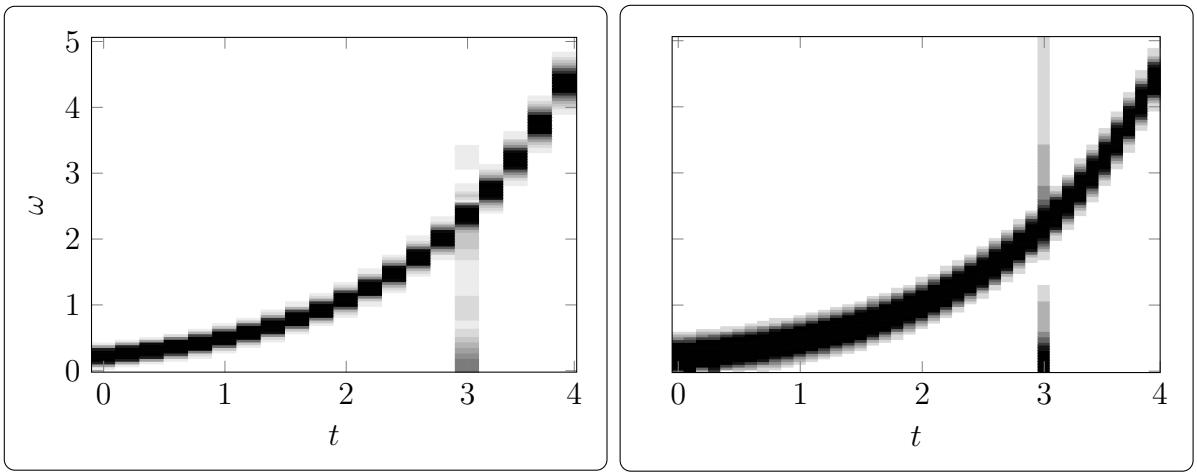

Figure 2.10: Spectrograms of a chirp signal with logarithmically increasing frequency and a short pulse at $t = 3$. A Hamming window $\phi(t) = 0.54 - 0.46\cos(2\pi n/N)$ (Hamming 1989) is used with a support of $N = 100$ (left) and $N = 50$ (right). Increasing pixel darkness denotes increasing amplitudes.

2.2.2 Windowed Fourier Transform

As can be seen in eq. (2.27), the Fourier Transform decomposes a signal using complex exponentials $e^{-j\omega t}$ which are covering the whole real line. This is futile in applications where local properties of signals, e.g. transient phenomena, are of interest. The Fourier Transform cannot give any details about the dynamics of the chirp signal shown in Fig. 2.7 but only about the frequencies w.r.t. all t.

Windowed Fourier Transform To overcome these limitations, Gabor proposed a windowed Fourier Transform by adding a window function (Gabor 1946):

$$\hat{x}(\omega, u) = \int_{-\infty}^{+\infty} x(t)\ \phi(t-u)\ e^{-j\omega t}\ \mathrm{d}t \tag{2.33}$$

The symmetric window function $\phi(t)$ defines which portion of $x(t)$ is analyzed by the conventional Fourier Transform. This allows acquiring a joint time-frequency representation. A typical visualization is shown in Fig. 2.10, which is the spectrogram

$$\left| \int_{-\infty}^{+\infty} x(t)\ \phi(t-u)\ e^{-j\omega t}\ \mathrm{d}t \right|^2 \tag{2.34}$$

that illustrates the energy density in the time-frequency plane (ω, u) (Feichtinger, Strohmer 1998). In Fig. 2.10 spectrograms using two different supports, are shown.

Window functions The so-called "resolution" of the transform introduced in eq. (2.33) is represented by the dimensions of the analyzed section of the time-frequency plane (ω, u), depending on the window function used. Typically, smooth functions are applied because windowing with sharp edges results in noise as the Fourier Transform of a rectangular function is the sinc function ($\rightarrow$ Fig. 2.9).

Fig. 2.10 shows two spectrograms of $x(t)$ computed with a short $\phi(t)$ (left) and a long $\phi(t)$ (right). In contrast to the disjoint time domain (eq. (2.19)) and frequency domain representation (eq. (2.27)), the accuracy of the joint representation is decreased: While $x(t)$ and $\hat{x}(\omega)$ give an exact information how much energy is available w.r.t. a given t or ω value ($\rightarrow$ Fig. 2.9), the joint information $\hat{x}(\omega, u)$ is only available in a non-exact areas of the (ω, u) plane. This inaccuracy is a result of applying the Fourier Transform to a finite-length sample, which cannot be circumvented (Hamming 1989).

Heisenberg boxes[2] The choice of window influences the resolution of $\hat{x}(\omega, u)$. For example, the point in time of the burst of noise in Fig. 2.10 can be localized accurately within the right spectrogram but not in the left. Vice versa, the resolution in ω in the right spectrogram is decreased compared to the left.

The resolution in time and frequency of a window function can be visualized as Heisenberg boxes as shown in Fig. 2.11. An individual box can be interpreted as probability distributions centered at a given coordinate with a spread in time

$$\sigma_t^2 = \int_{-\infty}^{+\infty} t^2 \, |\phi(t)|^2 \, \mathrm{d}t \tag{2.35}$$

and frequency

$$\sigma_\omega^2 = \frac{1}{2\pi} \int_{-\infty}^{+\infty} \omega^2 \, |\hat{\phi}(\omega)|^2 \, \mathrm{d}\omega \tag{2.36}$$

where a smaller (larger) value implies higher (lower) certainty. It can be seen that σ_t and σ_ω are both independent of the actual position in time (t', t'') or frequency (ω', ω''). As can be seen from the fixed side lengths of the Heisenberg boxes, the windowed Fourier Transform provides a fixed resolution for the (ω, u) plane.

[2]The boxes are named after W. Heisenberg (1901-1976) who received the Nobel Prize in Physics in 1932 for his contributions in the context of quantum mechanics.

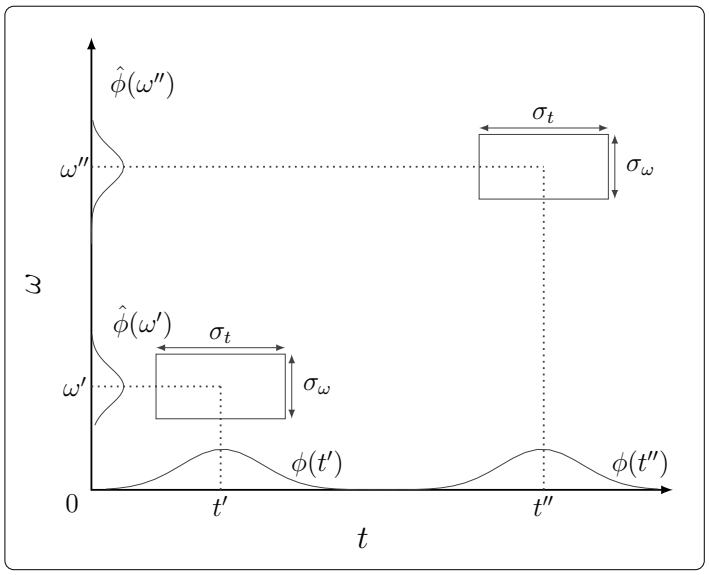

Figure 2.11: Heisenberg boxes of a window function. Dimensions are not up to scale.

Scaling The resolution of a window function can be manipulated intuitively by applying a scaling factor s. A dilated window function is defined by

$$\phi_s(t) = \sqrt{s}\,\phi(t/s), \tag{2.37}$$

resulting in a Heisenberg box with a spread of $s\sigma_t$ and and σ_ω/s. As can be seen, there is an inversely proportional relationship between both dimensions. A smaller side (higher certainty) in one dimension, results in a larger side (lower certainty) in the other dimension, and vice versa. However, s is fixed during calculation of the windowed Fourier Transform, thereby the subscript of $\phi(t)$ is not given in eq. (2.33).

Uncertainty Principle Based on the seminal works in quantum mechanics widely known today as the Heisenberg uncertainty principle (Heisenberg 1927), Gabor proved that (Gabor 1946) there is a lower bound of the area of a Heisenberg box that one cannot undercut:

$$\sigma_t\sigma_\omega \geq 1/2 \tag{2.38}$$

These limits the area of a Heisenberg box and prohibits reducing the uncertainty in both dimensions arbitrarily. It has been shown that using a Gaussian function as $\phi(t)$ minimizes the area, i.e., transforms the inequality in (2.38) to an equality (Feichtinger, Strohmer 1998).

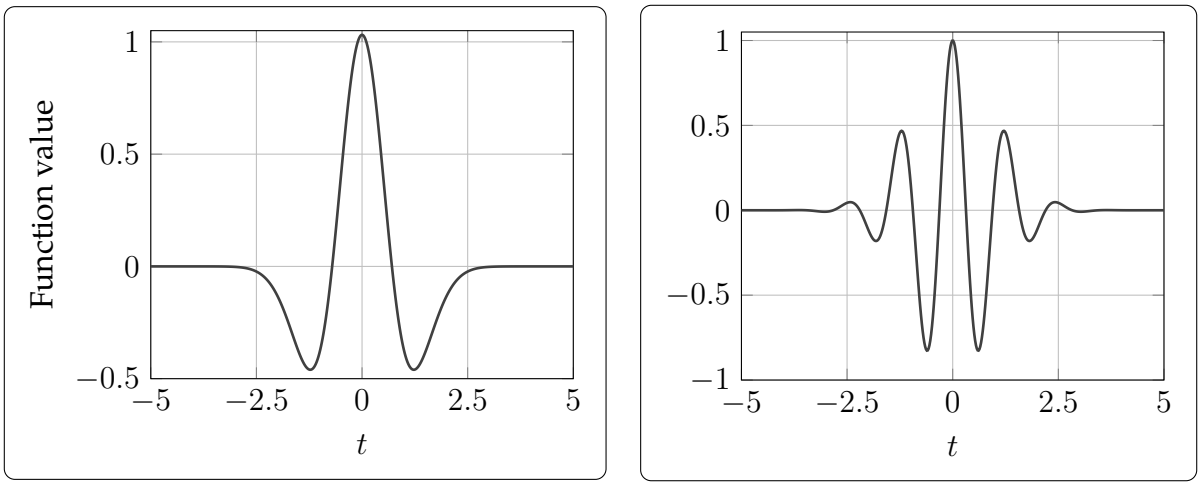

Figure 2.12: *Left:* "Mexican hat" wavelet $\Psi_{\mathrm{m}} = -(2/\pi)^{0.25}(1/\sqrt{3})(4t^2 - 2)e^{-t^2}$. *Right:* "Morlet" wavelet $\Psi_{\mathrm{M}} = e^{-t^2}\cos(5t)$ demonstrating the oscillatory nature of wavelets.

2.2.3 Wavelet Transform

Although the limitations described by the uncertainty principle regarding the area of a Heisenberg box cannot be overcome, the constraint of fixed side lengths throughout the whole (ω, u) plane can be relaxed by the Wavelet Transform. It provides a dynamic time-frequency resolution using dilated window functions by means of a scaling parameter s.

Wavelets The window functions of the Wavelet Transform are called wavelets and are derived from a "mother" wavelet $\Psi \in L^2(\mathbb{R})$ that usually satisfies the admissibility condition (Grossmann, Morlet 1984)

$$\int_{-\infty}^{\infty} \frac{|\hat{\Psi}(\omega)|^2}{|\omega|}\, \mathrm{d}\omega < \infty \tag{2.39}$$

which implies $\hat{\Psi}(0) = 0$ and ensures that the mother wavelet has zero average in time domain $\int_{-\infty}^{\infty} \Psi(t)\ \mathrm{d}t = 0$. This property is responsible for the oscillatory nature of wavelets with positive and negative fluctuations that cancel each other out. Two examples are shown in Fig. 2.12.

Scaling A "family" of wavelets $\{\psi_s\}_{s\in\mathbb{R}^+}$ can be derived from Ψ where each "child"

$$\psi_s(t) = \frac{1}{\sqrt{s}}\, \Psi\left(\frac{t-u}{s}\right) \tag{2.40}$$

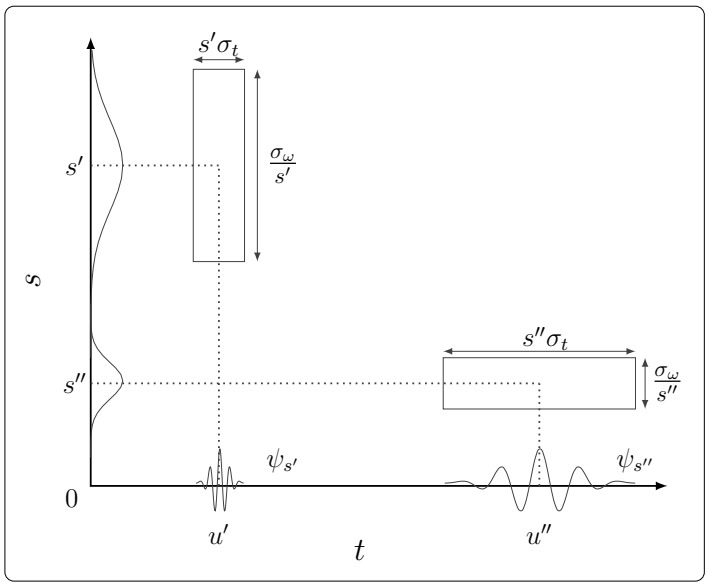

Figure 2.13: Heisenberg boxes of a Morlet wavelet (→ Fig. 2.12, right) with non-fixed lengths. Dimensions are not up to scale.

is dilated by s and shifted in time by u. The factor $s^{-1/2}$ normalizes the energy such that $\int_{-\infty}^{\infty} |\psi_s(t)|^2 \ \mathrm{d}t = 1$ holds. As introduced in eq. (2.37), a scaling factor allows modifying the side lengths of a Heisenberg box, i.e., the support of the window function in time and frequency. The effect of scaling on the Heisenberg boxes can be seen in the Fig. 2.13: A wavelet narrow in time domain $\psi_{s'}(t)$ has a wide support in frequency domain $\hat{\psi}_s(\omega)$ and vice versa.

Wavelet Transform These wavelets are applied to $x(t)$ by the Wavelet Transform

$$\bar{x}(s,u) = \int_{-\infty}^{+\infty} x(t)\ \psi_s(t-u)\ \mathrm{d}t, \tag{2.41}$$

which has some similarities to the windowed Fourier Transform eq. (2.33) but interchanges ω with s. Here lies the difference to the windowed Fourier Transform as scaling becomes part of the transform and thereby allows measuring the local properties of $x(t)$ proportional to s. Similar to the spectrogram (eq. (2.34)), the wavelet coefficients are visualized as a scalogram

$$\left| \int_{-\infty}^{+\infty} x(t)\ \psi_s(t-u)\ \mathrm{d}t \right|^2 \tag{2.42}$$

which is shown in Fig. 2.14 using the Gaussian derivative wavelet (→ Fig. 2.12, left).

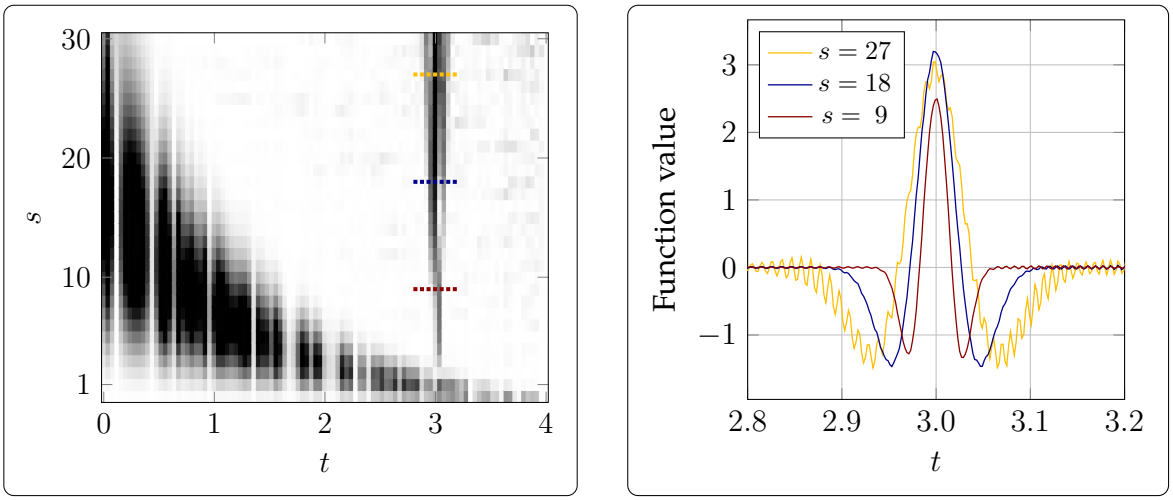

Figure 2.14: *Left:* Scalogram of the chirp signal shown in Fig. 2.10 for $t \in [0, 4]$ and $s \in [1, 30]$ *Right:* Segment $t \in [2.8, 3.2]$ for scales $s \in \{ 9,\ 18,\ 27 \}$.

Fig. 2.14 shows on the right side the interval $t \in [2.8, 3.2]$, containing the high-frequency pulse. The flexible time-frequency resolution visualized in Fig. 2.13 becomes apparent: At low scales (e.g. $s = 9$, red curve), the side of the Heisenberg box in time domain is narrow and therefore the pulse can be localized in time accurately. But, with higher scales (e.g. $s = 27$, yellow curve), the side of the Heisenberg box gets larger and therefore more inaccurate, resulting in a blurred information. In the following, the term "time-scale plane" will be used for (s, u).

Theory of lines in time-scale plane When choosing a Gaussian $e(-x^2)$ as mother wavelet, the Wavelet Transform can be rewritten as a multiscale differential operator (Mallat, Hwang 1992)

$$WT^n x(s, u) = s^n \frac{d^n}{du} \Big(x \star \theta_s \Big)(u) \tag{2.43}$$

where n denotes the number of derivatives and

$$\theta_s(t) = \frac{1}{\sqrt{s}}\, e^{-t^2/s^2} \tag{2.44}$$

is a Gaussian wavelet. WT^n is the n-th derivative of $f(t)$ smoothed by the Gaussian in a range proportional to the scaling factor s. Due to the convolution theorem (→ p. 21), one can interpret the convolution $x \star \theta_s$ as a filtering of $x(t)$ by using the Fourier Transform and θ_s as a window functions (→ Fig. 2.9: $\hat{h}(\omega)$) with scalable properties.

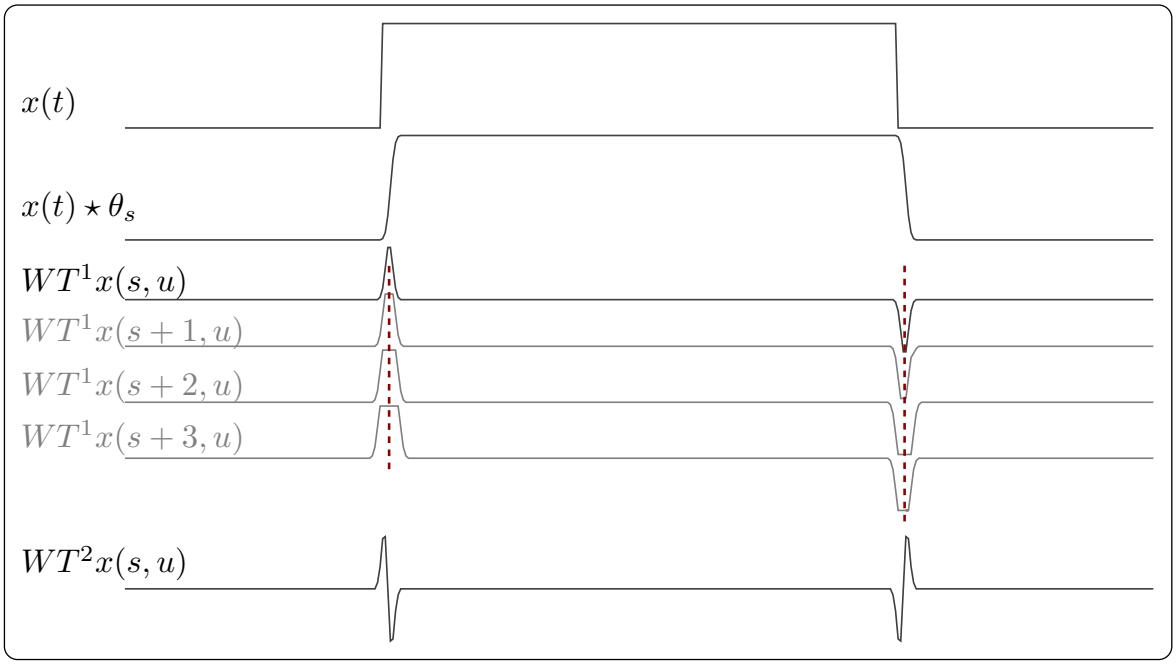

Figure 2.15: Applying the Wavelet Transform according to eq. (2.43) allows detecting singularities in a signal $x(t)$, such as a unit pulse ($\rightarrow$ Fig. 2.9). The convolution $x(t) \star \theta_s$ averages the signal, resulting in extrema in WT^1 and in extrema and zero-crossings in WT^2. Under certain conditions, those exist for all s (dotted line).

Hence, inflection points of $x(t)$ result in extrema in WT^1 and local extrema of $x(t)$ correspond to zero-crossings of WT^1 (Thomas, Finney 1995). The same correspondence exists between any WT^n and WT^{n+1} and is demonstrated in Fig. 2.15. As can be seen, throughout the whole time-scale plane (s, u) lines of extrema appear which are shown exemplarily for four scales of WT^1 (dotted lines). This property also holds for zero-crossings and it has been proven that these lines are never interrupted with decreasing scale when a Gaussian wavelet is used (Yuille, Poggio 1986). The properties of these lines have been part of intense research as they are a well adapted signal representation for many signal processing tasks (Mallat, Hwang 1992).

Digital Signals In this work, algorithms are developed making use of the introduced properties of Fourier Transform, Windowed Fourier Transform, and Wavelet Transform. As the algorithms are processed on quantized, sampled, and finite signals $\{x(nr)\}_{0 \leq n \leq \mathbb{N}}$ at a sampling rate r^{-1}, only approximating the true $x(t)_{t \in \mathbb{R}}$, algorithms have to be adjusted. This is realized by bounding variables and replacing integrals by finite sums. However, the fundamentals introduced in this chapter remain valid.

2.3 Cardiac assessment

In this work, the state of the cardiovascular system is assessed using electrical as well as optical measures, namely electrocardiography (ECG), photoplethysmography (PPG), and photoplethysmography imaging (PPGi). While ECG and PPG are contact-based methods, measurement of PPGi is performed remotely.

2.3.1 Cardiovascular physiology

In this section, anatomical and physiological fundamentals of the cardiovascular system are outlined. The focus lies on aspects required for understanding the assessment of the cardiovascular system using optical and electrical signals.

Cardiovascular system

The cyclic flow of body fluids throughout the human body is an essential requirement and is realized by a complex network of organs called circulatory system. It includes the lymphatic system, which circulates lymph fluid throughout a network of lymph nodes and vessels, and the cardiovascular system, which delivers oxygenated blood from the lungs through a network of blood vessels to the whole body. In the following, the cardiovascular system is of interest only.

Blood Blood is a red body fluid consisting of blood cells (45% of volume) and plasma (55%) (Faller, Schünke 2004). Blood cells comprise (i) erythrocytes, rich in hemoglobin which binds oxygen and is responsible for the blood's color, (ii) leukocytes, playing an important role as part of the immune system, and (iii) thrombocytes, which are responsible for blood clotting. Blood plasma consists of 90% water and is the transport medium for other constituents of the blood, such as proteins, glucose, and hormones (Faller, Schünke 2004).

Hemodynamics The blood is transported throughout the cardiovascular system in different types of blood vessels which are shown in Fig. 2.16 and are classified depending on their function (Costanzo 2009). The largest artery in the human body is the thick-walled aorta which receives oxygenated blood directly from the heart and transports it towards the abdomen. The aorta and other large arteries have an elastic wall, allowing to damp the pressure of the blood being ejected from the heart and

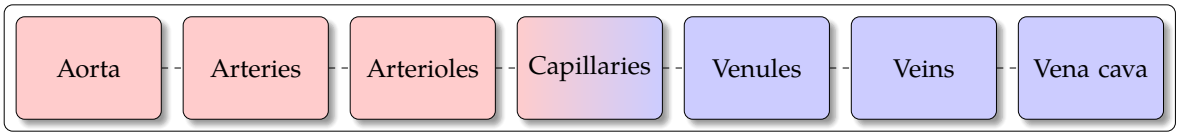

Figure 2.16: Schema of systematic circulation, the blood flow throughout the lower part of the body. Red indicates oxygenated blood and blue deoxygenated blood. In this figure, the heart connecting the aorta and vena cava is not shown (→ Fig. 2.17).

therefore provide a continuous flow of blood to the subsequent vessels (Silbernagl, Despopoulos 2008). Arteries and smaller arterioles transport the blood further until it reaches the capillaries, which are the blood vessels with the smallest diameter. Within them, oxygen, water, and glucose exit the blood and metabolites such as carbon dioxide, acids, urea and creatinine enter (Hall 2010). The capillaries join with venules which widen to veins and carry the deoxygenated blood from the lower part of the human body back into the heart via the inferior vena cava. A similar mechanism transports the blood from the upper part via the superior vena cava. Arteries as well as veins have in common that they do not play an active part in the transport of the blood, i.e. they do not have peristalsis but the blood is transported only by the pressure built up by the beating of the heart (Hall 2010).

Cardiac physiology

The heart is a highly specialized organ located in the middle compartment of the chest with a mass of approximately $250 - 350$ g in an adult (Silbernagl, Despopoulos 2008) and consists mainly of muscle tissue, called myocardium. The heart is divided in a left and right half with both consisting of an upper and a lower chamber, called atrium and ventricle, respectively. The chambers on one side are interconnected with two valves (right: tricuspid valve, left: mitral valve) and the right ventricle is connected to the pulmonary artery via the pulmonary valve and the left ventricle is connected to the aorta via the aortic valve (Costanzo 2009).

Blood circulation The ventricles act as pumps with the right ventricle periodically transporting deoxygenated blood to the lungs, where a process of gas exchange takes place which releases carbon dioxide and receives oxygen, and subsequently transports the oxygenated blood to the rest of the body. The first mechanism is

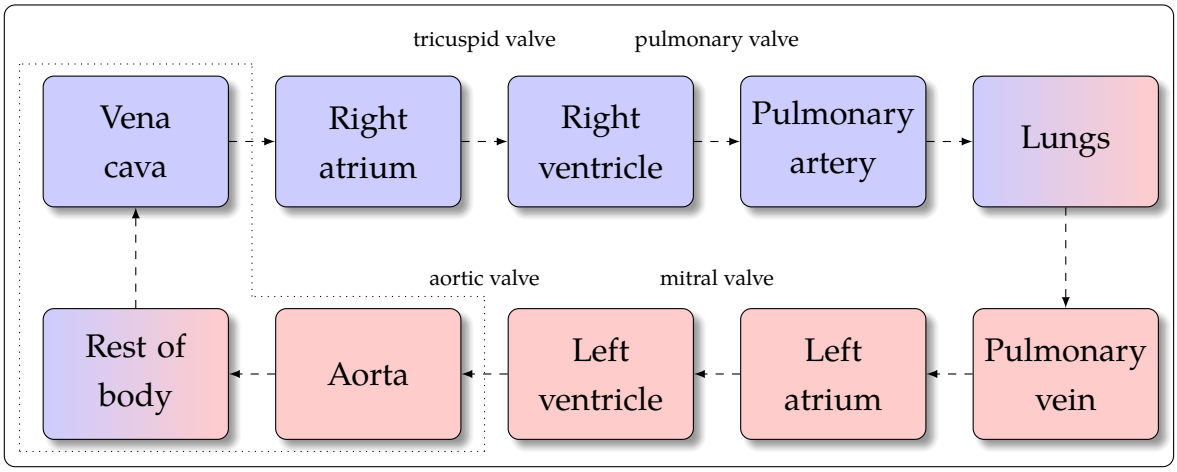

Figure 2.17: Schema of flow of blood throughout the body. Arrows indicate the direction of flow and text above arrows indicates the valves the blood is passing. The outlined area indicates the systemic circulation shown in Fig. 2.16. The remainder constitutes the circulation between the heart, consisting of atria, ventricles, and valves, and lungs termed pulmonary circulation.

shown in Fig. 2.16 and is called pulmonary circulation while the second is termed systemic circulation. The whole process of blood circulation throughout the human body is depicted schematically in Fig. 2.17: It commences with deoxygenated blood arriving via the vena cava in the right atrium, which is then pumped via the tricuspid valve into the right ventricle. When the tricuspid valve shuts and the ventricle is full, it contracts and the blood is pumped into the pulmonary artery and further into the lungs where it is oxygenated. Subsequently, the blood flows via the pulmonary vein into the left atrium and the left ventricle. Once the ventricle is full, the mitral valve shuts and the contraction of the left ventricle pumps the oxygenated blood into the aorta. The blood becomes deoxygenated as it passes the systemic circulation and the process starts again with the deoxygenated blood arriving at the vena cava.

Stages of a cardiac cycle The process described in the previous section is called cardiac cycle and a healthy human has approximately $50 - 75$ cycles per minute[3] in rest. A single cycle can be divided into four stages (I-IV) in which phases of ventricular and atrial contraction (systole), alternate with phases of relaxation (diastole)

[3]Colloquially, the terms heart beat and beats per minute (bpm) are used.

The foregoing cardiac cycle ends with the blood entering passively the atria, passing through the mitral and tricuspid valves into the ventricles (IVa, b). In the phase of atrial systole (IVc), the atrium contracts which completes the filling of the ventricles and the mitral and tricuspid valves close. With all four heart valves being closed, a new cardiac cycle commences with the phase of isovolumetric contraction (I). As the ventricles begin to contract, the pressure inside the ventricles increases fast and culminates in the ejection phase (II): The increasing pressure forces the aortic and pulmonary valves to open and the blood is ejected into the aorta and pulmonary artery (IIa). After blood ejection, the ventricles relax and the pressure decreases, resulting in the aortic and pulmonary valves beginning to close (IIb). Beginning with the closure of the aortic and pulmonary valves, the phase of isovolumetric relaxation (III) is initiated. During phases II and III the atria have been filled with blood again in preparation for the next cycle. In the last phase (IV) the mitral and tricuspid valves open and the blood ejects from the atria into the ventricles (IVa) and slows down shortly after (IVb). The cardiac cycle is completed with the phase of atrial systole (IVc) described before which is then followed by a new cardiac cycle.

Cardiac cells The activity of the heart during a cardiac cycle is made possible by two types of specialized cells. On the one hand there are muscle cells, which are the bulk of cells within the atria and ventricles and responsible for their contraction. On the other hand there are pacemaker cells which are enclosed in the myocardium as clusters and initiate the activity of the muscle cells (Hall 2010). Cardiac muscle cells propagate electrical voltages, often termed action potentials, from cell to cell due to the characteristics of their membranes which are illustrated in Fig. 2.18:

In a resting state ①, the cells are charged positively on the outside and negative on the inside due to a slight excess of positive ions on the outside. When the cell is stimulated, positive ions enter the cell which changes the electrical field by reversing polarity ② until the entire cell is fully depolarized, i.e. charged negatively on the outside and positively on the inside ③. This leads to a mechanical contraction of the cell. Subsequently, positive ions return to the outside and the cell repolarizes again ④ until the polarized state ① is reached again. Myocardial muscle cells are connected via gap junctions enabling a fast cell-to-cell stimulation transmission (Costanzo 2009) and therefore they can contract in unison, resulting in the muscle strength of the heart. The initiating stimulus is generated by the pacemaker cells (Hall 2010).

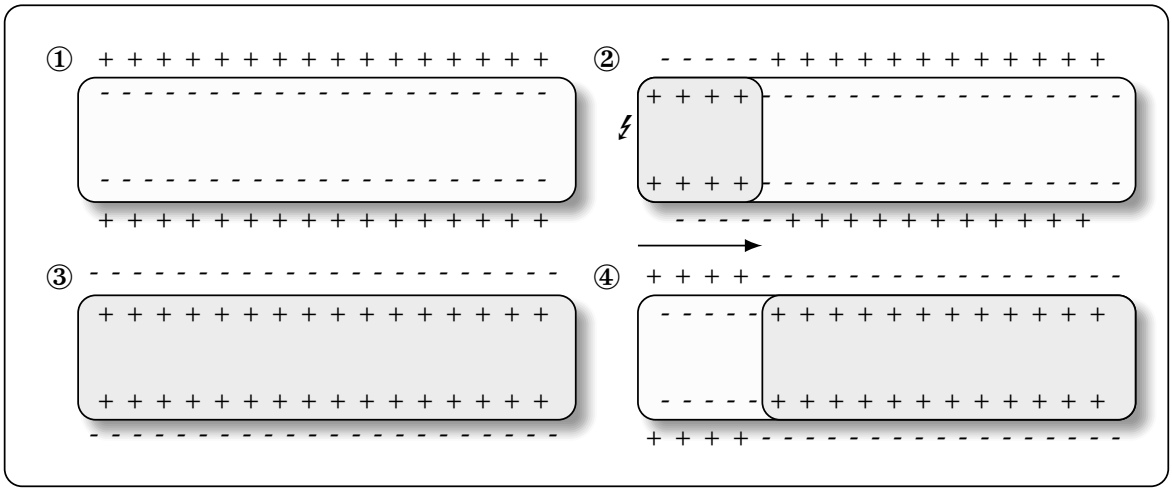

Figure 2.18: Four states of a cardiac muscle cell (rectangle): ① polarized resting state, ② state of depolarization (gray area) initiated by an external stimulus (lightning symbol), ③ fully depolarized state, and ④ state of repolarization. After state ④ the cell returns to state ①. The arrow indicates the direction of depolarization.

Cardiac conduction system The process performed by the pacemaker cells is depicted schematically in Fig. 2.19: The sinoatrial node is located in the right atrium and produces electrical impulses spontaneously, initiating the cardiac cycle. The electrical impulse propagates throughout the atria, results in their depolarization and systole (IVc). The impulse travels towards the atrioventricular node, which is located near the tissue wall separating both atria, which transfers the impulse towards the ventricles but with a delay, ensuring that the atria ejected the right amount of blood into the ventricles before their systole. The lower distal part of the atrioventricular node is called the bundle of His and transmits the impulse further via the bundle branches to the Purkinje fibers, which results in ventricular depolarization and systole (I). As shown in Fig. 2.20, the electrical activity spreads now from the inside out and from apex to base through the ventricular myocardium. In parallel, the atria repolarize. After ventricular systole, there is an isoelectric period without electrical activity (IIa) before the ventricles start to repolarize (IIb). During stages III-IVb the heart is isoelectric again before a new cycle is initated by the sinoatrial node. A comprehensive description of all mechanisms during the four stages of the cardiac cycle can be found in (Silbernagl, Despopoulos 2008).

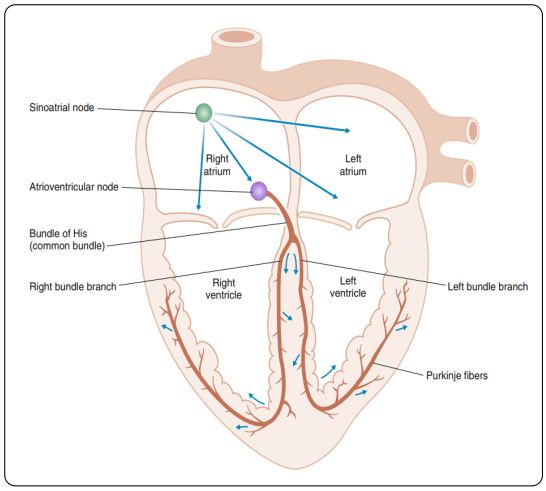

Figure 2.19: Diagram showing the direction of electrical impulses indicated by arrows. Taken from: (Costanzo 2009).

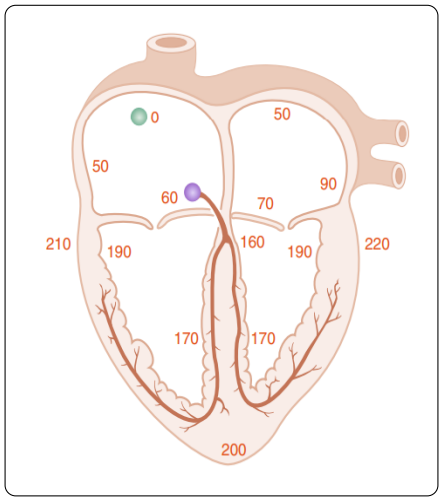

Figure 2.20: Diagram showing time [ms] until impulses arriving at superimposed locations. Taken from: (Costanzo 2009).

Skin physiology

The human skin is the outer barrier of the body, which protects it again harmful influence of the environment. It is composed of three distinctive layers, namely subcutis, dermis, epidermis (Patton, Thibodeau 2012) which are shown in Fig. 2.21.

The epidermis and dermis constitute the outer layers with the epidermis being the thinner region and below the subcutaneous tissue is located (Kamal et al. 1989). The thickness of the skin varies, depending on the body location, from 0.5 to $5\,\mathrm{mm}$ and the highest variability is in the thickness of the dermis (Patton, Thibodeau 2012). The subcutis acts as heat insulator and mainly consists of adipose tissue pervaded by arteries and veins. They rise as capillaries into the dermis where a variety of glands, hair follicles and roots, and mechanoreceptors of the somatosensory system are located as well (Faller, Schünke 2004).

The different phases of the cardiac cycle have an impact on the blood volume within vessels which also holds for the arteries embedded within the subcutis (Allen 2007). During ventricular relaxation, the volume is lowest as no blood is being ejected from the heart. Shortly after ventricular systole, oxygenated blood arrives at the arteries and increases their volume. Oxygenated blood carries oxygen in dissolved form (2%) but the remaining 98% is carried bound to the hemoglobin protein inside the red blood cells with each allowing to bind four oxygen molecules.

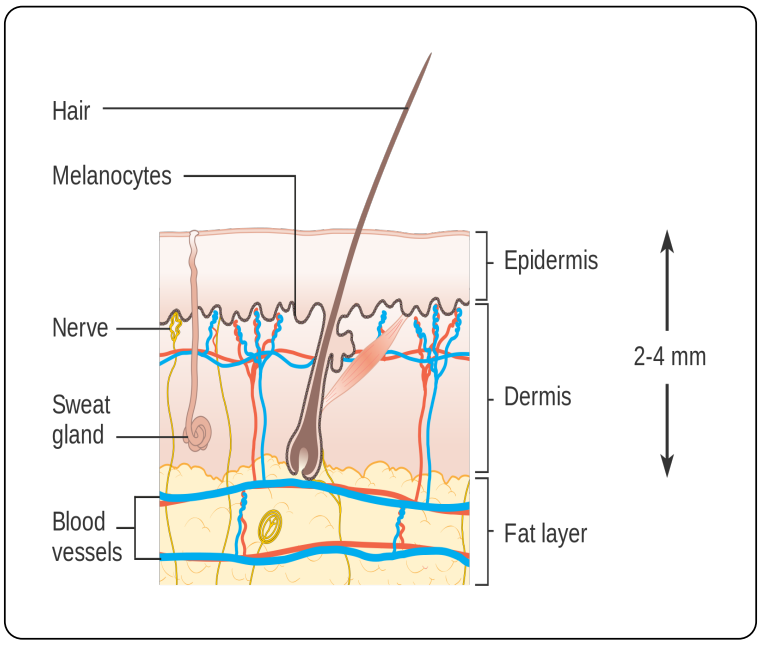

Figure 2.21: Anatomy of the human skin which consists of three layers denoted on the right. Veins and arteries are located in the fat layer called subcutis with capillaries rising into the dermis. Taken from: https://commons.wikimedia.org/wiki/File:Diagram_showing_the_structure_of_the_skin_CRUK_371.svg (Attribution: Cancer Research UK / CC BY-SA (https://creativecommons.org/licenses/by-sa/4.0)

2.3.2 Electrocardiography (ECG)

ECG is a non-invasive measurement of the heart's activity by using pairs of electrodes which are attached to the skin and measure electrical potential differences on its surface. These voltages are measured in units of mV and origin from the depolarization and repolarization of the myocardium during the cardiac cycle. Only the activity of the cardiac muscle cells can be measured; the voltages of the pacemaker cells are too small to be measured.

Lead considerations A fundamental consideration before applying ECG is the configuration of leads, i.e., the number and setup of electrodes used for measuring the potential difference. A basic configuration are bipolar Einthoven[4] leads, which are electrodes attached to the wrist of the left and right arm and one ground electrode

[4]W. Einthoven received the Nobel Prize in Physiology or Medicine in 1924 for inventing the first practical ECG device. He also assigned letters (P, QRS, T) to ECG waves that will be introduced later.

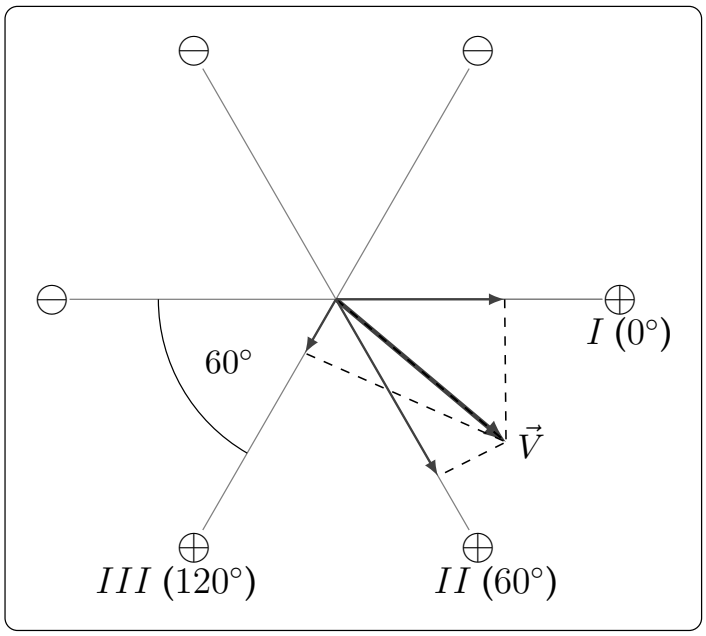

Figure 2.22: Relationship between the cardiac vector $\vec{V}$ (bold arrow) and the measured ECG signal using leads I-III (thin arrows). $\oplus$ and $\ominus$ indicate the positive and negative electrodes, respectively. For the given $\vec{V}$, all leads result in a positive value.

attached to the left leg (Silbernagl, Despopoulos 2008). This allows constructing the lead I by measuring the potential between the left arm's electrode vs. the right arm's electrode. This lead measures the heart's activity with a $0°$ angle of orientation. Leads II and III are obtained by measuring the voltages between the left leg and right arm ($60°$) as well as the left leg and the left arm ($120°$), respectively.

Thereby, the three leads allow to assess the heart's activity from three different angles as visualized in Fig. 2.22. In practice, it is not necessary to acquire the signals of all three leads as any single lead can be reconstructed from the other two (Sörnmo, Laguna 2005).

Cardiac vector The instantaneous, accumulated electrical activity of the heart is often represented as three-dimensional vector $\vec{V}$, moving in space and time throughout the cardiac cycle. However, a single lead can only measure one dimension of $\vec{V}$. The more $\vec{V}$ points in a lead's direction and the higher the magnitude, the higher the measured voltages will be at this lead. This underlines the usefulness of using multiple leads for assessing different properties of the cardiac conduction system.

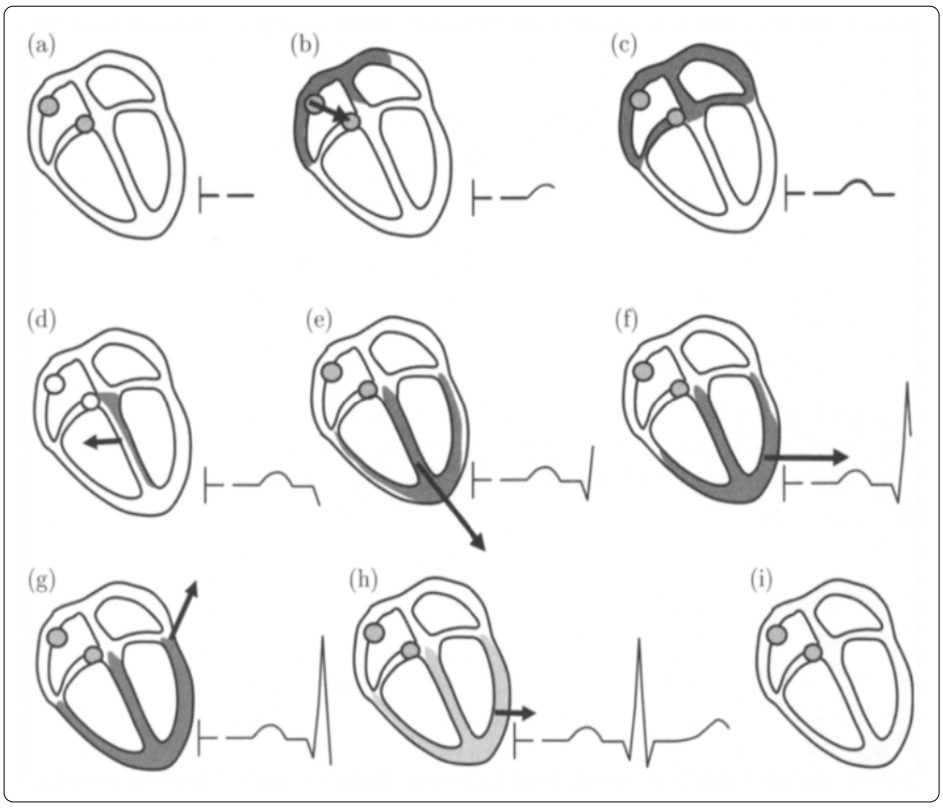

Figure 2.23: Cardiac electrical activity and direction of $\vec{V}$ throughout a cardiac cycle. Propagation of cardiac impulses is shown as gray areas. The ECG is assumed to be acquired from one electrode positioned at the $\vdash$ symbol therefore a lead similar to lead II shown in Fig. 2.22 is used. Taken from: (Sörnmo, Laguna 2005).

Depending on the aspect that is examined, the complex activity of the cardiac conduction system cannot be adequately represented by leads I-III only. Thereby, more sophisticated methods are available, e.g. the augmented unipolar limb leads ($-30°$, $90°$, $-150°$), that were introduced to fill the gaps of the bipolar leads ($\rightarrow$ Fig. 2.22) or 12-lead ECG making use of ten electrodes in total (Silbernagl, Despopoulos 2008). This allows obtaining a $360°$ view of the heart with a distance of $30°$ between each lead (Sörnmo, Laguna 2005).

ECG delineation Fig. 2.22 shows $\vec{V}$ for a single instant of time. Fig. 2.23 shows a visualization of its dynamics during one cardiac cycle. As can be seen, the acquired signal is plotted w.r.t. time and typically, the signal shows a constant baseline, called isoelectric line, which represents the accumulated resting membrane potentials of

the cardiac cells which is shown in Fig. 2.23 a). The signal deflects from and returns to the baseline in a pseudo-periodic pattern of "waves" with each corresponding to a different phase of the cardiac cycle (→ Chapter 2.3.1).

Those waves were given lettered names (P, QRS, T, U) and each has a typical duration and morphology. It is customary to define a wave by its fiducial points, i.e., their center, onset, and offset point in time, which is a compact representation of the most important information. The intervals between waves are given names based on the waves they lie between. Waves and intervals both contain clinically relevant information and a deviation from the normal values allows making a diagnosis of cardiac diseases. The following waves and intervals are contained within ECG signals acquired from healthy subjects:

- *P-wave* (stage IVb, Fig. 2.23 b-c)) is a result of the electrical impulse triggered by the sinoatrial node which initiates the cardiac cycle. As shown in Fig. 2.20, the impulse travels first throughout the atria, results in their synchronized depolarization, and a positive wave on leads $I - III$. Typically, a P-wave has a duration of approximately $0.1\,\mathrm{s}$ (Silbernagl, Despopoulos 2008).

- *PQ interval* (stage IVc, Fig. 2.23 c)) represents the interval between P- and Q-wave. Usually the signal is at isoline without dominant peaks as the voltages travel to the atrioventricular node without muscle activity. The normal duration of the PQ interval is up to $0.2\,\mathrm{s}$ (Silbernagl, Despopoulos 2008).

- *QRS complex* (Fig. 2.23 d-g)) represents three different waves: Q-, R-, and S-wave. They are often summarized as QRS complex as they occur in rapid succession during ventricular depolarization. The normal duration of the QRS complex is approximately $0.08\,\mathrm{s}$ (Silbernagl, Despopoulos 2008).

  - *Q-wave* (stage IVc, Fig. 2.23 d)) represents the electrical impulses arriving first at the bundle of His in the interventricular septum between left and right ventricles (→ Fig. 2.20). The potential spreads from the inside out and from apex to base through the ventricular interventricular septum. Therefore $\vec{V}$ points for a short time away from the positive electrodes of leads I-III, resulting in the short and negative Q-wave.
  - *R-wave* (stage I, Fig. 2.23 e)) represents the following depolarization of the main ventricles. This is usually the most dominant part of an ECG trace as it represents the depolarization of the large ventricular muscles.

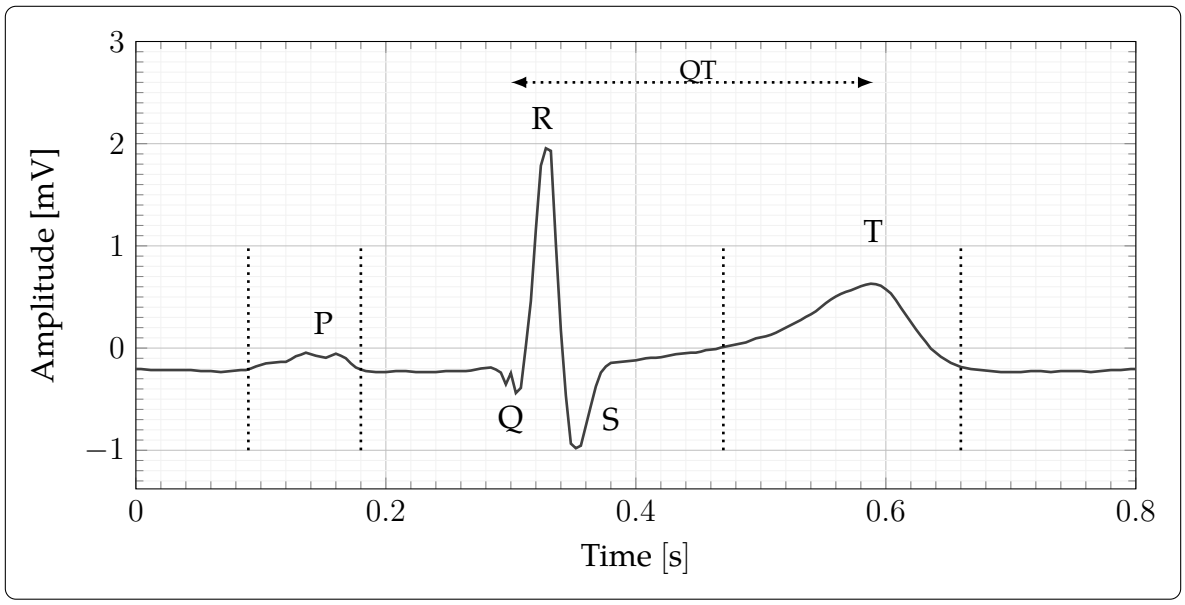

Figure 2.24: ECG signal (record id: 16483) from the MIT-BIH Normal Sinus Rhythm Database (The Beth Israel Deaconess Medical Center 1990) with manual annotations of all P-/Q-/R-/S- and T-waves, and the QT interval (arrow). Each wave has an onset and offset point, which are shown here for the P- and T-wave as dotted lines.

  - *S-wave* (stage I, Fig. 2.23 f-g)) represents the final step of depolarization at the base of the heart that leads to full ventricular depolarization. Before full depolarization, $\vec{V}$ points to the top right, leading to the negative S-wave.

- *ST segment* (stage I, IIa) represents the full ventricular depolarization. As there is no muscle activity similar to the PR interval, the ECG signal returns to isoline.

- *T-wave* (stage IIb, Fig. 2.23 h)) represents the repolarization of the ventricles which usually takes up to $0.25\,\mathrm{s}$. One could expect a negative repolarization wave but due to the perpendicular direction of repolarization, it is positive.

- *U-wave* (stage III) represents the repolarisation of the Purkinje fibres but is only rarely visible due to its minimal intensity. Thereby, it is not shown in Fig. 2.23.

A typical ECG signal from a healthy person is shown in Fig. 2.24 with annotated waves and intervals. Detecting these points automatically is called delineation. In-depth information on this line of techniques can be found in (Sörnmo, Laguna 2005).

Intervals Between two cardiac cycles, i.e., R-waves, the RR interval can be measured which gives the duration between two cardiac cycles and the reciprocal values gives the heart rate (HR) (Husar 2010). It is an important marker for cardiac health and indicates several diseases such as bradycardia (too low HR), tachycardia (too high HR), or dysrhythmia (Patton, Thibodeau 2012). The variation of HR over time is called heart rate variability (HRV) and allows assessing the state of the autonomic nervous system which regulates cardiac activity (Acharya et al. 2006).

There are more segments which can be derived for gaining insight into the cardiac health status, for example the QT interval which is measured from the Q-wave onset to the T-wave offset and represents the duration from ventricular depolarization to repolarization. As such, it is a meaningful marker for several cardiac diseases, e.g. a prolonged QT interval is a predictor for sudden death (Schwartz, Wolf 1978).

Artifacts Despite careful preparation, the acquisition of ECG signals can be distorted by noise introduced by the hardware used or by the patient (Husar 2010). Fig. 2.25 shows typical example artifacts introduced by a patient. There can be deformations due to cardiac diseases, such as ① fragmented QRS complexes or ② unexpected waveforms. Furthermore, noise due to motion such as ③ baseline shifts or ④ temporary high-frequency noise can occur.

Noise introduced by the measurement hardware can occur due to non-adequate configuration of the ECG recorder, non-adequate patient preparation, or external influence, such as 50 Hz interferences from power lines. In clinical practice, stationary ECG devices with disposable electrodes, typically silver–silver chloride electrodes, are applied to patients at rest. Usually, the skin is shaved and cleaned before the electrodes are attached because weak contact can lead to noise. In clinical practice, an examination takes in most cases up to one minute and the signal is printed on a grid for instantaneous visual analysis by the cardiologist.

For certain groups of patients, e.g. chronically ill patients or patients with an infrequently occurring arrhythmia, long-time ECG measurement can be beneficial. So-called Holter monitors, portable devices are available, where the signals are stored on memory cards and measurements can take up to 72 hours. In order to keep the patient's comfort during daily life as high as possible, usually a low number of electrodes is used. Of course, there is an increased risk of electrode detaching and motion artifacts in the measured signals due to the mobile setting (Zheng et al. 2014).

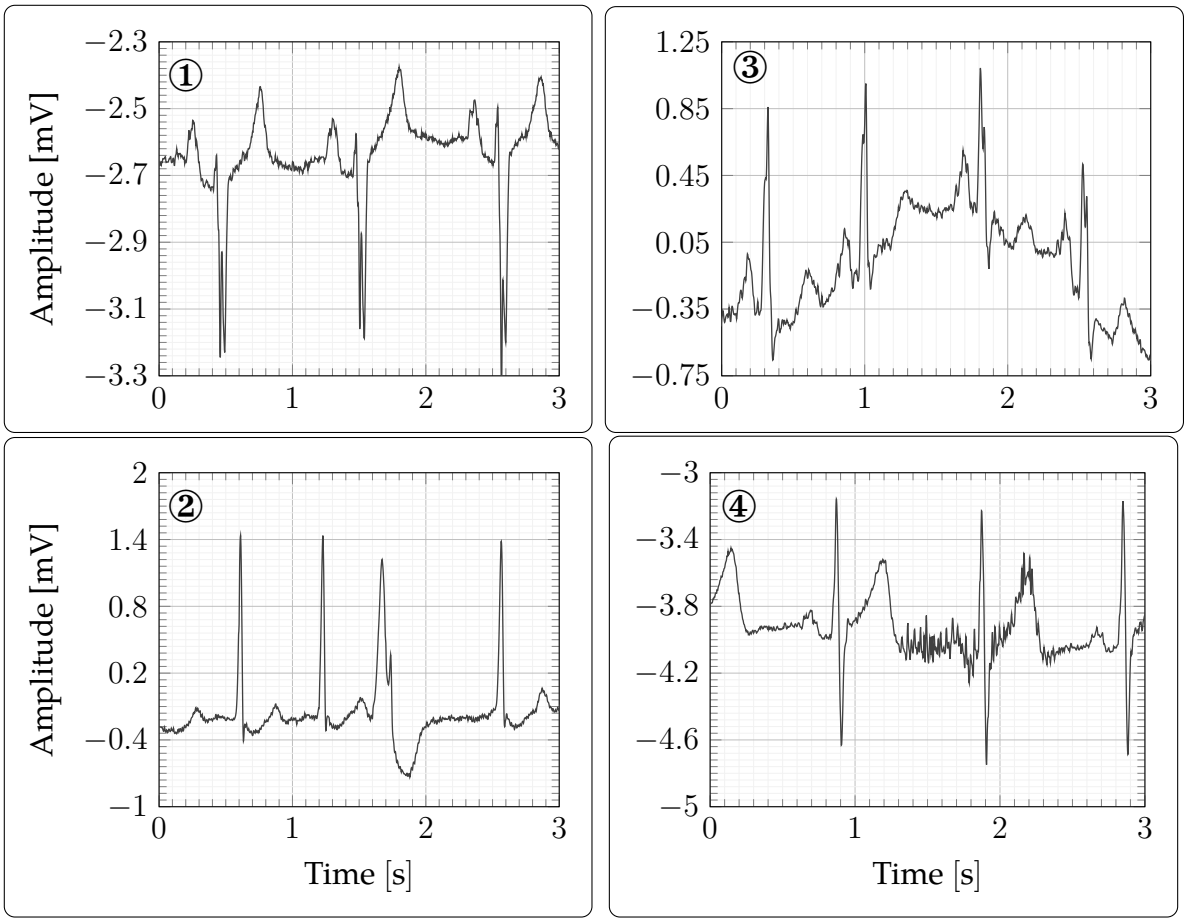

Figure 2.25: Example signals from the QT database (Laguna, Mark, et al. 1997) showing typical artifacts occurring during ECG acquisition: ① Atypical, fragmented QRS complex morphology (record: `sele0133`), ② Premature ventricular contraction (record: `sel221`), ③ Baseline wandering (record: `sel39`), ④ Bursts of high-frequency noise (record: `sele0129`). Further information on the QT database can be found in the Appendix.

Technical considerations The potential differences measured by the electrodes from the skin are sampled within an ECG device using several steps of amplification, filtering, analog-to-digital conversion, and finally storage which are omitted here. An in-depth analysis can be found in (Husar 2010).

Two parameters have a major effect on signal quality from a signal processing point of view: sampling and quantization. Quantization describes the process of mapping the values measured to the interval of quantization values, i.e., the range of

values the stored signal is about to contain, which is typically in the range $[1, 2^N]$. For most applications, quantization levels from 2^8 to 2^{12} are sufficient. The sampling rate defines the number of measured values per second which typically varies from 250 to 1000 Hz for ECG. The higher the sampling and quantization levels, the higher the required disk space and processing power. This aspect requires balancing accuracy versus run time if mobile or low-power ECG devices are in use (Zheng et al. 2014).

2.3.3 Photoplethysmography (PPG)

The term PPG describes the optical measurement of volume changes, which can be used for detecting volume changes of the blood circulating in the microvascular bed of tissue. This line of techniques makes use of the fact that there is a relationship between the blood's volume and the amount of light that is reflected from the blood.

PPG instrumentation Pulse oximetry is the most widely used method for measurement of a PPG waveform and is part of standard of care in anesthesiology and intensive care (Webster 1997). In most areas of application, it is used for monitoring HR or oxygen saturation (SpO_2) (Allen 2007). The success of pulse oximetry lies in its affordable price, minimal risk, and simple application. Usually, a probe consists of two light sources and a photodetector with probes for transmissive or reflective measurement being available.

In the first case, the source of light and the sensor are on opposite sides of the tissue while in the latter case, both are on the same side and the sensor measures the reflected light (Kamal et al. 1989). In clinical practice, the pulse oximeter is applied transmissively at regions of thin skin, such as the finger tip, a toe, or the earlobe. In the majority of cases, the finger is used since the probe can be fixed securely. Furthermore, the blood flow to the finger is usually decreasing before the blood flow to other organs (Webster 1997) allowing early detection of critical situations.

During measurement, light is emitted into the skin, which consists of multiple layers (→ Chapter 2.3.1), and the majority of light is scattered and absorbed by tissue, bones, or blood. However, some of the light reaches the arterial blood vessels that have a blood volume synchronized to the pulsations of the beating heart (Kamal et al. 1989). Therefore, when measuring the reflected or transmitted light, there is a slowly varying baseline and an alternating signal with a frequency similar to the HR.

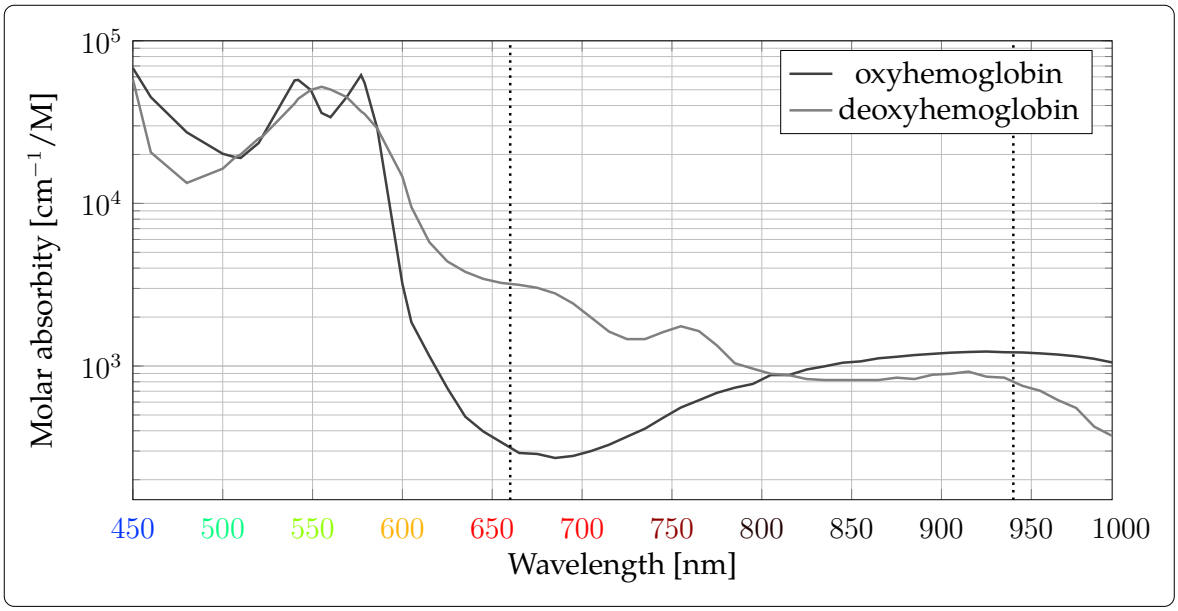

Figure 2.26: Light absorbance of hemoglobin & oxyhemoglobin with values taken from (Takatani, Graham 1979). The wavelength values on the x-axis have a color according to visible-light spectrum for humans, invisible wavelengths are shown in black. Dotted lines denote typical center wavelengths used for the light sources in pulse oximetry.

SpO_2 measurement One of the advantages of pulse oximetry is the ability to continuously and noninvasively measure the oxygen saturation. Oxygenated hemoglobin carries up to four oxygen molecules (→ Chapter 2.3.1) and bonding changes its light absorption properties. Therefore oxygen saturation can be estimated from the ratio between oxygenated hemoglobin concentration and total hemoglobin concentration.

The molar absorption coefficient describes how much light of a certain wavelength is filtered by a chemical species. As shown in Fig. 2.26, deoxygenated hemoglobin absorbs more red light while oxygenated hemoglobin absorbs more infrared light. Typically, two light emitting diodes (LEDs) with wavelengths of $660\,\text{nm}$ and $940\,\text{nm}$ (dotted lines) are used which are turned on and off alternately.

The synchronized photodiodes receive two signals, one for deoxygenated hemoglobin and one for oxygenated hemoglobin. The ratio between both is modified by empirical values obtained during calibration, resulting in the final SpO_2 value (Allen 2007). In a healthy human this value typically lies between 97% and 100% (Hall 2010).

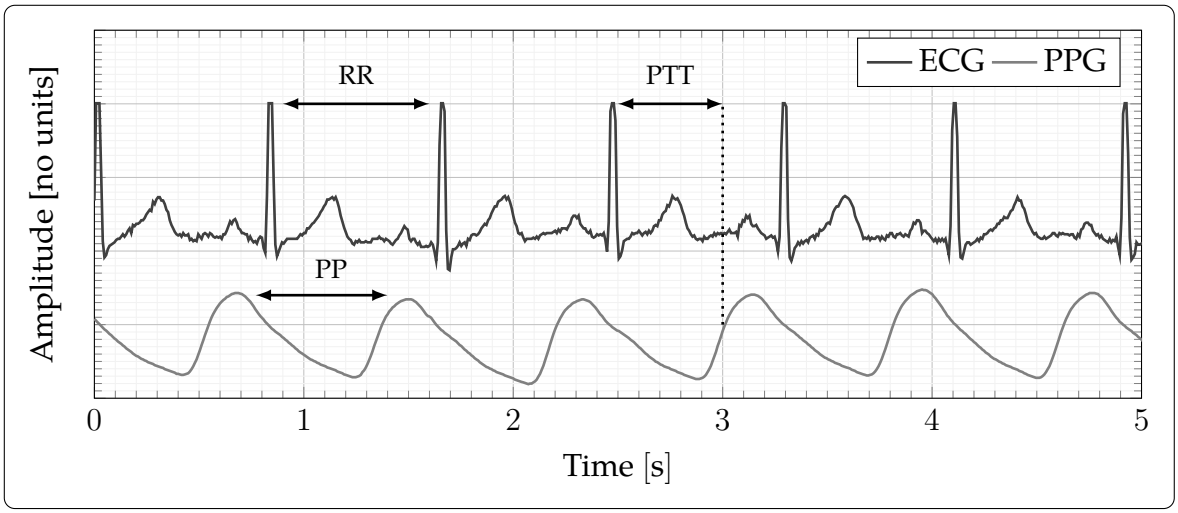

Figure 2.27: ECG and PPG (pulse oximeter) signal from the MIMIC II Waveform Database (Saeed et al. 2011). The peak-to-peak periods of the ECG signal (RR) and the PPG signal (PP) are similar but there is a phase shift between both due to PTT.

HR measurement During systole the amount of blood within the arteries increases and pressure builds up (→ Chapter 2.3.1). Therefore, the diameter of the arteries increases which results in a longer optical pathway (Webster 1997) and the intensity of light received at the photodetector is decreased. Vice versa, during ventricular diastole, the blood volume decreases, which decreases light absorption and therefore increases the measured light intensity. Due to the recurrence of these fluctuations with each cardiac cycle, subtle "waves" are measured by the photodetector. Fig. 2.27 depicts an example PPG signal where the alternating waveform can be clearly seen. The baseline signal is modulated by slowly changing aspects such as respiration, activity of the sympathetic nervous system, as well as thermoregulation (Allen 2007) and is therefore approximately constant during the $5\,\mathrm{s}$ period shown. Furthermore, it can be seen that the PPG waveform can also be used for delineating the cardiac cycle. By detecting the peaks of the PPG waveform, the HR can be estimated similar to ECG analysis by computing the reciprocal value of the peak-to-peak (PP) intervals.

Between ECG and PPG is a delay due to the period from ventricle depolarization to the arrival of the pulse wave at the location of PPG acquisition, termed pulse transit time (PTT). For its computation, the R-wave, representing the opening of the aortic valve, is used as starting point and the point in time where the PPG wave reaches 50%, denoting the influx of the pulse wave (Smith et al. 1999), is used as end point.

Artifacts Similar to ECG electrodes, pulse oximeter probes suffer from motion artifacts which can degrade SNR severely. These artifacts occur often in clinical settings where patient monitoring is of highest importance, such as intensive care or pediatric stations where patients suffer from involuntary movement (Allen 2007). Furthermore, low perfusion might lead to only minimal amplitudes of the PPG waveform which can lead to incorrect HR estimates (Hanning, Alexander-Williams 1995). Both aspects may lead to false alarms, resulting in alarm fatigue within the clinical staff which compromises patient safety.

2.3.4 Photoplethysmography imaging (PPGi)

PPGi is a modification of contact-based and single-point PPG measurement, such as pulse oximetry. This methodology is based on the same principal of optical blood volume estimation but is applied remotely by using a video camera. While initial works began two decades ago (Wu et al. 2000), the recent advances in computer processing power and the increased availability of high-quality consumer camera sensors led to an intense research activity in the scientific community in recent years (Sun, Thakor 2016; Zaunseder et al. 2018; Antink et al. 2019).

PPGi instrumentation The basic idea of PPGi is straightforward by using a video camera instead of a photodiode as sensor. This approach obtains a spatial image where each pixel can be assumed as an individual PPGi sensor. This is demonstrated in Fig. 2.28: An image stack from a video is shown, where each frame can be assumed as a matrix of single pixels/sensors. Depending on the captured local anatomy, a pixel might have i) no cardiac signal (e.g. hair), ii) a signal with low SNR due to noise (e.g. motion artifacts at the eyes), or iii) a signal with high SNR (e.g. the forehead) such that a cardiac component becomes visible. A common technique for increasing SNR is averaging multiple pixels by means of a region-of-interest (ROI), which is indicated by the red area in Fig. 2.28. The averaged value constitutes the value of the PPGi signal for a single frame. It can be seen that the local averaging increases SNR such that the close relationship between the PPGi signal and the PPG signal becomes apparent. Both have a similar dominant frequency, but evidently PPGi has lower SNR.

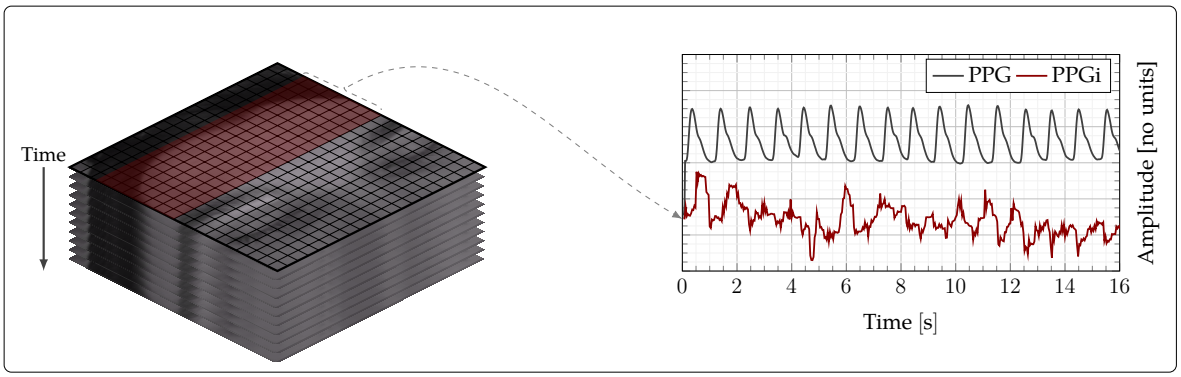

Figure 2.28: Computation of the PPGi signal from a video. The image stack from the video of a subject's forehead is shown (left) with a suitable ROI covering the forehead indicated by red color. The grid lines are not part of the actual video. The averaged pixel values within the ROI constitute the PPGi signal for each frame. Computing the averaged value for a sequence of frames results in the one-dimensional PPGi signal (right) similar to the PPG signal but with lower SNR.

PPGi signal At the beginning of PPGi research, it was assumed that the same underlying signal as in conventional pulse oximetry is measured. However, recently it has been shown that there might be other influencing signal sources than blood volume pulsations only. For example, it has been demonstrated that illumination of the skin by green light (approximately $[520, 560]$ nm) increases the SNR (Verkruysse et al. 2008). This is evidence against the assumption that the measured signal stems from arterial blood volume pulsations only because green light penetrates the skin only to a depth of approximately 1 mm (Bashkatov et al. 2005). This makes the interaction with arteries located in the subcutis ($\rightarrow$ Chapter 2.3.1) improbable. Furthermore, counter-phase PPGi signals measured at adjacent skin regions have been observed for which no explanation can be given in the frame of conventional blood volume theories (Kamshilin et al. 2015).

A potential explanation has been proposed by assuming that the periodic pressure changes in the arteries cause a deformation of the tissue in the dermis which influences the density of the capillaries ($\rightarrow$ Fig. 2.21). As this influences the volume of the blood as well, these local pressure changes could be an explanation for why using light, which penetrates the skin tissue only up to 1 mm, allows measuring the pulsations of the deeper arteries indirectly (Kamshilin et al. 2015).

Artifacts Due to the increased distance between signal source and sensor, it is obvious that PPGi signals have a significantly lower SNR than conventional PPG signals. Therefore, there are several sources of noise that can impact the SNR to a degree such that there is no cardiac signal portion left. For example, motion artifacts and sudden changes in illumination both result in sharp edges within the measured signal. Furthermore, there are motion artifacts resulting from biological processes with frequencies similar to the cardiac activity, which can superpose the cardiac signal: On the one hand, there are cardiac-related motions such as ballistocardiographic effects, i.e., the human body reacting with a subtle motion to the influx of blood. This effect is particularly pronounced in applications where the camera is pointed towards the head (Balakrishnan et al. 2013). On the other hand, there are respiration-related motions, such as the expansion of the chest during a respiration cycle.

2.4 Challenges of cardiac assessment in UHF MRI and related work

There are several challenges encountered when acquiring cardiac signals within UHF MRI and many works report on difficulties. For example, insufficient image quality in cardiac imaging in 20% of cases due to ECG artifacts are reported in (Brandts et al. 2010). An in-depth review on the problems encountered when acquiring ECG signals within MRI can be found in (Oster, Clifford 2017).

Usage of cardiac signals ECG and PPG signals are acquired within clinical MRI applications for HR monitoring and triggering of image acquisition. For the first application the dominant frequency of the signal (→ Fig. 2.27) is of interest which changes rather slowly in healthy persons undergoing MRI examinations due to the supine and resting position. But cardiac disease, e.g. atrial fibrillation, might introduce sudden changes and a fast and irregular rhythm, challenging accurate HR measurement. For the second application a fiducial point has to be detected in consecutive cardiac cycles robustly at the same phase of the cardiac cycle (→ Chapter 2.3.2). Commonly, when using ECG for triggering, the R-wave is used as the point in time for trigger activation with an acceptable delay of $20\,\mathrm{ms}$ (Fischer, Wickline, et al. 1999). When PPG is used, the maximum of the pulse wave is used (McRobbie 2006).

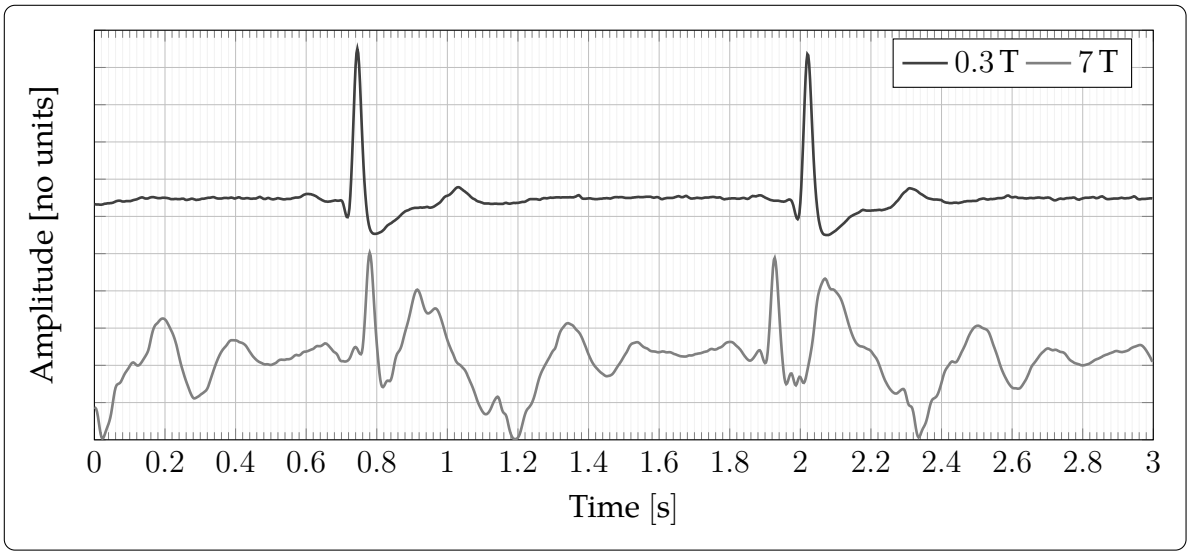

Figure 2.29: ECG signals acquired from a healthy volunteer with the patient table in home position (0.3 T) and imaging position (7 T). No imaging was performed, therefore the noise stems from the MHD effect only. The x-axes of both signals were manually adjusted. The signals are part of the dataset described in Chapter 3.1.1.

Challenges in ECG acquisition ECG acquisition suffers from artifacts which result from three different sources with the first being radio-frequency pulses (→ Chapter 2.1). As introduced, in MRI they are used for nuclei excitation but electromagnetic fields are picked up by the ECG device and cables as well. Their influence has been reduced efficiently in the past by careful hardware design, e.g. by using lowpass filters, hardware shielding, or fiber optic lines (Shetty 1988; Felblinger et al. 1994).

The second challenge is gradient activity. In addition to the static magnetic field $\overrightarrow{B0}$ and the time-dependent magnetic field $\overrightarrow{B1}$ (→ Chapter 2.1), MRI uses significantly smaller, varying magnetic fields called gradients for localization in space. The other magnetic fields are superposed by linear variations, resulting in gradually increasing Larmor frequencies along each axis in space which are used for differentiating positions. The associated induction is picked up by the ECG device as well. In the past, different algorithms have been proposed for attenuating the gradient noise, e.g. (Laudon et al. 1998; Odille et al. 2007; Oster, Pietquin, et al. 2010; Schmidt et al. 2018).

The MHD effect is the third obstacle which increases linearly with magnetic field strength (Gaffey, Tenforde 1981) and is therefore the most crucial in UHF MRI. As it results from the static $\overrightarrow{B0}$ field, its influence cannot be circumvented.

As the majority of blood consists of plasma (→ Chapter 2.3.1) which contains electrolytes, the blood is conductive. While the electrolytes are randomly scattered outside a magnetic field, they experience the so-called Lorentz force inside a magnetic field and are shifted in a direction perpendicular to their motion, i.e., to the vessel walls. Hence, MHD noise is the result of a conductive fluid, the blood, which is traveling through a magnetic field and is measurable as a voltage across a vessel with diameter L that can be expressed (simplified) as

$$V_{\text{mhd}} = \int_0^L (\vec{u} \times \overrightarrow{B0}) \, \mathrm{d}L \tag{2.45}$$

with $\vec{u}$ denoting the blood flow velocity and $\times$ the vector cross product. This potential difference reaches values that are measurable on the skin and superpose the ECG voltages. Typically, the influence of V_{mhd} shows artifacts in the form of elevated T-waves as has been demonstrated by several studies (Kangarlu et al. 1999; Chakeres et al. 2003; Gupta et al. 2008). Fig. 2.29 shows an ECG signal which was acquired outside and inside a 7 T MR bore from the same subject. Visually comparing the 7 T signal to ECG signals acquired normally (→ Fig. 2.25) shows the severe effect of MHD noise. As can be seen, MHD interactions disturb the signal with the SNR being lowest in the interval between QRS complex and T-wave. This is critical as it corrupts measurement of diagnostically important intervals, such as the QT-interval or ST-segment (→ Chapter 2.3). Although the R-peak is not severely influenced, QRS detection algorithms might fail due to detection of false peaks.

Challenges in PPG acquisition Although not affected by the magnetic field, PPG by means of pulse oximetry is not an equivalent alternative to ECG and can only be used to some extent for cardiac monitoring and triggering (Denslow, Buckles 1993). It is only of limited value for cardiac triggering due to the PTT (→ Fig. 2.27) which makes it unusable for examinations with a narrow latency between occurrence of a QRS complex and trigger activation, such as cardiac imaging (Stäb, Najjar, et al. 2019). Furthermore, it might suffer from jitter in trigger detection (Frauenrath et al. 2010) as the peaks of the PPG do not show a high frequency component as the QRS complex that can be detected easily (→ Fig. 2.27). Moreover, it suffers from involuntary and voluntary patient motion (Petterson et al. 2007) and from signal loss during longer examinations as soon as the patient's body temperature begins to fall (Hanning, Alexander-Williams 1995).

Related work

In the past, different approaches have been proposed and evaluated for overcoming the challenges of cardiac assessment in UHF MRI.

ECG On the one hand, several approaches have been proposed for making ECG feasible for UHF MRI: At lower field strengths pure signal processing techniques have been proposed (Fischer, Wickline, et al. 1999) while at UHF strengths most works apply dedicated hardware, e.g. high-fidelity 12-lead ECG measurement (Krug et al. 2013; Gregory et al. 2014). Moreover, a "learning phase" is often applied (Stäb, Roessler, et al. 2016) with a reference ECG signal being recorded outside the magnetic field. Both approaches, dedicated hardware and learning phases, show a positive improvement. However, the first approach is problematic as high-fidelity ECG hardware is not available in most MRI sites and learning phases prolong examination time, impeding the transfer to applications within clinical practice.

Other methods On the other hand novel methodologies have been proposed for measuring cardiac signals: ultrasound (Kording et al. 2017), ultra-wideband radar (Thiel et al. 2010), or acoustic measurement of cardiac activity (Frauenrath et al. 2010) with each modality having their own advantages and disadvantages. Many approaches suffer from i) a time-consuming setup time which prohibits to apply them in clinical practice and ii) new hardware introduced in the scanner room which increases the risk of radio-frequency interactions.

PPGi methods Although the application of cameras within MRI is common, e.g. as tracking device for prospective motion correction (Zaitsev et al. 2015), the body of research of PPGi within MRI is very limited. Cardiac monitoring has been proposed by Yang et al. but they used a mock-up MR scanner and a non-MR-compatible video camera. Furthermore, they did not validate their results by using ground truth (Yang et al. 2014). Maclaren et al. mounted a MR-compatible camera and a white LED on a head coil and captured videos from the forehead of three volunteers. Using offline frequency filtering with manually defined filter bands, they were able to acquire PPGi signals with high similarity to PPG signals measured in parallel. Realtime processing and cardiac triggering was not attempted but they rated PPGi-based cardiac triggering as a potential future application (Maclaren et al. 2015).

3 Material and methods

In this chapter, the contributions of this work are laid out in detail. In Chapter 3.1 two datasets are presented which were acquired during data collection studies with the aim to gain insight into ECG and PPGi signals acquired during UHF MRI. Based upon the results of these studies, a setup for PPGi-based cardiac triggering was devised. Subsequently, the main contributions of this work are presented: In Chapter 3.2 algorithms for applying PPGi to cardiac monitoring and triggering are presented. Algorithms for processing ECG signals are introduced in Chapter 3.3. To that extent, a novel analytical framework (msPE) is introduced, which is applied to ECG signals from the publicly available data first and then to PMU ECG signals acquired during one of the data collection studies.

3.1 Material

The first data collection study (→ Chapter 3.1.1) was motivated by the lack of available ECG, PPG, and PPGi data acquired within a MR scanner bore. The data obtained was used for developing first approaches towards PPGi methods and for gaining insight into the challenges encountered. Low SNR was identified as a major challenge which led to conducting a second study (→ Chapter 3.1.2), outside the MRI environment, with the aim to enhance the hardware setup for improved SNR. Subsequently, the results were transferred to UHF MRI and used for devising a feasible setup for PPGi measurement (→ Chapter 3.1.3) which was used for MRI triggering in a healthy volunteer with an algorithm that will be introduced in Chapter 3.2.

3.1.1 Dataset acquired within UHF MRI (ECG, PPG, PPGi)

As no public data was available, the motivation of this study was to acquire ECG, PPG, and PPGi signals in an UHF MRI environment for gaining insight into the signal's characteristics. Non-contrast-enhanced MRA of the lower extremity arteries at 7T (Fischer, Maderwald, et al. 2013) was chosen as MR examination as inadequate triggering results in periodic vessel signal declines (Johst et al. 2014) and thereby allows associating the accuracy of cardiac triggering to the quality of acquired images. However, during this data acquisition study, no actual MRI images were acquired.

Study population Eight healthy volunteers with no cardiac diseases (sex: $2/6\,\mathrm{f/m}$, age: $32.0 \pm 4.5\,\mathrm{years}$, weight: $74.5 \pm 11.5\,\mathrm{kg}$, height: $179.1 \pm 8.5\,\mathrm{cm}$, ethnic origin: 6 Europe, 1 West Asia, 1 South Asia) were part of this study which was approved by the Ethics Commission of the Medical Faculty of the University Duisburg-Essen (Study number: 11-4898-BO). The study was conducted in conformance with the Helsinki Declaration. Each volunteer gave informed consent in written form and was informed about the examination procedure by a physician.

MRI setup This study was conducted using an UHF whole-body MRI system (MAGNETOM 7 T; Siemens GmbH, Erlangen, Germany), customized for the acquisition of MRA. A custom-built transmit/receive coil was attached to the scanner table, allowing to perform imaging of the arteries of the lower extremity. More detail on the examination can be found in (Fischer, Maderwald, et al. 2013).

Considerations There are several considerations to be made when performing PPGi acquisition, including most important the area of measurement and illumination. In a preliminary study[1], a PPGi signal was measured from the finger tip inside a $3\,\mathrm{T}$ MR scanner bore during a routine brain examination. By using an amplification algorithm, it was shown that the measured signal contains a cardiac component but suffers from involuntary motion of the finger. Hence, in the current study, the signal was measured from the forehead instead as it is easily accessible because the MRA

[1]This work has been published in: Spicher, N., Brumann, C., Kukuk, M., Ladd, M. E., Maderwald, S. (2014): Eulerian video magnification for heart pulse measurement in MRI Scanners In: Proceedings of the 22nd Annual Meeting of the International Society for Magnetic Resonance in Medicine, Milan, Italy.

examination is performed feet-first and this area is often used for PPGi measurement due to high blood perfusion (Zaunseder et al. 2018). As the illumination inside the MR bore is low, an off-the-shelf video projector was used for increasing illumination by emitting white light from the back of the bore.

Experimental setup A commercially-available, UHF-compatible camera system (12M-i, MRC Systems, Heidelberg, Germany; $1/3$ inch monochromatic image sensor) was used for capturing the PPGi signal. The spectral sensitivity of the sensor was approximately 65% in the wavelength range $[450, 600]$ nm which has been reported by others as being optimal for measurement (McDuff et al. 2014). The camera was connected via the MR scanner waveguide with a vendor-provided filter box. This device attenuates noise in the captured images introduced by the scanner. The filtered signal was captured with an off-the-shelf video grabber (SC8113, Silan Microelectronics, Hangzhou, China) connected to an off-the-shelf laptop (Thinkpad T440s, Lenovo, Beijing, China). Fig. 3.1 shows the PPGi setup with the camera being pointed towards the forehead of the subject. This setup has the advantage of being installed quick and not having any physical contact with the patient.

ECG and PPG signals were acquired using a MR vendor-provided PMU hardware and software according to the manual provided. As the ECG signals are disturbed by MHD noise, PPG was acquired as ground truth. The ECG device was applied using a 3-lead configuration with electrodes attached to the sternum and left side of the thorax. The PPG probe was attached to the left index finger with the hand lying on the stomach to avoid motion. ECG and PPG signals were sent via Bluetooth signalling to the PMU and were stored. Additionally, triggers associated with the ECG R-peak and maxima of the PPG signal for MRI synchronization were detected by the software and stored. The acquired PPGi frames were stored on the laptop.

Study protocol In order to evaluate the influence of MRI-related artifacts, i.e. radio-frequency and gradient activity, as well as the MHD noise due to the magnetic field ($\rightarrow$ Chapter 2.4) on signal acquisition, an experiment with three stages was conducted:

① 0.3 T, patient table in home position, room illumination, no MRI activity

② 7.0 T, patient table in isocenter, illumination from projector, no MRI activity

③ 7.0 T, patient table in isocenter, illumination from projector, MRI activity

Figure 3.1: Experimental setup during stage ①: The patient is lying feet-first on the patient table and the camera (arrow) is pointed towards the forehead. The camera is mounted on a MR-compatible custom-built stand. During stages ② and ③ the setup remains identical but the patient table is located at the isocenter of the scanner.

The stages were performed in ascending order with duration of 5 minutes for each stage. MR activity was performed according to the MRA protocol (Fischer, Maderwald, et al. 2013), resulting in radio-frequency and gradient coil activity. However, during this data acquisition study, no MR images were acquired.

Acquired data For each stage, three signals were stored: ECG (400 Hz sampling rate), PPG (50 Hz), PPGi (25 Hz, 720×576 pixels per frame), resulting in nine signals per subject with a total duration of 15 min. The sampling rates of ECG and PPG were set to the maximum of the MR-vendor software. For acquisition of PPGi signals the maximum resolution and sampling rate provided by the camera was used.

3.1.2 Dataset acquired outside UHF MRI (PPG, PPGi)

The purpose of this study[2] was to improve the PPGi setup with regard to SNR of the PPGi signal. However, the low specifications of the MR-compatible camera could obscure relevant detail of the PPGi signal. In the first study (→ Chapter 3.1.1), no MR-related artifacts were observed in the PPGi signal. Therefore, this study was conducted in an office environment using a camera with superior hardware instead. Measures were taken to reproduce the illumination conditions inside the MR bore, thereby enabling the subsequent transfer of the results to MRI.

Study population 21 healthy volunteers (sex: 5/16 f/m, age: 29.7 ± 7.3 years, weight: 78.5 ± 9.6 kg, height: 177.6 ± 8.4 cm, ethnic origin: 17 Europe, 3 Asia, 1 Arabia) were part of this study population. The study was conducted in accordance with the principles of the Helsinki Declaration and all volunteers gave informed consent in written form. Furthermore, all subjects gave written consent that the obtained data was made publicly available.

Considerations As will be discussed in detail in Chapter 4, analysis of the dataset described in the previous chapter revealed that a major limitation is the low SNR of the acquired PPGi signals. This challenge was approached two-fold.

In the first study, passive illumination from a video projector placed at the back of the bore was emitted, which did not provide frontal illumination of the skin surface. Additionally, light intensity was rather low due to the distance between light source and the skin. In a preliminary study[3] it was shown that there is a quasi-linear relationship between strength of illumination with green light-emitting diodes (LEDs) and SNR of the PPGi signal measured. Therefore, dedicated illumination by green LEDs from a close distance was applied in this study.

Furthermore, it has been demonstrated that the SNR of a PPGi signal increases if external force is applied to the skin (Kamshilin et al. 2015). Therefore, the skin was placed on a glass plate and the video signal was recorded from the other side.

[2]The author thanks T. Lovelace who assisted in the execution of this study as part of his German Academic Exchange Service (DAAD) Research Internships in Science and Engineering (RISE) grant.

[3]This work has been published in: Spicher, N., Orzada, S., Maderwald, S., Kukuk, M., Ladd, M. E. (2017): An open-source hardware and software system for video-gated MRI In: Proceedings of the 25th Annual Meeting of the International Society for Magnetic Resonance in Medicine, Honolulu, USA.

Figure 3.2: Experimental setup with arrows indicating the camera and the dedicated LED illumination. The setup was placed in a portable sun shade which is not shown.

This approach eliminates the forehead for measurement as it would result in patient discomfort and the head's roundness circumvents placing a flat glass plate over a large area. Hence, the area of PPGi application was shifted towards the extremities. While the hands are located within the MR bore during imaging and are therefore available, but in a restricted space, the feet are easily accessible at the end of the bore. Acquiring PPGi signals from the palm of the hands has been part of early PPGi research (Wu et al. 2000) and has proven feasible for acquiring an adequate SNR in several studies (Zaunseder et al. 2018). However, there was no information available on the feasibility of the feet for PPGi measurement. Therefore, PPGi was measured from palm of the hands and sole of the feet for a quantitative comparison.

Experimental setup Fig. 3.2 shows the experimental setup. This study was conducted in an office environment using an industrial camera (uEye UI 154xSE-M, IDS Imaging Development Systems GmbH, Obersulm, Germany; object lens: 12 mm C-Mount Lens H1212B, Pentax, Tokyo, Japan). Ten LEDs (L-7113VGC-E, Kingbright, Taipei, Taiwan; peak wavelength: 518 nm) were installed next to the camera to pro-

vide frontal illumination of the skin and were powered by an off-the-shelf laboratory power supply. The illumination conditions within the MR bore were simulated by placing the whole experimental setup in a portable sun shade (ThinkTank Pixel Sunscreen V2.0) which filters out ambient illumination by black polyester fabric. A commercial device (MP30, BIOPAC, Goleta, USA; SS4LA PPG probe) was used for measuring finger pulse oximetry as ground truth.

Measurement protocol Before experiments, volunteers were asked to sit in an upright position and to relax. In this study, two stages with a duration of 60 s each were conducted for each volunteer:

① PPGi applied at the palm of the right hand, PPG acquired from the index finger of the left hand

② PPGi applied at the ball of the right foot, PPG acquired from the index finger of the left hand

During pretests it was observed that too firm or too soft contact with the glass plate might result in no clear cardiac component. Hence, after each experiment it was checked whether the measured PPGi contains a clearly visible cardiac component. If that was not the case, the experiment was repeated and the volunteer was asked to reduce or increase contact pressure.

Data acquisition At each stage, two signals were stored: PPG (200 Hz sampling rate) and PPGi (14 Hz, monochrome, 1280×1024 resolution, 8 bit depth).

3.1.3 A setup for PPGi-based cardiac triggering in UHF MRI

Based on the results of the data acquisition studies, which will be presented in Chapter 4, a setup for PPGi-based cardiac triggering was devised. It can be used within all MRI examinations where one foot of the subject is available.

In this work, it is customized for MRA of the lower extremity arteries (Fischer, Maderwald, et al. 2013) using PPGi signals acquired from the sole of the foot in contact with a glass plate.

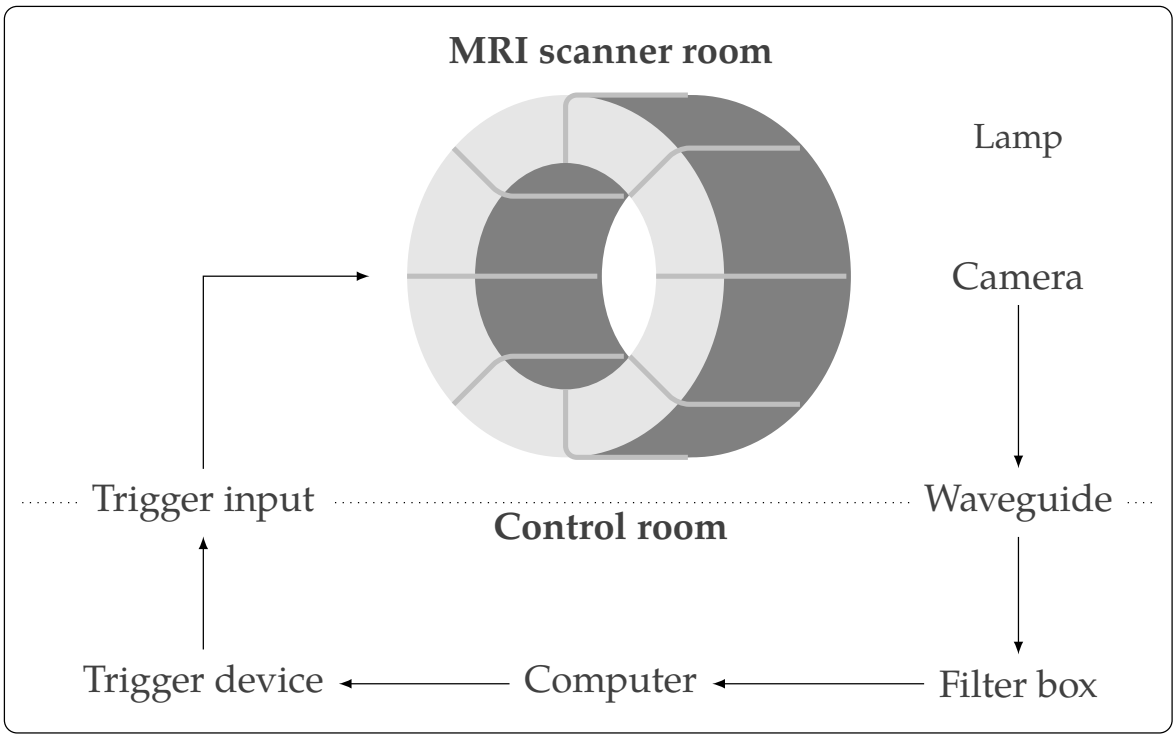

Figure 3.3: Schematic diagram of the setup for PPGi-based cardiac triggering. Dotted lines indicate room walls and arrows indicate cable connections. Providing illumination is optional but strongly advised for increasing the SNR of the PPGi signal.

Overall setup The proposed setup consists of several components which are arranged in a linear workflow depicted in Fig. 3.3. Within the MRI scanner room the camera is installed such that a PPGi signal can be acquired. In this work, the signal is measured from the sole of the foot as described in the next section, but the setup is independent of this aspect and PPGi could be measured from any other location.

The video signal is transmitted in real-time using cables provided by the camera vendor via a waveguide into the control room. Here, the signal is filtered using a camera vendor-provided filter box containing low-pass filters for suppressing noise artifacts that could be introduced by the MR scanner activity. Subsequently, the video signal is digitized on a computer by using an off-the-shelf frame grabber. Based upon this signal, triggers for MRI are computed and send to the trigger input of the MRI scanner via a custom-built, low-cost device. When a trigger arrives at the trigger input, image acquisition is activated. Further information on the device can be found in the Appendix.

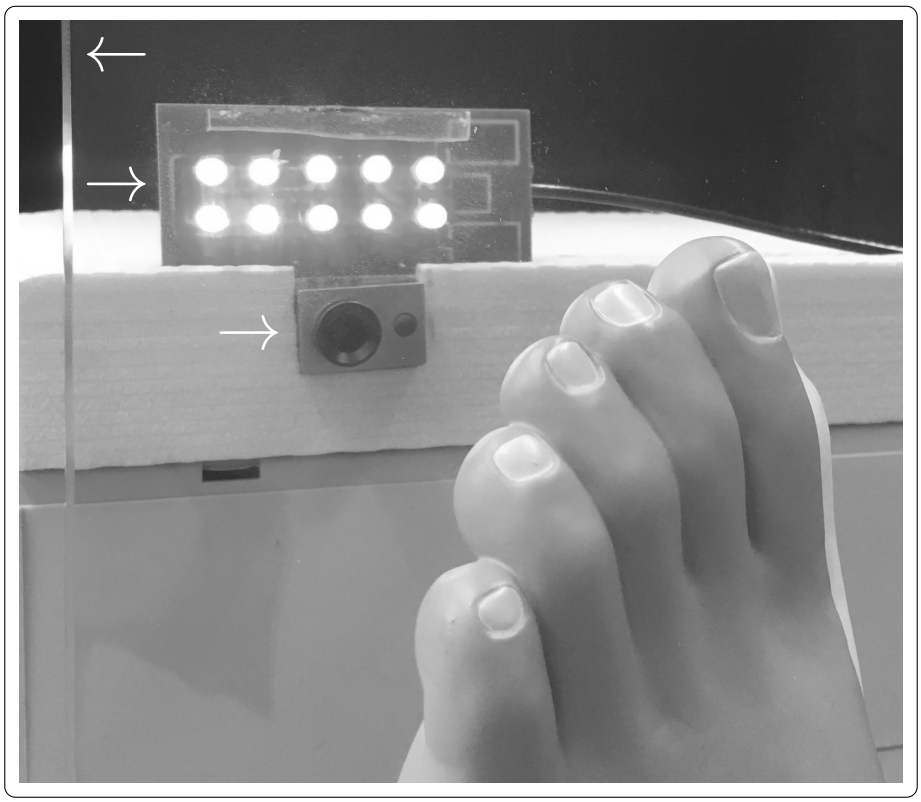

Figure 3.4: Setup for PPGi acquisition during 7 T MRA. Arrows indicate from top to bottom: glass plate, dedicated LED illumination, UHF MRI-compatible camera.

PPGi acquisition During MRA the patient lies on a sliding table which allows imaging different anatomical structures by sliding the table between a custom-built transmit/receive coil. Therefore, for practical feasibility during imaging, the setup described in the following was fixed to the sliding table.

The setup is depicted in Fig. 3.4: An off-the-shelf glass plate with dimensions $30 \times 30 \times 0.5$ cm was used to hold the sole of the foot and was placed in a $90°$ angle relative to the patient table. To increase patient comfort, it was non-rigidly fixed, such that it can budge up to a approximately $110°$ when pressure from the foot is applied. On the other side of the glass plate, the MR-compatible camera (12M-i, MRC Systems, Heidelberg, Germany) was fixed at a distance of approximately 10 cm. The same LED array as described in Chapter 3.1.2 was placed next to the camera. The fixture allows moving the whole setup with the sliding table. Leads of the camera and the LED array were guided through a waveguide into the MR control room.

3.2 PPGi-based methods

Using the data acquired in the experiments described in the previous chapter, the methods for processing PPGi signals are proposed. In Chapter 3.2.1 an algorithm for PPGi-based cardiac monitoring is presented and an algorithm for PPGi-based MRI triggering is introduced in Chapter 3.2.2. Moreover, experiments with the aim to gain information on the properties of PPGi signals are laid out in Chapter 3.2.3.

3.2.1 Cardiac monitoring during UHF MRI[4]

This chapter describes an algorithm for PPGi cardiac monitoring based on the principles of the Fourier Transform. The algorithm is evaluated using the material acquired in stages ① and ② of the first data acquisition study (→ Chapter 3.1.1).

Data As introduced in Chapter 2.3.2, the HR can be estimated from the reciprocal value of the RR (PP) interval in ECG (PPG) signals which requires peak detection. During the study, the MR-vendor provided software computed cardiac triggers for ECG and PPG signals, which were used for estimating HR. However, for raw PPGi signals accurate peak detection is challenging due to the low SNR. Therefore, HR was measured in PPGi signals by detecting the dominant frequency in the Fourier Transform, which constitutes an approach more robust to noise (Husar 2010).

Algorithm A soft realtime-feasible algorithm was developed for HR estimation in PPGi data which is able to process either all pixels within a frame or a subset of pixels. The latter is realized by a ROI (→ Fig. 2.28) which can be manually defined.

The algorithm consists of two parallel threads running in a continuous loop: The first thread acquires video frames $I : \mathbb{N}^2 \mapsto \mathbb{N}$, crops them to the ROI if one was defined, and stores them in a continuously updated list: $I_0(m,n), I_1(m,n), I_2(m,n), \cdots$. The second thread (→ Alg. 1) fetches the last N frames, computes a scalar for each frame by averaging the values in the ROI, and then estimates HR from the acquired one-dimensional PPGi signal using the magnitude (→ Chapter 2.2.1).

[4]This work has been published in: Spicher, N., Maderwald, S., Ladd, M. E., Kukuk, M. (2015): Heart rate monitoring in ultra-high-field MRI using frequency information obtained from video signals of the human skin compared to electrocardiography and pulse oximetry. Current Directions in Biomedical Engineering, 1(1), 69–72.

Algorithm 1: Heart rate estimation from a PPGi signal

Input: list of video frames I_t **Parameters:** N

A zero-padded signal $f_s(t)$ is acquired from the list of stored frames by

$$f_s : \mathbb{N}_0 \to \mathbb{N}_0, t \mapsto \begin{cases} \sum_m \sum_n I_t(m,n) & \text{if } t \in [a,b] \\ 0 & \text{otherwise} \end{cases}, t \in [c,d]. \tag{3.1}$$

where

$$[a,b] = \{x \in \mathbb{N}_0 \mid (a \leq x \leq b) \ \wedge \ (b-a = N-1)\} \tag{3.2}$$

and

$$[c,d] = \{x \in \mathbb{N}_0 \mid (c \leq a \leq x \leq b \leq d) \ \wedge \ (d-c = 2^p-1)\} \tag{3.3}$$

with p being the min. integer such that $2^p > N$ holds. A Hamming window

$$f_h : \mathbb{N}_0 \to \mathbb{R}, t \mapsto 0.54 - 0.46\cos(2\pi t/(2^p-1)), t \in [0, 2^p-1] \tag{3.4}$$

is applied before computation of the discrete Fourier Transform

$$F : \mathbb{N}_0 \to \mathbb{C}, k \mapsto \sum_t f_s(t) f_h(t) e^{-j2\pi tk/2^p}, k \in [0, 2^p-1]. \tag{3.5}$$

The first half of the Fourier Transform is analyzed and the function

$$f_{\text{Hz}} : \mathbb{N}_0 \to \mathbb{R}\,[\text{Hz}], k \mapsto kk_s/2^p, k \in [0, 2^{p-1}-1] \tag{3.6}$$

maps each bin of F to a frequency value in unit Hz. Subsequently, the position of the highest magnitude of the Fourier Transform

$$k_{\text{HR}} := \arg\max_{y \in [u,v]} |F(y)|. \tag{3.7}$$

is detected with $f_{\text{Hz}}(u)$ and $f_{\text{Hz}}(v)$ defining the interval $[0.8, 3]$ Hz.

Finally, the HR over the last N frames is estimated by acquiring

$$\gamma_{\text{HR}}\,[\text{Hz}] := f_{\text{Hz}}\big(k_{\text{HR}}\big). \tag{3.8}$$

Next, the algorithm returns to step (3.1).

Output: $\gamma_{\text{HR}} \cdot 60$ [cycles per minute]

As can be seen, Alg. 1 has a single parameter and is based on the underlying assumption that the cardiac component of the PPGi signal is represented by the maximum magnitude (→ p. 20) in the Fourier Transform. Due to the continuous update of $f_s(t)$ and the application of a window function, this algorithm has similarity to the windowed Fourier Transform with the frequency with the maximum value being stored for each column of the spectrogram (→ Fig. 2.10). Due to the problems occurring when computing the Fourier Transform of a signal with sharp edges (→ p. 22), the Hamming window (Hamming 1989) is used. F is symmetric because $f_s(t)f_h(t) \in \mathbb{R}$ and therefore the first half can be analyzed only (→ p. 21).

Different from the presentation in Chapter 2.2, the ordinary frequency in unit Hz instead of angular frequency ω is used in order to give a more intuitive understanding of the frequency ranges. The interval of analyzed frequencies was limited to the range $[0.8, 3]$ Hz as it represents $[48, 180]$ cardiac cycles per minutes, which is reasonable for healthy and relaxed humans. Furthermore, a discrete version of the Fourier Transform is given by replacing the integral with a Riemann sum. In the actual implementation, an efficient implementation of the Fourier Transform called Fast Fourier Transform (Cooley, Tukey 1965) was used.

Implementation The algorithm was implemented in C++11 using the `std::thread class` for the realization of both threads. The `OpenCV` library (https://www.opencv.org/, v2.4.9) was used for image acquisition and the `ROOT` library (https://root.cern.ch/, v5.34) was used for all other signal processing tasks.

Application Before initiation of the algorithm, a rectangular ROI covering the subject's forehead and excludes facial hair as well as the eyes was defined. The ROI was fixed for the whole duration of a single experiment.

The algorithm is based on the assumption that the current HR can be estimated from the foregoing N frames, associated to a certain duration which depends on the camera's framerate. Therefore, there is a trade-off between inaccuracy of the HR due to averaging over too many cardiac cycles (too high N) and inaccuracy of HR due to too few samples (too low N). After analysis of different values, $N = 125$ was manually chosen, averaging the HR over the last 5 s.

Evaluation Due to the different sampling rates of ECG, PPG, and PPGi signals, a 10s moving average (MA) filter was applied to the signals which was shifted in steps

of 1 s. The resulting signals $\mathrm{MA}_{\{\mathrm{ECG,\,PPG,\,PPGi}\}}$ were stored and analyzed by means of root-mean-square-error (RMSE) with the operator being defined as

$$\mathrm{RMSE}(\mathrm{MA_x}, \mathrm{MA_y}) = \sqrt{\sum_{t=1}^{T=291} \big(\mathrm{MA_x}(t) - \mathrm{MA_y}(t)\big)^2 / T} \tag{3.9}$$

with $x, y \in \{\mathrm{ECG}, \mathrm{PPG}, \mathrm{PPGi}\}$ and $x \neq y$, enabling an intuitive comparison of the three signals. Of course, the comparison only holds if one signal is as a robust ground truth.

3.2.2 Cardiac triggering during UHF MRI

In this chapter, the contributions towards UHF MRI cardiac triggering are presented. A novel algorithm for cardiac triggering processing PPGi signals is proposed. First, it is applied to the data from the first study (→ Chapter 3.1.1) and feasibility is evaluated by a quantitative comparison of ECG, PPG, and PPGi trigger. Second, it is used in combination with the proposed setup (→ Chapter 3.1.3) for MRA triggering and is evaluated by a qualitative comparison of PPG- and PPGi-triggered MRA images.

Algorithm The proposed algorithm is similar to the algorithm proposed in Chapter 3.2.1 consisting of two threads as well. While the first thread is identical, the second thread is identical up to step (3.7) but then uses the phase (→ Chapter 2.2.1) for estimating the duration until a trigger ought to be sent.

The algorithm is given in Alg. 2 and demonstrated in Fig. 3.5. As can be seen in Fig. 2.28, PPG and a PPGi signals have a periodicity with a frequency associated with the cardiac cycle due to the influx of blood and the reoccurring outflow of blood. Thereby, a sine wave with frequency γ_{HR} can be used to approximate the dynamics of a PPGi signal, which is shown in Fig. 3.5 (black line) for two cardiac cycles. A sine without phase shift (→ p. 20) is shown as reference (dotted line). The PPGi signal has the same periodicity but an unknown phase-shift, which equals here $\angle_{\mathrm{HR}} = -0.5\pi$. The desired point in time for sending a trigger to the MR scanner is associated with the maximum influx of blood (black dot). At the point in time the algorithm is performed (gray dot), the algorithm acquires the current PPGi signal. At this point, the future signal is unknown (dashed line) but the algorithm measures the phase of the past signal and estimates time Δ until the next trigger (right arrow).

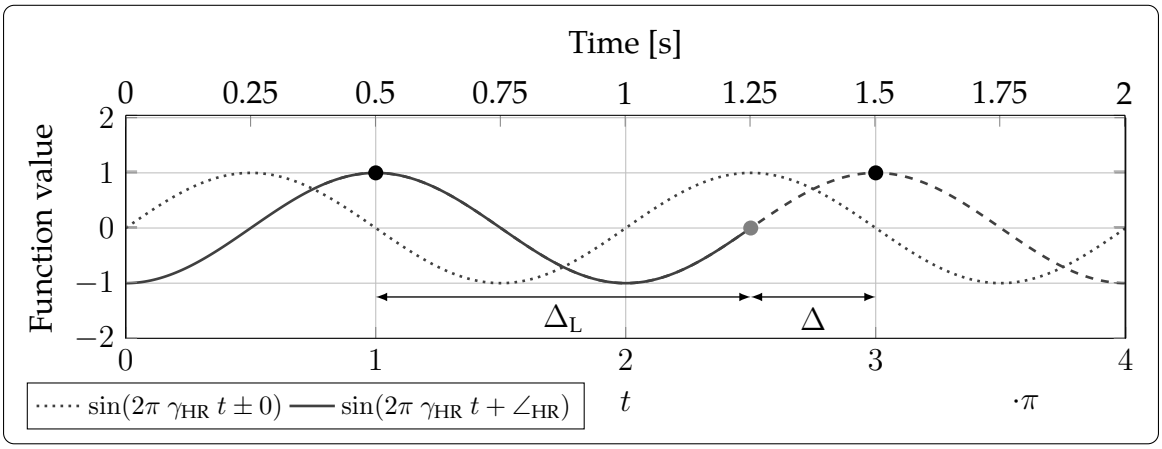

Figure 3.5: The PPGi signal (black curve) is assumed be similar to a sine (dotted curve), allowing to calculate, at a given point in time (gray dot), the phase and computing the time Δ (arrow) until the next trigger ought to be sent (black dot). 60 cycles/minute are assumed, i.e. $\gamma_{\text{HR}} = 1$ and therefore $\angle_{\text{HR}} = -0.5\pi$ and $\Delta = 0.25\,\text{s}$.

$\Delta[s]$ represents the phase of the HR in the range $[0.8, 3]$ ($\rightarrow$ Alg. 1). Thereby, it should correspond to the beat-to-beat interval of values $[0.333, 1.250]\,\text{s}$. The time passed since the activation of the last trigger Δ_{L} (left arrow) is used for correcting false triggers due to outliers, i.e. too soon or too late trigger activation. In the normal case, the time since the last trigger activation Δ_{L} is within $[0.333, 1.250]\,\text{s}$, the algorithm waits for Δs before the trigger is activated. However, if the time elapsed Δ_{L} is smaller than the lower limit, the current trigger is assessed as an outlier and omitted. If Δ_{L} is larger than the upper limit, a trigger was missed and one is activated immediately with the current trigger being skipped.

As can be seen, Alg. 2 introduces two additional parameters. Parameter M is used to average the computed bin of the HR frequency over several iterations. This is required as a single wrongly computed bin, e.g. due to a motion artifact, would result in a completely false $\angle_{\text{HR}}$ and therefore a completely false Δ value. As motion of a healthy volunteer should only be a transient event, averaging the value over a certain duration should filter out motion artifacts. Parameter T is required because there is no information available on the PTT ($\rightarrow$ Fig. 2.27) to the forehead's skin. Therefore, together with the parameter N which was introduced in Alg. 1, the algorithm has three open parameters. Optimization was performed by using synthetic PPGi signals for determining the best combination of parameters.

Algorithm 2: Trigger computation from PPGi signal

Input: Same as Alg. 1 **Parameters:** N, M, T

The algorithm starts with steps (3.1) to (3.7) of Alg. 1. Additionally, the value of k_{HR} is averaged over the last M computations to account for outliers.

The phase of the cardiac component (→ Chapter 2.2.1) is obtained from the Fourier Transform F at the (averaged) position of the highest magnitude k_{HR}:

$$\angle_{\text{HR}}[\text{rad}] := \arctan\left(\frac{\text{Im}\left(F(k_{\text{HR}})\right)}{\text{Re}\left(F(k_{\text{HR}})\right)}\right). \tag{3.10}$$

Subsequently, the time until the next trigger is ought to be send is calculated:

$$\Delta[s] = T \pm \begin{cases} \mid \angle_{\text{HR}}/(2\pi\ \gamma_{\text{HR}}) \mid & \text{if } \angle_{\text{HR}} < 0 \\ {\gamma_{\text{HR}}}^{-1} - \mid \angle_{\text{HR}}/(2\pi\ \gamma_{\text{HR}}) \mid & \text{otherwise} \end{cases} \tag{3.11}$$

where parameter T is a constant offset for correcting the PTT. The time elapsed since the activation of the previous trigger Δ_{L} is computed and $\Delta[s]$ is adjusted to

$$\Delta[s] = \begin{cases} \infty & \text{if } \Delta_{\text{L}} < 0.333\,\text{s} \\ 0 & \text{if } \Delta_{\text{L}} > 1.250\,\text{s} \\ \Delta & \text{else} \end{cases} \tag{3.12}$$

before activation of the trigger. Then, the algorithm returns to step (3.1).

Quantitative evaluation[5]

The quantitative evaluation was performed by comparing the agreement of ECG, PPG, and PPGi trigger points in time. While ECG and PPG trigger points were recorded during the MRI study, PPGi trigger points were computed retrospectively by using the proposed algorithm. As the algorithm has three open parameters, these were optimized before computing the triggers for the quantitative evaluation.

[5]This work has been published in: Spicher, N., Kukuk, M., Maderwald, S., Ladd, M. E. (2016): Initial evaluation of prospective cardiac triggering using photoplethysmography signals recorded with a video camera compared to pulse oximetry and electrocardiography at 7T MRI. BioMedical Engineering OnLine, 15(1), 126.

Data The ECG, PPG, and PPGi data acquired in the data acquisition study performed within UHF MRI (→ Chapter 3.1.1) was used.

Algorithm parameter optimization It is not possible to obtain a well-suited configuration of parameters M, N, T from physiological or technical considerations. Therefore, parameter optimization by means of an exhaustive parameter search was performed with a summary given here. Details be found in the referenced work[5].

The PPGi signals acquired within the first study (→ Chapter 3.1.1) have a length of 120min only, thereby reducing the value of an exhaustive parameter search. Instead synthetic PPGi signals were generated using physiological data acquired from the Normal Sinus Rhythm RR Interval Database (→ Appendix) for the optimization of parameters M and N. For each of the 54 subjects within the database, cardiac cycles are approximated by $f_{cc} : \mathbb{R} \mapsto \mathbb{R}, t \rightarrow -\cos(2\pi\ 1/t_n^{RR}\ t), t \in [0, t_n^{RR}]$ where t_n^{RR} represents the n-th RR interval from the recording. This step was performed with increasing n until cardiac cycles with a total length of 5 minutes were computed, which were then concatenated, resulting in a single, one-dimensional cardiac signal per subject of the database. Subsequently, the distribution of very low frequency noise ($[0, 0.1]$ Hz), low frequency noise ($[0.1, 0.8]$ Hz), and high frequency noise ($[3, 12.5]$ Hz) was estimated from the data of the first study and added to the synthetic signals.

Parameter optimization was performed in two steps: First, optimization was realized using a grid search approach with $N \in \{50, 100, \cdots, 550, 600\}$, $M \in \{1, 5, 10, 25, 50, 100, \cdots, 300\}$, and $T = 0$. Alg. 2 was applied to the synthetic signals with all parameter combinations from the Cartesian product of M and N. As parameter T is associated with an (unknown) PTT it could not be evaluated using this approach. As the ground truth in terms of the cosine maxima was known, the absolute difference in time between a computed trigger and the ground truth was used as error measure. Subsequently, the subset of best candidates was chosen and applied to the PPGi study data, with the single best combination being chosen by analyzing the trigger-to-trigger durations computed by the algorithm to PPG trigger-to-trigger durations (→ Fig. 2.27). The durations between successive triggers were used as reference as they are independent of parameter T and do not bias results due to PTT.

Second, parameter T was optimized using experimental data from the first study with the fixed best combination of M and N as well as $T \in \{-0.3, -0.2, \cdots, 0.3\}$ s. As the ECG was distorted due to MHD noise it, PPG was used as ground truth.

Application and Evaluation After parameter optimization, Alg. 2 was applied to the PPGi videos from the first study with optimized parameters. The durations between successive triggers were stored and compared to the RR- and PP-intervals of ECG and PPG signals (→ Fig. 2.27).

Qualitative evaluation[6]

The qualitative evaluation of MRI cardiac triggering was realized by performing UHF non-enhanced MRA in a volunteer (sex: female, age: 24 years) by combining the proposed PPGi setup (→ Chapter 3.1.3) and Alg. 2 which was introduced in the previous section.

MRA setup MRA images were acquired using three consecutive table positions with an overlap between two positions of approximately 2 cm. At each position, the MR coil was used to image 10 cm of the lower extremities, including the thigh, kneecap, and shank. PPG by means of the MRI vendor-provided finger pulse oximetry probe was used as reference. In order to have equal conditions regarding imaging and the cardiac condition of the volunteer, PPG and PPGi were used alternating for each table position instead of using a single modality for all positions and then starting over. At first PPG triggers were used for MRA image acquisition followed by PPGi triggers.

Evaluation The typical visualization of non-enhanced MRA images was chosen for the comparison of both trigger methods. Using the MR-vendor provided software, maximum intensity projection (MIP) images in coronal orientation were generated and exported. Subsequently, the overlap resulting from different table positions was determined manually by visual inspection and the individual images were blended into a single MIP file.

[6]This work has been published in: Spicher, N., Orzada, S., Maderwald, S., Ladd, M. E., Kukuk, M. (2018): A novel method for video-based cardiac gating in 7T MR angiography using a video of the foot In: Proceedings of the 26th Annual Meeting of the International Society for Magnetic Resonance in Medicine, Paris, France.

3.2.3 Investigation of PPGi signal characteristics

During the course of this work, the properties of PPGi signals acquired outside and inside the context of MRI were analyzed for gaining insight into possibilities to improve SNR.

PPGi signal strength as a function of wavelength[7]

In Fig. 2.26, the light absorbance of (oxy-)hemoglobin with respect to the wavelength of light is depicted which can be used to pick a wavelength with favorable conditions for PPG measurement. However, this cannot be mapped to PPGi as the underlying signal source is not the same and has not been identified yet for PPGi (→ p. 46).

Hence, an experiment was performed in three volunteers (sex: 3 m, age: $27 - 30$years) to assess the intensity of the PPGi signal with respect to wavelength. In this regard, a hyperspectral imaging system providing 16 color channels and covering 470 to 620 nm was applied. As the hardware is not MR-compatible, the experiment was conducted in an office environment. The foreheads of the volunteers were recorded using the hyperspectral camera (VRmagic D3, CMOS CMV2000) from a distance of approximately 10 cm for a duration of 20 s. Dedicated illumination was provided by a ring of ultraviolet and white LEDs (Falcon FLDR-i100B-UV24-W) which was attached to the camera.

As introduced in Chapter 3.2, pixel averaging is required when processing PPGi signals because a single pixel does not contain enough cardiac signal. Therefore, after data acquisition a ROI with a size of approximately 1×4 cm was manually defined for further processing. For each camera channel, the arithmetic mean value of all pixels within the ROI was computed and stored for each frame, resulting in a one-dimensional signal $x(t)$ for each color channel.

The intensity of the PPGi signal within a single channel was assessed by computing the Fourier Transform magnitude (→ p. 20) and computing the ratio of averaged magnitudes between the interval of HR frequencies ($[48, 72]$ cycles per minute) to all other frequencies.

[7]This work has been published in: Spicher, N., Tanriverdi, F., Thiem, J., Kukuk, M. (2017): PPG imaging: Investigating skin inhomogeneity using hyperspectral imaging and principal component analysis In: Proceedings of the 51st Annual Conference of the German Society of Biomedical Engineering, Dresden, Germany.

Influence of illumination on PPGi signal[8,9]

Illumination by green light is one possibility for increasing SNR (Sun, Thakor 2016) of PPGi signals although the reasons for green light being superior to other wavelengths are not completely clear (Kamshilin et al. 2015; Moço et al. 2018). After completion of the first study (→ Chapter 3.1.1) without dedicated illumination, the influence of dedicated illumination on the SNR of the PPGi signals was evaluated. The setup was similar to the first study but, additionally, the LED array (→ Chapter 3.1.2) was used. Three stages with different illumination conditions were acquired in a healthy volunteer (sex: male, age: 35 years):

① No dedicated illumination,

② 90 mA dedicated illumination,

③ 180 mA dedicated illumination.

Stage ① represents the situation during acquisition of the first study without dedicated illumination as reference. The illumination in stage ③ was set to 180 mA as higher values caused saturation of pixels and stage ② was set to the value in between both stages. Each stage had a duration of 60 s and PPGi was acquired from the forehead and PPG from finger pulse oximetry used as ground truth.

Analysis of the PPGi signals was performed by means of Fourier Transform's magnitude and phase (→ p. 20). The rationale is shown in Fig. 3.6: The PPGi frames were subdivided into a grid of overlapping ROIs (→ Fig. 2.28) applied at each pixel with a size of 10×10 pixels, thereby allowing to analyze local skin properties. For each pixel, the arithmetic mean $\mathrm{m}(\cdot)$ of the surrounding pixels was computed and stored for each frame, resulting in a one-dimensional PPGi signal $x(t)$. This signal represents a single PPGi spatial neighborhood that was analyzed by means of magnitude $|\hat{x}(\omega)|$ and phase $\angle\hat{x}(\omega)$ of the cardiac component of $x(t)$.

[8]This work has been published in: Spicher, N., Orzada, S., Maderwald, S., Kukuk, M., Ladd, M. E. (2017): An open-source hardware and software system for video-gated MRI In: Proceedings of the 25th Annual Meeting of the International Society for Magnetic Resonance in Medicine, Honolulu, USA.

[9]This work has been published in: Spicher, N., Orzada, S., Maderwald, S., Kukuk, M., Ladd, M. E. (2017): On the importance of skin color phase variations for video measurement of cardiac activity in MRI In: Proceedings of the 25th Annual Meeting of the International Society for Magnetic Resonance in Medicine, Honolulu, USA.

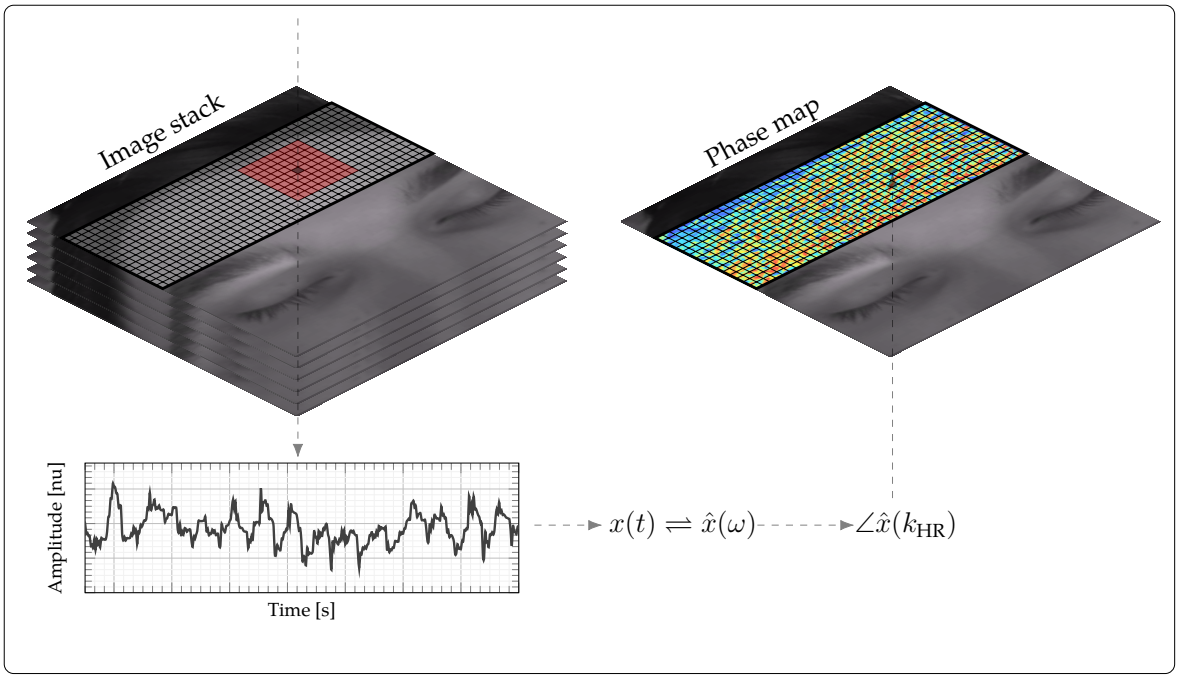

Figure 3.6: Synthesis of phase map: For each pixel in the video, demonstrated here for a single example pixel (black square), the surrounding 10×10 pixels (red squares) are averaged and the value is stored. This is done for all video frames, resulting in a one-dimensional signal $x(t)$. Subsequently, the Fourier Transform of the signal is computed and the phase $\angle\hat{x}(k_{\mathrm{HR}})$ is stored and visualized as a pseudo-colored image.

As can be seen in Fig. 3.6, the acquired values were stored in a pseudo-colored image at the same spatial location of the pixel. This allows a visual analysis of the distribution of the phase which is termed phase map. The same visualization can be generated using the magnitude which is shown in Fig. 3.7 exemplarily.

Feasibility of PPGi of the Sole of the Foot[10]

The dataset acquired in the non-MR environment (→ Chapter 3.1.2) was used to evaluate the feasibility of PPGi signals of the sole of the foot. To that extent, three aspects have been investigated: i) whether the setup used allows acquiring PPGi signals with an adequate SNR, ii) whether the sole of the foot is a suitable alternative

[10]This work has been published in: Spicher, N., Lovelace, T., Kukuk, M. (2018): Feasibility of photoplethysmography imaging of the sole of the foot In: Proceedings of the 13th IEEE International Symposium on Medical Measurements & Applications, Rome, Italy.

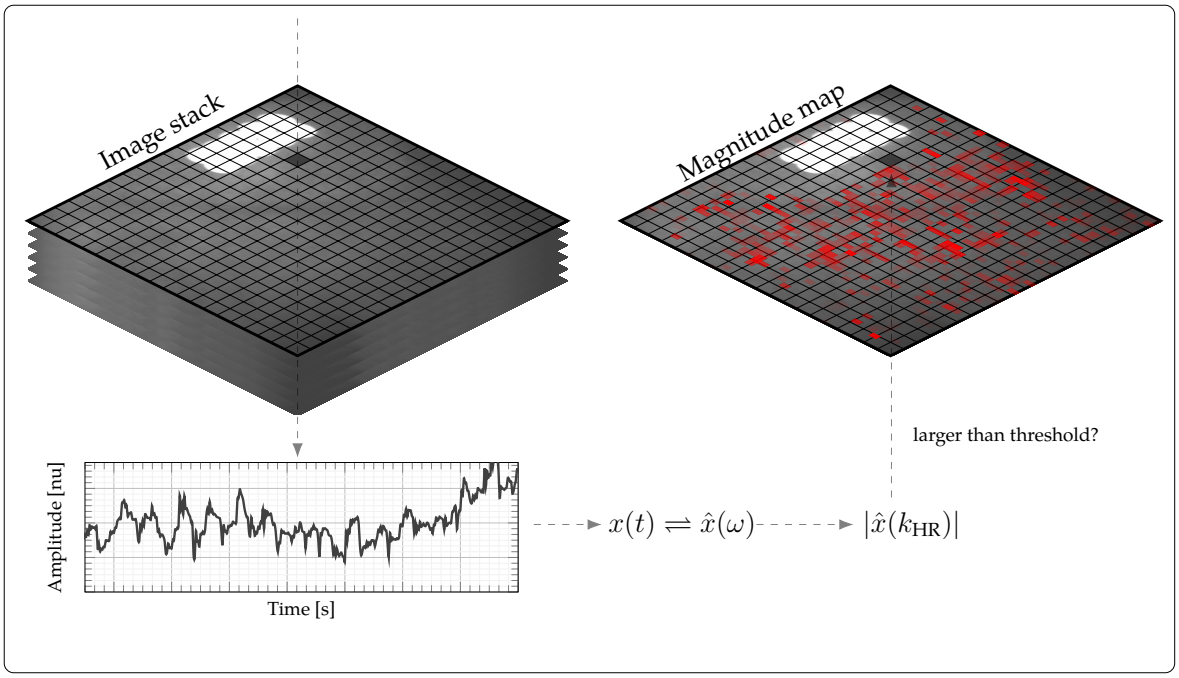

Figure 3.7: Synthesis of (selective) magnitude map: For each pixel in the video (palm of the hand), a PPGi signal $x(t)$ is computed by capturing the values of a single pixel over time. The Fourier Transform of the signal is computed and the magnitude $|\hat{x}(k_{\mathrm{HR}})|$ is stored in a pseudo-colored image if the magnitude belongs to the highest values of all pixels. Some pixels are saturated due to frontal LED illumination.

to the palm of the hand, and iii) whether using a carefully selected ROI results in an improved SNR compared to using all pixels. The latter investigation was motivated by the recent observations that the strengths of the PPGi signal is inhomogeneously distributed across the skin, as was reported by several groups, e.g. (Moço et al. 2016). Three approaches were chosen for data analysis: Qualitative analysis of PPGi spatial clusters on the skin, quantitative analysis using (selective) magnitude maps as shown in Fig. 3.7, and similarity in peak-to-peak durations using PPG as reference.

Qualitative analysis For each experiment of the second dataset (→ Chapter 3.1.2), the HR of the subject was manually determined by picking the dominant frequency bin k_{HR} in the range $[0.66, 3]$ Hz from the magnitudes of the PPG signal's Fourier Transform. Subsequently, the PPGi video were processed similar to the description in the previous section: Spatial averaging was not performed by using filter masks, but by means of scaling of the frames to a resolution of 160×128. The remaining

algorithm is shown in Fig. 3.7: For each pixel, the PPGi signal $x(t)$ was acquired and the Fourier Transform was computed, followed by acquisition of the magnitude at the ground truth HR $|\hat{x}(k_{\text{HR}})|$. Finally, only the $1/16$ pixels containing a PPGi signal with highest magnitudes were stored in a magnitude map for visual analysis of spatial clusters with high intensity of the cardiac component.

Quantitative analysis The signals of all pixels were combined by averaging into a signal $\text{PPGi}_{\text{all}}(t)$ and the pixels with a cardiac signal larger than the threshold (→ Fig. 3.7, red pixels) were combined into a signal $\text{PPGi}_{\text{best}}(t)$. Both signals as well as the ground truth PPG signals were filtered by applying a unit pulse function (→ Fig. 2.9) to their respective Fourier Transforms with a passband $[0.66, 3]$ Hz and then using the inverse Fourier Transform. Finally, the time axes were synchronized, enabling the comparison of the signals despite different sampling rates.

Regarding the comparison of the signals, the problem lies in the fact that to-date there is no established best practice regarding SNR measurement for PPGi signals. Therefore, in order to compare the signals, three metrics from literature were used. The first which offers a SNR measurement in time domain

$$\text{SNR}_{\text{td}} \equiv \frac{\|s(t)\|^2}{\|n(t)\|^2} \tag{3.13}$$

where

$$s(t) \equiv \frac{\langle x(t), y(t)\rangle}{\langle y(t), y(t)\rangle} \cdot y(t) \tag{3.14}$$

and

$$n(t) \equiv x(t) - \frac{\langle x(t), y(t)\rangle}{\langle y(t), y(t)\rangle} \cdot y(t) \tag{3.15}$$

with one either $\text{PPGi}_{\text{all}}(t)$ or $\text{PPGi}_{\text{best}}(t)$ being represented by $x(t)$ and the ground truth PPG signal by $y(t)$. Angled brackets represent the scalar dot product.

The second is an SNR metric based on the frequency domain (de Haan, Jeanne 2013)

$$\text{SNR}_{\text{td}} \equiv \frac{\sum W(f) \cdot \hat{x}(f)}{\sum 1 - W(f) \cdot \hat{x}(f)} \tag{3.16}$$

where $\hat{x}$ is the Fourier Transform of the either $\text{PPGi}_{\text{best}}(t)$ or $\text{PPGi}_{\text{best}}(t)$ as a function of frequency f in Hz. $W(f)$ is a window function that is centered on the HR with a width of ± 0.25 Hz. HR was estimated from the spectrum of the PPG signal the same as during qualitative analysis (→ p. 72).

The last measure is based on the Pearson correlation coefficient (Amelard et al. 2015)

$$PCC \equiv \frac{\mathrm{cov}(x(t), y(t))}{\mathrm{sd}(x(t)) \cdot \mathrm{sd}(y(t))} \tag{3.17}$$

where the $\mathrm{cov}(\cdot)$ and $\mathrm{sd}(\cdot)$ operators denote the covariance between both signals and the standard deviation, respectively. If resulting values are close to -1 ($+1$) this indicates a negative (positive) linear relationship and 0 indicates no correlation.

However, as the aim of this work is MRI cardiac triggering, which requires the accurate localization of maxima in PPGi signals, two other metrics were proposed which are more suited to this application. The duration between subsequent peaks in the $\mathrm{PPGi}_{\mathrm{all}}(t)$, $\mathrm{PPGi}_{\mathrm{best}}(t)$, and the ground truth PPG signal were compared. First, peak detection was performed in all three signals by customizing an algorithm for detecting peaks in near-infrared spectroscopy signals (Scholkmann et al. 2012). Subsequently, the durations between subsequent peaks were computed and stored. The SNR for one of the PPGi signals was estimated by comparing the durations t to the durations of the PPG signal:

$$\mathrm{TD}_{\mathrm{mean}} = \mathrm{m}(t - t_{\mathrm{PPG}}) \tag{3.18}$$

$$\mathrm{TD}_{\mathrm{sd}} = \mathrm{sd}(t - t_{\mathrm{PPG}}) \tag{3.19}$$

with t being the points in time of peaks in either $\mathrm{PPGi}_{\mathrm{all}}(t)$ or $\mathrm{PPGi}_{\mathrm{best}}(t)$. Operator $\mathrm{m}(\cdot)$ represents the arithmetic mean. A value near 0 indicates a high similarity between both signals while larger values indicate a mismatch. It was ensured manually that t and t_{PPG} are synchronized, i.e. the same cardiac cycles are analyzed by both.

3.3 ECG-based methods

In this chapter, the methods developed with the aim of robustly processing ECG signals acquired from a PMU within UHF MRI are presented. In this regard, the msPE framework was developed, which allows processing of signals with morphologies typically encountered in biomedical engineering applications.

The framework is introduced (→ Chapter 3.3.1) and its capabilities and limitations are assessed first using synthetic signals (→ Chapter 3.3.2). As an initial step towards ECG processing, the framework is customized for the delineation of ECG signals from a (non-MR) benchmark database and its performance is compared to state-of-the-art algorithms (→ Chapter 3.3.3). Subsequently, the customization for processing ECG signals recorded within UHF MRI is introduced and evaluated (→ Chapter 3.3.4).

3.3.1 A novel framework for multiscale parameter estimation[11]

The msPE framework makes use of the multiscale properties of the Wavelet Transform for estimating the parameters of a one-dimensional input signal. The input signal is assumed to follow a 5-parameter model (amplitude A, width σ, extent of undershoot τ, position μ, baseline B) which allows a seamless transition from a Gaussian function to its second derivative (→ Fig. 2.12, left). This model is generalized further towards a piecewise 8-parameter model with different parameters on the left and right side.

Both models are depicted in Fig. 3.8 and comparing the different configurations to shapes typically found in biosignals (e.g. → Figs. 2.24, 2.27, 2.29) demonstrates its usefulness. Many biosignals have a shape similar to a Gaussian, e.g. ECG P-/T-waves. Furthermore, undershoots can often be observed, for example the Q- and S-wave of a QRS complex can be assumed as undershoots of the R-wave. Other than that, many signals show very small undershoots or a smooth transition over time from having no undershoot to showing a subtle undershoot. For example, Fig. 2.25 ② and ③ depict QRS complexes with Q- and S-waves showing only a merely visible amplitude which also changes over time. Therefore, a parameter τ representing an undershoot's extent is included in the model which enables a smooth transition from a Gaussian model (no undershoot, $\tau = 0$) to the model with undershoot ($\tau > 0$).

[11]This work has been published in: Kukuk, M., Spicher, N. (2019): Parameter estimation based on scale-dependent algebraic expressions and scale-space fitting. IEEE Transactions on Signal Processing, 67(6), 1431–1446.

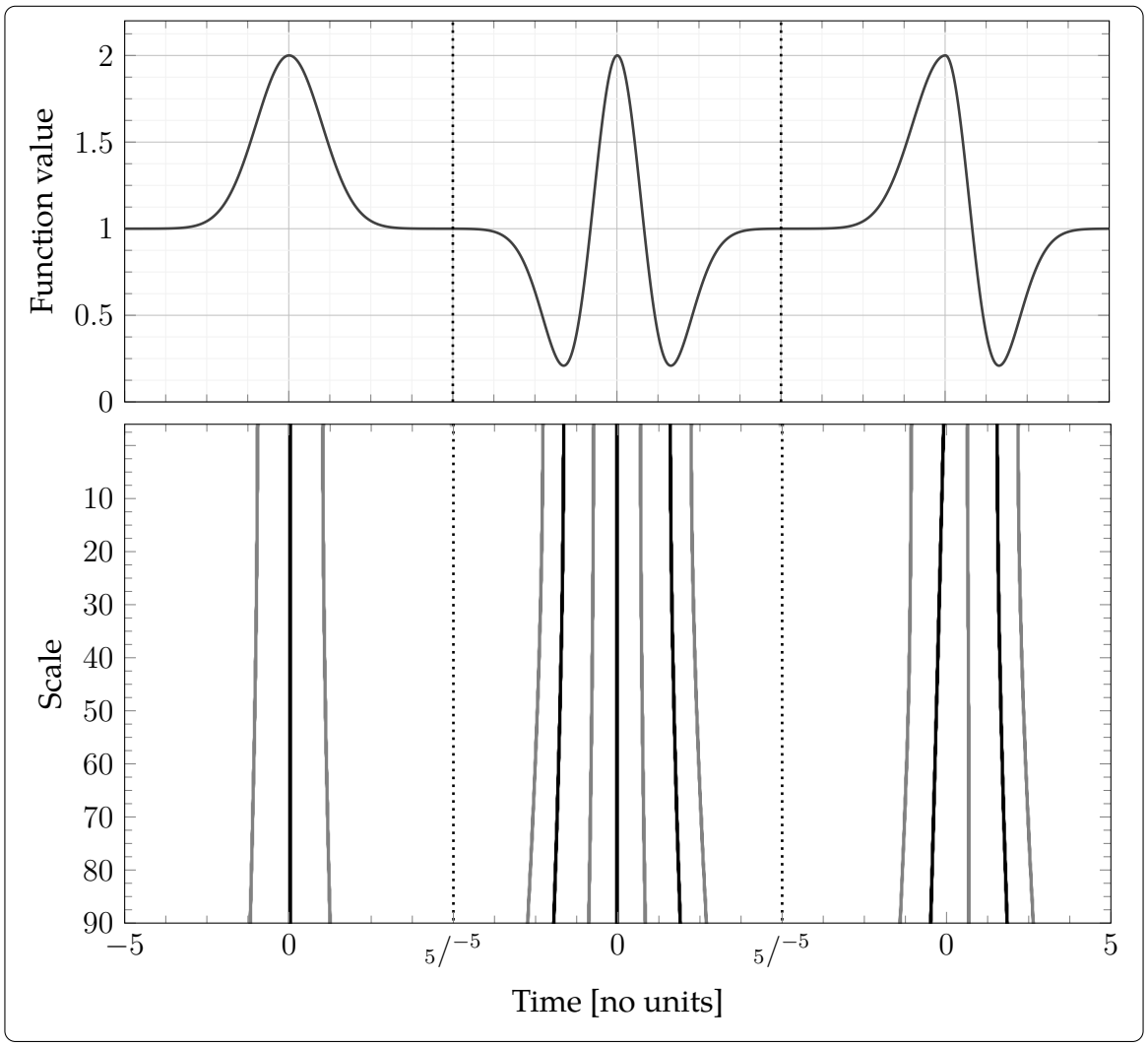

Figure 3.8: *Top row:* Two configurations of the 5-parameter model function defined by parameters $(A, \sigma, \tau, \mu, B)^T$ and one configuration of the 8-parameter model with the left half being identical to the first and the right half identical to the second configuration. Parameter sets are $\vec{P}_1 = (1, 1, 0, 0, 1)^T$, $\vec{P}_2 = (1, 1, 3, 0, 1)^T$, and for the piecewise model $\vec{P}_{\text{left}} = \vec{P}_1$ and $\vec{P}_{\text{right}} = \vec{P}_2$. *Bottom row:* Corresponding zero-crossings in the WT^1 (black lines) and WT^2 (gray lines) scalograms. Black lines are associated to local extrema of the input signals and gray lines are associated to inflection points.

The piecewise extension of the model (→ Fig. 3.8, right) provides even more flexibility and is necessary due to the variability of biosignals. For example, many QRS complexes are asymmetric (→ Fig. 2.24), i.e. both sides have different undershoots, which requires different parameter values on both sides.

The bottom of Fig. 3.8 displays a subset of the WT^1 and WT^2 scalograms using the Wavelet Transform according to eq. (2.43) and showing only zero-crossings which are indicated by black (WT^1) and gray pixels (WT^2). As was introduced in Chapter 2.2.3, extrema of the input signal result in zero-crossings in WT^1 and inflection points result in zero-crossings in WT^2.

The msPE framework can be used to measure the model parameters from these zero-crossings. At the core of the framework lie scale-dependent algebraic expressions which allow to calculate model parameters from zero-crossings in the Wavelet Transform scalogram. Based upon that analytical framework, a numeric counterpart will be introduced which allows estimating the parameters of discrete signals. Optionally, the estimated parameters can be fine-tuned using subsequent numerical optimization/fitting with two methods being proposed in this work. Depending on the area of application, several customizations of this framework are conceivable and allow to adjust the implementation to the scientific problem.

Analytical framework The msPE framework is based on a mathematical analysis of the Wavelet Transform of the 5-parameter model $G_{A,\sigma,\tau,\mu,B}(t)$ ($\rightarrow$ Fig. 3.8, center). A flowchart describing the analytic framework is depicted in Fig. 3.9 with the input signal $x(t)$ being assumed to follow the 5-parameter model. The multiscale differential operator introduced in eq. (2.43) is applied with $n \in \{1, 2\}$, resulting in $WT^1(u, s)$ and $WT^2(u, s)$. By detecting the roots at a given scale s and interchanging, one can obtain solutions for μ, σ, and τ. A and B can not be obtained from zero-crossings and are obtained from the analytical convolution x_c instead. The output are scalar values for each parameter at scale s. In the following, this analytic framework is explained in detail, including the model, algebraic expressions for zero-crossings and for model parameters. Subsequently, an equivalent framework for numeric signal processing is proposed, which serves as basis for an implementation introduced afterwards.

5-parameter Model Let the normalized Gaussian function being defined by

$$G_\sigma(t) = \frac{1}{\sigma\sqrt{2\pi}} e^{-t^2/2\sigma^2} \tag{3.20}$$

and its second derivative by

$$\frac{\mathrm{d}^2}{\mathrm{d}t^2} G_\sigma(t) = \frac{1}{\sigma^2}\left(\frac{t^2}{\sigma^2} - 1\right) G_\sigma(t). \tag{3.21}$$

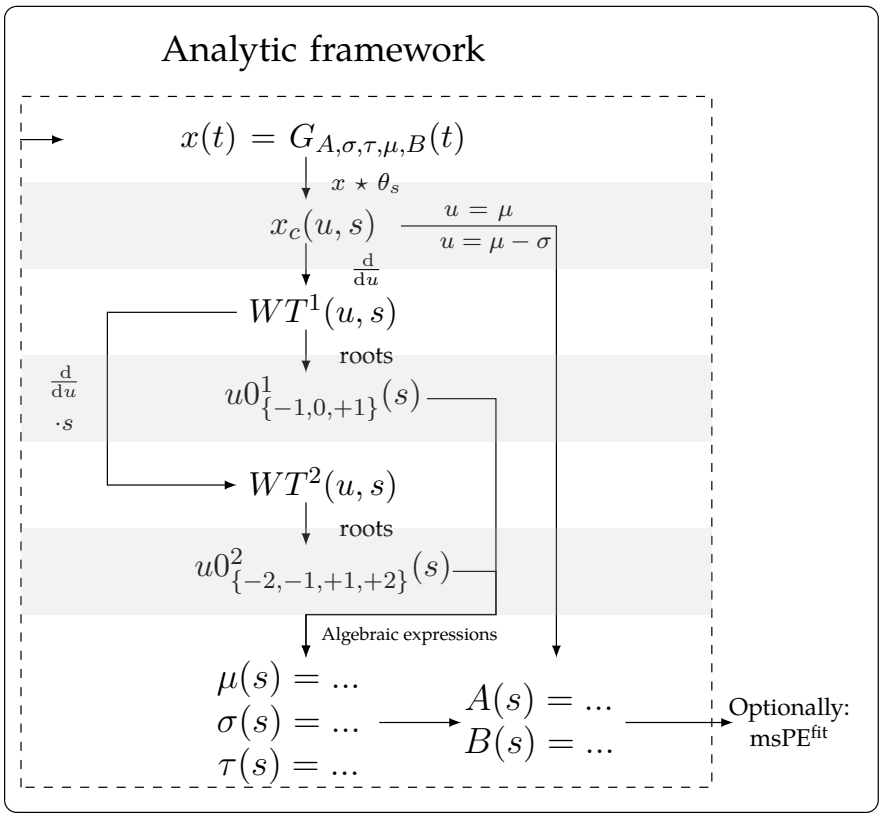

Figure 3.9: Analytic framework for calculating parameters of signal $x(t)$. Zero-crossings of WT^1 and WT^2 are denoted by $u0^1$ and $u0^2$, respectively. The input function $x(t)$ follows the model function $G_{A,\sigma,\tau,\mu,B}(t)$ and the output values are a scalar for each parameter (A, σ, τ, μ, B) at scale s. Optionally, these values can be refined using non-analytical optimization (fitting) which will be denoted msPE$^{\text{fit}}$.

The model function underlying msPE is derived from this equation by adding parameters A, τ, and μ, reflecting about the t-axis, and multiplying by -1:

$$G_{A,\sigma,\tau,\mu,B}(t) = A\left(1 - \frac{\tau\,(t-\mu)^2}{2\sigma^2}\right) e\left(-\frac{(t-\mu)^2}{2\sigma^2}\right) + B. \tag{3.22}$$

As can be seen in Fig. 3.8, a peak following the model is centered at μ, parameter A represents the amplitude, σ the width, and τ the extent of the undershoot. Parameter B represents a constant shift of the baseline on the y-axis. If parameter $\tau = 0$, the undershoot vanishes and the model is equivalent to the Gaussian given in eq. (3.20). If $\tau = 2$, the model represents the Gaussian second derivative given in eq. (3.21). If parameter $A < 0$, parameter τ represents the extent of an overshoot.

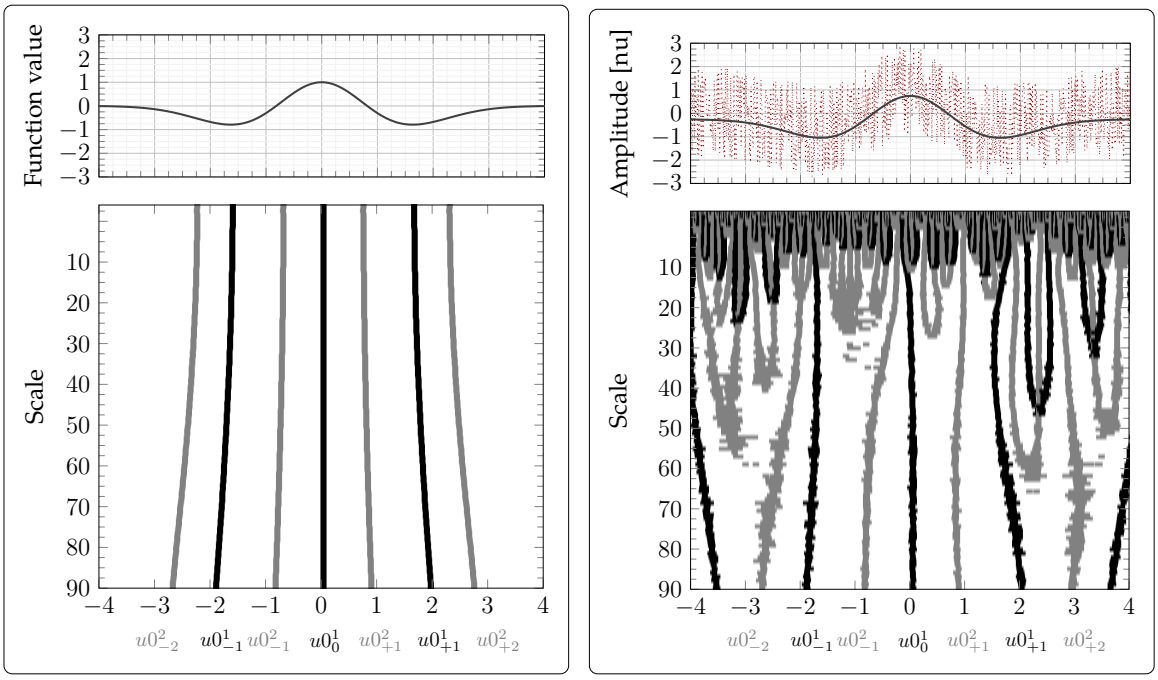

Figure 3.10: *Top left:* $x(t) = G_{A,\sigma,\tau,\mu,B}(t)$ (black curve). *Right:* $x(t)$ biased by uniformly distributed noise (red curve). *Bottom:* Zero-crossings in the time-scale plane associated with extrema (WT^1, black) and inflection points (WT^2, gray) are indicated.

Wavelet Transform An input signal $x(t)$ following the symmetric 5-parameter model (3.22) is substituted into the analytical expressions for calculating the Wavelet Transform of order $n \in (1, 2)$

$$WT^n x(s,u) = s^n \frac{\mathrm{d}^n}{\mathrm{d}u} \Big(x \star \theta_s \Big)(u) \tag{3.23}$$

where n denotes the number of derivatives, $\star$ the convolution, and the wavelet applied is a Gaussian

$$\theta_s(t) = \frac{1}{\sqrt{s}}\, e^{-t^2/s^2}. \tag{3.24}$$

WT^1 and WT^2 are the Wavelet Transforms of the input signal $x(t)$. This representation has the advantage of a filtering effect with increasing scale. For example, Fig. 3.10 depicts on the left side $G_{A,\sigma,\tau,\mu,B}$ (top) and the corresponding zero-crossings of WT^1 and WT^2 (bottom). On the right side, uniform noise has been added to the model, resulting in additional zero-crossings, especially at lower scales. The filtering effect becomes apparent starting at approximately scale 70 at which the lines become similar to the lines of the noise-free signal.

Algebraic expressions for zero-crossings As can be seen in Fig. 3.10, at each scale the model function results in zero-crossings associated to the features (extrema, inflection points) of the model. Thereby, an analytic model for these zero-crossings can be obtained by solving WT^1 and WT^2 for their roots. As their position depends on the model's parameters, one can rewrite the equation for obtaining scale-dependend expressions for each parameter as a function of given zero-crossings.

In Fig. 3.9 and Fig. 3.10, zero-crossings are denoted by $u0$ and are distinguished by superscripts denoting the used transform ($u0^1$ zero-crossing of WT^1, $u0^2$ zero-crossing of WT^2). Zero-crossings of a common transform are distinguished by subscripts. For example, in the 5-parameter model ($\rightarrow$ Fig. 3.10, left), $u0^1_0$ represents the central line associated with the maximum and $u0^1_{\{-1,+1\}}$ represent the left and right zero-crossing associated with the minimum of the undershoots. $u0^2_{\{-2,-1,+1,+2\}}$ are the zero-crossings of the WT^2 which correspond to the inflection points of the input signal. First, the convolution is solved by substituting $x(t)$ with the model and $B = 0$

$$(G_{A,\sigma,\tau,\mu,0} \star \theta_s)(u,s) = K_1 K_2^2 \sigma \sqrt{(K_2 \pi s)/2} \Big(-2K_3^2 + \tau \big(s^4 + 2\sigma^2 (s^2 + 2(u-\mu)^2) \big) \Big) \quad (3.25)$$

where $K_1 = A\, e^{-K_2 (u-\mu)^2}$, $K_2 = 1/K_3$, and $K_3 = s^2 + 2\sigma^2$. Multiplication with s^n and differentiation results in the analytical Wavelet Transforms

$$\begin{aligned} WT^1(u,s) = &- K_1 \sqrt{2\pi s^3 K_2^7} (u-\mu) \sigma \Big(s^4(\tau - 2) - 2\sigma^2 \\ &s^2(\tau + 4) + 4\sigma^2 \big(\tau (u-\mu)^2 - 2\sigma^2 (\tau + 1) \big) \Big) \end{aligned} \quad (3.26)$$

and

$$\begin{aligned} WT^2(u,s) = K_1 \sqrt{2\pi\ s^5\ K_2^9}\ \sigma\ \Big(& 2K_3^2 \big(K_3 - 2(u-\mu)^2 \big) + \tau \\ & \big(-s^6 + 2s^4 (u-\mu)^2 + 4\sigma^2 s^2 \big(3\sigma^2 - 4(u-\mu)^2 \big) \\ & + 8\sigma^2 \big(2\sigma^4 - 5\sigma^2 (u-\mu)^2 + (u-\mu)^4 \big) \big) \Big) . \end{aligned} \quad (3.27)$$

The zero-crossings of WT^1 and WT^2 are derived by solving $WT^1(u,s) = 0$ and $WT^2(u,s) = 0$. The three WT^1 zero-crossings with respect to a given scale are

$$\begin{aligned} u0^1_0(s) &= \mu \quad \text{and} \\ u0^1_{\{-1,+1\}}(s) &= \mu \pm \frac{1}{2\sigma\tau} \sqrt{K_3\ \tau\ \big(4\sigma^2(\tau+1) - s^2(\tau-2) \big)} \ . \end{aligned} \quad (3.28)$$

There are four zero-crossings of WT^2 with respect to a given scale s

$$u0^2_{\{-2,-1,+1,+2\}}(s) = \mu \pm \frac{1}{2\sqrt{2}\sigma\tau} \sqrt{K_3 \tau \big(-s^2(\tau-2) + 2\sigma^2(5\tau+2) \pm \sqrt{K_4} \big)} \quad (3.29)$$

with $K_4 = s^4(\tau-2)^2 + 4\sigma^4 \big(\tau(17\tau + 12) + 4 \big) + 4\sigma^2 s^2 \big(\tau(4 - 3\tau) + 4 \big)$.

Algebraic expressions for model parameters In the following, the analytical expressions are derived for calculating model parameters from zero-crossings in the time-scale plane. As they are interchangeable, a single zero-crossing of $u0^1_{\{-1,+1\}}(s)$ and $u0^2_{\{-2,-1,+1,+2\}}(s)$ is denoted by $u0^1_s$ and $u0^2_s$, respectively.

As can be seen in Fig. 3.10, parameter μ defines the position of the peak's minimum ($A < 0$) or maximum ($A > 0$) and is associated to the central WT^1 zero-crossing

$$\mu(s) = u0^1_0(s) \ . \tag{3.30}$$

Parameter τ can be obtained from WT^1 zero-crossing only by solving (3.28), which yields a single solution

$$\tau^1(s) = 2K_3^2 \ / \ (s^4 - 8\sigma^4 - 2\sigma^2(s^2 - 2(u0^1_s - \mu)^2)) \tag{3.31}$$

and solving (3.29) gives another solution making use of WT^1 and WT^2 zero-crossings

$$\begin{aligned}\tau^2(s) = 2K_3^2 \ (s^2 - 2(u0^2_s - \mu)^2 + 2\sigma^2) \ / \ \big(s^6 - 16\sigma^6 - 2s^4(u0^2_s - \mu)^2 + \\ 4s^2\sigma^2(4(u0^2_s - \mu)^2 - 3\sigma^2) + \ 40\sigma^4(u0^2_s - \mu)^2 - 8\sigma^2(u0^2_s - \mu)^4\big)\end{aligned} \tag{3.32}$$

which both are distinguished using the superscripts. Equating both allows solving for parameter σ:

$$\sigma(s) = \pm \sqrt{(2(u0^1_s - u0^2_s)(u0^1_s + u0^2_s - 2\mu)(u0^2_s - \mu)^2 - s^2 \ K_5/2K_5} \tag{3.33}$$

with $K_5 = -2\mu^2 + {u0^1_s}^2 - 2\mu u0^1_s - 3{u0^2_s}^2 + 6\mu u0^2_s$.

Parameters A and B can not be acquired from zero-crossings of the Wavelet Transform as they are canceled out. Therefore, a multiscale analysis using the convolution $(G_{A,\sigma,\tau,\mu,B} \star \theta_s)$ is performed

$$x_c(\mu, s) = \Big(\sqrt{\pi}\sqrt{s}\Big(\sqrt{2}A\sigma\left(s^2(\tau - 2) - 4\sigma^2\right) - 2B\sqrt{K_3^3}\Big)\Big) \Big/ \left(2\sqrt{K_3^3}\right) \tag{3.34}$$

which is solved for parameter A at a given scale s

$$A(s) = \frac{\sqrt{2/\pi}\sqrt{K_3^3}\big(\sqrt{\pi}\, B\, \sqrt{s} + x_c(\mu, s)\big)}{\sqrt{s}\,\sigma\left(s^2(\tau - 2) - 4\sigma^2\right)} \ . \tag{3.35}$$

For parameter B the convolution at point in time $\mu - \sigma$ is required

$$\begin{aligned}x_c(\mu - \sigma, s) = \Big(- \sqrt{\pi}\sqrt{s}\,\sigma\, e^{-\sigma^2/s^2}\left(2\, B\, e^{\sigma^2/s^2}\sqrt{K_3^5}\,\sigma^{-1} - \right. \\ \left. \sqrt{2}\, A\, K_6\, e^{2\sigma^4/s^4 + 2\sigma^2 s^2}\right)\Big) \Big/ \left(2\sqrt{K_3^5}\right)\end{aligned} \tag{3.36}$$

with $K_6 = \left(s^4(\tau-2) + 4\sigma^4(\tau-2) + 2\sigma^2 s^2(\tau-4)\right)$. By substituting A for (3.35), parameter B can be calculated using:

$$B(s) = \frac{-2x_c(\mu,s)\,K_3^2 + f_c(\mu,s)\,K_{11}\,\tau + K_{10}\,x_c(\mu-\sigma,s)}{\sqrt{\pi}\,\sqrt{s}\,(2K_{11} + 4s^2\sigma^2 - K_{10} - \tau\,K_{11})}\,, \tag{3.37}$$

with $K_{10} = e^{K_2\,\sigma^2} K_3\left(4\sigma^2 - s^2(\tau-2)\right)$ and $K_{11} = \left(s^4 + 4\sigma^4 + 2\sigma^2 s^2\right)$.

Special case: Gaussian model[12] As can be seen in Fig. 3.8 (left), the model is equivalent to the Gaussian function eq. (3.20) for parameter estimation. which is represented by a single WT^1 zero-crossing and two WT^2 zero-crossings

$$u0_0^1(s) = \mu, \tag{3.38}$$

$$u0_{\{-1,+1\}}^2(s) = \mu \pm \sqrt{K_3/2}. \tag{3.39}$$

In this case, parameter μ can be obtained as described in eq. (3.30). Setting eq. (3.32) zero and solving for σ yields

$$\sigma(s) = \pm\sqrt{\left(u0^2(s) - \mu(s)\right)^2 - s^2/2}. \tag{3.40}$$

Parameters A and B are computed using the same approach as before but using the model with $\tau = 0$ as input for the convolution $x_c(\mu,s) = (G_{A,\sigma,0,\mu,B} \star \theta_s)$

$$x_c(\mu,s) = -\sqrt{\pi}\,\left(B\sqrt{s} + \sqrt{2}\,A\,\sigma\sqrt{K_2\,s}\,e^{-K_2\,(u-\mu)^2}\right) \tag{3.41}$$

which is solved for A at a given scale s:

$$A(s) = -\sqrt{2\sigma^2/s + s}\left(\sqrt{\pi}\,B\,\sqrt{s} + x_c(\mu,s)\right) \Big/ \sqrt{2\pi}\,\sigma. \tag{3.42}$$

Using $u = \mu - \sigma$ in (3.41) and solving for B results in

$$B = -\frac{x_c(\mu-\sigma,s)}{\sqrt{\pi}\sqrt{s}} - \frac{\sqrt{2}\,A\,\sigma\,e^{-K_2\,\sigma^2}}{\sqrt{K_3}}. \tag{3.43}$$

Substituting A for (3.42) and solving for B yields the final model parameter

$$B(s) = \frac{1}{\sqrt{\pi}\,\sqrt{s}}\left(\frac{x_c(\mu,s) - x_c(\mu-\sigma,s)}{e^{K_2\,\sigma^2} - 1} - x_c(\mu-\sigma,s)\right). \tag{3.44}$$

[12]Similar derivations for parameters μ (3.30) and σ (3.40) were published in the context of mass spectroscopy (Nguyen et al. 2010).

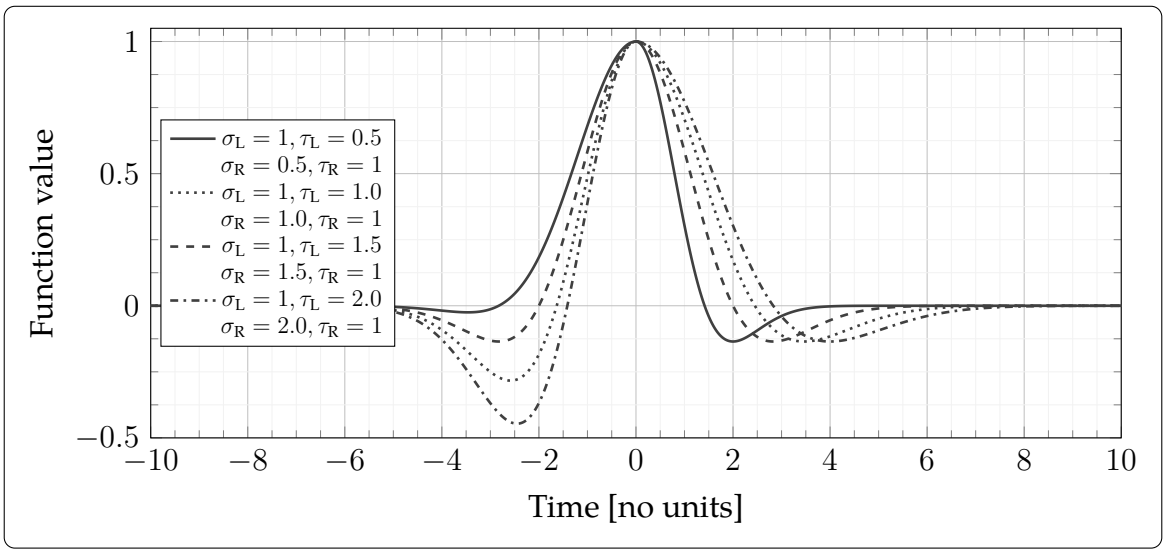

Figure 3.11: Configurations of the piecewise model $G_{\text{pw}}(t)$ described by eq. (3.45) with $A = \bar{A} = 1$, $\mu = 0$, $B_{\text{L}} = B_{\text{R}} = 0$ and remaining parameters given in the legend.

Special case: 8-parameter model In order to be able to represent signals with different shapes on the left and right side, the 5-parameter model the can be extended towards a piecewise model by splitting at parameter μ

$$G_{\text{pw}}(t) = \begin{cases} G_{A,\sigma_{\text{L}},\tau_{\text{L}},\mu,B_{\text{L}}}(t), & \text{for } t < \mu \\ G_{\bar{A},\sigma_{\text{R}},\tau_{\text{R}},\mu,B_{\text{R}}}(t), & \text{for } t \geq \mu, \end{cases} \tag{3.45}$$

with $\bar{A} = B_{\text{L}} + A - B_{\text{R}}$ resulting in a smooth transition between both sides. In the following, the parameter sets of $G_{A,\sigma_{\text{L}},\tau_{\text{L}},\mu,B_{\text{L}}}(t)$ and $G_{\bar{A},\sigma_{\text{R}},\tau_{\text{R}},\mu,B_{\text{R}}}(t)$ will be termed $\vec{P}_{\text{left}}$ and $\vec{P}_{\text{right}}$, respectively. Examples of $G_{\text{pw}}(t)$ can be seen in Fig. 3.8 (right) and in Fig. 3.11. Parameter estimation is identical to the 5-parameter model by simply splitting the model at the center, i.e. parameter μ, and using the zero-crossings on the left for computing the parameters of the left side and vice versa for the right side.

Interchangeability property In the previous section, a single zero-crossing of WT^1 (except $u0_0^1$) was denoted by variable $u0_s^1$ and a single zero-crossing of WT^2 was denoted by variable $u0_s^2$ in the equations for parameter estimation. This constitutes a useful property of the msPE framework which will be termed "interchangeability property". It describes the fact that $u0^1_{\{-1,+1\}}(s)$ are mutually interchangeable which holds for $u0^2_{\{-2,-1,+1,+2\}}(s)$ as well.

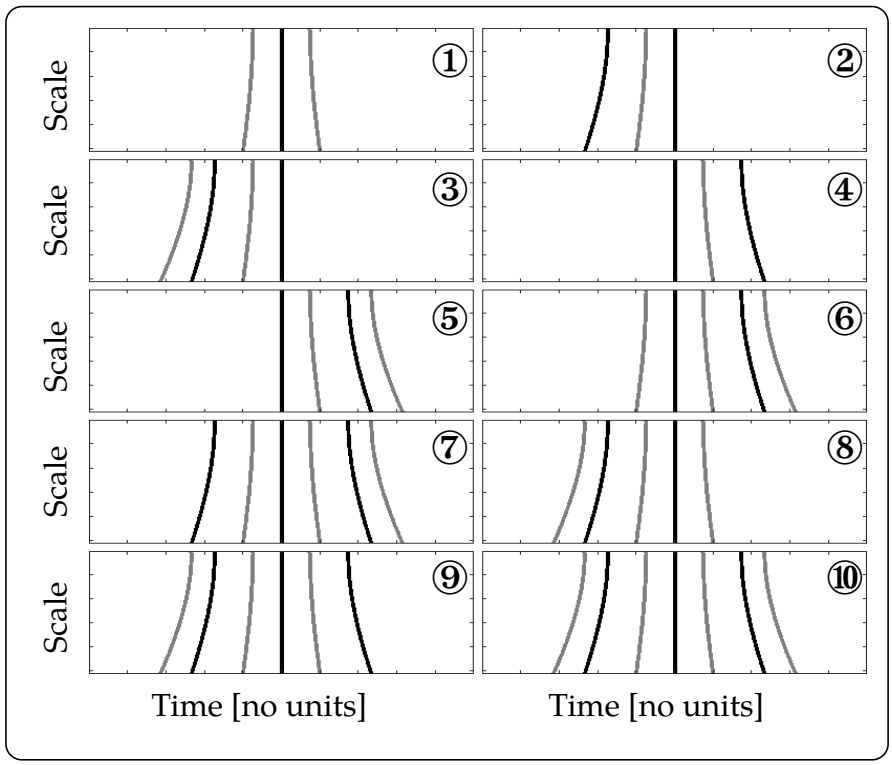

Figure 3.12: Same visualization as in Fig. 3.10 showing different combinations of lines of WT^1 (black) and WT^2 zero-crossings (gray) of the model $G_{A,\sigma,\tau,\mu,B}(t)$. Panel ⑩ shows all lines and panels ① to ⑨ depict subsets. The lines shown in panel ① are equivalent to the Gaussian model ($\rightarrow$ Fig. 3.8, left) and do not allow to compute parameter τ.

This property can be exploited in two regards: First, the higher number of lines ($u0^1_{\{-1,+1\}}$, $u0^2_{\{-2,-1,+1,+2\}}$) than variables ($u0^1_s$, $u0^2_s$) can be used to increase the number of estimated parameter values by combining all available lines. For example, if all lines of the 5-parameter model are available (⑩), parameter σ can be computed using eq. (3.33) from $2 \cdot 4 = 8$ combinations of $u0^1_{\{-1,+1\}}$ and $u0^2_{\{-2,-1,+1,+2\}}$. This holds for all parameters except μ and allows increasing robustness of parameter estimates. Second, the interchangeability property brings the advantage that not all lines are required for parameter estimation. For example, estimating the parameters of the 5-parameter model requires, next to the central WT^1 zero-crossing, a single WT^1 and a single WT^2 zero-crossing only (e.g. panels ①, ②, ④). Hence, combinations shown in panels ② to ⑩ could be used for estimating all model parameters. This allows neglecting lines which are corrupted by noise.

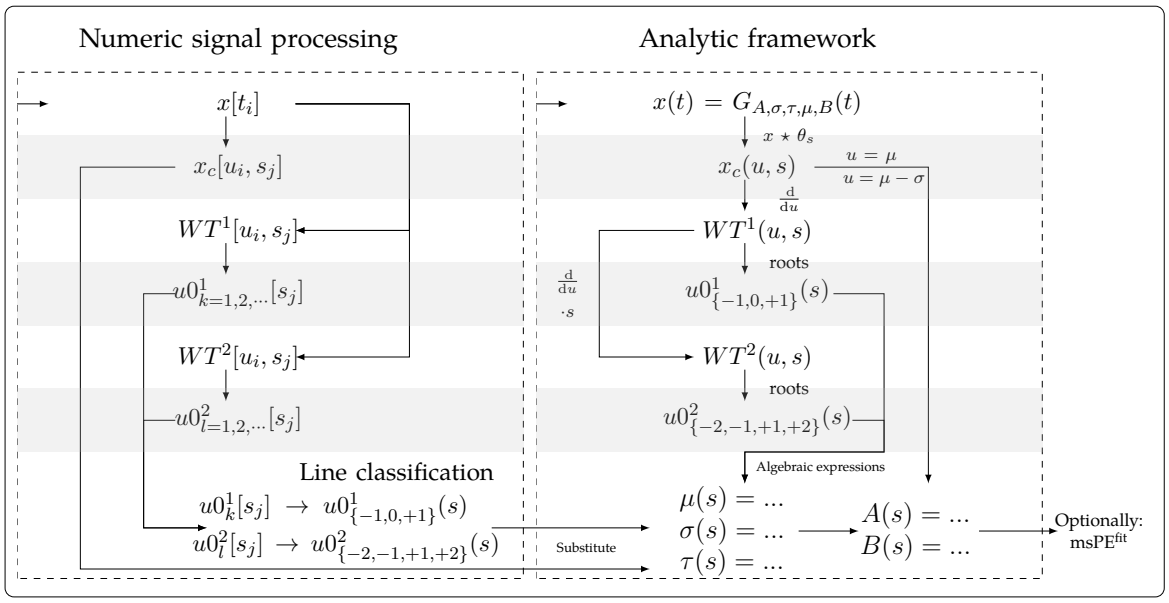

Figure 3.13: Numerical counterpart to the analytic framework. Discrete signals are denoted by square brackets and discrete versions of parameters (e.g. u, s) by subscripts. The input signal $x[t_i]$ is processed numerically to obtain zero-crossing lines with the individual zero-crossings at a certain scale are substituted into the expressions stemming from the analytical framework resulting in model parameters.

Numeric signal processing In the following, the numerical counterpart of the analytical framework is introduced which is depicted in Fig. 3.13. This numerical framework computes the convolution, WT^1 and WT^2 of the input signal $x[t_i]$ numerically and subsequently detects all zero-crossings $u0^1_{k=1,2,\cdots}$ and $u0^2_{l=1,2,\cdots}$ in WT^1 and WT^2, respectively. As can be seen in Fig. 3.10, these zero-crossings associated to the model form lines. The algorithm makes use of this fact by linking zero-crossings over multiple scales to lines and thereby provides a robust method for detecting zero-crossings associated to a feature of the input signal within the time-scale plane.

The number of zero-crossing lines might be higher than the minimum of three ($\rightarrow$ Fig. 3.12, panel ①) or the maximum number of seven (panel ⑩) due to noise ($\rightarrow$ Fig. 3.10, right). Thereby, from the set of detected zero-crossing lines $u0^1_k$ and $u0^2_l$, "valid" lines associated to the model have to be identified within a step of line classification and assigned to a given index ($u0^1_k[s_j] \rightarrow u0^1_{\{-1,0,+1\}}(s)$, $u0^2_l[s_j] \rightarrow u0^2_{\{-2,-1,+1,+2\}}(s)$). Subsequently, only the zero-crossings of valid lines are substituted into the algebraic expressions.

The resulting model parameter values for a given scale can be further refined by repeating the computation for more scales and averaging the resulting values and/or by using optimization (msPE$^{\text{fit}}$).

Line classification The step of line classification, i.e. the step of dividing all detected zero-crossing lines into one of the two classes "valid" and "invalid" is critical for the accuracy of the proposed method. Ideally, the first class represents zero-crossing lines that result from the model, while the second class comprises lines resulting from noise. For example in Fig. 3.10 (left), there are only valid lines while in Fig. 3.10 (right), the number of lines is increased due to the appearance of invalid lines resulting from noise.

In this work, two classifiers for zero-crossing lines are applied. The first method is based on detecting the central zero-crossing line, associated to parameter μ ($\rightarrow$ Fig. 3.10, $t = 0$) followed by a linear search for detecting the remaining lines. This approach will be described and used in sections 3.3.2 and 3.3.4. The second method is computationally more demanding by making full use of the interchangeability property and will be described in section 3.3.3.

Parameter optimization The msPE frameworks provides analytical expressions for the input model $G_{A,\sigma,\tau,\mu,B}(t)$ and zero-crossings in time-scale plane $u0^1_{\{-1,0,+1\}}(s)$ and $u0^2_{\{-2,-1,+1,+2\}}(s)$. This allows fine-tuning the obtained parameters by substituting them into these equations, adjusting a parameter value, compute an error to the signal at hand, and repeated parameter adjustment until a minimum error is reached.

In this work, two methods which are termed msPE$^{\text{fit}}_{\text{td}}$ (msPE + fitting in time-domain) and msPE$^{\text{fit}}_{\text{tsp}}$ (msPE + fitting in the time-scale plane) are proposed.

msPE$^{\text{fit}}_{\text{td}}$: The first method is applied in time domain by using the input signal $x[t_i]$ as reference. The estimated parameters are substituted into to the model eq. (3.22) and are allowed to change independently to adjust to the input signal $x[t_i]$. The parameters estimated by msPE serve as starting values for an optimization by minimizing the error between model and input signal. For the 5-parameter model, the cost function is described by

$$\underset{A,\sigma,\tau,\mu,B}{\operatorname{argmin}} \sum_{t_i} \Big(x[t_i] - G_{A,\sigma,\tau,\mu,B}(t_i) \Big)^2 . \tag{3.46}$$

This can be adjusted for the 8-parameter model by splitting computations in a left

$$\underset{A,\sigma_L,\tau_L,\mu,B_L}{\operatorname{argmin}} \sum_{t_i} \left(x[t_i] - G_{A,\sigma_L,\tau_L,\mu,B_L}(t_i) \right)^2 \text{ for } t_i \leq \mu \tag{3.47}$$

and right

$$\underset{\bar{A},\sigma_R,\tau_R,\mu,B_R}{\operatorname{argmin}} \sum_{t_i} \left(x[t_i] - G_{\bar{A},\sigma_R,\tau_R,\mu,B_R}(t_i) \right)^2 \text{ for } t_i > \mu \tag{3.48}$$

side.

msPE$^{\text{fit}}_{\text{tsp}}$: The second method allows fine-tuning the parameters which are represented in the time-space plane (μ, σ, τ) by changing them independently to adjust the $u0^1$ and $u0^2$ lines described analytically by eq. (3.28) and eq. (3.29) to the lines of the input signal that were chosen by the line classifier $u0^1_m$ and $u0^2_n$. This results in a least-squares approach which is computed for a range of scales s_j:

$$\tilde{\mu}, \tilde{\sigma}, \tilde{\tau} = \underset{\mu,\sigma,\tau}{\operatorname{argmin}} \sum_{s_j=s_{\min}}^{s_{\max}} \left(\sum_{m=-1}^{+1} (u0^1_m(s_j) - u0^1_m[s_j])^2 + \sum_{n=-2}^{+2} (u0^2_n(s_j) - \tilde{u0}^2_n[s_j])^2 \right) \tag{3.49}$$

This description assumes that the 5-parameter model is at hand and that all model lines are available ($m \in \{-1, 0, 1\}$, $n \in \{-2, -1, +1, +2\}$. If that is not the case, the limits have to be adjusted. This approach can be used for the 8-parameter model by using $m \in \{-1, 0\}$, $n \in \{-2, -1\}$ for the left half and $m \in \{0, 1\}$, $n \in \{+1, +2\}$ for the right half.

Implementation The implementation of the numerical part of the msPE framework was realized by means of a custom C++11 library making use of data structures and functions provided by the `Armadillo` linear algebra library (http://arma.sourceforge.net/, v9.8) (Sanderson, Curtin 2016) with parameters being summarized in Table 3.1.

The convolution is computed numerically using an implementation provided by the Armadillo framework and a discrete version of a Gaussian function serving as θ_s. Wavelet Transforms WT^1 and WT^2 are computed using a custom implementation of eq. (2.41) which applies wavelets calculated using Hermite polynomials, resulting in a linear discretization of the time-scale plane. Hence, the time axis is identical to the one of the input signal and the scale axis is defined in integer steps starting at 1 to a manually defined maximum $s_{\max}$.

Table 3.1: Core parameters of the numerical part of the msPE framework.

▼ **Parameter name**	Typical values
$[s_{\text{min}}, s_{\text{max}}]$	$[50, 100]$, $[250, 1000]$, $\cdots$
w	10, 50, $\cdots$
Averaging operator	$\text{mean}(\cdot)$, $\text{median}(\cdot)$
Optimization	none, $\text{msPE}^{\text{fit}}_{\text{td}}$, $\text{msPE}^{\text{fit}}_{\text{tsp}}$

Zero-crossings $u0^1_k$ and $u0^2_l$ are located by detecting intercepts with the time axis within WT^1 and WT^2 which are further refined using cubic spline interpolation. Afterwards, lines of zero-crossings covering all scales are detected by tracing a single zero-crossing, starting at scale 1 to s_{max} and by requiring that at each scale there has to be a neighboring zero-crossing within an interval w. Only if there is a zero-crossing at each scale within w, this line is stored for further processing. Subsequently, from the set of all detected lines, a line classifier classifies a subset of lines as valid ($u0^1_k \rightarrow u0^1_{\{-1,0,+1\}}$) and ($u0^2_l \rightarrow u0^2_{\{-2,-1,+1,+2\}}$) that will be used for parameter estimation.

Parameters are computed for a single scale or an interval of scales $s = [s_{\text{min}}, s_{\text{max}}]$: First, parameter μ is computed using (3.30). If there is more than one $u0^1$ zero-crossing line, σ is computed using (3.33), followed by τ using (3.31) and (3.32). Model parameters A and B are computed from the convolution only, using eq. (3.35) and eq. (3.37), respectively. If only a single $u0^1$ representing μ is available, there is no under-/overshoot and therefore σ is computed using eq. (3.40), followed by the computation of A and B using eq. (3.42) and eq. (3.44), respectively.

To increase robustness, all possible permutations of available lines are used during substitution into equations and subsequently averaged into a single value using basic statistical measures (e.g. $\text{median}(\cdot)$ operator). If parameters were estimated for a range of scales, they are averaged as well. Finally, parameter optimization can be applied optionally by using either the input signal in time domain ($\text{msPE}^{\text{fit}}_{\text{td}}$) or its zero-crossing lines in the time-scale plane ($\text{msPE}^{\text{fit}}_{\text{tsp}}$) as reference. For this task, the optimization routines provided by the `NLopt` library (https://nlopt.readthedocs.io/, v2.6.1) (Johnson 2019) were customized.

In the following, several experiments are proposed with different customizations of this library being introduced throughout.

3.3.2 msPE of synthetic signals

In this chapter, four experiments are described that were conducted with the aim to evaluate the capabilities and limitations of the msPE framework using synthetic data. In the first experiment, the underlying model is defined as a Gaussian function $G_{A,\sigma,\tau=0,\mu,B=0}(t)$ which is biased by noise and the accuracy of estimated parameters is compared to state-of-the-art methods (Caruana et al. 1986), (Guo 2011), (Roonizi 2013). In the second experiment, the accuracy for parameter estimation of the model with under-/overshoots $G_{A,\sigma,\tau>0,\mu,B}(t)$ is analyzed and in the third experiment, the piecewise model $G_{\text{pw}}(t)$ with different parameters on the left and right side is used. In the experiments described so far, noise is drawn from a normal distribution while in the fourth experiment the influence of non-Gaussian noise is evaluated.

Notation In all experiments, the following notation will be used. A discrete test signal $\tilde{x}[t_i]$ is obtained by generating a signal $x[t_i]$ following the model eq. (3.22) which is biased by a noise signal $\eta[t_i]$:

$$\tilde{x}[t_i] = x[t_i] + \eta[t_i] \quad \text{with} \quad t_i \in [t_{\min}, t_{\max}] \ . \tag{3.50}$$

The noise is drawn from different distributions with the standard deviation σ_η being computed to obtain an approximately constant SNR for varying model parameters:

$$\text{SNR [dB]} = 10 \log_{10} \left(\frac{\text{Var}(x[t_i])}{\text{Var}(\eta[t_i])} \right) \text{ and } \sigma_\eta = \sqrt{\frac{\frac{\text{Var}(x[t_i])}{\text{Var}(\eta[t_i])}}{10^{\frac{\text{SNR}}{10}}}} \ , t_i \in [\mu - 3\sigma, \mu + 3\sigma] \ . \tag{3.51}$$

$\text{Var}(\cdot)$ defines the variance operator and t_i is limited to the given time interval such that it reflects the non-flat part of the signal only.

Experiment 1: Model with $B = \tau = 0$ In order to compare the performance of the msPE framework to state-of-the-art methods, a test case from literature (Roonizi 2013) is used. A Gaussian signal $G_{A,\sigma,\tau=0,\mu,B=0}(t)$ is generated with noise being added which is drawn from a normal distribution. Subsequently, model parameters μ, A, σ are estimated using methods proposed by (Caruana et al. 1986), (Guo 2011), and (Roonizi 2013). As the model of the msPE framework ($\rightarrow$ eq. (3.22)) is equal to a Gaussian when setting $B = \tau = 0$, this test suitable for comparing its accuracy to the reference methods.

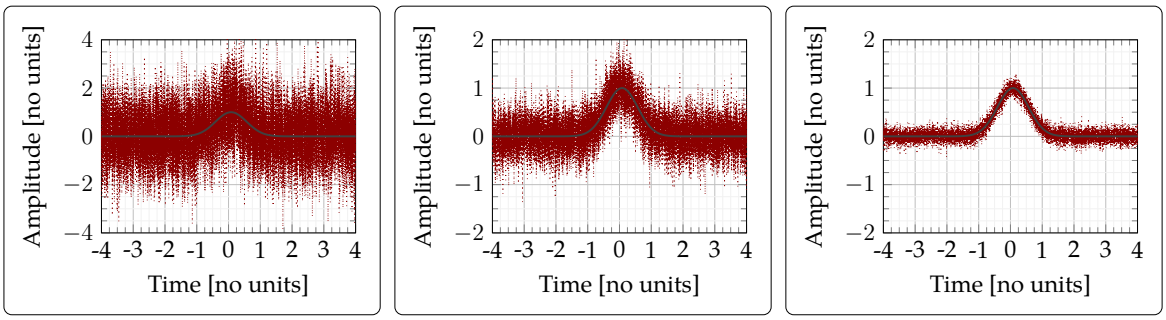

Figure 3.14: Example signals from experiment 1. Gaussian signals $x[t_i]$ (black curves) are generated which are superposed by noise signals $\eta[t_i]$ drawn from a normal distribution, resulting in $\tilde{x}[t_i]$ signals (red curves). Model parameters are $A = 1$, $\mu = 0.08$, $\sigma = 0.51$ and SNR increases from -10 (left), 0 (center), to 10dB (right).

For each of twelve SNR levels $(-10, 0, \cdots, 100)$ dB, signals with a sampling rate of 0.01 Hz within the interval $[-4, 4)$ (8000 samples) are generated. Parameters of $x[t_i]$ are defined according to (Roonizi 2013): $A = 1$, $\mu_i \in \{0.08, 0.56, 0.92\}$, $\sigma_i \in \{0.01, 0.03, ..., 1\}$, and $B = \tau = 0$. Noise signals $\eta[t_i]$ are drawn from a normal distribution and are added to $x[t_i]$ signals, resulting in 150 $\tilde{x}[t_i]$ signals for each SNR level. Three example signals are shown in Fig. 3.14. The customization of the msPE framework is summarized in Alg. 3 and uses only the core functionality by applying the Gaussian model, a basic line classifier which chooses the straightest $u0^1$ line as $u0^1_0$, and a linear line search.

Algorithm 3: Parameter estimation of a Gaussian

Input: $\tilde{x}[t_i]$ **Parameters:** $s_{\text{min}} = 650$, $s_{\text{max}} = 800$, $w = 30$

1) Numerical computation of $WT^1[u_i, s_j]$ and $WT^2[u_i, s_j]$

2) Detection of zero-crossing lines $u0^1_k[s_j]$ and $u0^2_l[s_j]$ spanning all s_{max} using w

3) Detection of central zero-crossing line $u0^1_0$ by choosing the one zero-crossing line from $u0^1_k[s_j]$ with minimum variance in u-direction.

4) Detection of zero-crossing lines $u0^2_{-1}$ and $u0^2_{+1}$ by choosing nearest $u0^2_l[s_j]$ lines left and right of the $u0^1_k[s_j]$ line that has been previously chosen as $u0^1_0$.

For $s \in [s_{\text{min}}, s_{\text{max}}]$:

5) Substitution of zero-crossings of $u0^1_0$ and $u0^2_{\{-1,+1\}}$ into (3.30), (3.40), (3.42)

6) Application of $\text{median}(\cdot)$ to obtained values, resulting in scalars for μ, σ, A

7) Substitution of μ, σ, A and $\tau = B = 0$ into eq. (3.22), resulting in $\tilde{y}[t_i]$

Output: $\tilde{y}[t_i]$

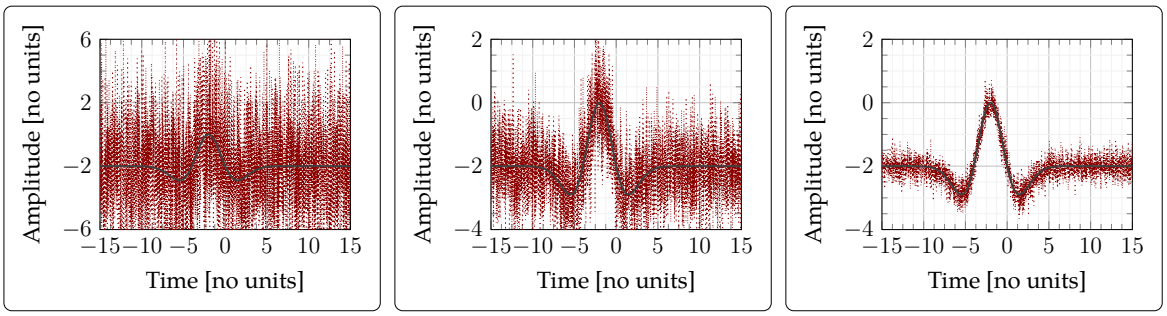

Figure 3.15: Example signals from experiment 2. Signals $x[t_i]$ (black curves) are generated with parameters ($A = \sigma = \tau = 2$, $\mu = B = -2$) which are superposed by noise signals $\eta[t_i]$ which are drawn from a normal distribution, resulting in $\tilde{x}[t_i]$ signals (red curves). SNR increases from -10 (left), 0 (center), to 10 dB (right).

As proposed in (Roonizi 2013), the percentage of root-mean-squared difference (PRD) error measure is used for determining the accuracy of parameter estimation methods. For each $\tilde{x}[t_i]$, an error value is computed by measuring the difference between the signal and a signal $\tilde{y}[t_i]$ that is generated by substituting the estimated parameters into the model eq. (3.22) and computing

$$\text{PRD } [\%] := \sqrt{\frac{\sum_{t_i=-4}^{4} \left(\tilde{x}[t_i] - \tilde{y}[t_i]\right)^2}{\sum_{t_i=-4}^{4} \tilde{x}[t_i]^2}} \cdot 100. \tag{3.52}$$

This is done for all 150 signals of a given SNR and as last step of the processing chain, the arithmetic mean is computed. This results in twelve values describing the accuracy of a single parameter estimation method depending on SNR. However, as the PRD metric is susceptible to outliers and does not give detailed information on the accuracy in estimating a single parameter, a visual analysis of parameter estimation accuracy is performed as well.

Experiment 2: Model with $B \neq 0$ and $\tau \neq 0$ In the first experiment, the msPE framework was used to estimate parameters of Gaussian functions ($\tau = 0$) only. In this experiment, the model is extended towards values other than zero for τ and B, resulting in undershoots and baselines shifts. Due to the novelty of the proposed model function, there are no test cases in literature. Therefore, a test similar to the one proposed in the first experiment is used.

Algorithm 4: Parameter estimation of 5-parameter model

Input: $\tilde{x}[t_i]$ **Parameters:** $s_{\text{min}} = 100$, $s_{\text{max}} = 150$, $w = 30$

1-3) Identical to Alg. 3

4) Detection of zero-crossing lines $u0^1_{\{-1,+1\}}$ and $u0^2_{\{-2,-1,+1,+2\}}$ lines left and right of the $u0^1_k[s_j]$ line that has been previously chosen as $u0^1_0$: The first line found on the left is assumed to be $u0^2_{-1}$ and the first line found on the right is assumed to be $u0^2_{+1}$. Similarly, $u0^1_{\{-1,+1\}}$ are detected, starting at the lines defined as $u0^2_{\{-1,+1\}}$ and $u0^2_{\{-2,+2\}}$ are detected starting at the lines previously defined as $u0^1_{\{-1,+1\}}$.

For $s \in [s_{\text{min}}, s_{\text{max}}]$:

5) Substitution of zero-crossings of all detected lines into eq. (3.30), eq. (3.40), eq. (3.42), and eq. (3.44)

6) Application of $\text{median}(\cdot)$ to parameters, resulting in scalars for μ, σ, τ, A, B.

7) Application of $\text{msPE}^{\text{fit}}_{\text{tsp}}$ for parameter fine-tuning, resulting in $\underline{A}, \underline{\sigma}, \underline{\tau}, \underline{\mu}, \underline{B}$.

Output: $\vec{\underline{P}} = (\underline{A}, \underline{\sigma}, \underline{\tau}, \underline{\mu}, \underline{B})^T$

The same SNR levels $(-10, 0, \cdots, 100)$ dB are considered and for each level 1024 signals with a sampling rate of 0.01 Hz and $N = 3000$ samples over the interval $[-15, 15)$ are generated which are flawed by noise as in the first experiment. Parameters μ, A, and B are drawn from the set $\{-2, -1, 1, 2\}$, σ from the set $\{0.5, 1, 1.5, 2\}$ and parameter τ from the set $\{0, 1, 2, 3\}$. By using each combination of parameters, 1024 combinations are generated.

The algorithm is given in Alg. 4 and similar to the algorithm used in experiment 1, but here the full model ($B \neq 0$, $\tau \neq 0$) is assumed, thereby all seven zero-crossing lines are detected. Moreover, parameter fine-tuning is realized using $\text{msPE}^{\text{fit}}_{\text{tsp}}$.

Due to the limitations of the PRD metric, an error metric based on parameter values is used instead which will be termed parameter vector error (PVE). Vector $\vec{P} = (A, \sigma, \tau, \mu, B)^T$ contains the true model parameters and vector $\vec{\underline{P}} = (\underline{A}, \underline{\sigma}, \underline{\tau}, \underline{\mu}, \underline{B})^T$ the corresponding estimated values by Alg. 4. The error between both is defined as

$$\text{PVE}\,[\%] := \frac{||\vec{P}_n - \vec{\underline{P}}_n||_2}{||\vec{P}_n||_2} \cdot 100, \tag{3.53}$$

where subscript n denotes a normalized vector with the components being normalized to range $[0, 1]$. Hence, for each SNR range, 1024 pairs ($\vec{P}$, $\vec{\underline{P}}$) are used for computing PVE values.

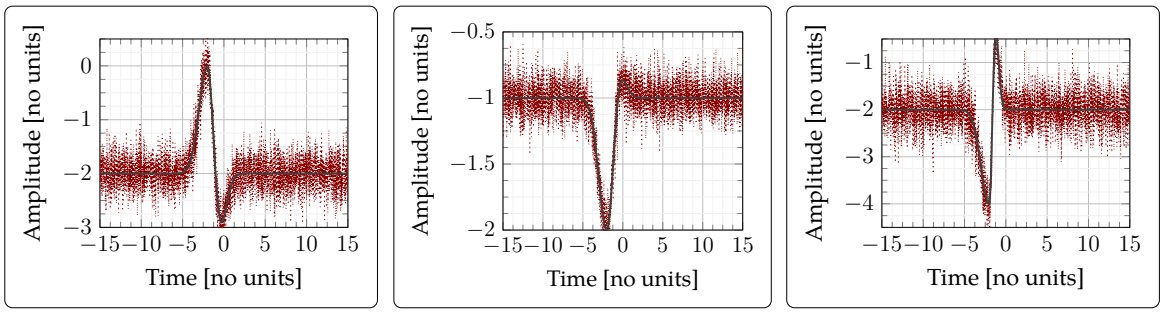

Figure 3.16: Example signals from experiment 3 (SNR 10 dB). $\tilde{x}[t_i]$ signals (red curves) are generated by using signals $x[t_i]$ (black curves) following the piecewise model eq. (3.45) which are superposed by noise signals $\eta[t_i]$ drawn from a normal distribution.

Experiment 3: Piecewise model In the third experiment, the second experiment is extended by using the piecewise model. In this regard, the $G_{\text{pw}}(t)$ is used for generating $x[t_i]$ as is demonstrated in Fig. 3.16. Parameters $\sigma_L = 1$ and $\tau_L = 0$ are fixed, such that the left side has always the same shape while the parameters of the right side are interchanged as described in the previous section.

The algorithm is identical to the one of the previous experiment ($\rightarrow$ Alg. 4), but the piecewise model is assumed. Therefore, steps 1-4 are identical but then the left and right halves are computed independently. msPE$^{\text{fit}}_{\text{tsp}}$ is applied as well, but customized for processing both halves independently. The same error measure (PVE) is used but vectors are adjusted to

$$\vec{P}_{\text{pw}} = (A_L, A_R, \sigma_L, \sigma_R, \tau_L, \tau_R, B_L, B_R)^T \text{ with } B_L = B_R \text{ and } A_L = A_R \tag{3.54}$$

$$\underline{\vec{P}}_{\text{pw}} = (\underline{A}_L, \underline{A}_R, \underline{\sigma}_L, \underline{\sigma}_R, \underline{\tau}_L, \underline{\tau}_R, \underline{B}_L, \underline{B}_R)^T \tag{3.55}$$

Experiment 4: Non-Gaussian and correlated noise In the fourth experiment, the algorithm and evaluation methodology is identical to the methods proposed in the second experiment ($\rightarrow$ Alg. 4). However, in contrast to experiments 1-3, noise vector $\eta[x_i]$ was not generated using a normal distribution ($\rightarrow$ Fig. 3.17, left (solid curve)).

In this experiment, the influence of other types of noise on accuracy is analyzed, which includes uniform noise (dotted) and lognormally-distributed noise (dashed) as well as correlated noise. The latter is characterized by a frequency spectrum following $1/f^{\alpha}$ where f denotes frequency and α describes the level of correlation, ranging from "white" noise ($\alpha = 0$) to "pink" ($\alpha = 1$) and "brown" ($\alpha = 2$) noise with the names being defined referencing to light colors with similar spectra.

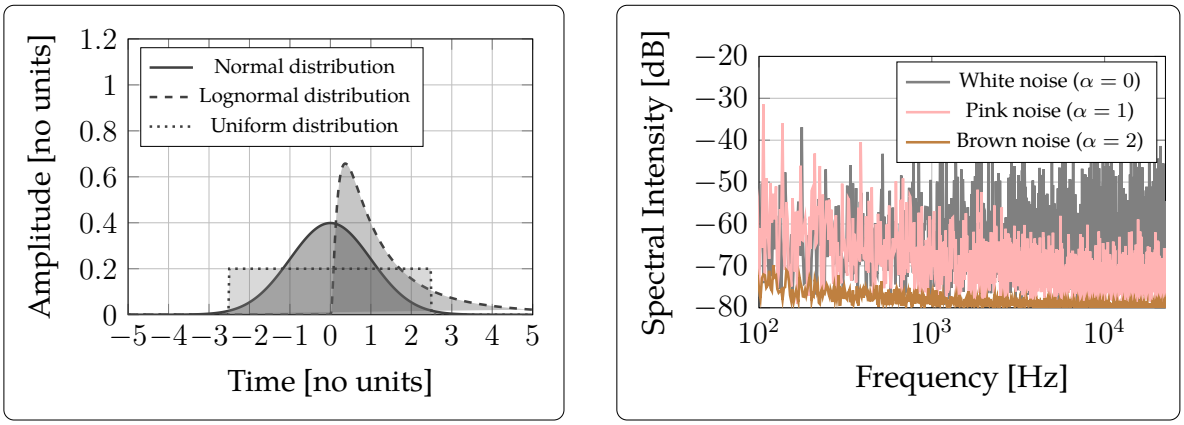

Figure 3.17: *Left:* Normal, lognormal, and uniform distribution *Right:* Example spectra of correlated noise generated using the method proposed in (Kasdin 1995).

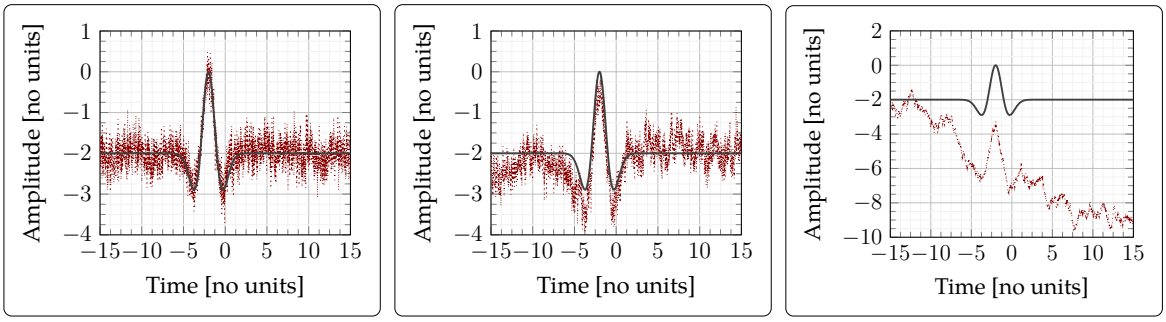

Figure 3.18: Example signals from experiment 4 (SNR 10 dB). $x[t_i]$ signals (black curves) follow the symmetric model eq. (3.22) and noise $\eta[t_i]$ is drawn from correlated noise with $\alpha = 0$ (left, no correlation), $\alpha = 1$ (center, pink noise), $\alpha = 2$ (right, brown noise), resulting in $\tilde{x}[t_i]$ signals (red curves).

For $\alpha = 0$ the noise is identical to noise drawn from a normal distribution. Fig. 3.17 (right) shows example frequency spectra for white, pink, and brown noise. As can be seen, with increasing α the slope of the spectra increases, resulting in a higher portion of low frequency noise and a higher degree of correlation. As can be observed in Fig. 3.18, although the SNR is identical, the increase in α results in more intense signal distortions. In this work, correlated noise is generated using a method proposed in (Kasdin 1995) with α values of 0.5, 1.0, and 2.0.

3.3.3 msPE of ECG signals from a standard database[13]

This study was conducted to evaluate the capabilities and limitations of the msPE framework regarding processing of clinical ECG signals in general before processing ECG signals flawed by UHF MRI noise. A typical task in ECG processing is delineation of P-/T-waves and the QRS complex, i.e. the computation of their onset, peak, and offset fiducial points (→ p. 38). Hence, the msPE framework is customized for the detection of these fiducial points which will be denoted $\{\text{P, QRS, T}\}_{\{\text{on, peak, off}\}}$.

Data ECG signals provided by the QT database (→ Appendix) were processed. Raw signals were upsampled from 250 to 1000 Hz, reducing the sampling interval from 4 to 1 ms. Annotations from two expert cardiologists, who manually defined the positions of fiducial points of 3194 P-waves, 3542 T-waves, and 3623 QRS complexes in both leads serve as ground truth. Additionally, the peak fiducial point of QRS complexes QRS_{peak} detected by an automatic algorithm and contained within the QT database was used as starting point for the proposed method.

Preliminary work[14] In a preliminary study, the positions $\{\text{P, QRS, T}\}_{\text{peak}}$ detected by an automatic algorithm and provided within the QT database were used as starting point of a linear search for zero-crossing lines, similar to the approach proposed in Chapter 3.3.2. For each $\{\text{P, QRS, T}\}_{\text{peak}}$, the nearest lines were selected and used for computing onset and offset fiducial points.

Analysis of the resulting parameter estimates showed a high accuracy for the QRS complexes but often inaccurate results for P- and T-waves. This is explained by the fact that detection of $\{\text{P, T}\}_{\text{peak}}$ poses a higher challenge than QRS complex detection due to a high susceptibility to noise and high variability in morphology (Lenis et al. 2016). Therefore, results of applying msPE at precomputed positions $\{\text{P, T}\}_{\text{peak}}$ is limited by the accuracy of the peak detector used.

[13] This work has been published in: Spicher, N., Kukuk, M. (2020): Delineation of electrocardiograms using multiscale parameter estimation. IEEE Journal of Biomedical and Health Informatics, 24(8), 2216–2229.

[14] This work has been published in: Spicher, N., Kukuk, M. (2019): ECG delineation using a piecewise Gaussian derivative model with parameters estimated from scale-dependent algebraic expressions In: Proceedings of the 41st Annual International Conference of the IEEE Engineering in Medicine and Biology Society, Berlin, Germany.

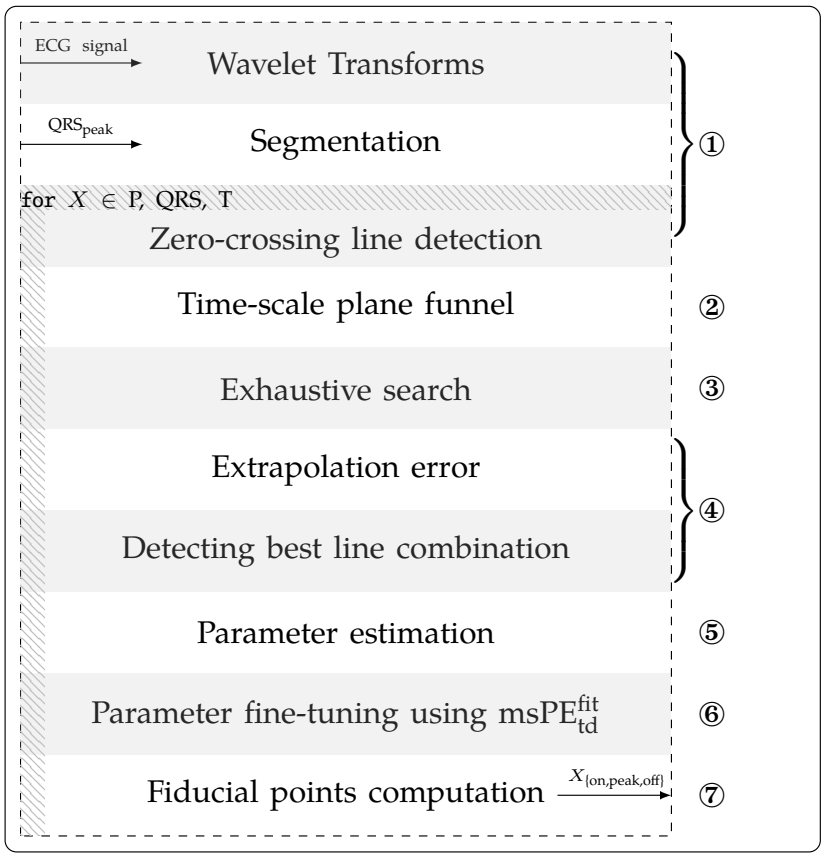

Figure 3.19: Flowchart of the proposed method for ECG delineation with the individual steps (white/gray boxes) being performed from top to bottom in seven stages, denotes by numbers in circles. Input and output data is visualized as arrows. Stage ① is performed once while stages ② to ⑦ (dashed region) are performed once for each ECG wave (P, QRS, T).

Hence, a new customization of the msPE framework is proposed which does only require a position QRS_{peak} as starting point for computing all fiducial points $\{\text{P, QRS, T}\}_{\{\text{on, peak, off}\}}$. This is realized by incorporating domain knowledge into the algorithm and making full use of the interchangeability property (→ Chapter 3.3.1).

Overview of method The flowchart of the msPE framework customized for delineating ECG signals is depicted in Fig. 3.19: Input of the algorithm are an ECG signal and the position of the QRS complex (QRS_{peak}).

First, the input signal is converted into the time-scale plane by computing WT^1 and WT^2 which are then split into three segments for P-/T-waves and the QRS complex.

Subsequently, each segment respectively ECG wave is processed individually for computing its fiducial points.

At first, zero-crossing lines in the segments of WT^1, WT^2 are detected. Subsequently, a "time-scale plane funnel" is used to filter out zero-crossing lines in the time-scale plane that can not be associated to a ECG wave. Subsequently, among all remaining lines, an exhaustive search is conducted which computes each possible combination of lines ($\rightarrow$ Fig. 3.12) and subsequently for each combination an "extrapolation error" is computed which assigns a scalar error value. Subsequently, the one combination with the lowest error is chosen and its zero-crossings are substituted into the algebraic equations of the msPE framework. The values are refined using $\text{msPE}^{\text{fit}}_{\text{td}}$ and the fiducial points are computed using a basic algebraic equation.

① **Wavelet Transform and segmentation (Alg. 5)** The input ECG signal is converted into the time-scale plane by computing WT^1 and WT^2 which are subsequently segmented as shown in Fig. 3.20. QRS_{peak} and domain knowledge (ECG interval times) are used for splitting WT^1 and WT^2 in a segment for each ECG wave (e.g. QRS complex: blue box).

As QRS_{peak} might be inaccurate and due to the high variability in morphology of ECG waves, rather large intervals $I_{\{\text{P, QRS, T}\}}$ were manually defined ($I_{\text{P}} = I_{\text{QRS}} = 0.2\,\text{s}$, $I_{\text{T}} = 0.3\,\text{s}$) for the segmentation of the input signal ($\rightarrow$ Fig. 3.20, top). Normal PQ- and QT-interval durations are known from domain knowledge, therefore for P-/T-waves an offset is used to shift segments to the position where they should be located.

For the segmentation of WT^1 and WT^2 ($\rightarrow$ Fig. 3.20, bottom), $I_{\{\text{P, QRS, T}\}}$ is increased by 0.1s due to the increasing range of zero-crossing lines with increasing scales. The segmentation in scale-direction is realized using an iterative approach: In the first iteration ($iter = 0$) of the algorithm s_{max} is set to 2^6 and the segment $[s_{\text{max}}/2, s_{\text{max}}]$ is extracted. If no ECG wave can be found using this limit in stages ② to ⑦, in the next run ($iter = 1$), s_{max} is reduced to 2^5 or even further to 2^4 ($iter = 2$). If no wave is detected in the last iteration, the wave is considered missed and processing stops.

Within each of the WT^1 and WT^2 segments, uninterrupted lines of zero-crossings from scale 1 to s_{max} are detected. Interrupted lines with a missing zero-crossing at one scale are discarded. As can be seen in Fig. 3.20 (bottom), there can be a high number of zero-crossing lines ($u0^1_?$, $u0^1_?$) but it is not clear to which lines of the model ($u0^1_{\{-1,+1\}}$, $u0^2_{\{-2,-1,+1,+2\}}$) they correspond or if they results from noise only.

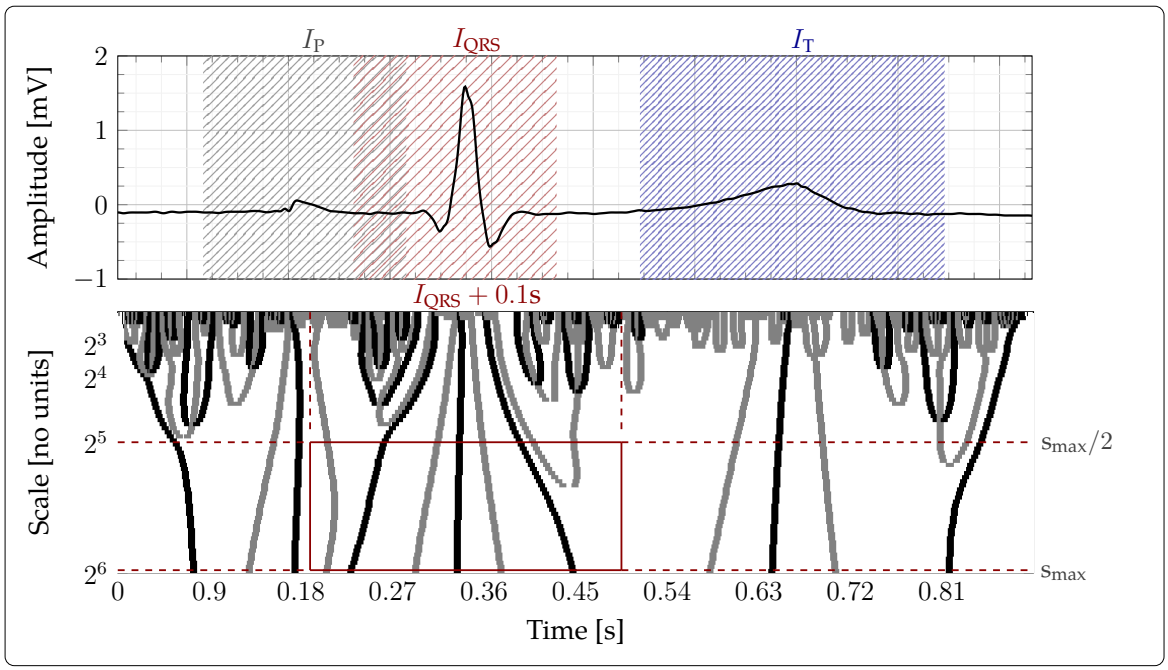

Figure 3.20: ① Visualization of segmentation of ECG signal $\tilde{x}[t_i]$. *Top:* The input signal is split into three segments for the P-wave (gray), QRS complex (red), and T-wave (blue). *Bottom:* Segmentation of the time-scale plane of the QRS complex.

Algorithm 5: ① Wavelet Transform and segmentation

Input: ECG signal $\tilde{x}[t_i]$, QRS_{peak} **Parameters:** $I_P = I_{QRS} = 0.2\,\text{s}$, $I_T = 0.3\,\text{s}$, $iter$

0) If $iter == 3 \rightarrow$ `break()`

1) Numerical computation of $WT^1[u_i, s_j]$ and $WT^2[u_i, s_j]$

2) Segmentation of $\tilde{x}[t_i]$ using $I_{\{P,\,QRS,\,T\}}$ with offsets of $-0.18\,\text{s}$ (P) and $0.27\,\text{s}$ (T)

3a) Segmentation of $WT^1[u_i, s_j]$ and $WT^2[u_i, s_j]$ in u-direction by $I_{\{P,\,QRS,\,T\}} + 0.1$.

3b) Segmentation of $WT^1[u_i, s_j]$ and $WT^2[u_i, s_j]$ in s-direction by $[s_{max}/2, s_{max}]$ with

$$s_{max} = \begin{cases} 2^6 & \text{if } iter == 0 \\ 2^5 & \text{if } iter == 1 \\ 2^4 & \text{if } iter == 2 \end{cases} \tag{3.56}$$

For each $WT^1[u_i, s_j]$ and $WT^2[u_i, s_j]$ segment:

4) Detection of zero-crossing lines $u0_k^1[s_j]$ and $u0_l^2[s_j]$ spanning $[1, s_{max}]$

Output: 3 times: $\tilde{x}[t_i]$, $WT^1[u_i, s_j]$, $WT^2[u_i, s_j]$, set of $u0_k^1[s_j]$, set of $u0_l^2[s_j]$

② **Time-scale plane funnel (Alg. 6)** This stage is applied to reduce the number of zero-crossing lines in the segments computed in the previous stage. Thereby, lines are removed that by no means can represent an ECG component which decreases the run time of the following stages and increases accuracy by reducing the number potentially falsely chosen lines for parameter estimation. The basic idea is that each $u0_?^1$ line in a segment (e.g. Fig. 3.20 red box: 3 lines) could be the central line associated with parameter μ. Depending on the parameters of the ECG wave, it is surrounded by two ($\rightarrow$ Fig. 3.8, left) up to six ($\rightarrow$ Fig. 3.8, center) other lines. But, there are also lines not associated to the wave of interest, e.g. lines resulting from noise or lines from other waves which rise into the segment at higher scales.

It is known from ECG domain-knowledge, that each wave has a typical waveform. Therefore, a "funnel" for the time-scale plane is used to filter out combinations of zero-crossing lines that can not represent a given ECG wave. For example, P-/T-waves both typically do not show an undershoot, therefore the Gaussian model ($\tau = 0$) is used. Typical durations are between $120\,\text{ms}$ (P-wave) and $250\,\text{ms}$ (T-wave) (Sörnmo, Laguna 2005), therefore σ_{min} and σ_{max} were chosen such that they cover a full width at half maximum between $25\,\text{ms}$ and $320\,\text{ms}$. QRS complexes typically have an undershoot, therefore the model with undershoot ($\tau \geq 0$) is used, and a normal duration of $70 - 110\text{ms}$ but it can be prolonged up to $250\,\text{ms}$ in ectopic beats (Sörnmo, Laguna 2005). Therefore, σ_{min} and σ_{max} as well as τ_{min} and τ_{max} are chosen such that a large interval is defined which covers peaks having a full width at half maximum from $25\,\text{ms}$ up to $1\,\text{s}$. Parameters are summarized in Table 3.2.

The functionality of the funnel is explained in Alg. 6 and depicted in Fig. 3.21 exemplarily for the QRS complex: The top and center plot show the valid intervals (dashed region) for WT^1 and WT^2 zero-crossing lines, respectively. The intervals are defined by substituting parameters given in Table 3.2 into the analytic equations for WT^1 and WT^2 zero-crossings (3.28) and (3.29), respectively.

Table 3.2: Parameterization of the time-space plane funnel.

▼ **ECG Wave**	Parameter values
P-/T-wave	$\sigma_{\text{min}} = 0.01$, $\sigma_{\text{max}} = 0.15$
QRS complex	$\sigma_{\text{min}} = 0.02$, $\sigma_{\text{max}} = 0.5$, $\tau_{\text{min}} = 2$, $\tau_{\text{max}} = 0.1$

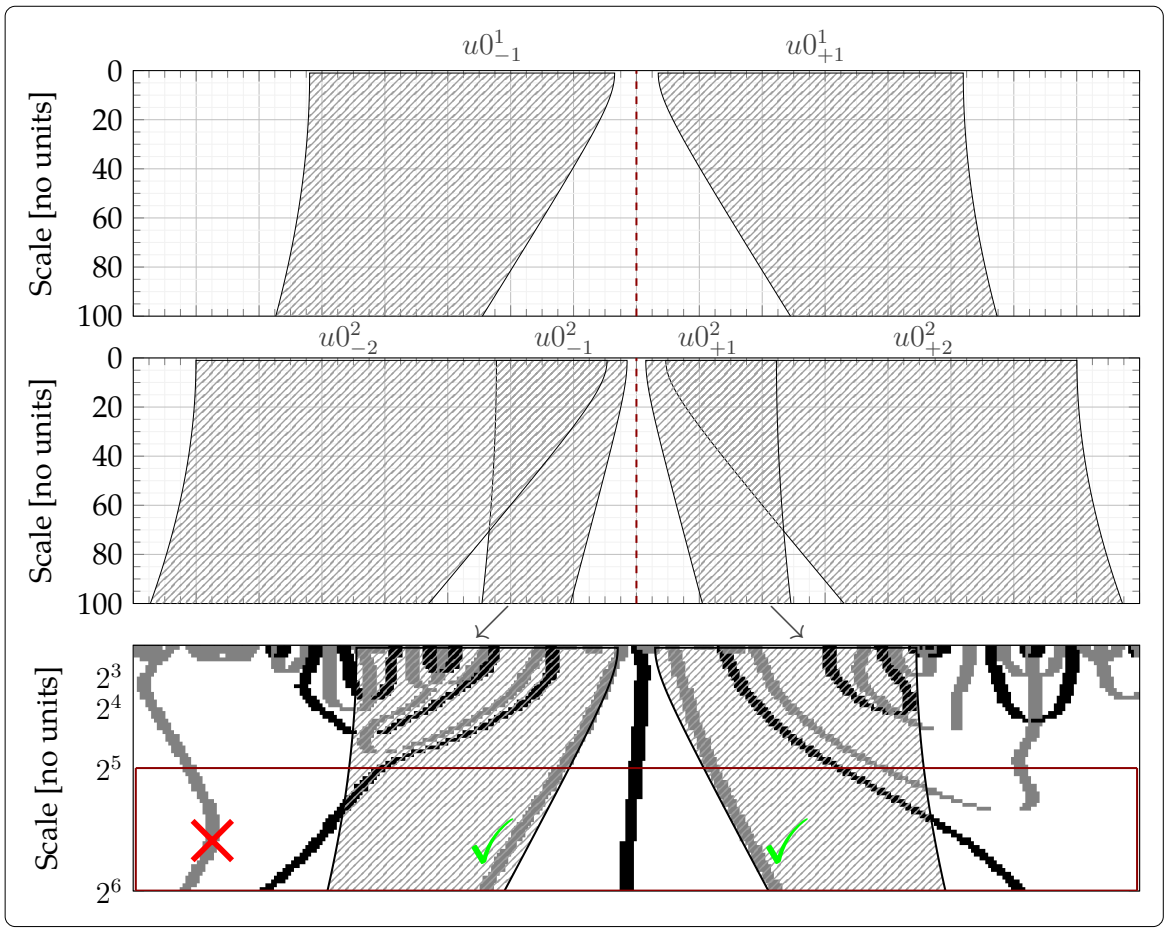

Figure 3.21: ② Visualization of time-scale plane funnel with the lines of the model ($u0^1_{\{-1,+1\}}$, $u0^2_{\{-2,-1,+1,+2\}}$) associated to a given funnel are indicated above it. Hatched regions indicate the valid intervals in which zero-crossing lines are kept. *Bottom:* Application of the $u0^2_{\{-1,+1\}}$ funnel to the time-scale plane shown in Fig. 3.20.

Algorithm 6: ② Time-scale plane funnel (QRS complex)

Input: set of $u0^1[s_j]$, set of $u0^2[s_j]$ **Parameters:** $\sigma_{\{\text{min, max}\}}$, $\tau_{\{\text{min, max}\}}$ (Table 3.2)

1) Substitution of min/max parameters into (3.28) and (3.29) for s_j

For each $u0^1[s_j]$ line:

2a) Detect surrounding zero-crossing lines from set of $u0^1[s_j]$ within the interval computed in step 1) ($\rightarrow$ Fig. 3.21, top)

2b) Detect surrounding zero-crossing lines from set of $u0^2[s_j]$ within the interval computed in step 1) ($\rightarrow$ Fig. 3.21, center)

3) Store currently analyzed $u0^1[s_j]$ line together with lines detected in 2a,b)

Output: set of $u0^1[s_j]$ assumed as $u0^1_0$ and associated $u0^1[s_j]$ and $u0^2[s_j]$ lines

In the bottom plot, the funnel for WT^2 zero-crossing lines is applied at the central WT^1 zero-crossing lines. All WT^2 zero-crossing lines within the intervals are kept (green checkmarks) and all outside the intervals are neglected (red cross). This is repeated using the funnel for WT^1 zero-crossing lines. Subsequently, the funnel is centered on the next WT^1 zero-crossing line and this is repeated until all WT^1 zero-crossing lines are processed.

③ **Exhaustive search** After application of the time-scale plane funnel, only zero-crossing lines that could potentially represent an ECG wave remain in a segment. As introduced earlier, the msPE framework possesses an interchangeability property (→ p. 83), i.e. the model $G_{A,\sigma,\tau,\mu,B}(t)$ has more lines than required for parameter estimation. Hence, in this stage all possible combinations of lines are computed and in the next stage for each an error value is computed. This value gives information about the (dis)agreement with the model function and allows selecting the one combination with the lowest error/highest agreement for further processing.

Fig. 3.12 panel ⑩ shows all lines of the model function. Assuming all lines passed the funnel, $N = 2^6 + 2 \cdot 2^4 - 8 = 88$ line combinations can be computed in total: 2^6 represents the number of combinations when assuming the central $u0^1_0$ line which is surrounded by three lines on the left and on the right and 2^4 is the number of combinations when choosing one of $u0^1_{\{-1,+1\}}$. The subtracted eight lines result from combinations with WT^1 lines only because one WT^2 line is required as minimum for parameter estimation. Fig. 3.12 show ten out of the 88 combinations. The equation for N holds only if there is one candidate for each line. If there is more than one, the following equation can be used:

$$N = \left(\prod_{i=-1}^{+1} (\gamma^{u0^1}(i) + 1) \prod_{j=-2}^{+2} (\gamma^{u0^2}(j) + 1) \right) - \prod_{i=-1}^{+1} (\gamma^{u0^1}(i) + 1) \tag{3.57}$$

with $i, j \in \mathbb{Z}_{\neq 0}$ and $\gamma^{u0^1}(i)$, $\gamma^{u0^2}(j)$ being functions that return number of available line candidates for the given index. After computing all N combinations of lines, each line combination is passed to the next stage which computes an error value.

④ **Extrapolation error (Alg. 7)** In this stage, an error value is computed for each combination of zero-crossing lines expressing their deviation from the expressions given in eq. (3.28) and eq. (3.29). Subsequently, only the one combination with the lowest error, respectively the highest agreement is used for further processing.

Eq. (3.28) and eq. (3.29) depend on the model parameters μ, σ and τ. Hence, values for these parameters are required but due to the high variability of ECG morphology and intra-/inter-subject variability it is not possible to find generalized values. Instead an "extrapolation error" is proposed which does not require any predefined parameter values. They are obtained from the zero-crossing lines in the lower half of scales, are used for extrapolating line positions in higher scales which are then compared to the actual positions of lines. The error measure is defined by the residuals between the extrapolated and observed lines at higher scales.

The rationale of this approach is depicted in Fig. 3.22: A synthetic signal following the model function $G_{A,\sigma,\tau,\mu,B}(t)$ with additive pink noise (→ p. 94) is the input signal. As reference, the positions of zero-crossings $u0^1_{\{-1,0,+1\}}$ and $u0^2_{\{-2,-1,+1,+2\}}$ at scale 1 are indicated on top. The computation of the error measure is shown for a single combination of zero-crossing lines which are marked by bold circles at scale s. The lines $u0^1_{\{0,+1\}}$ and $u0^2_{\{-1,+1,+2\}}$ were chosen with $u0^2_{+2}$ being highly distorted by noise. For $u0^1_{-1}$, a wrong line was chosen which results from noise fluctuations and not from the model. It is measured how well the zero-crossing positions at s correspond to their positions at a higher scale $s+k$. To that extent, the zero-crossings at scale s are substituted into the equations for model parameters eq. (3.30), eq. (3.31), eq. (3.32), eq. (3.33), and the obtained parameters are then substituted into eq. (3.28) and eq. (3.29) with $s+k$. The extrapolated positions $(\hat{u0}^1(s+k), \hat{u0}^2(s+k))$ are then compared to the actually observed line positions at scale $s+k$ and their mismatch is stored.

This is repeated for multiple scales $s+1, s+2, \cdots$ and errors are accumulated in

$$E_n = \frac{1}{7(s_{\max}/2+1)} \sum_{s=s_{\max}/2+1}^{s_{\max}} E^{u0^1}(s) + E^{u0^2}(s) \quad \text{with} \tag{3.58}$$

$$E^{u0^1}(s) = \sum_{i=-1}^{+1} \left(\hat{u0}^1_i(s) - u0^1_i(s)\right)^2 \tag{3.59}$$

$$E^{u0^2}(s) = \sum_{j=-2}^{+2} \left(\hat{u0}^2_j(s) - u0^2_j(s)\right)^2 \tag{3.60}$$

with $i \in \mathbb{Z}$ and $j \in \mathbb{Z}_{\neq 0}$. This description assumes, that all seven lines of the model are available. Otherwise, indices i, j and the normalization factor are adjusted accordingly.

This error measure is computed for each line combinations, i.e. E_n is computed for $n \in [1, N]$. Only the one combination with the lowest error is passed to the next stage for parameter estimation.

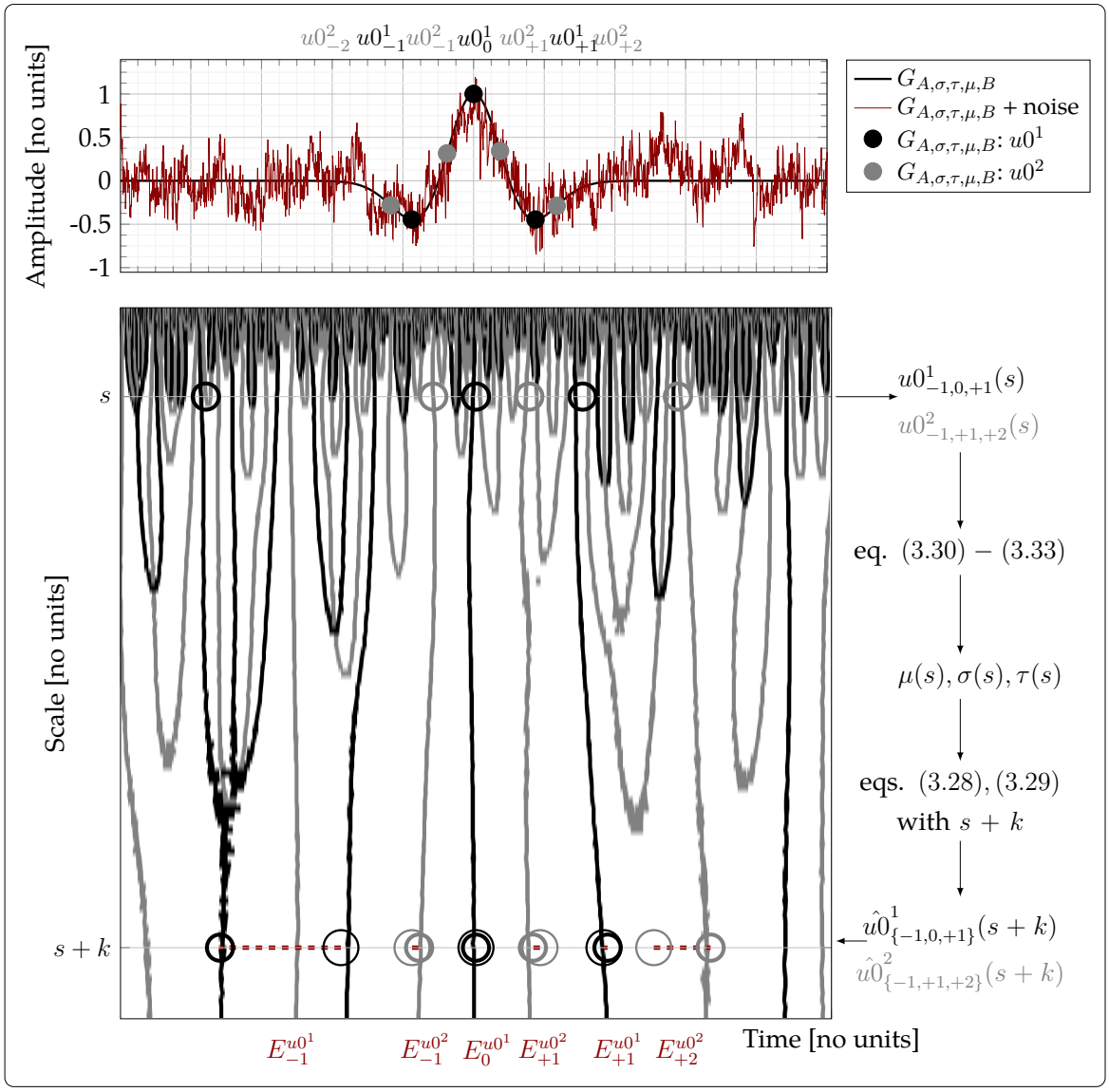

Figure 3.22: ④ Visualization of method for computing the error measure for a given noisy signal (red curve). Zero-crossings at scale 1 of the input signal without noise (black curve) are indicated by black and gray dots. For each possible combination of available zero-crossings lines, one E_n value can be computed which is demonstrated here for a single combination at a single scale (bold circles). They are substituted into equations for parameter estimation which are then used to predict the positions at $s + k$ (thin circles). The mismatch between predicted/extrapolated position and actual occurrence is then stored for each zero-crossing individually (red letters). In the shown case, the lines $u0^1_{-1}$ and $u0^2_{+2}$ show a high error. Therefore, it would be favorable to use the the remaining lines for parameter estimation only.

Algorithm 7: ④ Extrapolation error

Input: multiple combinations of $u0^1[s_j]$ and $u0^2[s_j]$ **Parameters:** none

For each line combination:

For each scale in the interval $s_{\text{current}} \in [s, s+k-1]$:

1) Substitute $u0^1$ and $u0^2$ into eqs. (3.30), (3.31), (3.32), (3.33) with s_{current}

2) Average obtained values for μ, σ, τ and substitute them into eqs. (3.28) and (3.29) with $(s_{\text{current}} + k)$, resulting in $\hat{u0^1}(s_{\text{current}} + k)$, $\hat{u0^2}(s_{\text{current}} + k)$

3) Compute $E^{u0^1}(s_{\text{current}})$ and $E^{u0^2}(s_{\text{current}})$ by computing residuals between $\hat{u0^1}$ and $u0^1$ as well as $\hat{u0^2}$ and $u0^2$

4) Compute E_n by accumulating E^{u0^1} and E^{u0^2} for all s_{current}

5) Pick line combination with minimum E_n value

Output: one combination of $u0^1[s_j]$ and $u0^2[s_j]$

⑤ Parameter estimation The one zero-crossing line combination with lower error is then processed by the msPE framework as described in the description of the implementation (→ p. 87). The piecewise model $G_{\text{pw}}(t)$ (→ p. 83) is applied by splitting the signal at the central WT^1 zero-crossing line associated with μ. If there is no WT^1 line on the left or right side, parameters are computed according to eq. (3.30), eq. (3.40), eq. (3.44), and eq. (3.42) for this side. If there is one WT^1 line on the left or right side, eq. (3.30), eq. (3.31), eq. (3.32), and eq. (3.33) are used. To increase robustness to noise, only the upper half of scales $s \in [s_{\text{max}}/2, s_{\text{max}}]$ is used for parameter estimation. In order to make full use of the interchangeability property, all possible combinations of available lines are substituted into the equations for parameter estimation. The resulting values for the range of scales are averaged into a single value using the $\text{median}(\cdot)$ operator.

⑥ Parameter fine-tuning using msPE$^{\text{fit}}_{\text{td}}$ Parameters are optimized using the approach based on fitting in time domain (→ p. 86) using eq. (3.47) and eq. (3.48). msPE$^{\text{fit}}_{\text{tsp}}$ cannot be applied as the range of scales covered is too small, leading to too few samples for accurate results. The Nelder-Mead method is applied and limits are defined according to the bounds of the time-scale plane funnel given in Table 3.2. For the QRS complex, the 8-parameter model as described in eq. (3.47) and eq. (3.48) is used but for P- and T-waves, $\tau_{\{\text{L, R}\}}$ are fixed to zero.

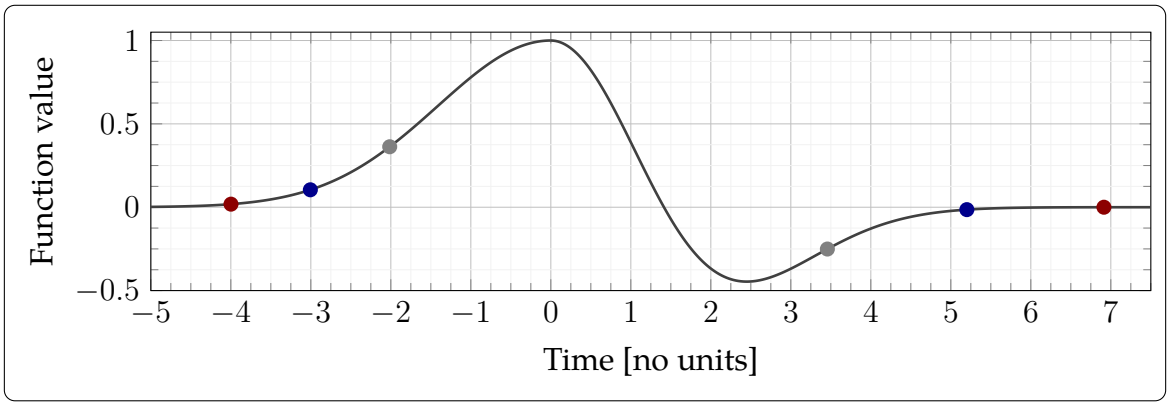

Figure 3.23: $G_{\text{pw}}(t)$ with $\sigma_{\text{L}} = \sigma_{\text{R}} = 1$ and $\tau = 0$ (left) and $\tau = 2$ (right). $c_{\text{on}} = c_{\text{off}} \in \{1, 1.5, 2\}$ with X_{on} and X_{off} indicated by gray (1), blue (1.5), and red (2) dots.

⑦ **Fiducial points computation** In the last stage, the optimized parameters are used for computations of $\{\text{P, QRS, T}\}_{\{\text{on, peak, off}\}}$. The peak centers $\{\text{P, QRS, T}\}_{\text{peak}}$ are defined by simply using the optimized μ value. Onset and offset fiducial points are computed using equation

$$\text{X}_{\text{on}} = \begin{cases} \mu - c_{\text{on}} \sqrt{2\sigma_{\text{L}}^2 \tau_{\text{L}}(\tau_{\text{L}} + 1)}/\tau_{\text{L}} & \text{for } \tau_{\text{L}} > 0 \\ \mu - c_{\text{on}}\, \sigma_{\text{L}} & \text{for } \tau_{\text{L}} = 0 \end{cases} \tag{3.61}$$

and

$$\text{X}_{\text{off}} = \begin{cases} \mu + c_{\text{on}} \sqrt{2\sigma_{\text{R}}^2 \tau_{\text{R}}(\tau_{\text{R}} + 1)}/\tau_{\text{R}} & \text{for } \tau_{\text{R}} > 0 \\ \mu + c_{\text{on}}\, \sigma_{\text{R}} & \text{for } \tau_{\text{R}} = 0 \end{cases}, \tag{3.62}$$

respectively. Values of variables $\mu_{\{\text{L, R}\}}, \sigma_{\{\text{L, R}\}}, \tau_{\{\text{L, R}\}}$ are assigned depending on the analyzed ECG wave $\text{X} \in \{\text{P, QRS, T}\}$.

Fig. 3.23 displays example X_{on} and X_{off} fiducial points for $1, 1.5, 2$ as c_{on} and c_{off} values. As can be seen, both parameters allow scaling the position of a fiducial point in relation to the shape of the underlying signal with lower values resulting in earlier and higher values resulting in later appearing fiducial points. This emulates the process a human cardiologist performs during annotation of ECG fiducial points: The ECG curve is traced until its baseline deflects from or returns to the baseline.

Due to the difference in the morphologies of P-/T-waves and the QRS complex (→ Chapter 2.3.2) different values for $c_{\{\text{on, off}\}}$ have to be defined. These were obtained by visually analyzing the fiducial points defined by the human annotators in the QT database and estimating corresponding values which are given in Table 3.3.

Table 3.3: Parameterization of eqs. (3.61) and (3.62)

▼ **ECG wave**	Parameter c_{on}	Parameter c_{off}
P-wave	2.9	1.8
QRS complex ($\tau = 0$)	3.5	3.5
QRS complex ($\tau > 0$)	1.8	1.8
T-wave	2.1	2.7

Evaluation The standard evaluation methodology proposed in (Martinez et al. 2004) is used. Time differences between the ground truth fiducial points, which were annotated by the human experts, are compared to the points computed by the algorithm. As both leads were provided to the human annotators and the proposed method processes single leads only, both leads are processed independently. Subsequently, for each fiducial point the errors of both leads are compared and the lower one is chosen for further processing.

Subsequently, for each of the 105 ECG records, the mean and standard deviation ($\mathrm{m} \pm \mathrm{sd}$) error is computed for each fiducial point $\{\text{P, QRS, T}\}_{\{\text{on, peak, off}\}}$. These values are averaged, resulting in an $\mathrm{m} \pm \mathrm{sd}$ value for each fiducial point. This allows to compare the proposed method with other delineation methods and with the guidelines provided by the Common Standards in Quantitative Electrocardiography committee, expressing *"what can be expected from an expert cardiologist"* (The CSE Working Party 1985). Moreover, the algorithm run times are stored for analyzing durations for delineating a single ECG wave.

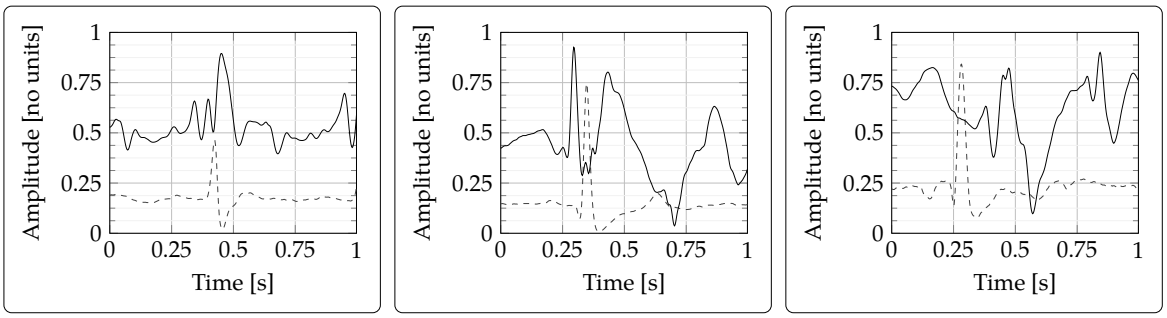

Figure 3.24: Three example segments $\tilde{x}[t_i]$ of ECG signals acquired within a 7 T UHF MRI bore (black curve) and with the patient table in home position (0.3 T, dashed).

3.3.4 msPE of QRS complexes acquired within UHF MRI[15]

In this study, the msPE framework is applied to ECG signals acquired within the stage ① and stage ② of the study introduced in Chapter 3.1.1. This allows to compare the performance of the msPE framework in processing ECG signals in the presence and absence of UHF MRI noise.

Compared to the method introduced in the previous chapter (→ Fig. 3.19) including many sub-algorithms, the proposed method aims at short run time and, as the maximum of the R-wave is commonly used for trigger activation, only at detecting the QRS complex. If one is detected, the trigger device proposed in Chapter 3.2.2 could be used for sending a trigger immediately to the MR scanner for trigger activation. However, this study is performed retrospectively and without actual MR imaging.

Data and notation ECG data from three randomly chosen subjects from the ECG dataset (→ Chapter 3.1.1) is used. For both stages and each subject, 100 segments that contain a QRS complex were manually extracted with each having a duration of 400 ms, resulting in 600 segments in total. Hence each segment will be assumed as

$$\tilde{x}[t_i] = x[t_i] + \eta[t_i] \tag{3.63}$$

with unknown $x[t_i]$ and $\eta[t_i]$. One $\tilde{x}[t_i]$ from each subject acquired within UHF MRI is shown in Fig. 3.24. The point in time when the R-wave reaches its maximum was manually detected and stored as ground truth.

[15]This work has been published in Spicher, N., Kukuk, M., Maderwald, S., Ladd, M. E. (2019): Multiscale parameter estimation (msPE) of QRS complexes distorted by magnetohydrodynamic effects at 7 Tesla. Current Directions in Biomedical Engineering, 5(1), 365–368.

Algorithm 8: QRS detector

Input: ECG segment $\tilde{x}[t_i]$ **Parameters:** $s_{\text{min}} = 11$, $s_{\text{max}} = 20$, $w = 30$

1-4) Identical to Alg. 3

5) Substitution of zero-crossings of $u0_0^1[s_j]$ and $u0_{-1}^2[s_j]$ into eq. (3.40), eq. (3.42), and eq. (3.44) for obtaining values of σ_{L}, A, B_{L}.

6) Substitution of zero-crossings of $u0_0^1[s_j]$ and $u0_{+1}^2[s_j]$ into eq. (3.40), eq. (3.42), and eq. (3.44) for obtaining values of σ_{R}, $\bar{A}$, B_{R}.

6) Application of $\text{median}(\cdot)$ to all parameters, resulting in scalar values for each parameter that are substituted into $\vec{P}_{\text{left}}$ and $\vec{P}_{\text{right}}$.

Output: $\vec{P}_{\text{left}}$, $\vec{P}_{\text{right}}$

Method The developed QRS detector is shown in Alg. 8. The proposed method is similar to Alg. 3 but the piecewise model $G_{\text{pw}}(t)$ is used. As can be seen in Fig. 3.24, the QRS complexes do not have an undershoot (left, center) or a significantly increased amplitude of the undershoot (right). Therefore, the piecewise model function $G_{\text{pw}}(t)$ is applied but restricted to the Gaussian function ($\tau_L = \tau_R = 0$).

As can be seen, the given implementation returns the complete parameter vectors $\vec{P}_{\text{left}}$ and $\vec{P}_{\text{right}}$. For the pure task of QRS detection it would be sufficient to return parameter μ but to allow a qualitative analysis of all estimated parameters by visual analysis, all parameters are stored.

Evaluation Regarding evaluation of the algorithm's performance, three measures are computed. For each run of the algorithm, the processing time was stored which will be analyzed. Moreover, the accuracy in detecting the QRS complex accurately is evaluated by detecting the difference between the manually annotated ground truth (R-wave maximum) and the computed position μ. If the deviation is larger than ± 50 ms, the QRS complex is considered missed by the detector. This information will be used for the sensitivity measures, which provides the percentage of segments in which the algorithm was able to detect a QRS complex successfully.

4 Results

This chapter contains the results acquired using the methods proposed in Chapter 3: Results obtained by applying the proposed algorithms for cardiac monitoring and triggering using optical cardiac signals (PPGi) in the context of UHF MRI are given in Chapter 4.1. Subsequently, results with regard to processing electrical cardiac signals (ECG), which were measured inside and outside of an MRI environment, are given in Chapter 4.2.

4.1 PPGi-based methods

In Chapter 4.1.1 results of using PPGi for cardiac monitoring within UHF MRI are given and compared to the standard methods PPG and ECG. Chapter 4.1.2 contains a quantitative and a qualitative evaluation of applying PPGi as a novel method for cardiac triggering which includes MR images acquired during MRA.

Apart from the application within UHF MRI, characteristics of PPGi signals have been analyzed in several experiments which are presented in Chapter 4.1.3. This includes i) analysis of PPGi signal intensity as a function of wavelength using a hyperspectral camera with 16 camera channels, ii) analysis of the influence of green light illumination on PPGi signal SNR, and iii) an evaluation of the feasibility of measuring PPGi at the sole of the foot compared to the commonly used palm of the hand.

Table 4.1: RMSE in HR of 8 subjects during stage ① at 0.3 T. Ground Truth: ECG

▶ **Subject**	S1	S2	S3	S4	S5	S6	S7	S8
RMSE (MA_{ECG}, MA_{PPG})	0.6	0.3	3.3	4.3	4.4	3.0	1.9	0.3
RMSE (MA_{ECG}, MA_{PPGi})	6.1	4.9	3.3	1.3	5.8	5.0	1.0	1.2
ECG HR [cycles per minute]	52.5	52.0	66.4	58.7	53.6	50.4	57.0	60.2

Table 4.2: RMSE in HR of 8 subjects during stage ② at 7 T. Ground Truth: PPG

▶ **Subject**	S1	S2	S3	S4	S5	S6	S7	S8
RMSE (MA_{PPG}, MA_{ECG})	56.8	36.3	47.0	56.0	13.2	58.7	60.0	65.4
RMSE (MA_{PPG}, MA_{PPGi})	8.9	12.3	6.0	4.4	9.0	3.4	2.3	1.8
PPG HR [cycles per minute]	49.7	52.0	65.5	57.1	49.7	51.5	56.0	59.5

4.1.1 Cardiac monitoring during UHF MRI

The algorithm for cardiac monitoring (→ Alg. 1) was applied to the data acquired within stages ① and ② of the first data acquisition study (→ Chapter 3.1.1). This two-stage evaluation was performed to evaluate the influence of different illumination conditions on PPGi SNR and, consequently, accuracy of computed HR. As the illumination is identical in stages ② and ③ the latter was not considered.

RMSE results for all eight subjects (S1 - S8) during both stages of the study are summarized in Table 4.1 and Table 4.2, respectively. In the first stage, the patient table was in home position (0.3 T) where ECG signals are not influenced severely by MHD noise and therefore, ECG is assumed as the ground truth. In the second stage (7 T), the ECG signals were severely distorted and therefore PPG is assumed as the ground truth. Hence, RMSE values were computed between the ground truth modality and the two other signals to assess the accuracy of PPGi compared to existing modalities.

In stage ① the moving average signals of ECG and PPG are very similar with an average RMSE of 2.26. The error between ECG and PPGi is higher with an average of 3.58. In stage ② the ECG signals are flawed by MHD interferences, resulting in completely false HR values due to many false triggers. Hence, the resulting error is significantly larger than the errors observed in the first stage with an average RMSE of 49.18. The error of PPGi is increased as well with a mean RMSE of 6.01.

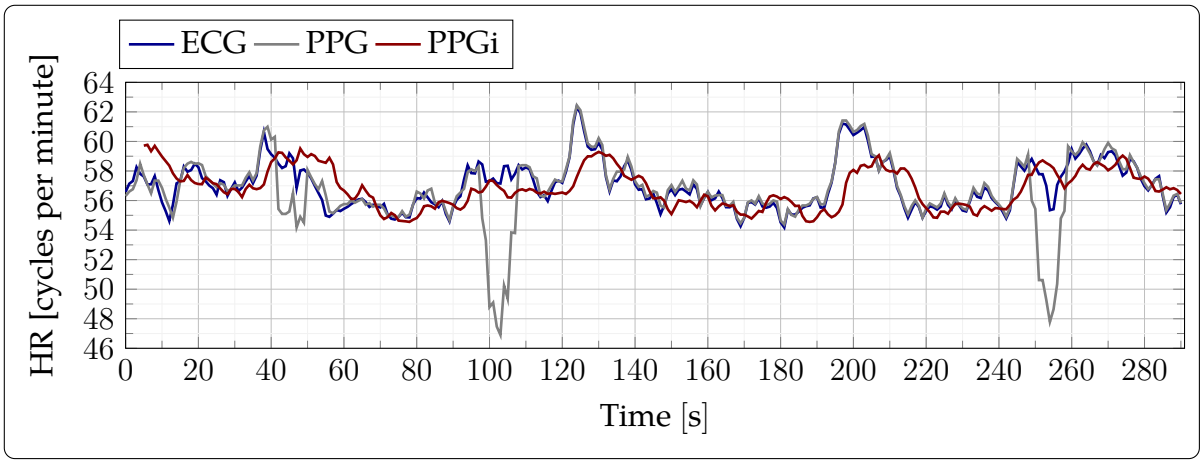

Figure 4.1: HR estimates obtained from ECG, PPG, and PPGi signals of subject seven during stage ① (→ Table 4.1: S7).

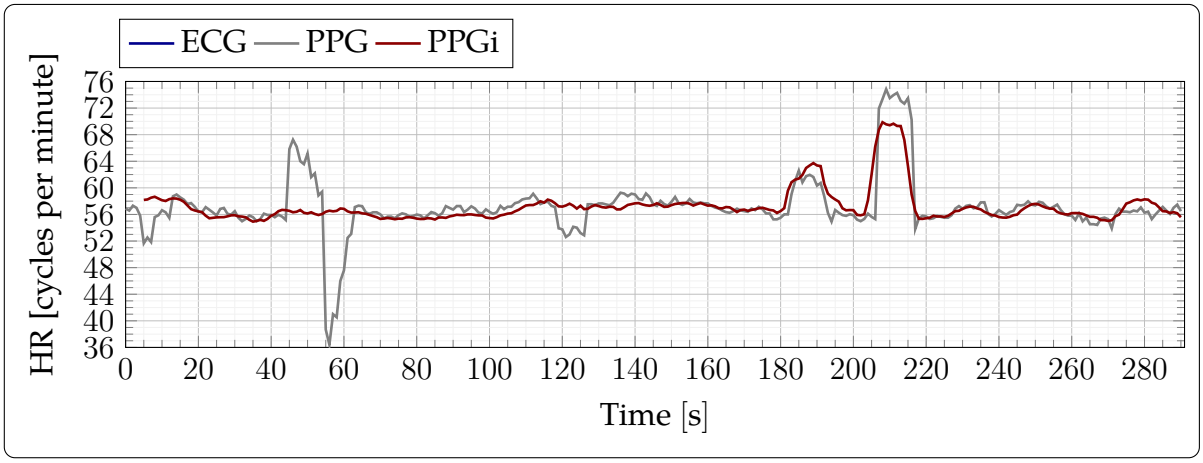

Figure 4.2: HR results for subject four during stage ② (→ Table 4.2: S4). As the ECG signal is biased severely due to MHD artifacts, resulting in HR values larger than 100 cycles per minute, they can not be seen.

One example for each stage is shown in Fig. 4.1 and Fig. 4.2. In the first, the ECG and PPG signals are very similar and nearly identical in some periods, underlining that both are free of artifacts. However, there are two periods ($[97, 108]$ s, $[248, 259]$ s) in which the PPG signal results in a HR decrease that is not visible in the ECG signal. Analysis of raw data showed that this results from missed triggers by the PPG probe and is not physiologically correct. The PPGi signal is similar to ECG and PPG but does not capture fine details, i.e. short-time variations such as the peaks in HR at

approximately $120\,\mathrm{s}$ and $200\,\mathrm{s}$. Additionally, a slight time delay can be observed. Analyzing the raw data showed that this is not due to algorithm run time but due averaging by parameter N. In Fig. 4.2 signals were acquired within the UHF MRI bore at $7\,\mathrm{T}$. The y-axis is limited to ensure the visibility of fine details. Again, there are incorrectly detected HR values by PPG in the period $[40-60]\,\mathrm{s}$ which were manually confirmed in the raw data. HR values of PPGi are similar to PPG over the whole period, including the peaks at $190\,\mathrm{s}$ and $210\,\mathrm{s}$.

4.1.2 Cardiac triggering during UHF MRI

The proposed algorithm for MRI cardiac triggering based on the phase of the PPGi signal (→ Alg. 2) requires three open input parameters. Hence, at first results of a parameter optimization (→ p. 67) using synthetic and real PPGi signals are given. This results in a single set of best-performing parameter which are used in a two-fold evaluation of the algorithm's feasibility: i) A quantitative evaluation was performed based on a comparison of PPGi triggers to PPG and ECG triggers (→ p. 66), and ii) a qualitative evaluation based on MR image quality obtained using PPGi and PPG as trigger modalities (→ p. 68) was performed.

Optimization of algorithm parameters

Before application of the algorithm for PPGi triggering given in Alg. 2 to PPGi data, adequate algorithm parameters were searched by means of a three-step procedure:

Step 1: Synthetic PPGi signals → Restriction of search area of M and N
Step 2: Real PPGi signals → Refinement of parameters M and N
Step 3: Real PPGi signals → Detection of parameter T

The signals being used are given on the left side of the arrow and the aim of the corresponding step is given on the right. Synthetic PPGi signals were generated according to the description given before (→ p. 67) and real PPGi signals were used from the UHF MRI dataset (→ p. 53). Fig. 4.3 shows examples for real PPGi synthetic PPGi signals. As can be seen, both signals have a high qualitative agreement and all synthetic signals were visually inspected and were assessed as a sufficient approximation of the real PPGi signals.

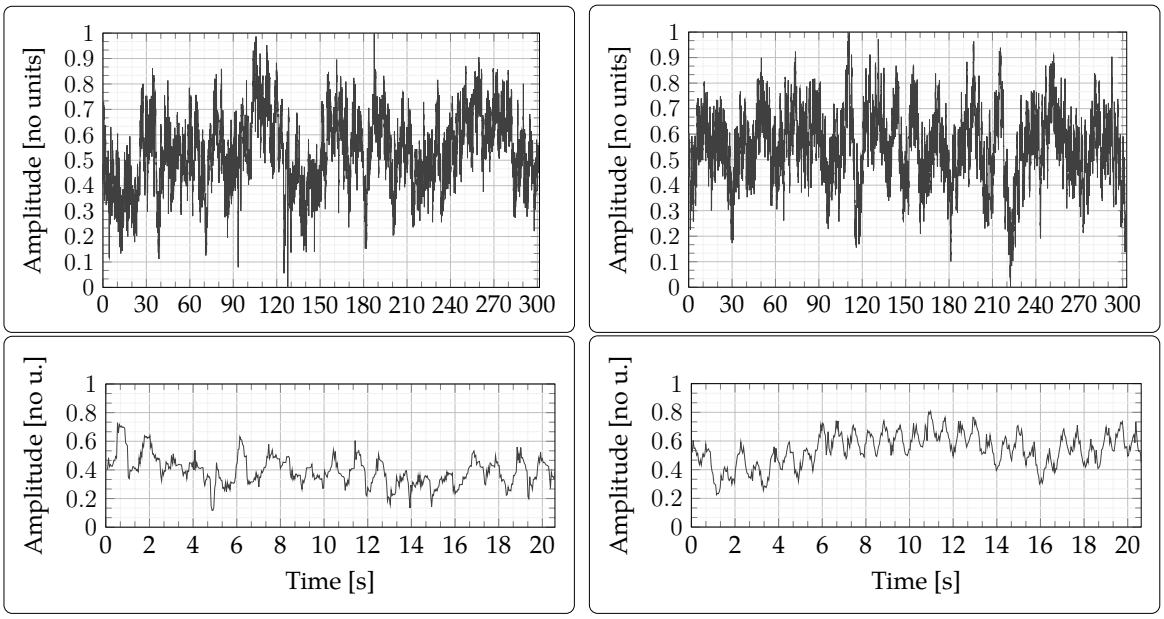

Figure 4.3: *Left*: Real PPGi signals acquired during UHF MRI study. *Right*: Synthetic PPGi signal computed using concatenated cosine waves with cardiac cycle lengths acquired from the Normal Sinus Rhythm RR Interval Database and noise estimated from real PPGi signals. The bottom plots depict the first 20 seconds of both signals.

Step 1: Parameters M and N were optimized in a coarse-to-fine approach. The first optimization step was performed to find a reasonable interval for parameters M and N. Therefore, parameter values were defined in wide intervals ($M \in [1, 150]$, $N \in [50, 600]$) to gain initial information on the relationship between parameters and trigger accuracy. Parameter T was set to zero as the PTT could not be considered in synthetic signal generation. The algorithm proposed in Alg. 2 was applied to the synthetic signals using each combination of M and N. Fig. 4.4 depicts $\mathrm{m} \pm \mathrm{sd}$ error values with the grid of mean errors showing a minimum error valley (red ellipse) reaching two minima at ($N = 50$, $M = 10$) and ($N = 300$, $M = 150$). The sd errors show that the first parameter combination results in a higher error than the second. This confirms the expected influence of HRV on the algorithm performance: A low N value results in a small window function (→ p. 24) covering only a short portion of cardiac activity, which should lead to accurate results of the instantaneous cardiac activity. However, due to the low number of samples this approach is also prone to noise. Vice versa, increasing N is more robust to noise, but also averages the cardiac information over a longer period, which decreases accuracy as well.

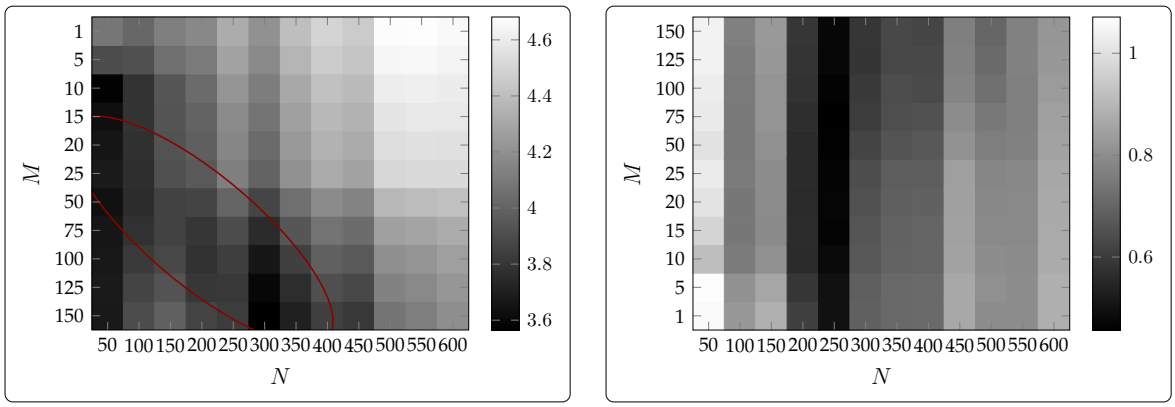

Figure 4.4: Results of application of Alg. 2 to synthetic PPGi signals w.r.t. different combinations of M and N. Absolute differences between estimated and ground truth trigger points in time were computed for each cardiac cycle within a signal and averaged over the whole signal. Subsequently, $\mathrm{m}(\cdot)$ (left) and $\mathrm{sd}(\cdot)$ (right) of all errors were computed and stored in the corresponding coordinate with values being displayed in unit samples. A minimum error valley is highlighted in red color.

Step 2: In the second step, the guideline obtained using synthetic data (minimum error valley) was used to refine M and N in order to find the best combination using real PPGi data. As the results of the first optimization step show that the N value has a higher influence on accuracy, N values were refined to smaller intervals $N \in \{\, 25, 50, \cdots, 400 \,\}$ and applied to the real PPGi data with M values being read from the corresponding value in the minimum error valley.

A heartbeat-wise comparison of the PPGi triggers to the PPG triggers was not possible as the PTT is unknown and a reasonable value for T was not known, therefore a direct mapping from a heartbeat in the PPGi signal to the PPG signal was not possible. Instead, histograms of trigger-to-trigger periods were computed for each PPGi signal and parameter combination and compared visually to the trigger-to-trigger periods of the PPG signal. Three examples are shown in Fig. 4.5 which stem from the same experiment, i.e. the PPG data is identical in all examples but trigger-to-trigger durations computed from the PPGi signal change due to different values for M and N. Results of all experiments showed that neither configuration with minimum mean error in Fig. 4.4 ($N = 50$, $M = 10$) or ($N = 300$, $M = 150$) is optimal for the real PPGi signals as they result in a too broad ($\rightarrow$ Fig. 4.5, left) or to narrow (right) histogram compared to PPG trigger-to-trigger times. In most cases, the configuration ($N = 125$, $M = 50$) resulted in histograms similar to the PPG data.

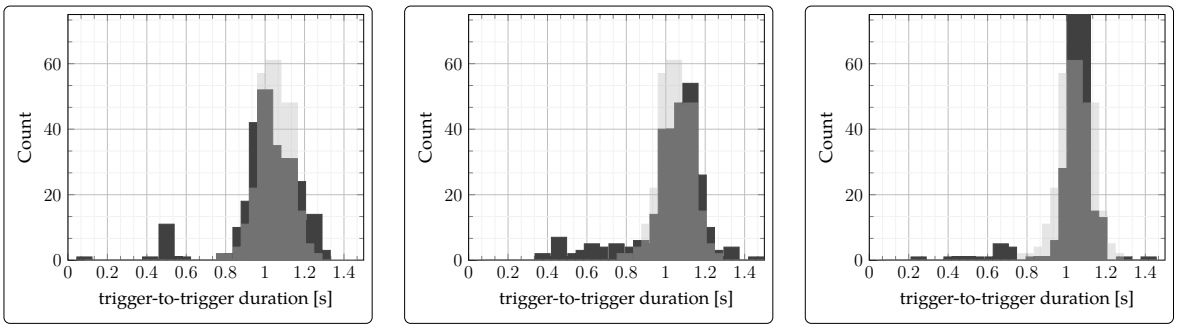

Figure 4.5: Histograms of trigger-to-trigger durations of PPG (gray) and PPGi (black) signals. Data is from the same experiment, therefore the PPG histograms are identical. PPGi triggers were obtained with N set to 50 (left), 125 (center), and 300 (right).

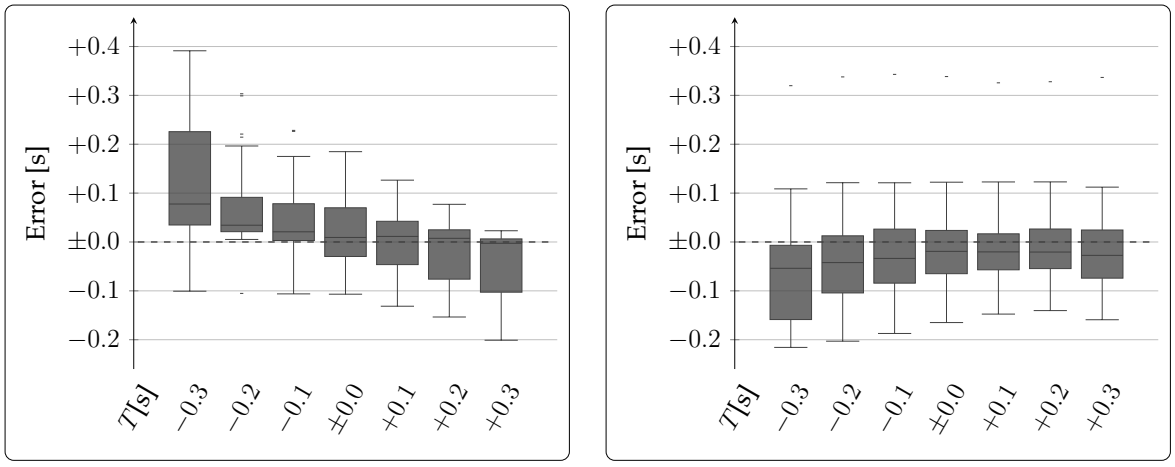

Figure 4.6: Error of Alg. 2 w.r.t. parameter T ($M = 50$ and $N = 125$). For each experiment, the $\mathrm{m}(\cdot)$ and $\mathrm{sd}(\cdot)$ of PPGi trigger-to-trigger durations were computed. The boxplots show the differences between these values and $\mathrm{m}(\cdot)$ (left) and $\mathrm{sd}(\cdot)$ (right) of trigger-to-trigger durations computed from the ground truth PPG signals.

Step 3: After selecting the best performing N and M parameters, a search for parameter T was conducted by applying the algorithm to the real PPGi data with $N = 125$, $M = 50$, and $T \in \{-300, 200, \ \ldots \ 300\}$ ms. For each signal, trigger-to-trigger durations from the PPGi signal were stored and compared to trigger-to-trigger durations from the corresponding PPG signal by means of boxplots. Fig. 4.6 shows boxplots of $\mathrm{m} \pm \mathrm{sd}$ errors and it can be observed that the best configuration is achieved using $T = 0.2$ s. $T = 0.3$ s has a median value closer to zero but is skewed towards negative values. Hence, the optimal parameter configuration was defined as being $M = 50$, $N = 125$, $T = 0.2$ s and was used during the following steps.

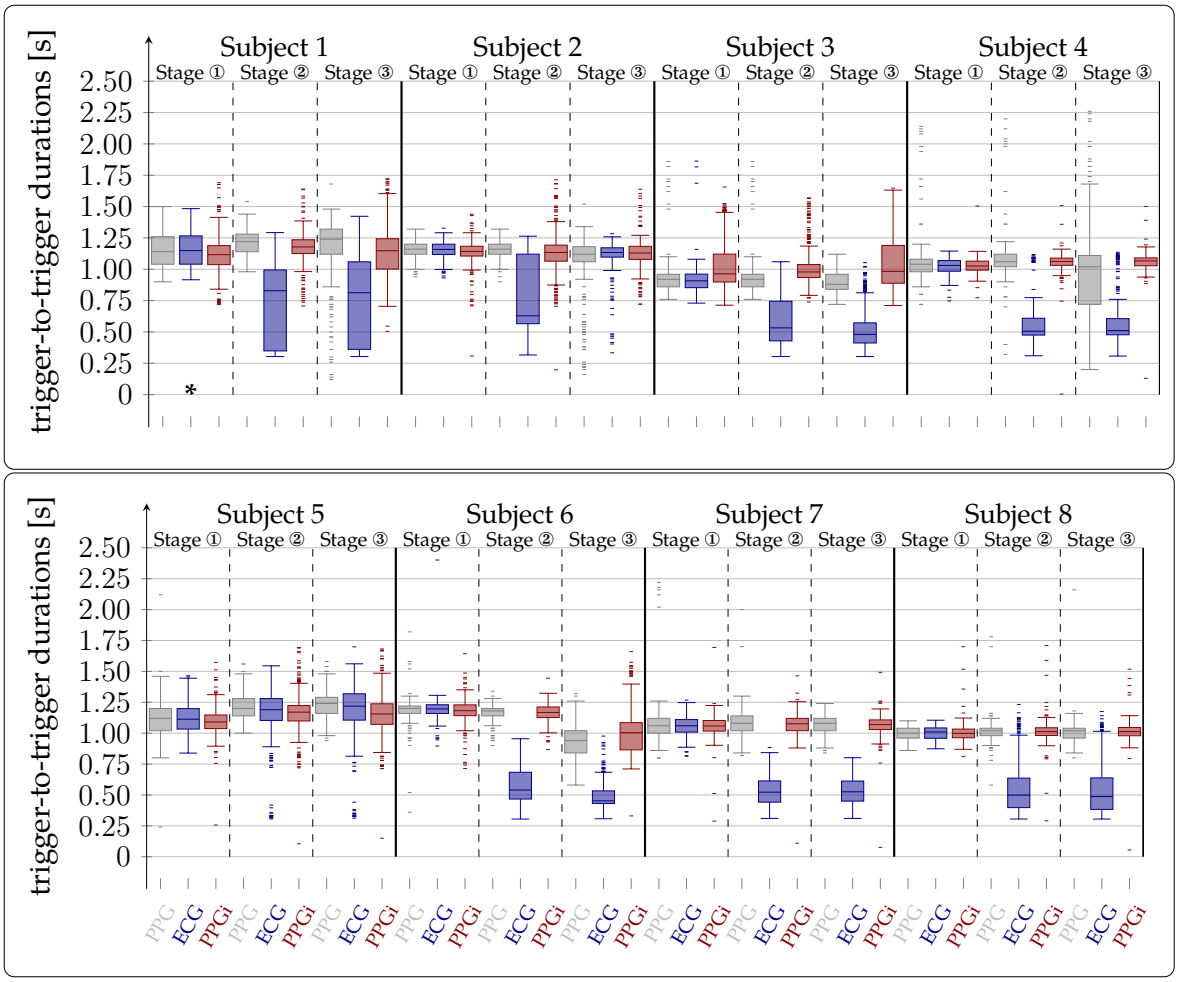

Figure 4.7: Comparison of trigger-to-trigger durations in PPG, ECG and PPGi signals with the latter being obtained by using Alg. 2 with optimized parameters ($M = 50$, $N = 125$, $T = 0.2\,\mathrm{s}$). Stage ① was conducted at $0.3\,\mathrm{T}$ and stages ② ③ at $7\,\mathrm{T}$. During stage ③ MR imaging was performed. The raw data of the experiment marked with an asterisk (first subject, first stage) is shown in Fig. 4.8.

Quantitative evaluation

In the quantitative evaluation, the algorithm proposed in Alg. 2 was applied with optimized parameters ($M = 50$, $N = 125$, $T = 0.2\,\mathrm{s}$) to the PPGi videos acquired in the UHF MRI dataset (→ Chapter 3.1.1) and computed triggers were compared to PPG and ECG triggers computed by the MR vendor-provided hardware. Fig. 4.7 depicts boxplots of the trigger-to-trigger durations for each volunteer, each stage, and each triggering modality.

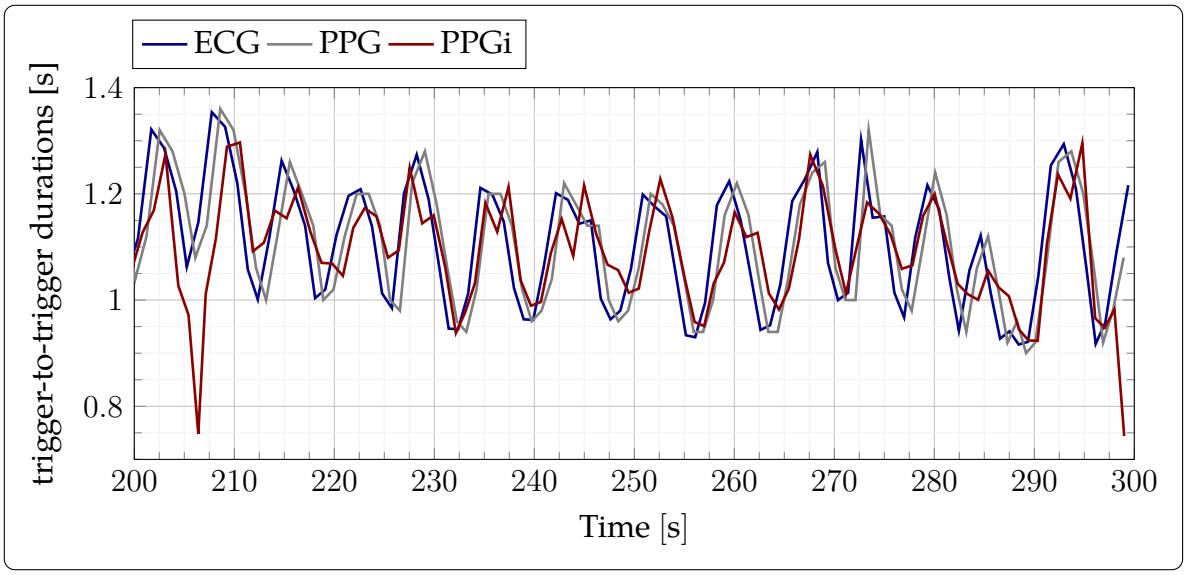

Figure 4.8: ECG, PPG, and PPGi trigger-to-trigger durations.

As the study population consisted of healthy volunteers only, they should show a healthy sinus rhythm with similar cardiac cycle lengths over time without abnormally shortened or prolonged heart cycles or extrasystoles. Therefore, vertical narrow boxplots can be used as an indicator of accuracy of trigger algorithms as too soon or too late detected triggers increase the vertical spread of the boxplots.

Results show a high agreement between PPG and ECG during the stage ① while PPGi has in most cases a similar median but more outliers. During stages ② and ③, which were performed within the UHF MRI bore, the accuracy of ECG was critically reduced in all subjects except the fifth. The PPG signal was more robust but distorted during stage ③ in subjects 4 and 6, most presumably due to MRI gradient activity, resulting in vibrations affecting the pulse oximeter probe. Regarding PPGi, the differences between stages were not as severe compared to ECG and PPG; however, the number of outliers in the stages ② and ③ is increased, presumably due to the reduced brightness. Analyzing the raw data showed that it negatively effects SNR of the PPGi signals.

Fig. 4.8 shows 100 s of the first stage of the first subject which is a representative example of accurate PPGi triggering, demonstrating the accuracy of the method under adequate circumstances. Except for two outliers (205 s, 300 s), all triggers were sent in time intervals similar to the contact-based methods.

Qualitative evaluation

The foregoing quantitative evaluation was based on PPGi data measured from the forehead without dedicated illumination. It revealed that the proposed method is able to compute triggers similar to ECG and PPG under good conditions (→ Fig. 4.8) but the method also fails at times (→ Fig. 4.7) due to low SNR. Hence, in the qualitative evaluation, the advanced setup (→ Chapter 3.1.3) making use of PPGi measurement from the sole of the foot, dedicated illumination, and contact pressure to the skin, was used. The algorithm with the same optimized parameters as in the previous section was applied and PPGi signals were used for triggering of MRA image acquisition in a healthy volunteer.

Fig. 4.9 shows the MIP image acquired using vendor-provided PPG (left) and the proposed PPGi-based method (right) for cardiac triggering. Both images were obtained by blending three images from different table positions with blended regions being indicated (gray area). Both show a uniform and intense delineation of the arteries as well as similar contrast. The thigh and kneecap are very homogeneous within the PPGi-triggered image while there are short vessel declines in the PPG-triggered image. In the PPGi-triggered image there is a small vessel which is less visible compared to the PPG-triggered image (A). Additionally, there are artifacts in both images that are not related to triggering (B).

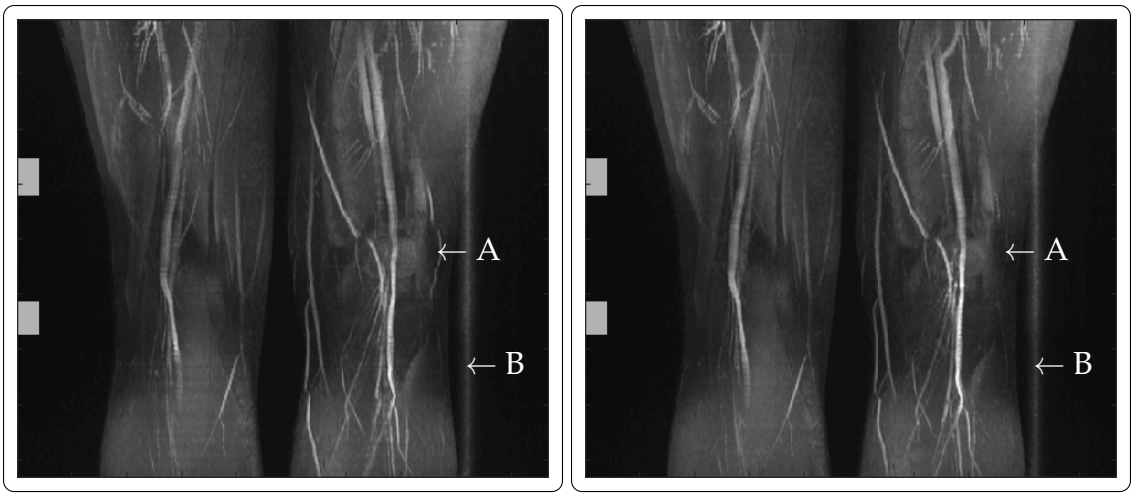

Figure 4.9: MIP images obtained using PPG (left) and PPGi triggering (right). A) shows a vessel only visible in the PPG-gated MIP image and B) a vertical radio-frequency artifact visible in both images. Gray areas shows regions that were blended.

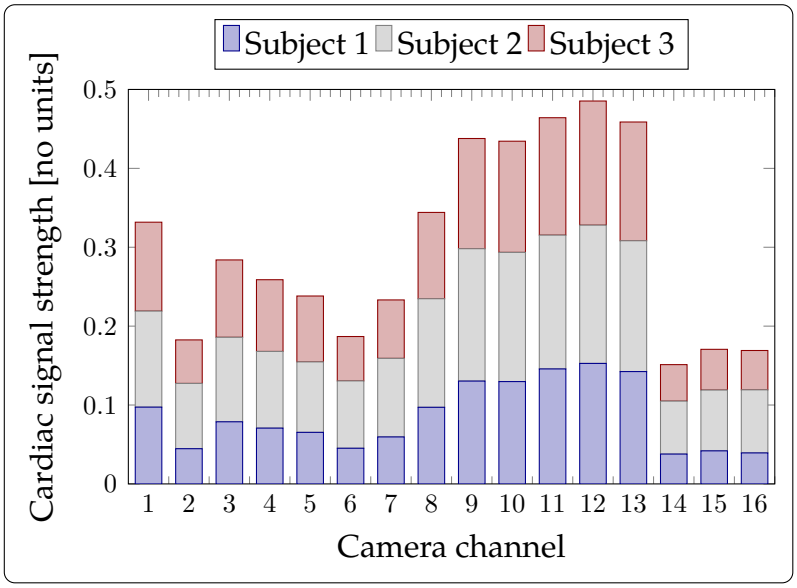

Chan.	Wavelength [nm]
1	470
2	478
3	480
4	490
5	502
6	517
7	523
8	539
9	551
10	552
11	565
12	580
13	590
14	600
15	610
16	620

Figure 4.10: *Left:* Chart of cardiac signal strength w.r.t. camera channel. *Right:* Peak wavelengths of the camera channels obtained from the camera's datasheet.

4.1.3 Investigation on PPGi signal characteristics

In the following chapter results of three studies are given which were performed to gain insight into the characteristics of PPGi signals. This information was used for devising the advanced setup for PPGi acquisition in UHF MRI (→ Chapter 3.1.3).

PPGi signal strength as a function of wavelength

Using a hyperspectral camera, the foreheads of three healthy volunteers were recorded in a non-MR environment. Fig. 4.10 (left) depicts the cardiac signal strength for each of the 16 camera channels which was obtained by computing the Fourier Transform magnitude of the PPGi signal and computing the ratio between magnitudes within the HR interval ($[0.8, 1.2]$ Hz $\leftrightarrow$ $[48, 82]$ cycles per minute) to all other.

As can be seen, the values of all three subjects follow a similar distribution with a maximum signal strength within the interval of camera channels $9 - 13$ and a sudden drop-off starting at camera channel 14. Fig. 4.10 (right) shows the peak wavelengths of the camera channels with the channels $9 - 13$ corresponding to the interval $[551, 590]$ nm. This is in line with results from literature and refines them, for example McDuff et al. 2014 report the cyan-green-orange color channels (approximately $[450, 600]$ nm) as being optimal (McDuff et al. 2014).

Influence of illumination on PPGi signal

The forehead of a single healthy volunteer in a UHF MRI environment was analyzed by means of pseudo-colored magnitude and phase maps computed from the PPGi signal which are depicted in Fig. 4.11 on the left and right, respectively. The whole forehead of the subject was acquired by the camera. The frames were cropped manually at the first appearance of hair of the head (top) and at the first appearance of hair of the eyebrows (bottom). For each of the three stages ① - ③ (no illumination, $90\,\mathrm{mA}$ dedicated LED illumination, $180\,\mathrm{mA}$ dedicated LED illumination) maps were generated.

Visually analyzing the spatial distribution of the magnitude maps (left column) reveals that increasing the intensity of illumination increases the magnitude at frequencies associated with the HR (”signal”) to magnitudes at all other frequencies (”noise”), i.e. the SNR of the PPGi signal increases. This can be observed within each individual map as the intensity increases quasi-linearly from the top ($y = 300$) to the bottom of the maps ($y = 0$) as light intensity was higher on the bottom due to the curvature of the forehead.

The same effect can be observed when analyzing the overall intensity within the maps from the first to the last stage. Fig. 4.12 depicts PPGi signals during the first (blue), second (gray), and third (red) stage. The shown signals were obtained by averaging all pixels within each frame over a duration of $10\,\mathrm{s}$. As reference, the corresponding PPG signals obtained via MR vendor-provided finger pulse oximetry is shown. A positive relationship between illumination and the cardiac component of the PPGi signals, showing fluctuations similar to the PPG signal, can be observed.

The magnitude maps do not show large and continuous areas on the skin with a high SNR but rather scattered regions with interchanging regions of higher and lower values. The region in the bottom right (gray circle) has a high SNR compared to the remaining area with and without illumination which might result from well-suited local skin properties.

Analyzing the phase maps (right column) shows a similar fragmented spatial distribution. In the first stage without illumination, the local differences on the forehead are highest, covering values from the lower to the upper limit of the colormap. By increasing illumination this effect is reduced. In order to get a more intuitive visualization of the differences in phase, in the bottom phase map a region is magnified. Two pixels are highlighted and their values over time are plotted in Fig. 4.13.

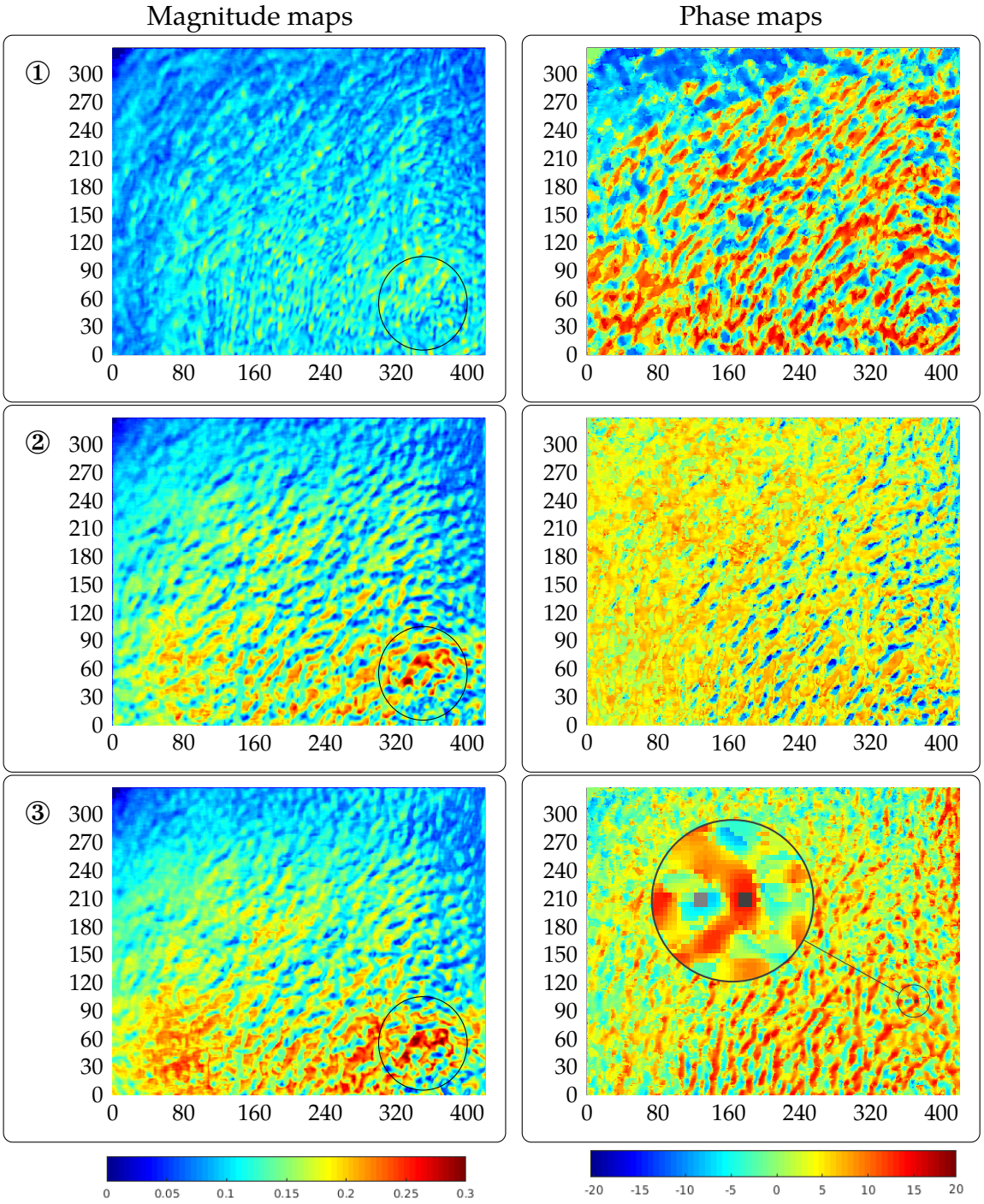

Figure 4.11: *Left:* Magnitude maps *Right:* Phase maps. Both were computed for all three stages ① - ③ and color values were normalized with regard to the min/max values within a type of map. In the magnitude maps, a "hot spot" of SNR can be observed in all three stages and is marked by a circle. In the phase map of stage ③, two regions are indicated that are used in Fig. 4.13 and magnified here.

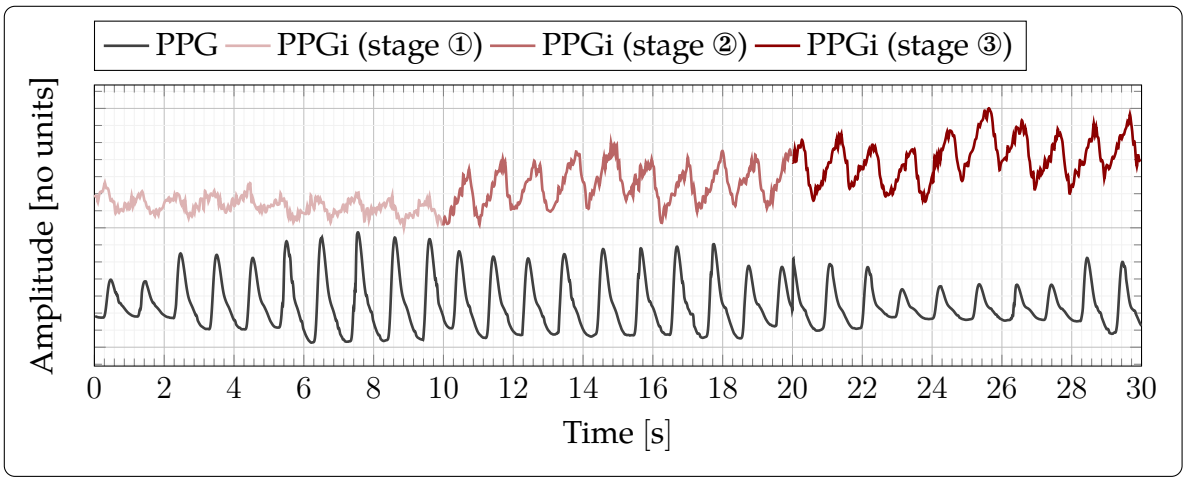

Figure 4.12: Averaged values of all pixels of the raw PPGi data of the three stages and as ground truth the PPG signal is given.

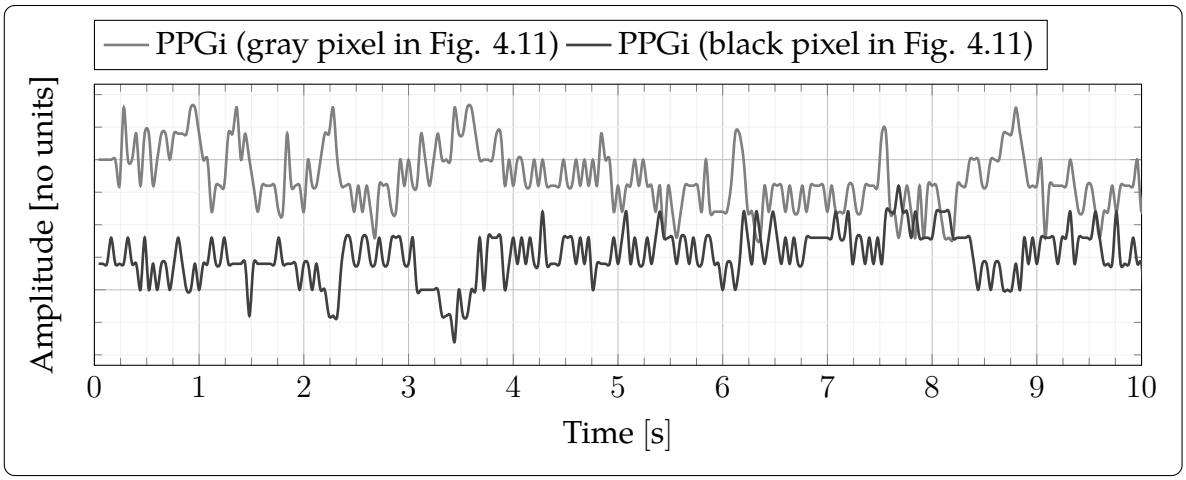

Figure 4.13: Same visualization of PPGi data as shown in Fig. 4.12, but using only the two pixels indicated in the phase map of stage ③ shown in Fig. 4.11.

In difference to Fig. 4.12, the course of two individual pixels are visualized. Both signals show a clearly inverted behaviour: At the point in time where one signal has a local maximum, the other has a minimum. Assuming the cardiac component of the PPGi signal as a pseudo-periodic function similar to a trigonometric function one could describe this behaviour as both signals exhibiting a $180°$ phase shift (→ p. 20). Apparently, one of both waveforms has a higher rate of occurrence such that both waveforms do not cancel each other out completely when averaged as in Fig. 4.12.

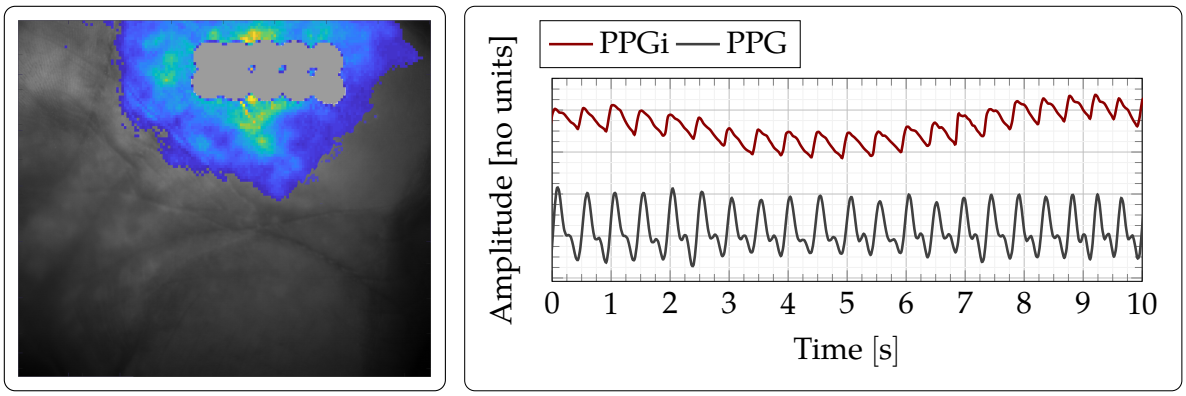

Figure 4.14: *Left:* Example magnitude map of a palm of the hand with pixels showing the highest portion of cardiac signal being pseudo-colored from low (blue) to high (yellow). *Right:* PPGi signal obtained from all pixel within the video and PPG signal.

Feasibility of PPGi of the sole of the foot

Data from the non-MR dataset (→ Chapter 3.1.2) was analyzed to evaluate the feasibility of using green light illumination and contact pressure applied to the sole of the foot for increasing SNR. Regarding the qualitative evaluation, Fig. 4.14 (left) depicts an example of the magnitude maps as an overlay on the first frame of the corresponding raw PPGi video. Due to space limitations, not more examples are shown here but results were consistent for most subjects: Regarding the aspect of illumination, it can be seen that areas of high illumination show a higher SNR compared to others which verifies the results shown in Fig. 4.12. Additionally, in regions in the vicinity of high contact pressure applied to the skin (e.g. ball of the thumb), the SNR is increased as well. Fig. 4.14 (right) shows the corresponding PPGi signal w.r.t. time which shows a high SNR, i.e. a clearly visible cardiac component similar to PPG.

Result of the quantitative evaluation are summarized in Table 4.3 which shows results of computing five SNR metrics. Each row shows the data of a single subject with the columns $1-6$ showing data for PPGi signals being acquired from the palm of the hand and columns $7-12$ showing data for PPGi signals being acquired from the ball of the foot. The left (right) side shows results for using the palm of the hand (sole of the foot) for PPGi measurement. Within the bottom row, scores are summarized using the mean of absolute values operator $\mathrm{ma}(\cdot)$ allowing to compare both points of measurement quantitatively. Four PPGi measurements were excluded (bright background) from averaging because trigger matching to PPG was ambiguous.

Table 4.3: Results of comparing PPGi measurements from the hand to the foot. Each row represents a subject and columns $1-5$ and $7-11$ display SNR values using different metrics for the hand and foot, respectively. The last row shows $\mathrm{ma}(\cdot)$ values.

Hand ($\mathrm{PPGi}_{\mathrm{all}}(t)$ / $\mathrm{PPGi}_{\mathrm{best}}(t)$)						Foot ($\mathrm{PPGi}_{\mathrm{all}}(t)$ / $\mathrm{PPGi}_{\mathrm{best}}(t)$)					
$\mathrm{SNR}_{\mathrm{td}}$[dB]	$\mathrm{SNR}_{\mathrm{fd}}$[dB]	PCC [n.u.]	$\mathrm{TD}_{\mathrm{mean}}$[ms]	$\mathrm{TD}_{\mathrm{sd}}$[ms]		$\mathrm{SNR}_{\mathrm{td}}$[dB]	$\mathrm{SNR}_{\mathrm{fd}}$[dB]	PCC[n.u.]	$\mathrm{TD}_{\mathrm{mean}}$[ms]	$\mathrm{TD}_{\mathrm{sd}}$[ms]	
-1.8/-1.1	4.9/3.5	.56/.62	-48/13	178/169	↗	-1.0/0.8	-0.2/7.5	.36/.68	33/-16	173/147	↗
1.1/2.2	4.1/7.4	.68/.82	-53/7	103/101	↗	3.5/3.1	10.3/9.7	.92/.91	-40/-49	95/80	↘
2.0/1.9	1.7/1.9	.87/.87	18/16	60/62	–	0.7/1.1	0.9/3.1	.63/.66	-17/-17	70/60	↗
0.4/0.2	3.0/2.4	.65/.54	10/13	115/136	↘	-2.2/-3.2	-2.4/-3.8	.21/.14	46/-8	187/189	↘
3.8/4.0	8.0/8.1	.92/.94	-17/-12	37/35	↗	3.6/3.7	4.3/5.1	.93/.93	-15/-6	51/47	↗
1.8/2.1	16.4/12.0	.86/.62	11/-9	53/74	–	2.3/2.7	7.8/5.6	.84/.89	26/25	60/52	↗
-0.2/0.7	2.5/3.8	.57/.64	-15/7	60/57	↗	2.1/2.5	12.9/14.0	.79/.82	8/3	63/62	↗
2.7/2.7	11.7/11.4	.89/.90	12/4	41/43	–	3.1/3.3	-7.5/-4.2	.87/.92	-11/-14	64/60	↗
2.2/2.0	1.3/1.7	.68/.69	-14/-26	63/62	–	1.4/1.2	0.2/0.3	.81/.80	-31/-40	57/50	–
0.5/0.8	-0.3/10.5	.45/76	43/30	90/68	↗	-4.5/-3.9	9.3/12.5	.32/.37	53/15	186/166	↗
2.3/2.0	9.4/12.7	.72/.80	-13/3	50/48	↗	2.4/3.4	2.0/3.7	.84/.81	20/0	80/63	↗
4.7/4.4	3.0/1.9	.95/.94	-1/14	35/33	↘	2.5/4.0	-2.6/-0.4	.83/.93	7/7	56/39	↗
3.0/3.0	17.5/18.9	.89/.87	23/38	73/74	–	-1.2/0.5	2.3/6.2	.41/.56	46/32	145/133	↗
2.4/3.2	3.2/5.1	.88/.91	-14/28	81/50	↗	1.9/2.9	15.2/16.8	.78/.89	20/8	49/49	↗
0.3/0.4	2.6/3.1	.74/.74	13/-8	108/104	↗	1.9/1.9	9.9/11.8	.82/.83	-17/-19	68/62	–
2.1/2.1	12.2/13.9	.86/.84	-45/-39	67/60	–	-1.4/0.5	-9.4/-3.6	.18/.37	35/21	154/138	↗
-2.1/-2.1	1.5/3.7	.32/.43	21/11	130/137	–	-2/0.0	-2.7/2.2	.51/.70	-7/-40	154/119	↗
3.5/2.6	8.6/8.4	.92/.82	27/53	51/75	↘	2.0/2.6	9.1/14.9	.74/.88	-69/-107	145/81	↗
0.1/-1.3	10.7/5.5	.69/.46	67/34	56/58	↘	1.0/1.1	2.0/1.5	.72/.65	25/-18	100/61	–
-0.6/1.7	-4.0/3.3	.39/.70	-14/-20	65/64	↗	-3.1/-5.5	-7.2/-12.7	.40/.28	-11/-5	86/100	↘
-2.6/-6.2	-3.0/-9.2	.48/.13	-1/-12	123/140	↘	-8.5/-4.5	-11.2/-0.4	.28/.36	11/39	120/99	↗
1.6/1.7	9.5/9.9	0.7/0.7	24.2/19.7	73.0/72.3		1.0/1.6	7.1/9.2	0.6/0.7	23.3/18.9	97.6/82.6	

At first, results are given for the comparison between $\mathrm{PPGi}_{\mathrm{all}}(t)$ and $\mathrm{PPGi}_{\mathrm{best}}(t)$. Due to the five different metrics for SNR estimation, a majority decision was introduced. An unambiguous improvement (symbol: ↗) or degradation (symbol: ↘) in SNR is defined as having ≥ 4 metrics being improved or degraded for a single measurement. In 42% (71%) of the experiments using the hand (foot), using $\mathrm{PPGi}_{\mathrm{best}}(t)$ instead of $\mathrm{PPGi}_{\mathrm{all}}(t)$ increases SNR. Vice versa, in 24% (14%) using the assumed best pixel subset degrades the SNR. In the remaining cases, there was no majority according to the previously defined rule (symbol: $-$).

Next, results are given for the comparison between the two points of measurement. When $\mathrm{PPGi}_{\mathrm{all}}(t)$ is used most SNR metrics are higher at the hands than at the feet. For example, $\mathrm{SNR}_{\mathrm{td}}$ is 1.6 dB (hand) compared to 1.0 dB (feet) and $\mathrm{SNR}_{\mathrm{fd}}$ is 9.5 dB vs. 7.1 dB. However, when using $\mathrm{PPGi}_{\mathrm{best}}(t)$, the SNR at the feet becomes comparable to the SNR at the hand, e.g. 1.7 vs. 1.6 dB ($\mathrm{SNR}_{\mathrm{td}}$) and 9.9 dB vs. 9.2 dB ($\mathrm{SNR}_{\mathrm{fd}}$). $\mathrm{TD}_{\mathrm{mean}}$ shows no clear difference between both but $\mathrm{TD}_{\mathrm{sd}}$ is clearly improved when using best pixels (72.3 vs. 82.6 ms) compared to all pixel (73.0 vs. 97.6 ms).

Summary

- Cardiac monitoring during UHF MRI using PPGi (→ Chapter 3.2.1)
  - HR estimation using PPGi signals acquired from the forehead without dedicated illumination allows reproducing the general trend of HR values.
  - The proposed Alg. 1 is able to compute HR values in (soft) real-time.
  - Accuracy is lower inside than outside the MR bore, indicating that lowering illumination reduces SNR.
  - PPGi HR estimation outperforms ECG at 7 T due to MHD artifacts.
- Cardiac triggering during UHF MRI using PPGi (→ Chapter 3.2.2)
  - Synthetic PPGi signals were generated with a high degree of similarity to real PPGi data and both were used for parameter optimization of Alg. 2.
  - Applying Alg. 2 to PPGi data recorded from the forehead within UHF MRI (→ Chapter 3.1.1) results in trigger-to-trigger durations with a slightly lower accuracy compared to PPG and ECG at 0.3 T. At 7 T PPGi outperforms ECG with regard to trigger accuracy.
  - Using the advanced hardware setup with dedicated illumination and PPGi measurement from the foot (→ Chapter 3.1.3) for triggering MRA image acquisition from a healthy volunteer results in an image quality comparable to MRA images triggered by PPG.
- PPGi signal characteristics (→ Chapter 3.2.3).
  - The wavelength interval $[551 - 590]$ nm is well-suited for PPGi acquisition.
  - Using green LED illumination increases the intensity of the cardiac portion of the PPGi signal considerably.
  - PPGi signals measured from skin regions in close proximity (< 1 cm) might exhibit phase shifts.
  - The advanced setup (→ Chapter 3.1.3) with dedicated illumination and a glass plate allows acquiring PPGi signals with a high SNR
  - Using the same setup and analyzing only the assumed best pixels allows to acquire a signal from the foot with an SNR similar to the hand which constitutes a standard point of measurement.

4.2 ECG-based methods

In Chapter 4.2.1 results of applying the msPE framework to synthetic signals flawed by different noise models including correlated noise are given. This includes a comparison with state-of-the-art Gaussian parameter estimation methods (Caruana et al. 1986), (Guo 2011), (Roonizi 2013). The feasibility of using the msPE framework for ECG delineation is assessed using the publicly-available QT database with results given in Chapter 4.2.2. Chapter 4 concludes with a presentation of results from applying msPE to ECG signals flawed by MHD noise for QRS complex detection.

4.2.1 msPE of synthetic signals

Experiment 1: Model with $B = \tau = 0$ Signals according to the model $G_{A,\sigma,\tau=0,\mu,B=0}$ ($\rightarrow$ eq. (3.20)) were generated with additive noise being drawn from a normal distribution with SNR values ranging from -10 db to 100 dB. For each SNR level 150 signals were generated and processed by the msPE framework customized for the estimation of parameters A, σ, and μ as described by Alg. 3. Apart from that, signals were processed using algorithms proposed by Caruana et al., Guo, and Roonizi. Implementations of the three algorithm were kindly provided by Roonizi.

As proposed in (Roonizi 2013), PRD was used as error measure which measures the difference at each sample t_i between an input signal $\tilde{x}[t_i]$ and a signal $\tilde{y}[t_i]$ which was generated by substituting the Gaussian parameters estimated from one of the four methods into the Gaussian model. Fig. 4.15 depicts the mean PRD values of each method for each SNR value. Over the whole range of SNR values, the ranking of algorithm performance is quite similar except for Guo's algorithm which exhibits a drop at 80 dB. The Caruana algorithm (gray curve) is outperformed by the Guo algorithm (black curve) and the Roonizi algorithm (red curve) with the latter two showing a similar performance. The algorithm by Roonizi is more accurate at SNR values smaller than 10 dB while the algorithm by Guo is more accurate at values larger than 60 dB. The msPE implementation proposed in Alg. 3 (dark blue) outperforms the methods from literature at each SNR value in the interval $[-10, 70]$ dB.

As the PRD metric does not give any information on the accuracy regarding a single parameter further analysis was performed. This was realized by plotting the ground truth parameter values, the estimates obtained by Alg. 3, and the best performing algorithm from literature (Roonizi 2013) within the same axis.

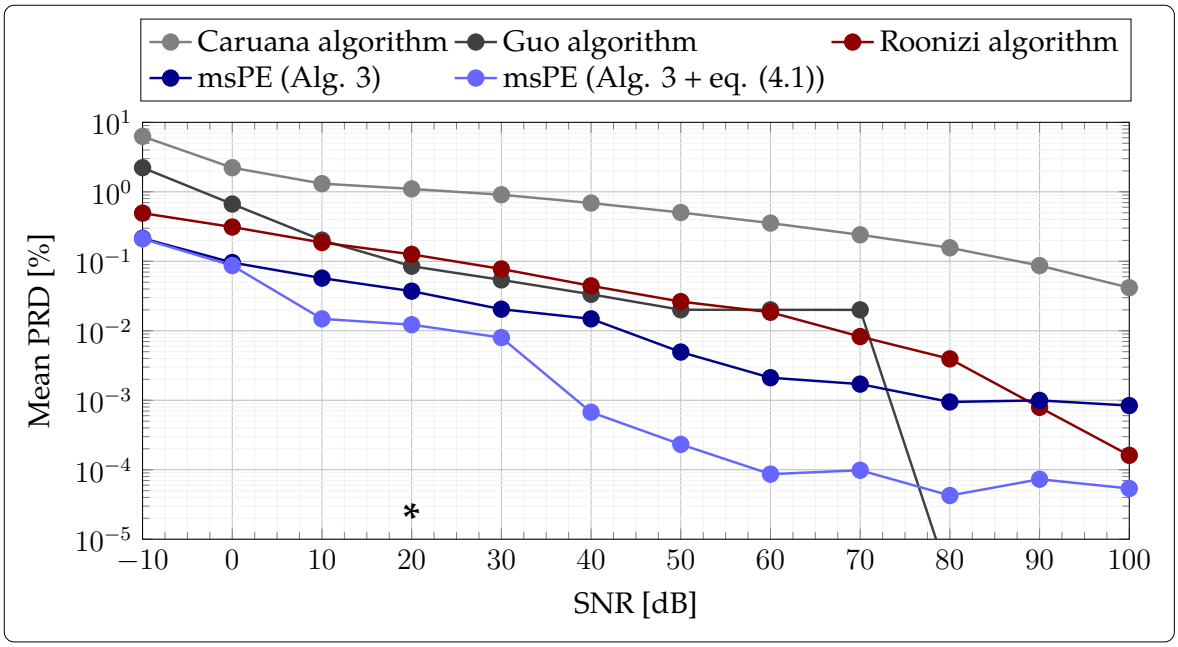

Figure 4.15: Log-log error plot showing mean PRD values resulting from applying Alg. 3 and the reference methods proposed by (Caruana et al. 1986), (Guo 2011), (Roonizi 2013) to 150 synthetic signals w.r.t. SNR. Adding an assumption regarding signal shape to Alg. 3 allows improving PRD values considerably. Raw data of 20 dB SNR (asterisk) is shown in Fig. 4.16.

Fig. 4.16 panels ① to ③ displays this information for 20 dB SNR and parameters μ, A, σ, respectively. msPE results in clearly more accurate estimates of all three parameters. This underlines the limitation of using PRD as a method of accuracy as the PRD values of both methods are quite similar at 20 dB (→ Fig. 4.15).

Errors of both algorithms are highest for Gaussian signals with low σ values (dashed region). Raw data was analyzed to find the reason for inaccurate parameter estimates by msPE when processing narrow signals. As has been shown earlier (e.g. → Fig. 2.14), wavelet theory is motivated by the possibility of analyzing signals at different scales suited for the signal at hand. Thereby, using a single scale for all generated signals with a wide variety of shapes ($\sigma_i \in (0.01, 0.03, ..., 1)$) therefore does not unlock the full potential of time-frequency analysis. In order to demonstrate this effect, the interval $[s_{\text{min}}, s_{\text{max}}]$ used for parameter estimation in Alg. 3 was reduced from $[650, 800]$ to $[50, 100]$. Comparing Fig. 4.16 ③ ($[650, 800]$) and ④ ($[50, 100]$), shows that this simple modification increases accuracy of the method considerably for low

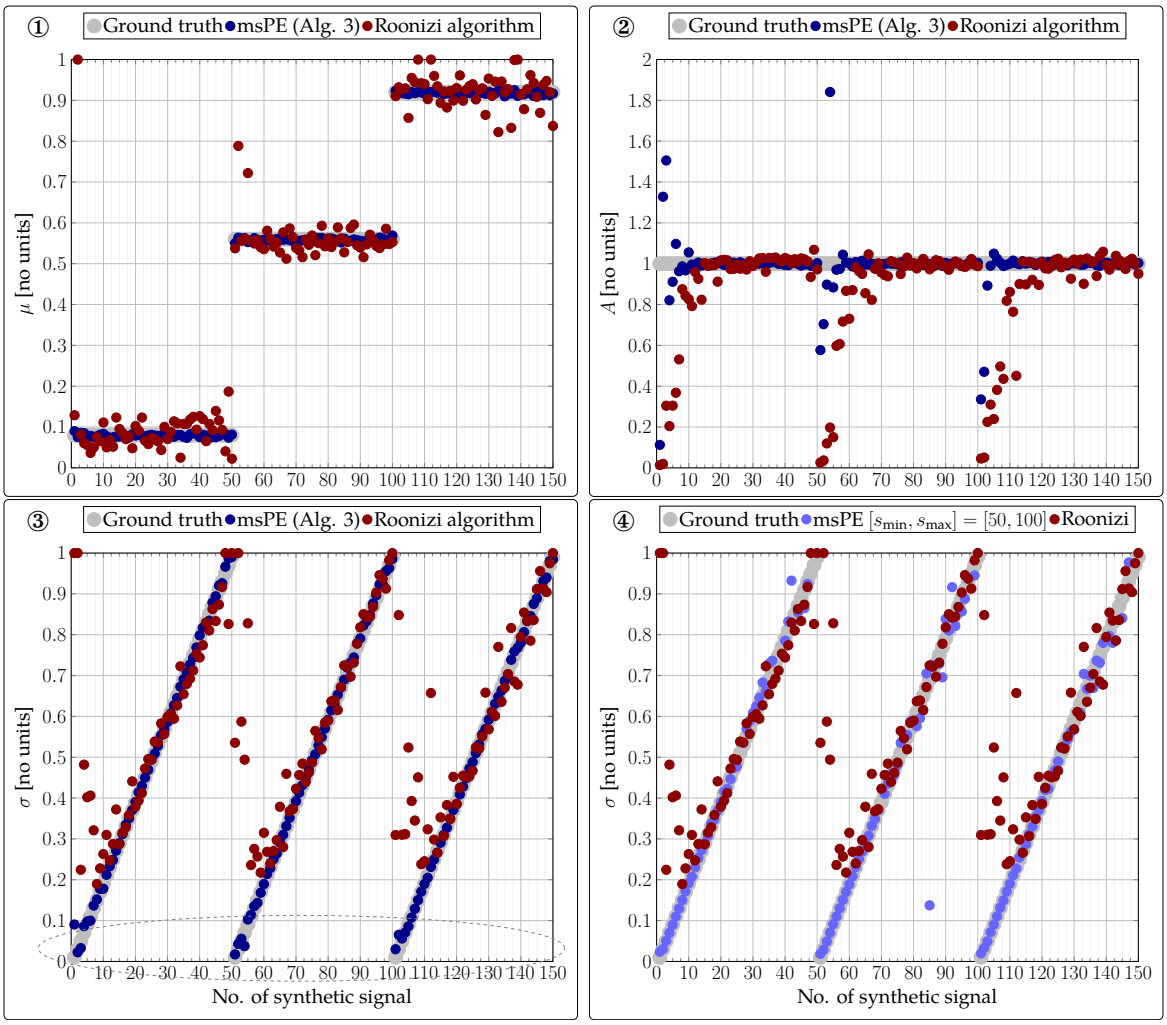

Figure 4.16: *Panels* ① to ③: Error in estimation of true parameters μ, A, σ (gray) by Alg. 3 (blue) and the Roonizi algorithm (red). A dashed region indicates particular high errors in σ estimation. *Panel:* ④ Results after modifying Alg. 3 by eq. (4.1).

σ values. On the downside, results for larger σ values are now more inaccurate. Hence, the usefulness of adding a weak assumption regarding parameter σ was demonstrated by modifying Alg. 3 according to

$$[s_{\min}, s_{\max}] = \begin{cases} [50, 100] & \text{if } \sigma < 0.05 \\ [650, 800] & \text{else} \end{cases} \tag{4.1}$$

Results acquired using this decision stage are shown in Fig. 4.15 (bright blue line). This improvement holds for all SNR levels ≥ 10 dB and fades to zero for lower levels.

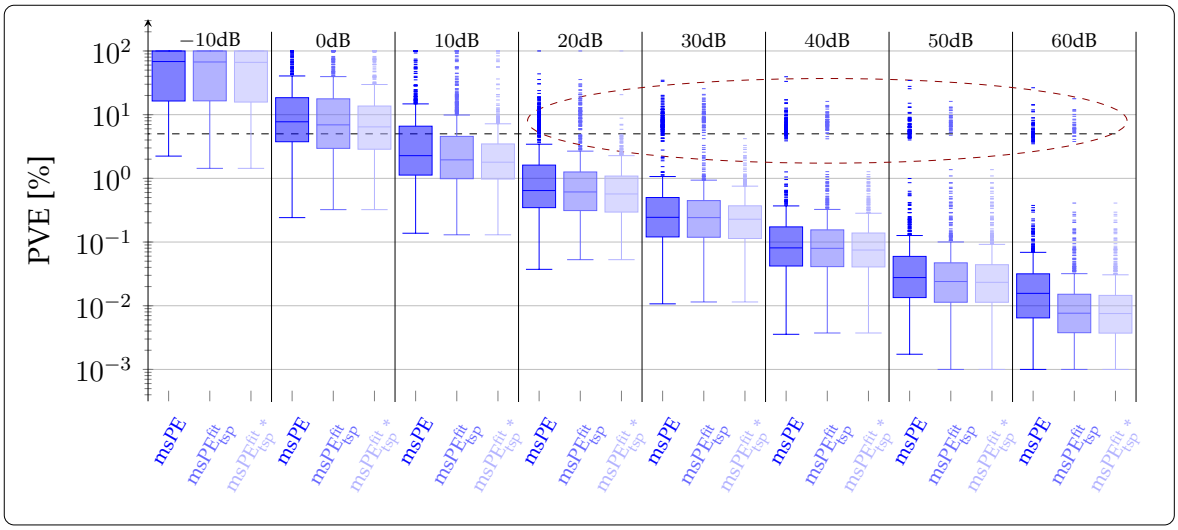

Figure 4.17: PVE distribution of experiment 2. At each SNR level, 1024 random signals of the 5-parameter model $G_{A,\sigma,\tau,\mu,B}(t)$ were generated and corrupted by Gaussian noise. Each signal was processed by three implementations of msPE. The red ellipse is used to underline the difference in accuracy of the three methods with regards to outliers. A dashed line marks the 5% error level.

Experiment 2: Model with $B \neq 0$ and $\tau \neq 0$ Results of the second experiment are summarized in Fig. 4.17 for SNR levels -10 to 60 dB. The PVE measure is based on measuring the difference between ground truth and estimated parameters, with the latter being obtained by three different algorithms. For each column respectively SNR level, the first boxplot depicts the pure msPE method without parameter refinement (Alg. 4 without step 7) and the second depicts the performance including parameter refinement $\text{msPE}^{\text{fit}}_{\text{tsp}}$(Alg. 4). The third boxplot will be introduced later.

As expected, the PVE values decrease with increasing SNR values. Experiments were performed up to 100 dB but are not shown here as a plateau of similar median values ($\approx 0.01\%$) is reached at 60 dB with only outlier being reduced at higher SNR values. At 60 dB, the parameter optimization $\text{msPE}^{\text{fit}}_{\text{tsp}}$ decreases the error considerably. With decreasing SNR accuracy is reduced but boxplots stay below 5% until 20 dB. At 10 dB, median values are still below 5% and at 0 db at approximately 7%. At SNR -10 dB the limit of usability of msPE as well as $\text{msPE}^{\text{fit}}_{\text{tsp}}$ is reached with multiple outliers and a median PVE of approximately 70%.

The raw data of boxplot outliers which are marked for SNR levels 20 to 60 dB (red ellipse) was analyzed. In nearly all cases, the reason for low accuracy was a wrong

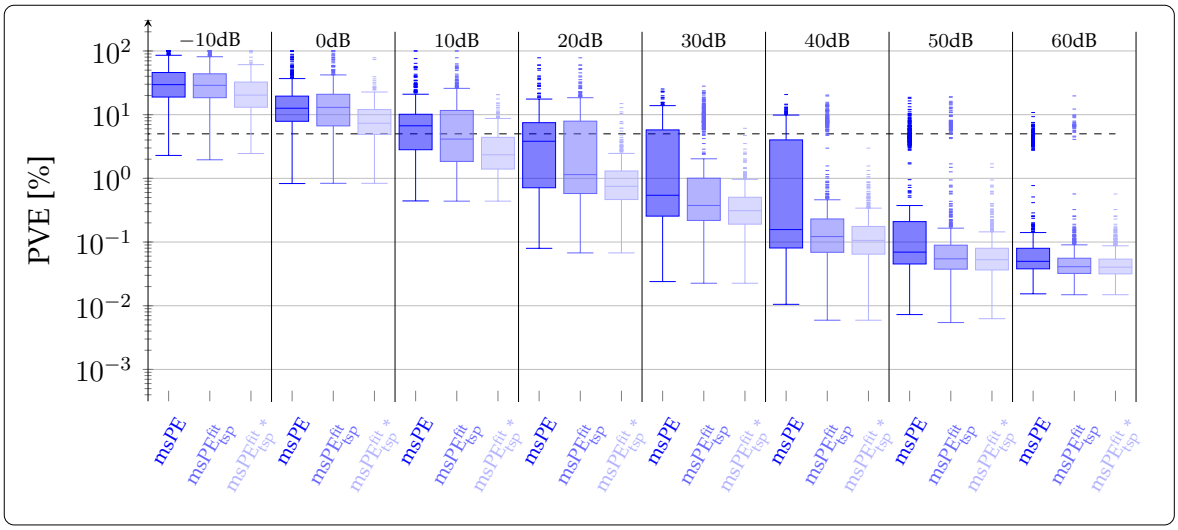

Figure 4.18: PVE distribution of experiment 3. At each SNR level, 1024 signals of the 8-parameter model $G_{\text{pw}}(t)$ were generated and corrupted by Gaussian noise.

classification of zero-crossing lines (→ p. 86), i.e. "wrong" lines not associated to the model but noise were used for parameter estimation leading to wrong results. To evaluate the influence of a wrong line classification, the algorithm using msPE$^{\text{fit}}_{\text{tsp}}$ was modified such that a correct line detection was enforced, with results being depicted in Fig. 4.17 as the third boxplot in each column.

The method is denoted msPE$^{\text{fit}}_{\text{tsp}}*$ and was realized by using the ground truth parameter τ of the model as an input for Alg. 4. If $\tau = 0$, there are only a single WT^1 and two WT^2 lines (→ Fig. 3.8). Therefore, after detecting these lines as described in Alg. 4, no further lines were searched. Vice versa, if $\tau > 0$, it was ensured that three WT^1 and four WT^2 lines were detected as the model is represented by them (→ Fig. 3.8). By making use of this modification, it can be seen in Fig. 4.17 that this approach reduces the number of outliers considerably. For example, at 30 dB there are no PVE values higher than 5% using msPE$^{\text{fit}}_{\text{tsp}}*$.

Experiment 3: Piecewise model This experiment was similar to the previous but signals were generated using the piecewise model function $G_{\text{pw}}(t)$ (→ eq. (3.45)). Results are depicted in Fig. 4.18 and comparing them to Fig. 4.17 shows that the error of the second experiment follows the same SNR-dependend trend but on a higher overall level. This is explained by the reduced number of zero-crossing lines available for parameter estimation as the parameters of the left and right side of the

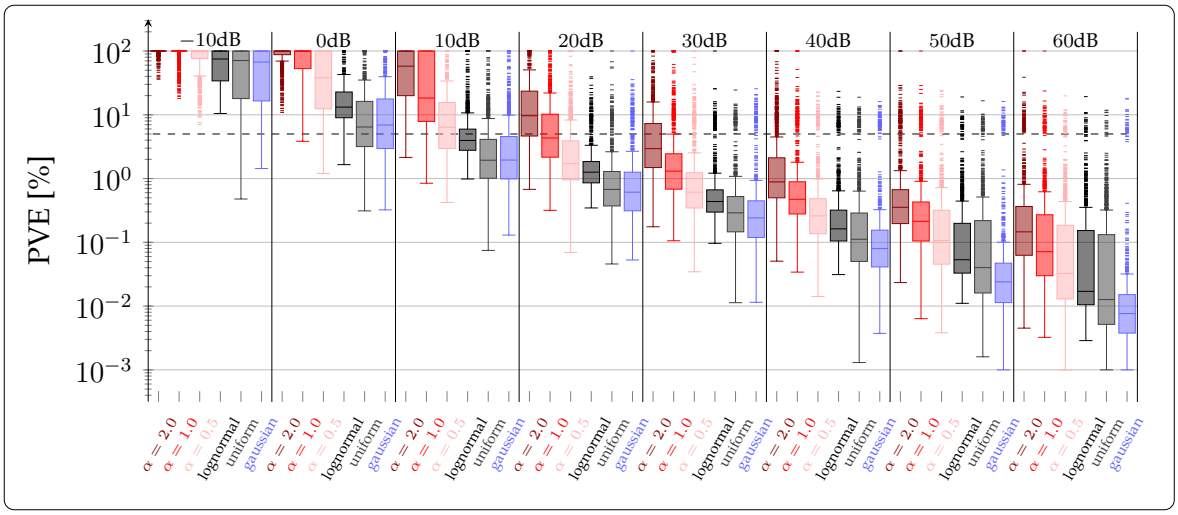

Figure 4.19: PVE distribution of experiment 4. At each SNR level, 1024 random signals of the 5-parameter model $G_{A,\sigma,\tau,\mu,B}(t)$ were generated and corrupted by correlated (red boxplots) or non-Gaussian noise (gray boxplots). The boxplots from Fig. 4.17 for Gaussian noise are given as reference. All signals were processed by the same implementation of $\text{msPE}^{\text{fit}}_{\text{tsp}}$ ($\rightarrow$ Alg. 4 including step 7).

model are estimated independently, dividing their number in in halves. Similar to the previous experiment, if an input signal's shape with regard to parameters $\tau_{\text{L,R}}$ is known during parameter estimation ($\text{msPE}^{\text{fit}}_{\text{tsp}}*$), the number of outliers can be reduced considerably.

Experiment 4: Non-Gaussian and correlated noise In the previous experiments, all noise was drawn from a normal distribution which limits the generalization of results to real-world signals. In this experiment, noise was drawn from non-Gaussian distributions by means of a uniform and a lognormal distribution ($\rightarrow$ Fig. 3.17 (left)). Correlated noise using α values of 0.5, 1.0 (pink noise), and 2.0 (brown noise) was used as well ($\rightarrow$ Fig. 3.17 (right)). Other than that, the experiment was identical to experiment 2 but instead of all three implementation, $\text{msPE}^{\text{fit}}_{\text{tsp}}$ was used only.

As can be seen in Fig. 4.19, uniform and lognormal noise (gray) results in higher errors compared to normally-distributed noise across all scales, with lognormal being slightly worse than uniform. Similarly, correlated noise (red) results in even larger errors, increasing with the level of correlation. At SNR of 20 dB the median error of correlated noise with $\alpha \leq 1$ is still lower than 5%. But, at 10 dB median errors are

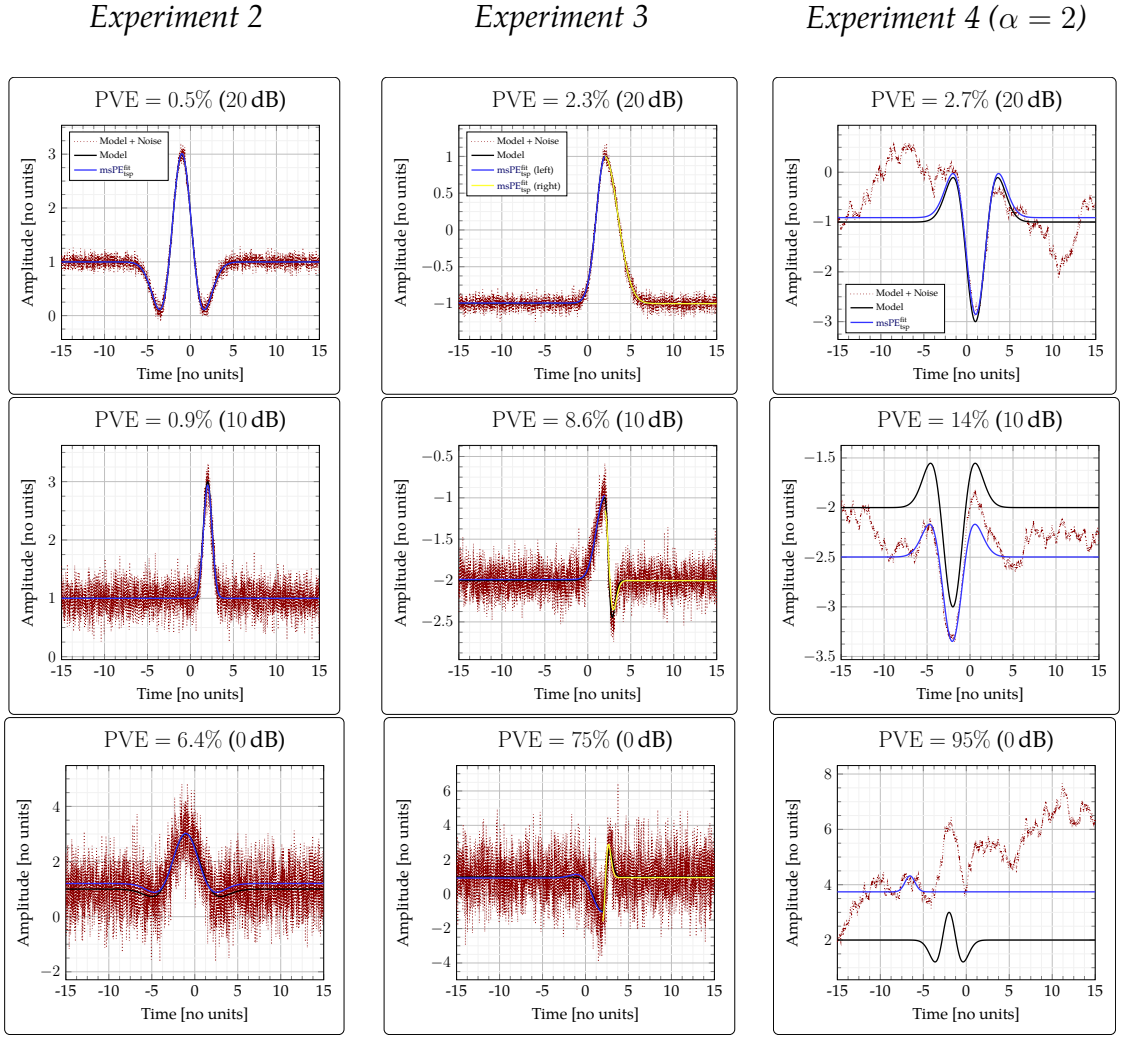

Figure 4.20: Exemplary results from experiments 2, 3, and 4 for SNR levels 20, 10, and 0 dB. In the first two columns, additive noise is drawn from a normal distribution while in the third column noise is drawn from correlated "brown" noise with $\alpha = 2$.

already approximately 7% ($\alpha = 0.5$), 20% ($\alpha = 1$), 50% ($\alpha = 0.5$) and at 0 dB correlated noise for all α values results in large errors, rendering them unusable for practical applications.

Examples Fig. 4.20 depicts examples from previous experiments. The different characteristics of noise models become apparent: Normally-distributed noise (left, center column), uniform and lognormal noise (not shown) do not change the shape of the signal's baseline but correlated noise (right column) introduces variations to the baseline. At 0 dB correlated noise a limit of the algorithm's feasibility is reached.

4.2.2 msPE of ECG signals from a standard database

Evaluation of time-scale plane funnel (Alg. 6) The efficiency of the time-scale plane funnel was evaluated by simply counting the number of zero-crossing line combinations before and after its application to each ECG signal of the QT database. However, this approach does not give any information on the quality of line reduction as ground truth information on which zero-crossing lines are best representing an ECG wave are not available. This can only be analyzed indirectly by the quality of ECG delineation given later. But, this approach allows assessing the efficiency of the method for reducing computational steps and therefore run time.

In the following $\mathrm{m} \pm \mathrm{sd}$ values and intervals from minimum to maximum values are given. Before application of the funnel there were 111.0 ± 550.8 $[8-26415]$ (QRS), 17.4 ± 79.2 $[3-1868]$ (T), and 22.6 ± 252.6 $[3-11869]$ (P) zero-crossing lines available in the segments around each ECG wave with the values given being $\mathrm{m} \pm \mathrm{sd}$ and range. After application of the funnel, 65.4 ± 295.7 $[3-13793]$, 13.5 ± 59.8 $[3-1464]$, and 21.7 ± 243.3 $[3-11449]$ lines were left. Hence, their number was reduced by 41.1% (QRS), 22.5% (T), and 4.2% (P).

The higher values for QRS complexes are explained by the fact that the full 5-parameter model $G_{A,\sigma,\tau,\mu,B}(t)$ was used for their representation which can be associated with up to seven lines ($\rightarrow$ Fig. 3.8, center). This results in a considerably higher number of possible combinations compared to the model with $\tau = 0$ used for P- and T-waves which is represented by three lines only ($\rightarrow$ Fig. 3.8, left).

Evaluation of extrapolation error (Alg. 7) The underlying assumption of the proposed extrapolation error measure is that ECG waves can be represented adequately by the model function $G_{A,\sigma,\tau,\mu,B}(t)$ while other signal components, e.g. noise, cannot. This assumption was derived from the high degree of visual similarity of P-/T-waves and the QRS complex to different parameterizations of the model function. With the proposed error measure one can make use of this assumption by computing the error for each available zero-crossing line combination and by subsequently detecting only the one combination with lowest error, i.e. highest similarity to $G_{A,\sigma,\tau,\mu,B}(t)$.

However, it cannot be assessed directly if this assumption holds as there is no ground truth information that defines classes of "poor" or "well-suited" zero-crossing line combinations for ECG waves. Instead, for each ECG wave of the QT database, E values for each available combination of zero-crossing lines were com-

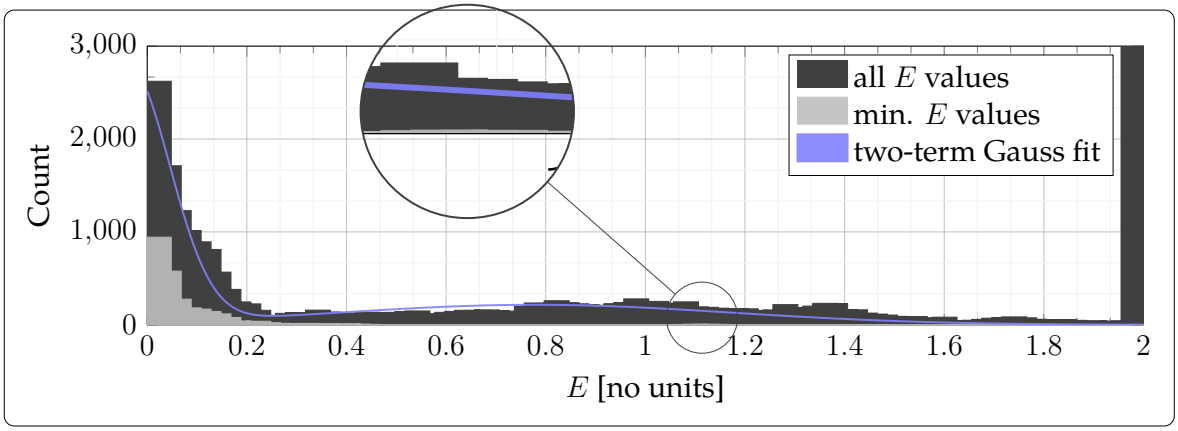

Figure 4.21: E values computed for each line combination of QRS complexes of the QT database (black) and the subset of the one line combination with minimum E value for each individual QRS complex (gray). The first distribution is bimodal with 97.3% of all minimum E values lying in the left term. Values $E > 2$ were clamped.

puted. Additionally, the minimum E values associated to the one combination chosen for subsequent ECG delineation was tagged. If the underlying idea of the extrapolation error holds adequately, the first set of values represents both classes (poor and well-suited combinations) while the latter should contain a considerably higher number of well-suited combinations.

Fig. 4.20 shows results obtained from all first-lead QRS complexes of the QT database. As can be seen, the E values of all combinations (black bars) follow an approximately bimodal distribution. A two-term Gaussian fit is shown (blue line) with the valley point between both Gaussians being at approximately $E = 0.3$. This indicates that the first group $E \leq 0.3$ adequately represents the underlying model function $G_{A,\sigma,\tau,\mu,B}(t)$ used for QRS complex representation while the line combinations of the second group $E > 0.3$ do not. The majority of values from the minimum group lies left of the valley point and 2.7% are larger (magnified region).

Furthermore it can be seen that there is a an approximately three-fold number of combinations with low error within the interval $[0, 0.315]$ of the group containing all combinations compared to only minimal combinations (arrow). This is a direct result of the exhaustive search: Next to the one combination with minimum error, there might be similar combinations, for example with one fewer or one additional line, that result in a similar low error. Results of P- and T-waves show similar distributions of E values.

Evaluation of ECG delineation Fig. 4.22 shows representative delineation results for three P-/T-waves and QRS complexes from the processed ECG signals (black curve) of the QT database. The ground truth onsets, offsets, and center fiducial points $\{\mathrm{P, QRS, T}\}_{\{\mathrm{on,\ peak,\ off}\}}$ which were defined by one of the two human annotators are shown (gray dots). Results of the proposed algorithms are depicted by means of the piecewise model function $G_{\mathrm{pw}}(t)$ with parameters estimated by $\mathrm{msPE}^{\mathrm{fit}}_{\mathrm{tsp}}$ (blue curve) and computed fiducial points $\{\mathrm{P, QRS, T}\}_{\{\mathrm{on,\ peak,\ off}\}}$ (red lines).

The first two rows show typical ECG signals similar to the ones shown in Chapter 2.3.2 with the P- and T-waves being similar to a Gaussian with non-symmetric halves. The P-wave in the second and the T-wave in the third row show different baseline levels on the left and right side which is adequately reproduced by the estimated parameters $B_{\{\mathrm{L,\ R}\}}$. The QRS complex in the first row has an undershoot on the right side ($\tau_{\mathrm{L}} = 0$, $\tau_{\mathrm{R}} > 0$) while the one in the second row is Gaussian-shaped ($\tau_{\mathrm{L,\ R}} = 0$). The parameters of the ECG waves shown in the first two rows are estimated accurately, demonstrated by a high overlap of $G_{\mathrm{pw}}(t)$ with the ECG signals.

The third row shows noisy ECG signals with the P-wave and the QRS complex showing many signal notches and the T-wave showing a clearly non-symmetric shape. While the latter is processed successfully, the center of the P-wave has not been detected correctly which is presumably to a high number of false zero-crossing lines. Additionally, the undershoot of the QRS complex is not adequately detected, i.e. parameter τ is zero but should be considerably larger. This is a result of the algorithm missing zero-crossing lines associated to the QRS complex and leads to inaccurate fiducial point computation, i.e. a high mismatch between $\mathrm{QRS}_{\mathrm{off}}$ computed by the algorithm and the one defined by the human annotator.

Table 4.4 shows results of processing the entire QT database according to the standard evaluation methodology (→ p. 106) by comparing the difference in time between ground truth and annotated fiducial points. Each column represents a single fiducial point and each row a different algorithm from literature. In each cell, the sensitivity is given in percentage and the accuracy using $\mathrm{m} \pm \mathrm{sd}$. Bold sensitivity values denote the highest value within a column. In some works not all fiducial points have been detected, e.g. an exclusive P-wave detector was proposed in (Lenis et al. 2016) and in (Hesar, Mohebbi 2018) sensitivity values were not reported.

In the penultimate row, results are shown using the developed evaluation algorithm, according to the standard evaluation methodology, for processing the fiducial

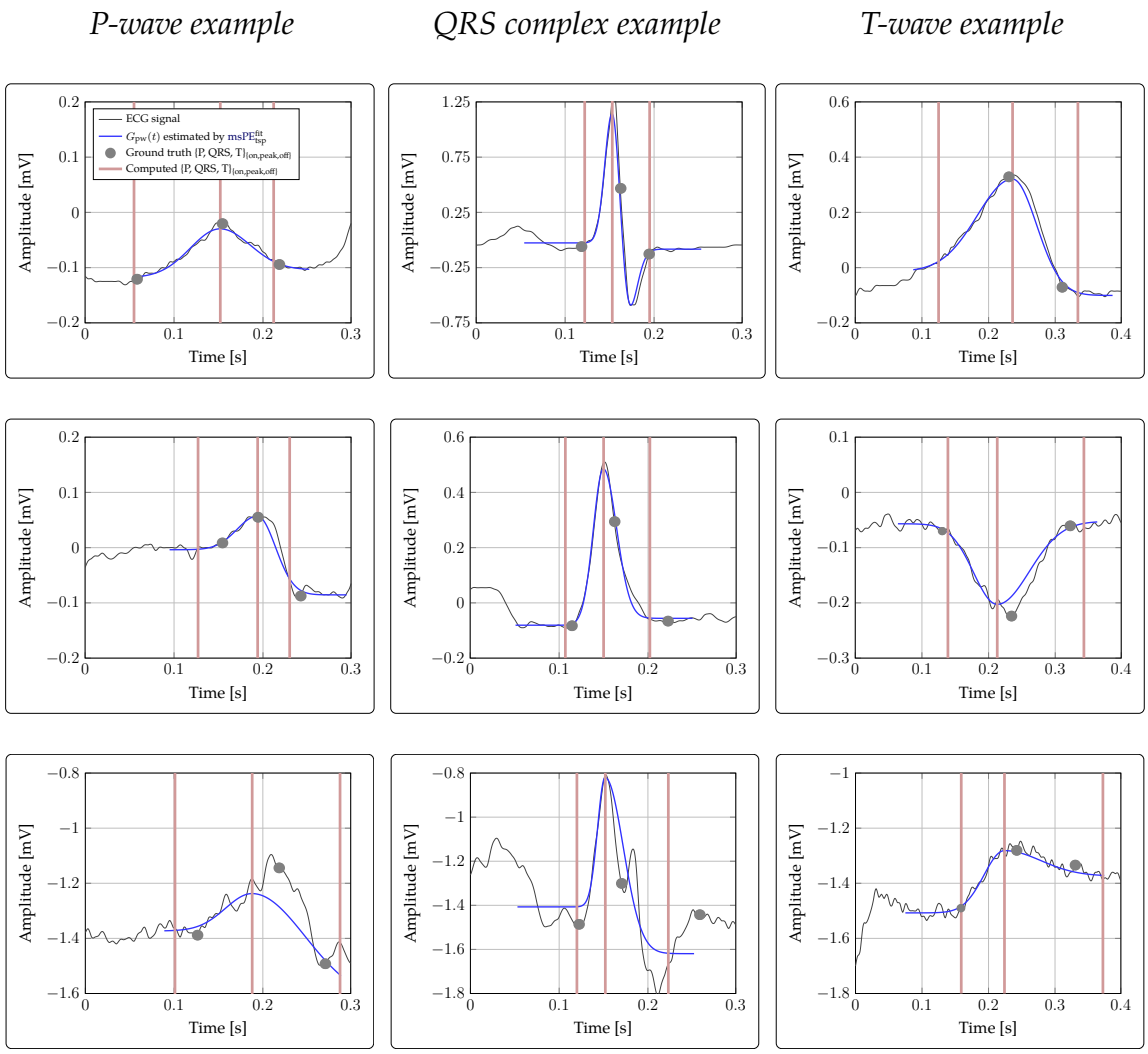

Figure 4.22: Three example delineation results that were randomly chosen out of 3194 P-waves, 3542 T-waves, and 3623 QRS complexes from the QT database. Computed fiducial points {P, QRS, T}$_{\{on,\ peak,\ off\}}$ are depicted as red lines to avoid overlapping with the dots used for the visualization of annotations of human experts. T_{on} was not defined by the human annotator within the first row.

Table 4.4: Delineation of ECG signals from the QT database [Sensitivity, $\mathrm{m} \pm \mathrm{sd}$]

▶ **Fiducial point**	P_{on}	P_{peak}	P_{off}	QRS_{on}	QRS_{peak}	QRS_{off}	T_{on}	T_{peak}	T_{off}
▶ **# Annotations**	3194	3194	3194	3623	3623	3623	1412	3542	3542
This work	99.91	99.91	**99.91**	99.92	99.92	99.92	**99.93**	**99.89**	**99.89**
	0.5±15.1	5.1±10.9	0.5±15.0	0.9±8.5	-4.1±4.6	-0.4±9.6	-0.3±23.7	-4.5±14.7	0.6±20.3
Preliminary work	97.62	97.62	97.62	99.92	99.92	99.92	97.0	99.01	99.01
	0.3±15.0	4.8±10.6	-0.3±16.9	1.6±7.6	-4.3±4.8	-0.9±11.0	-0.1±26.6	-3.1±11.6	0.6±20.3
Hesar, Mohebbi 2018	-	-	-	-	-	-	-	-	-
	16±37	5±34	-10±34	-	-	-	23±42	-3±24	-16±35
Bote et al. 2018	98.22	99.34	99.87	**100**	-	99.97	-	**99.89**	97.49
	22.3±14.0	13.5±7.3	-0.7±9.5	7.0±4.3	-	-5.0±9.9	-	8.4±14.3	-11.7±15.0
Cesari et al. 2017	-	-	-	**100**	**100**	**100**	-	99.50	98.73
	-	-	-	2.8±7.7	2.2±3.9	2.7±9.7	-	-2.6±12.2	-2.7±20.7
Lenis et al. 2016	**100**	**100**	-	-	-	-	-	-	-
	-0.3±12.2	5.8±9.1	-	-	-	-	-	-	-
Marco, Chiari 2011	98.15	98.15	98.15	**100**	-	**100**	-	99.72	99.77
	-4.5±13.4	-4.7±9.7	-2.5±13.0	-5.1±7.2	-	0.9±8.7	-	-0.3±12.8	1.3±18.6
Lin et al. 2010	98.93	98.9	98.93	-	-	-	99.01	99.81	99.81
	3.7±17.3	4.1±8.6	-3.1±15.1	-	-	-	7.1±18.5	1.3±10.5	4.3±20.8
Martinez et al. 2004	98.87	98.87	98.75	99.97	-	99.97	-	99.77	99.77
	2.0±14.8	3.6±13.2	1.9±12.8	4.6±7.7	-	0.8±8.7	-	0.2±13.9	-1.6±18.1
Laguna, Jané, et al. 1994	97.7	97.7	97.7	99.92	99.92	99.92	-	99.0	99.0
	14.0±13.3	4.8±10.6	-0.1±12.3	-3.6±8.6	-4.2±4.7	-1.1±8.3	-	-7.2±14.3	13.5±27.0
Laguna, Jané, et al. 1994*	97.71	97.71	97.71	99.92	99.92	99.92	97.0	99.01	99.01
	14.0±13.3	4.8±10.6	-0.1±12.3	-3.6±8.6	-4.2±4.7	-1.1±8.3	8.5±30.0	-3.1±11.6	13.5±26.2
$2 \cdot \mathrm{sd}_{CSE}$	10.2	-	12.7	6.5	-	11.6	-	-	30.6

points detected by the (Laguna, Jané, et al. 1994) algorithm. This step was performed to verify that the evaluation algorithms are free from error by comparing results to the values given in (Martinez et al. 2004). As can be seen in the columns representing fiducial points of P-waves and QRS complexes results are identical. However, for T-waves, results are slightly different. As the same algorithms are used this cannot be explained by different data processing. Potentially, extreme outliers have been removed in (Martinez et al. 2004) leading to the difference.

In the ultimate row, tolerance values are given which were defined by the Common Standards in Quantitative Electrocardiography (CSE) working party with the aim to provide information which accuracy *"can be expected from an expert cardiologist"* (The CSE Working Party 1985). The given values are $2 \cdot \mathrm{sd}$ values of the difference between the median of the several human annotators and the final referee estimates but using another ECG database. Therefore, these values cannot be mapped directly to the QT database but they constitute a guideline.

Analyzing the sensitivity values shows that the proposed algorithm is able to process all QRS complexes indicated by the peak detector (99.92%) and shows a high sensitivity for P- (99.91%) and T-waves (99.81%) as well. Comparing sensitivity

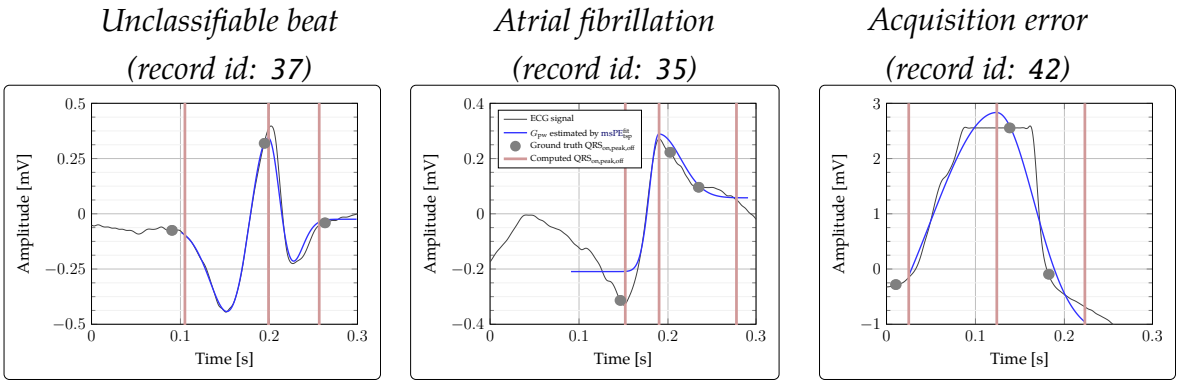

Figure 4.23: QRS complexes with irregular shapes using the same visualization as used in Fig. 4.22. The first QRS complex as marked by the annotators as being "unclassifiable", the second shows a case of severe atrial fibrillation distorting the typical QRS waveform, and the third shows an indadequate configuration of the ECG measurement hardware as values above a certain limit are cropped.

values to the other works shows that it is highest for T-waves and second-highest for P-waves. In direct comparison to early work in which $\{\text{P, QRS, T}\}_{\text{peak}}$ (Laguna, Jané, et al. 1994) were used as starting point for a linear line search, sensitivity is increased by a minimum of 0.88% (T_{peak}) up to a maximum of of 2.29% ($\text{P}_{\{\text{on, peak, off}\}}$).

Regarding accuracy the proposed method shows low mean errors which are $\leq 1\,\text{ms}$ for all onset and offset fiducial points $\{\text{P, QRS, T}\}_{\{\text{on, off}\}}$. At the same time, standard deviation errors are slightly increased compared to the best-performing algorithms from literature. For example, QRS_{off} is increased by $3.6\,\text{ms}$ and P_{on} by $2.9\,\text{ms}$. Compared to the guidelines proposed by the CSE committee (The CSE Working Party 1985), the sd values of QRS_{off} and T_{off} are within the limits while $\text{P}_{\{\text{on, off}\}}$ and QRS_{on} are not.

Analysis of uncommon QRS complexes Fig. 4.23 shows three examples of uncommon QRS complexes from the data processed. The first QRS complex was labeled by the human annotators as "unclassifiable", the second was recorded from a patient suffering from atrial fibrillation, and the third was recorded with an inadequate configuration of the ECG monitor. As can be seen, the maximum values are clamped such that the QRS complex does not show a real peak but a plateau instead. However, due to the flexibility of $G_{\text{pw}}(t)$, the algorithm estimates signal shapes robustly in all three cases, explaining the high accuracy reported in Table 4.4.

Run time The processing time for delineation of each ECG wave with Alg. 1 was stored. This allows computing $\mathrm{m} \pm \mathrm{sd}$ values which were 143.9 ± 38.5 ms (QRS complex), 132.4 ± 20.5 ms (T-wave) and 110.7 ± 12.6 ms (P-wave) on an off-the-shelf laptop.

4.2.3 msPE of QRS complexes acquired during UHF MRI

As can be seen from the previous section, the ECG delineation algorithm requires a high number of computation and therefore results in run times larger than 140 ms for a single QRS complex. This is not acceptable for MRI cardiac triggering with a maximum latency guideline of 20ms after an R-wave (Fischer, Wickline, et al. 1999).

Hence, a faster algorithm for detection of $\mathrm{QRS}_{\mathrm{peak}}$ only was devised in Alg. 8 and applied to ECG signals from three subjects acquired inside and outside a UHF MRI bore. For each of the six experiments, 100 QRS complexes were manually extracted and the point in time $\mathrm{QRS}_{\mathrm{peak}}$ was stored as ground truth. Results are given in Table 4.5 by means of sensitivity and accuracy with the latter being defined similar to Table 4.4 as the time difference between the manually annotated $\mathrm{QRS}_{\mathrm{peak}}$ and the computed position by the algorithm. If the difference between both was larger than 50 ms, the wave was considered as missed and sensitivity was reduced by approximately 1% for this experiment. Additionally, the latency is given which is the time period Alg. 8 took for the detection of $\mathrm{QRS}_{\mathrm{peak}}$. Bold values in the fourth and eighth row show mean values for the first (0.3 T) and second experiment (7 T), respectively.

As can be seen from Table 4.5, the proposed QRS detector shows a high sensitivity which is $\geq 94\%$ for each experiment with an average of 97% for the first stage of experiments without considerable MHD noise and an average of 95.7% for the second stage with a high level of MHD noise. Comparing the accuracy shows that it is slightly degraded with an increase of 1.1 mean and 1.3 standard deviation error. Regarding the acceptable latency for accurate MRI cardiac gating, the algorithm was below the guideline of 20 ms (Fischer, Wickline, et al. 1999) on average. However, $\mathrm{m} \pm 2 \cdot \mathrm{sd}$ is longer than 20 ms, thereby approximately 32% took longer.

Fig. 4.24 shows exemplary results for each subject of the study with the last example showing a case of a "missed" QRS complex depicted in red color. As can be seen, Alg. 8 detected the wrong line as central line $u0_0^1$ which led to parameter estimation of the larger undershoot due to MHD noise. In the remaining examples, msPE was successful showing high accuracy in processing QRS complexes.

Table 4.5: Results of QRS_{peak} detection in ECG data obtained at $0.3\,T$ and $7\,T$.

Subject	Tesla [T]	Sensitivity [%]	Accuracy [ms]	Latency [ms]
I	0.3	99.0	11.5 ± 1.8	17.5 ± 3.4
II	0.3	94.0	3.4 ± 2.0	16.4 ± 2.0
III	0.3	98.0	-4.4 ± 2.6	15.4 ± 2.5
		97.0	$\mathbf{3.5 \pm 2.2}$	$\mathbf{16.4 \pm 2.6}$
I	7.0	95.0	-2.3 ± 2.7	17.4 ± 3.0
II	7.0	97.0	8.4 ± 4.8	16.4 ± 2.0
III	7.0	95.0	7.8 ± 2.9	17.5 ± 2.6
		95.7	$\mathbf{4.6 \pm 3.5}$	$\mathbf{17.1 \pm 2.6}$

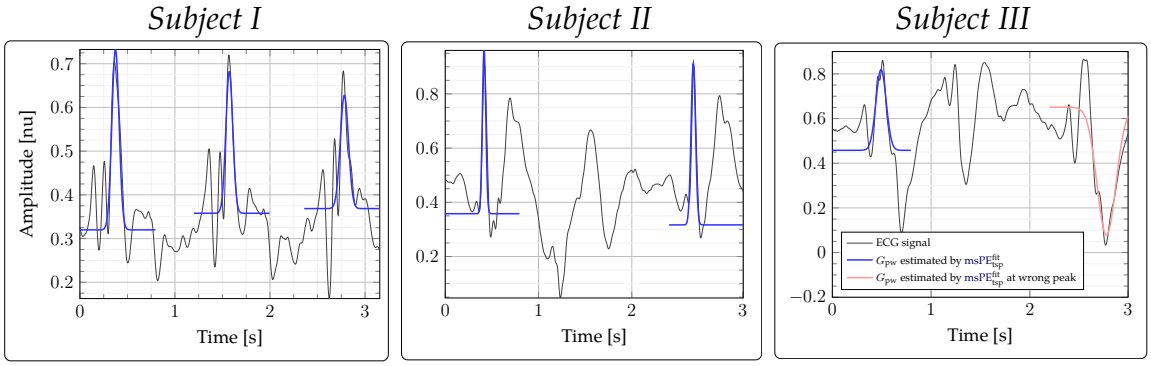

Figure 4.24: Example results from the $7\,T$ experiments for each subject. Due to the MHD noise the morphologies of the QRS complexes are abnormal, i.e. they are very similar to a Gaussian (left), or in proximity to a T-wave which shows high amplitude (center), or exhibit large undershoots (right). $G_{pw}(t)$ is plotted in blue color if the distance between QRS_{peak} and the ground truth value is $\leq 50\,ms$ or in red color else.

Summary

- msPE of synthetic signals (→ Chapter 4.2.1)
  - msPE outperforms state-of-the-art algorithms for Gaussian parameter estimation (Caruana et al. 1986) (Guo 2011) (Roonizi 2013) w.r.t. accuracy.
  - The accuracy of msPE can be improved by adding weak assumptions regarding the input signal or by using parameter fine-tuning ($\text{msPE}^{\text{fit}}_{\text{tsp}}$).
  - The accuracy of msPE is highest for signals biased by Gaussian noise, followed by uniform, lognormal, and correlated noise.
- msPE of ECG signals from a standard database (→ Chapter 4.2.2)
  - The time-scale plane funnel reduces the number of processed zero-crossing line combinations from 4.2% (P-wave) up to 41.1% (QRS complex).
  - Analyzing the distribution of E values indicates that for 97% of ECG waves there is one or multiple well-suited zero-crossing line combinations.
  - $G_{\text{pw}}(t)$ is able to accurately resemble typical ECG waveforms and some irregular morphologies such as atrial fibrillation.
  - Comparing results to state-of-the-art ECG delineators from literature shows highest sensitivity for $4/9$ fiducial points and particularly low mean errors for all onset and offset fiducial points below 1 ms.
  - Delineation of a single ECG wave takes up to 150 ms .
- msPE of QRS complexes acquired during UHF MRI (→ Chapter 4.2.3)
  - The proposed QRS detector achieves a sensitivity of 97% for ECG signals acquired at 0.3 T and 95.7% for signals acquired at 7 T.
  - The accuracy of QRS detection is slightly decreased for signals acquired at 7 T (4.6 ± 3.5 ms) compared to signals acquired at 0.3 T (3.5 ± 2.2 ms).
  - QRS detection takes on average 17 ms which is below the 20 ms guideline for accurate MRI triggering but $\text{m} + 2 \cdot \text{sd}$ is above.

5 Discussion

The results obtained in this work contribute to the field of cardiac assessment in UHF MRI in two ways: The first approach was motivated by introducing PPGi to this context and evaluating to which degree it can be used as a replacement for ECG and PPG for cardiac monitoring and triggering, despite the numerous limitations of this environment. The second approach aimed at making use of the already existing PMU hardware which measures MHD-flawed ECG signals by proposing algorithms able to compensate for these effects. In the following, results given in the previous chapters are discussed and potential developments for future work are suggested.

5.1 PPGi-based methods

The first aim of this work was to answer the question to what degree PPGi can be used for cardiac assessment in the context of MRI. The motivation behind this question lied in the imperfection of ECG and PPG for this task in UHF MRI.

The methods proposed in Chapter 3.2, their analysis in Chapter 4.1 and the one-page summary (→ p. 125) answer this question comprehensively: Using PPGi within an MRI bore is feasible and PPGi signals obtained from the forehead without dedicated illumination allow to obtain HR values more accurate than HR values measured from ECG. Moreover, a first evaluation of MRI triggering via PPGi using a quantitative analysis showed that this approach is feasible but suffers from low SNR, resulting in inaccurate triggers.

The problem of SNR Hence, a major limitation of this contact- and (dedicated) illumination-free approach was the low SNR of the PPGi signal. Therefore, several experiments were conducted to find possibilities for enhancing a PPGi signal's cardiac portion. It was shown that the combination of dedicated LED illumination and contact pressure applied to the skin by means of a glass plate allows acquiring PPGi signals with considerably higher SNR. While the first can be realized without any major drawback, the latter abandons the advantage of a completely contact-free setup. The sole of the feet for measurement was chosen as they are easily accessible and the glass plate acts as a footrest decreasing patient comfort only slightly.

Using this improved setup for cardiac triggering showed promising results in a healthy subject undergoing UHF MRA with images acquired being qualitatively similar to PPG-triggered images. However, to make a statement regarding generalization, a larger study with more subjects should be conducted. The volunteer was cooperative and tried to keep still. Uncooperative or sick patients might make large body movements which most likely decrease accuracy, similar to contact-based methods. Thus, a large study analyzing these aspects should be performed in the future to evaluate the aspect of SNR in clinical routine.

PPGi hardware considerations Another problematic aspect was the quite limited availability of MRI-compatible cameras. Hence, the specifications of the MR-compatible camera used are rather simple ($25\,\mathrm{Hz}$, 720×576 pixels). For comparison, the ECG of the MR-vendor is acquired with a 16-fold sampling rate and the PPG signal with a rate twice as high. This limits the value of the measured PPGi signal and makes certain analysis of the cardiac signal impossible, e.g. analysis of HR variability requires considerably higher sampling rates (Merri et al. 1990).

During the course of this work an MRI-compatible, high-speed camera entered the market and could be tested for several days[1]. Using a high-speed camera offers the possibility to acquire a significantly higher number of frames which increases the value for PPGi analysis. However, for MRI triggering this requires finding a finely-balanced compromise between the number of processed frames and algorithm latency due to the run time restrictions for accurate MR image acquisition.

[1]This work has been published in: Spicher, N., Maderwald, S., Ladd, M. E., Kukuk, M. (2016): High-speed, contact-free measurement of the photoplethysmography waveform for MRI triggering In: Proceedings of the 24th Annual Meeting of the International Society for Magnetic Resonance in Medicine, Singapore.

Moreover, the sensitivity w.r.t. wavelength of the camera used is not optimal. As has been shown by others (McDuff et al. 2014; de Haan, Jeanne 2013) and has been confirmed in this work using hyperspectral imaging, the wavelength range from approximately 500 to 600 nm is optimal for measuring the cardiac component of the PPGi signal. However, within this range the camera used has a sensitivity up to approximately 65% only and reaches a maximum at 800 nm. Thereby, in future work a camera with a more adequate sensitivity could potentially increase the SNR of the PPGi signal and thereby the usefulness of the proposed methods for cardiac monitoring and triggering. As no camera with these specifications is commercially-available to date, a camera could be custom-build which has been done in related work (Maclaren et al. 2015) and offers an alternative. Moreover, polarization filtration (Trumpp et al. 2017) could be used to potentially increase SNR.

PPGi signal considerations Regarding the detection of a "best" pixel subset for increasing PPGi SNR, it was shown in a study in a non-MRI environment that using pixels in the vicinity of high illumination and adequate contact pressure allows increasing the SNR when measuring PPGi from the sole of the foot to a similar level as the palm of the hand. However, furthermore, it was found in the MRI environment that local phase variations, attributed to skin inhomogeneity (Moço et al. 2016), occur during PPGi measurement. It was demonstrated in this work that there are no large regions of similar phase on the skin and that very close pixels can exhibit a $180°$ phase shift. This is a serious limitation for applying a fixed ROI as these color variations may cancel each other out. Future work may explore strategies for selecting well-suited PPGi signals from pixels with similar phases.

Summary Fig. 5.1 summarizes the advantages and disadvantages of the contact-based methods for cardiac assessment, ECG and PPG, and the same for the proposed PPGi methods. Categories are: *safety*, which describes potential safety hazards for the patient due to the hardware, *reliability*, which describes the susceptibility regarding environment variables (e.g. field strength, illumination), *accuracy* which describes the latency between occurrence of a QRS complex and the sending of a trigger, *robustness* which is similar to reliability but describes the susceptibility regarding patient influence (e.g. involuntary motion, increased HRV), *comfort*, which describes the level of patient discomfort when the method is applied, and *set-up convenience*,

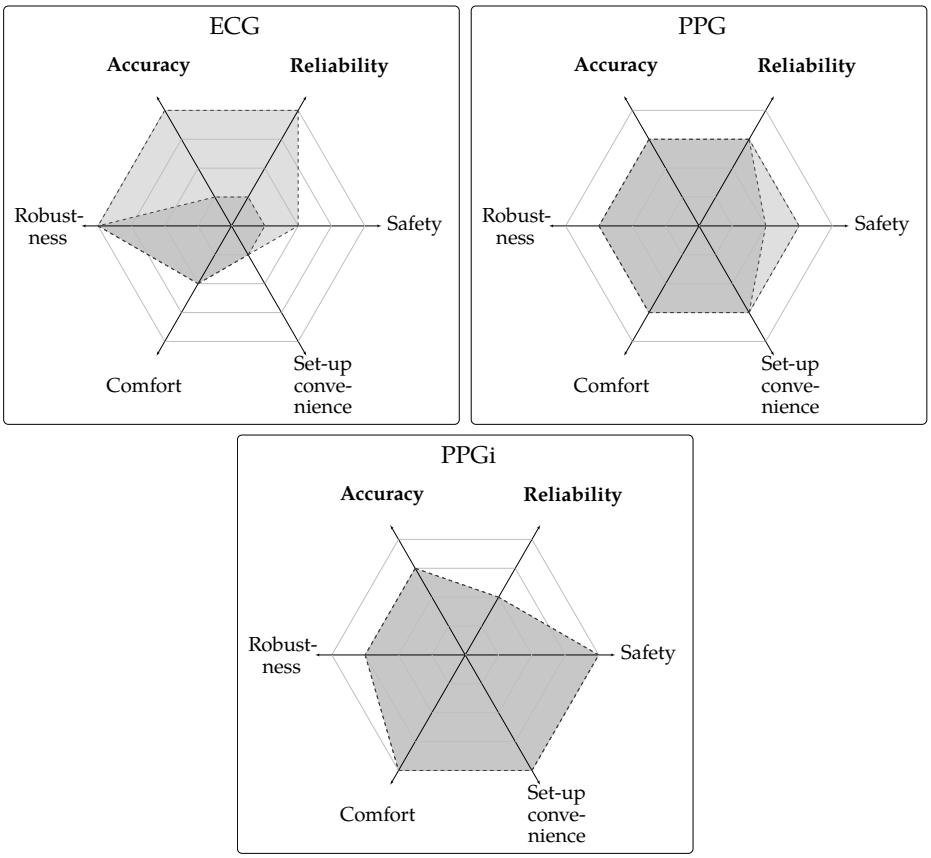

Figure 5.1: Qualitative assessment of the feasibility of ECG, PPG, and PPGi for cardiac monitoring and triggering within clinical MRI (light gray) and UHF MRI (dark gray). For PPGi, results are identical for both environments. Each category is evaluated using a measure ranging from low (center) to high (border) and the assessment of categories reliability and accuracy (bold values) is backed by results presented in this work while the remaining categories are subjective evaluations.

which describes the efforts of clinical staff it takes to apply the method to the patient.

Results obtained during the data acquisition study (→ Chapter 3.1.1) are in accordance with literature, showing that ECG clearly outperforms the two other methods at low field strengths regarding accuracy and reliability, but its value is lessened considerably at UHF MRI. The value of PPG is not as dependent on the magnetic field as it is an optical measurement but at higher fields the risk of heating of probes and cables is increased, thereby reducing safety. Additionally, during experiments several dropouts of trigger detection were observed, most presumably due to low perfusion of the subjects hands or involuntary movement, reducing robustness.

On the one hand, the proposed PPGi system has the major advantage of not being influenced by the MRI environment, once installed the set-up time is basically zero, and due to the missing contact of contact probes with the patient, safety is maximized.

On the other hand, reliability suffers from a high dependence on adequate illumination. Robustness could be shown to be adequate for healthy and cooperative volunteers, but needs to be evaluated within a larger patient population and especially for patients suffering from cardiac disease.

5.2 ECG-based methods

The second aim of this work was to answer the research question whether MHD-flawed ECG signals acquired in UHF MRI can be processed by algorithms from the field of time-frequency transforms such that relevant information can be extracted robustly. To answer this question, instead of providing a narrowly tailored method for only this task, a top-down approach was followed. This led to the development of the msPE framework which constitutes an analytical framework for multiscale parameter estimation of signals following a flexible Gaussian derivative model. The numerical counterpart of the framework can be used as part of a computer algorithm and was customized for several tasks within this work.

Results are summarized in a one-page summary (→ p. 141): Using synthetic data, it was demonstrated that msPE robustly detects parameters of noisy Gaussian signals and outperforms state-of-the-art competing methods. As a first approach towards processing real ECG signals, the well-known test case of detecting the onsets, peaks, and offsets of ECG waves was adopted. It could be shown that the underlying model of msPE is well-suited for ECG signals and that the algorithm outperforms several state-of-the-art algorithms w.r.t. sensitivity and mean errors.

Subsequently, a computationally more efficient method for detecting only the peak of the QRS complex, which acts as a trigger for MRI triggering, was devised. Evaluation with ECG data acquired inside and outside an UHF MRI bore showed sensitivity $\geq 95\%$ and mean run times below $20\,\mathrm{ms}$ which was considered to be the maximum duration for accurate triggering (Fischer, Wickline, et al. 1999).

Usage of msPE for ECG delineation Regarding the usage of msPE for delineation of ECG signals there are several avenues for future work. In this work, to obtain a bottom-line performance, each fiducial point in each ECG wave in each record was treated exactly the same way by the algorithm. As specific heuristics have not been applied, this leaves room for improvement in future work. For example, the used segments are adequate in the vast majority of cases, but there are certain records where the P- or T-waves are abnormally far away from the QRS complex and are therefore not covered by $I_{\{\mathrm{P,\,QRS,\,T}\}}$. This could be improved by analyzing the ECG record before delineation and computing specific interval sizes. Other than that, the tweaking parameters $c_{\{\mathrm{on,\,off}\}}$ were manually defined by visually inspecting the expert annotations in the QT database. Again, this leaves room for improvement by using record-specific values; however, this is a challenging task due to a high level of intra- and inter-observer variability (Willems et al. 1985) and the risk of overfitting parameters to a given data set.

The QT database is a valuable resource of signals from a variety of patients, including patients suffering from arrhythmia or experiencing sudden cardiac death during the ECG measurement. Although the achieved results are satisfying, there are certainly irregular ECG morphologies, not contained within the QT database, which cannot be represented by the underlying model function adequately. For example in ST elevation myocardial infarction ECG signals, the ST segment (→ Chapter 2.3.2) is often very short due to an elevated T-wave, decreasing the distance between QRS complex and T-wave. Thereby, estimation of the offset of the QRS complex and the onset of the T-wave can be expected to be inaccurate. Another potential problem are fragmented QRS complexes resulting from myocardial scars which can show additional notches in the ECG signal. Thereby, the proposed method should be applied to a larger and more diverse ECG database than the QT database. However, this is problematic as no such database with ground truth annotations has been made publicly-available to date.

Usage of msPE for QRS detection in MHD-flawed ECG signals The application of the msPE framework for QRS detection required to reduce run time to a suitable level which was a non-trivial task as a minimum implementation requires two Wavelet Transforms. By testing different scale ranges, a suitable range could be found which offers an adequate compromise between computation time and accuracy. The results

obtained were positive with the non-optimized source code reaching a mean run time within the limit of 20 ms. This leaves room for an in-depth analysis of the accuracy of the detected QRS complex positions vs. the scale range used.

Analysis of raw data showed that the QRS detection works robustly and the missed QRS complexes reducing sensitivity stem from a wrong line selection (→ Fig. 4.24, right panel) and not from algorithm failure. These miss-classifications are a result of the rather basic line classifier which selects the central line by detecting the one line with minimum variance, i.e. it is based on its straightness. In related work, higher sensitivity was reported (e.g. 99.1% (Krug et al. 2013)) but also they made use of a 12-lead ECG device and not the PMU. To increase the sensitivity to a comparable level, a more elaborate, but also computationally lightweight, line classifier should be devised in future work. Although it is too computational expensive, the time-scale plane funnel proposed in Chapter 3.3.3 might serve as a guideline.

Moreover, only the (piecewise) Gaussian model of msPE was used and it should be evaluated in future work if using the full (piecewise) model with undershoots might offer added value.

In summary, the results obtained during this feasibility study in which the proposed QRS detector was applied to MHD-flawed ECG signals acquired in UHF MRI warrant the development of a real-time implementation for actual MRI cardiac triggering in future work. The proposed setup for PPGi-based cardiac triggering (→ Chapter 3.1.3 / Fig. 3.3) can be adjusted for this task effortlessly by replacing the camera signal with the PMU ECG signal.

Potential applications to other signals Due to the high generability of the underlying model function, msPE offers a variety of potential applications beyond cardiac signals. The Gaussian model function can be found in many fields of research, for example in spectroscopy where it represents the shape of spectral lines. The Gaussian derivative model function with undershoots and its piecewise extension can be found in functional MRI where the blood-oxygen-level-dependent response shows an undershoot before developing a peak (Yacoub et al. 2001) or in electromyography as motor unit action potentials (Shahid et al. 2005). Therefore, the proposed msPE framework and the given implementations for parameter estimation as well as computation of fiducial points might be of interest for other areas of research.

6 Summary

Electrocardiography (ECG) is the standard method for assessing the state of the cardiovascular system non-invasively. In the context of magnetic resonance imaging (MRI) the ECG signal is used for cardiac monitoring and triggering, i.e., the acquisition of images synchronized to the cardiac cycle. However, ECG acquisition is impeded by the static and dynamic magnetic fields which alter the measured voltages and may reduce signal-to-noise ratio (SNR), leading to false alarms during cardiac monitoring or to image artifacts during cardiac triggering. A major source of noise is the magnetohydrodynamic (MHD) effect as it is proportional to field strength and represents a key challenge in application of ultra-high-field (UHF) MRI $\geq 7\,\mathrm{T}$.

In this work, two approaches for overcoming these limitations were proposed: i) Development of a hardware and software system based on the principal of photoplethysmography imaging (PPGi) as an optical method for acquiring a cardiac signal, and ii) development of algorithms for detecting fiducial points in ECG signals despite the low SNR. Due to the non-stationary dynamics of the cardiac activity, extraction of information from both types of signals was realized by time-frequency analysis.

The feasibility of the PPGi system for heart rate measurement was demonstrated in an UHF MRI study where PPGi signals acquired from the forehead outperformed ECG in terms of accuracy and reliability. Application of the system at the sole of the foot for triggering allowed producing UHF MR angiography images with a quality similar to pulse oximetry triggering in a healthy volunteer.

During the work on ECG algorithms, a general framework for multiscale parameter estimation (msPE) was developed. First, it was customized for delineation of (non-MR related) ECG signals from the reference QT database. Second, it was used for QRS detection in ECG signals acquired within UHF MRI. Processing the QT database shows that msPE is well-suited for processing ECG waves and outperforms state-of-the-art algorithms w.r.t. sensitivity in $4/9$ fiducial points. QRS detection in ECG signals acquired within $7\,\mathrm{T}$ was shown to be robust with a sensitivity $\geq 95\%$ and an accuracy degraded by $1\,\mathrm{ms}$ compared to ECG signals without MHD noise.

In summary, the methods proposed may provide useful steps towards unlocking the full potential of cardiac assessment in UHF MRI.

7 References

1) Acharya, U. R., Joseph, K. P., Kannathal, N., Lim, C. M., Suri, J. S. (2006): Heart rate variability: a review. Medical & Biological Engineering & Computing, 44(12), 1031–1051.

2) Allen, J. (2007): Photoplethysmography and its application in clinical physiological measurement. Physiological Measurement, 28(3), R1–R39.

3) Amelard, R., Scharfenberger, C., Kazemzadeh, F., Pfisterer, K. J., Lin, B. S., Clausi, D. A., Wong, A. (2015): Feasibility of long-distance heart rate monitoring using transmittance photoplethysmographic imaging (PPGI). Scientific Reports, 5(1).

4) Antink, C. H., Lyra, S., Paul, M., Yu, X., Leonhardt, S. (2019): A Broader Look: Camera-Based Vital Sign Estimation across the Spectrum. Yearbook of Medical Informatics, 28(01), 102–114.

5) Balakrishnan, G., Durand, F., Guttag, J. (2013): Detecting Pulse from Head Motions in Video In: IEEE Conference on Computer Vision and Pattern Recognition. IEEE.

6) Bashkatov, A. N., Genina, E. A., Kochubey, V. I., Tuchin, V. V. (2005): Optical properties of human skin, subcutaneous and mucous tissues in the wavelength range from 400 to 2000nm. Journal of Physics D: Applied Physics, 38(15), 2543–2555.

7) Birkholz, T., Schmid, M., Nimsky, C., Schüttler, J., Schmitz, B. (2004): ECG Artifacts During Intraoperative High-Field MRI Scanning. Journal of Neurosurgical Anesthesiology, 16(4), 271–276.

8) Bote, J. M., Recas, J., Rincon, F., Atienza, D., Hermida, R. (2018): A Modular Low-Complexity ECG Delineation Algorithm for Real-Time Embedded Systems. IEEE Journal of Biomedical and Health Informatics, 22(2), 429–441.

9) Brandts, A., Westenberg, J. J. M., Versluis, M. J., Kroft, L. J. M., Smith, N. B., Webb, A. G., de Roos, A. (2010): Quantitative assessment of left ventricular function in humans at 7 T. Magnetic Resonance in Medicine, 64(5), 1471–1477.

10) Bronstein, I. N., Mühlig, H., Musiol, G., Semendjajew, K. A. (2016): Taschenbuch der Mathematik. Europa Lehrmittel Verlag.

11) Budinger, T. F., Bird, M. D. (2018): MRI and MRS of the human brain at magnetic fields of 14 T to 20 T: Technical feasibility, safety, and neuroscience horizons. NeuroImage, 168, 509–531.

12) Caruana, R. A., Searle, R. B., Shupack, S. I. (1986): Fast algorithm for the resolution of spectra. Analytical Chemistry, 58(6), 1162–1167.

13) Cesari, M., Mehlsen, J., Mehlsen, A.-B., Sorensen, H. B. D. (2017): A New Wavelet-Based ECG Delineator for the Evaluation of the Ventricular Innervation. IEEE Journal of Translational Engineering in Health and Medicine, 5, 1–15.

14) Chakeres, D. W., Kangarlu, A., Boudoulas, H., Young, D. C. (2003): Effect of static magnetic field exposure of up to 8 Tesla on sequential human vital sign measurements. Journal of Magnetic Resonance Imaging, 18(3), 346–352.

15) Cooley, J. W., Tukey, J. W. (1965): An algorithm for the machine calculation of complex Fourier series. Mathematics of Computation, 19(90), 297–297.

16) Costanzo, L. S. (2009): Physiology (5. Ed.). Philadelphia: Saunders.

17) de Haan, G., Jeanne, V. (2013): Robust Pulse Rate From Chrominance-Based rPPG. IEEE Transactions on Biomedical Engineering, 60(10), 2878–2886.

18) Denslow, S., Buckles, D. S. (1993): Pulse oximetry-gated acquisition of cardiac MR images in patients with congenital cardiac abnormalities. American Journal of Roentgenology, 160(4), 831–833.

19) Ertürk, M. A., Wu, X., Eryaman, Y., Moortele, P.-F., Auerbach, E. J., Lagore, R. L., ... Metzger, G. J. (2016): Toward imaging the body at 10.5 tesla. Magnetic Resonance in Medicine, 77(1), 434–443.

20) Faller, A., Schünke, M. (2004): The Human Body: An Introduction to Structure and Function (7. Ed.). Stuttgart: Thieme.

21) Feichtinger, H. G., Strohmer, T. (1998): Gabor Analysis and Algorithms: Theory and Applications. Basel: Birkhäuser.

22) Felblinger, J., Lehmann, C., Boesch, C. (1994): Electrocardiogram acquisition during MR examinations for patient monitoring and sequence triggering. Magnetic Resonance in Medicine, 32(4), 523–529.

23) Fischer, A., Maderwald, S., Orzada, S., Johst, S., Schäfer, L. C., Ladd, M. E., ... Lauenstein, T. C. (2013): Nonenhanced Magnetic Resonance Angiography of the Lower Extremity Vessels at 7 Tesla. Investigative Radiology, 48(7), 525–534.

24) Fischer, S. E., Wickline, S. A., Lorenz, C. H. (1999): Novel real-time R-wave detection algorithm based on the vectorcardiogram for accurate gated magnetic resonance acquisitions. Magnetic Resonance in Medicine, 42(2), 361–370.

25) Frauenrath, T., Hezel, F., Renz, W., de Geyer d'Orth, T., Dieringer, M., von Knobelsdorff-Brenkenhoff, F., ... Niendorf, T. (2010): Acoustic cardiac triggering: a practical solution for synchronization and gating of cardiovascular magnetic resonance at 7 Tesla. Journal of Cardiovascular Magnetic Resonance, 12(1).

26) Gabor, D. (1946): Theory of communication. Part 1: The analysis of information. Journal of the Institution of Electrical Engineers - Part III: Radio and Communication Engineering, 93(26), 429–441.

27) Gaffey, C. T., Tenforde, T. S. (1981): Alterations in the rat electrocardiogram induced by stationary magnetic fields. Bioelectromagnetics, 2(4), 357–370.

28) Goldberger, A. L., Amaral, L. A. N., Glass, L., Hausdorff, J. M., Ivanov, P. C., Mark, R. G., ... Stanley, H. E. (2000): PhysioBank, PhysioToolkit, and PhysioNet. Circulation, 101(23).

29) Gregory, T. S., Schmidt, E. J., Zhang, S. H., Tse, Z. T. H. (2014): 3DQRS: A method to obtain reliable QRS complex detection within high field MRI using 12-lead electrocardiogram traces. Magnetic Resonance in Medicine, 71(4), 1374–1380.

30) Grossmann, A., Morlet, J. (1984): Decomposition of Hardy Functions into Square Integrable Wavelets of Constant Shape. SIAM Journal on Mathematical Analysis, 15(4), 723–736

31) Guo, H. (2011): A Simple Algorithm for Fitting a Gaussian Function. IEEE Signal Processing Magazine, 28(5), 134–137.

32) Gupta, A., Weeks, A. R., Richie, S. M. (2008): Simulation of Elevated T-Waves of an ECG Inside a Static Magnetic Field (MRI). IEEE Transactions on Biomedical Engineering, 55(7), 1890–1896.

33) Hall, J. E. (2010): Guyton and Hall Textbook of Medical Physiology (12. Ed.). Philadelphia: Saunders.
34) Hamming, R. W. (1989): Digital Filters (3. Ed.). Mineola: Dover Publications Inc.
35) Hanning, C. D., Alexander-Williams, J. M. (1995): Pulse oximetry: a practical review. BMJ, 311(7001), 367–370.
36) Heisenberg, W. (1927): Über den anschaulichen inhalt der quantentheoretischen Kinematik und Mechanik. Zeitschrift für Physik, 43(3-4), 172–198.
37) Hesar, H. D., Mohebbi, M. (2018): A Multi Rate Marginalized Particle Extended Kalman Filter for P and T Wave Segmentation in ECG Signals. IEEE Journal of Biomedical and Health Informatics, 23, 112–122.
38) Husar, P. (2010): Biosignalverarbeitung. Heidelberg, Dordrecht, London usw.: Springer-Verlag GmbH.
39) Johnson, S. G. (2019): The NLopt nonlinear-optimization package.
40) Johst, S., Orzada, S., Fischer, A., Schäfer, L. C., Nassenstein, K., Umutlu, L., ... Maderwald, S. (2014): Sequence Comparison for Non-Enhanced MRA of the Lower Extremity Arteries at 7 Tesla. PLoS ONE, 9(1), e86274.
41) Kamal, A. A. R., Harness, J. B., Irving, G., Mearns, A. J. (1989): Skin photoplethysmography - a review. Computer Methods and Programs in Biomedicine, 28(4), 257–269.
42) Kamshilin, A. A., Nippolainen, E., Sidorov, I. S., Vasilev, P. V., Erofeev, N. P., Podolian, N. P., Romashko, R. V. (2015): A new look at the essence of the imaging photoplethysmography. Scientific Reports, 5(1).
43) Kangarlu, A., Burgess, R. E., Zhu, H., Nakayama, T., Hamlin, R. L., Abduljalil, A. M., Robitaille, P. M. L. (1999): Cognitive, cardiac, and physiological safety studies in ultra high field magnetic resonance imaging. Magnetic Resonance Imaging, 17(10), 1407–1416.
44) Kasdin, N. J. (1995): Discrete simulation of colored noise and stochastic processes and $1/f^{\alpha}$ power law noise generation. Proceedings of the IEEE, 83(5), 802–827.
45) Kording, F., Ruprecht, C., Schoennagel, B., Fehrs, K., Yamamura, J., Adam, G., ... Kraff, O. (2017): Doppler ultrasound triggering for cardiac MRI at 7T. Magnetic Resonance in Medicine, 80(1), 239–247.
46) Krug, J. W., Rose, G., Clifford, G. D., Oster, J. (2013): ECG-based gating in ultra high field cardiovascular magnetic resonance using an independent component analysis approach. Journal of Cardiovascular Magnetic Resonance, 15(1).

47) Ladd, M. E., Bachert, P., Meyerspeer, M., Moser, E., Nagel, A. M., Norris, D. G., ... Zaiss, M. (2018): Pros and cons of ultra-high-field MRI/MRS for human application. Progress in Nuclear Magnetic Resonance Spectroscopy, 109, 1–50.

48) Laguna, P., Jané, R., Caminal, P. (1994): Automatic Detection of Wave Boundaries in Multilead ECG Signals: Validation with the CSE Database. Computers and Biomedical Research, 27(1), 45–60.

49) Laguna, P., Mark, R. G., Goldberger, A., Moody, G. B. (1997): A Database for Evaluation of Algorithms for Measurement of QT and Other Waveform Intervals in the ECG. Computers in Cardiology, 24, 673–676.

50) Lanzer, P., Botvinick, E. H., Schiller, N. B., Crooks, L. E., Arakawa, M., Kaufman, L., ... Higgins, C. B. (1984): Cardiac imaging using gated magnetic resonance. Radiology, 150(1), 121–127.

51) Laudon, M. K., Webster, J. G., Frayne, R., Grist, T. M. (1998): Minimizing interference from magnetic resonance imagers during electrocardiography. IEEE Transactions on Biomedical Engineering, 45(2), 160–164.

52) Lenis, G., Pilia, N., Oesterlein, T., Luik, A., Schmitt, C., Dössel, O. (2016): P wave detection and delineation in the ECG based on the phase free stationary wavelet transform and using intracardiac atrial electrograms as reference. Biomedizinische Technik. Biomedical engineering, 61, 37–56.

53) Lin, C., Mailhes, C., Tourneret, J.-Y. (2010): P- and T-Wave Delineation in ECG Signals Using a Bayesian Approach and a Partially Collapsed Gibbs Sampler. IEEE Transactions on Biomedical Engineering, 57(12), 2840–2849.

54) Maclaren, J., Aksoy, M., Bammer, R. (2015): Contact-free physiological monitoring using a markerless optical system. Magnetic Resonance in Medicine, 74(2), 571–577.

55) Mallat, S. (2008): A Wavelet Tour of Signal Processing (3. Ed.). Cambridge: Academic Press.

56) Mallat, S., Hwang, W.-L. (1992): Singularity detection and processing with wavelets. IEEE Transactions on Information Theory, 38(2), 617–643.

57) Marco, L. Y. D., Chiari, L. (2011): A wavelet-based ECG delineation algorithm for 32-bit integer online processing. BioMedical Engineering OnLine, 10(1), 23.

58) Martinez, J. P., Almeida, R., Olmos, S., Rocha, A. P., Laguna, P. (2004): A Wavelet-Based ECG Delineator: Evaluation on Standard Databases. IEEE Transactions on Biomedical Engineering, 51(4), 570–581.

59) McDuff, D., Gontarek, S., Picard, R. W. (2014): Improvements in Remote Cardiopulmonary Measurement Using a Five Band Digital Camera. IEEE Transactions on Biomedical Engineering, 61(10), 2593–2601.

60) McRobbie, D. W. (2006): MRI From Picture to Proton (2. Ed.). Cambridge, New York, Melbourne, usw.: Cambridge University Press.

61) Merri, M., Farden, D. C., Mottley, J. G., Titlebaum, E. L. (1990): Sampling frequency of the electrocardiogram for spectral analysis of the heart rate variability. IEEE Transactions on Biomedical Engineering, 37(1), 99–106.

62) Moço, A. V., Stuijk, S., de Haan, G. (2018): New insights into the origin of remote PPG signals in visible light and infrared. Scientific Reports, 8(1).

63) Moço, A. V., Stuijk, S., de Haan, G. (2016): Skin inhomogeneity as a source of error in remote PPG-imaging. Biomedical Optics Express, 7(11), 4718.

64) Nagel, A. M., Umathum, R., Rösler, M. B., Ladd, M. E., Litvak, I., Gorkov, P. L., ... Schepkin, V. D. (2016): 12339K and 23Na relaxation times and MRI of rat head at 21.1T. NMR in Biomedicine, 29(6), 759–766.

65) Nguyen, N., Huang, H., Oraintara, S., Vo, A. (2010): Mass spectrometry data processing using zero-crossing lines in multi-scale of Gaussian derivative wavelet. Bioinformatics (Oxford, England), 26, i659–i665.

66) Odille, F., Pasquier, C., Abacherli, R., Vuissoz, P.-A., Zientara, G. P., Felblinger, J. (2007): Noise Cancellation Signal Processing Method and Computer System for Improved Real-Time Electrocardiogram Artifact Correction During MRI Data Acquisition. IEEE Transactions on Biomedical Engineering, 54(4), 630–640.

67) Oster, J., Clifford, G. D. (2017): Acquisition of electrocardiogram signals during magnetic resonance imaging. Physiological Measurement, 38(7), R119–R142.

68) Oster, J., Pietquin, O., Kraemer, M., Felblinger, J. (2010): Nonlinear Bayesian Filtering for Denoising of Electrocardiograms Acquired in a Magnetic Resonance Environment. IEEE Transactions on Biomedical Engineering, 57(7), 1628–1638.

69) Patton, K. T., Thibodeau, G. A. (2012): Anatomy & Physiology (8. Ed.). St. Louis: Mosby.

70) Petterson, M. T., Begnoche, V. L., Graybeal, J. M. (2007): The Effect of Motion on Pulse Oximetry and Its Clinical Significance. Anesthesia & Analgesia, 105(On Line Suppl.), S78–S84.

71) Roonizi, E. K. (2013): A New Algorithm for Fitting a Gaussian Function Riding on the Polynomial Background. IEEE Signal Processing Letters, 20(11), 1062–1065.

72) Saeed, M., Villarroel, M., Reisner, A. T., Clifford, G., Lehman, L.-W., Moody, G., ... Mark, R. G. (2011): Multiparameter Intelligent Monitoring in Intensive Care II: A public-access intensive care unit database. Critical Care Medicine, 39(5), 952–960.

73) Sanderson, C., Curtin, R. (2016): Armadillo: a template-based c++ library for linear algebra. The Journal of Open Source Software, 1(2), 26.

74) Schmidt, M., Krug, J. W., Rosenheimer, M. N., Rose, G. (2018): Filtering of ECG signals distorted by magnetic field gradients during MRI using non-linear filters and higher-order statistics. Biomedical Engineering / Biomedizinische Technik, 63(4), 395–406.

75) Scholkmann, F., Boss, J., Wolf, M. (2012): An Efficient Algorithm for Automatic Peak Detection in Noisy Periodic and Quasi-Periodic Signals. Algorithms, 5(4), 588–603.

76) Schwartz, P. J., Wolf, S. (1978): QT interval prolongation as predictor of sudden death in patients with myocardial infarction. Circulation, 57(6), 1074–1077.

77) Scott, A. D., Keegan, J., Firmin, D. N. (2009): Motion in Cardiovascular MR Imaging. Radiology, 250(2), 331–351.

78) Shahid, S., Walker, J., Lyons, G. M., Byrne, C. A., Nene, A. V. (2005, July): Application of Higher Order Statistics Techniques to EMG Signals to Characterize the Motor Unit Action Potential. IEEE Transactions on Biomedical Engineering, 52(7), 1195–1209.

79) Shetty, A. N. (1988): Suppression of radiofrequency interference in cardiac gated MRI: A simple design. Magnetic Resonance in Medicine, 8(1), 84–88.

80) Silbernagl, S., Despopoulos, A. (2008): Color Atlas of Physiology (6. Ed.). Stuttgart: Thieme.

81) Smith, R. P., Argod, J., Pepin, J.-L., Levy, P. A. (1999): Pulse transit time: an appraisal of potential clinical applications. Thorax, 54(5), 452–457.

82) Sörnmo, L., Laguna, P. (2005): Bioelectrical Signal Processing in Cardiac and Neurological Applications. Cambridge: Academic Press.

83) Stäb, D., Najjar, A. A., O'Brien, K., Strugnell, W., Richer, J., Rieger, J., ... Barth, M. (2019): Cardiac Magnetic Resonance Imaging at 7 Tesla. Journal of Visualized Experiments, (143).

84) Stäb, D., Roessler, J., O'Brien, K., Hamilton-Craig, C., Barth, M. (2016): ECG Triggering in Ultra-High Field Cardiovascular MRI. Tomography (Ann Arbor, Mich.), 2, 167–174.

85) Sun, Y., Thakor, N. (2016): Photoplethysmography Revisited: From Contact to Noncontact, From Point to Imaging. IEEE Transactions on Biomedical Engineering, 63(3), 463–477.

86) Takatani, S., Graham, M. D. (1979): Theoretical Analysis of Diffuse Reflectance from a Two-Layer Tissue Model. IEEE Transactions on Biomedical Engineering, 26(12), 656–664.

87) The Beth Israel Deaconess Medical Center. (1990). The MIT-BIH Normal Sinus Rhythm Database. physionet.org.

88) The CSE Working Party. (1985): Recommendations for measurement standards in quantitative electrocardiography. European Heart Journal, 6, 815–825.

89) Thiel, F., Kosch, O., Seifert, F. (2010): Ultra-Wideband Sensors for Improved Magnetic Resonance Imaging, Cardiovascular Monitoring and Tumour Diagnostics. Sensors, 10(12), 10778–10802.

90) Thomas, G. B., Finney, R. L. (1995): Calculus and analytic geometry (9. Ed.). London: Pearson.

91) Trumpp, A., Bauer, P. L., Rasche, S., Malberg, H., Zaunseder, S. (2017, May): The value of polarization in camera-based photoplethysmography. Biomedical Optics Express, 8(6), 2822.

92) Truong, T.-K., Chakeres, D. W., Beversdorf, D. Q., Scharre, D. W., Schmalbrock, P. (2006): Effects of static and radiofrequency magnetic field inhomogeneity in ultra-high field magnetic resonance imaging. Magnetic Resonance Imaging, 24(2), 103–112.

93) Verkruysse, W., Svaasand, L. O., Nelson, J. S. (2008): Remote plethysmographic imaging using ambient light. Optics Express, 16.

94) Viola, P., Jones, M. (2001): Rapid object detection using a boosted cascade of simple features In: Proceedings of the 2001 IEEE computer society conference on computer vision and pattern recognition. CVPR 2001. IEEE Comput. Soc.

95) Webster, J. G. (1997): Design of Pulse Oximeters. Bristol: IOP Publishing.

96) Willems, J. L., Arnaud, P., van Bemmel, J. H., Bourdillon, P. J., Brohet, C., Volta, S. D., . . . Demeester, M. (1985): Assessment of the performance of electrocardio-

graphic computer programs with the use of a reference data base. Circulation, 71(3), 523–534.

97) Wu, T., Blazek, V., Schmitt, H. J. (2000): Photoplethysmography imaging: a new noninvasive and noncontact method for mapping of the dermal perfusion changes In: A. V. Priezzhev, P. A. Oberg (Eds.) In: Optical techniques and instrumentation for the measurement of blood composition, structure, and dynamics. SPIE.

98) Yacoub, E., Shmuel, A., Pfeuffer, J., Moortele, P.-F. V. D., Adriany, G., Ugurbil, K., Hu, X. (2001): Investigation of the initial dip in fMRI at 7 Tesla. NMR in Biomedicine, 14(7-8), 408–412.

99) Yang, S.-Y., Huang, H.-H., Liang, C.-W., Tsai, S.-Y., Huang, T.-Y. (2014): Noncontact physiological measurements using video recording inside an MRI scanner In: Proceedings of the 22nd Annual Meeting of the International Society for Magnetic Resonance in Medicine, Milan, Italy.

100) Yuille, A. L., Poggio, T. A. (1986): Scaling Theorems for Zero Crossings. IEEE Transactions on Pattern Analysis and Machine Intelligence, 8(1), 15–25.

101) Zaitsev, M., Maclaren, J., Herbst, M. (2015): Motion artifacts in MRI: A complex problem with many partial solutions. Journal of Magnetic Resonance Imaging, 42(4), 887–901.

102) Zaunseder, S., Trumpp, A., Wedekind, D., Malberg, H. (2018): Cardiovascular assessment by imaging photoplethysmography - a review. Biomedical Engineering / Biomedizinische Technik, 63(5), 617–634.

103) Zheng, Y.-L., Ding, X.-R., Poon, C. C. Y., Lo, B. P. L., Zhang, H., Zhou, X.-L., ... Zhang, Y.-T. (2014): Unobtrusive Sensing and Wearable Devices for Health Informatics. IEEE Transactions on Biomedical Engineering, 61(5), 1538–1554.

Glossary

ECG

Electrocardiography. 9, 10, 30, 36–43, 45, 46, 48–55, 61, 63, 64, 66–68, 75, 95–99, 101, 102, 105–107, 109–112, 116–118, 125, 126, 133–135, 137–149, 164, 165, 168, 169, 172, 173, 175

HR

Heart Rate. 9, 41, 43, 45, 46, 48, 61–63, 65, 69, 72, 73, 110–112, 119, 120, 125, 142, 143, 168, 169, 173

HRV

Heart Rate Variability. 41, 113, 144

LED

Light emitting diodes. 44, 51, 56, 57, 60, 69, 70, 72, 120, 125, 143, 165, 166

MA

moving average. 63, 110

MHD

Magnetohydrodynamic. 9, 49, 50, 54, 67, 110, 111, 125, 126, 139, 140, 142, 146–149, 165, 169, 172

MIP

Maximum intensity projection. 68, 118, 170

MR

Magnetic Resonance. 8–10, 50–61, 64, 68, 69, 71, 75, 107, 109, 112, 116, 119, 120, 123, 125, 143, 149, 165, 169, 174

MRA

Magnetic Resonance Angiography. 53, 55, 58, 60, 64, 68, 109, 118, 125, 143, 165

MRI

Magnetic Resonance Imaging. 8–11, 14, 17, 48, 49, 51–54, 56, 58–61, 64, 66–69, 74, 75, 95, 107, 109, 112, 113, 116, 117, 119, 120, 125, 139, 141–146, 148, 149, 165, 168, 169, 172, 174, 176

msPE

Multiscale Parameter Estimation. 10, 52, 75, 77, 78, 83, 86–93, 95–97, 101, 104, 107, 126, 127, 129–131, 135, 139, 141, 146–149, 171, 173, 176

PMU

Physiological Measurement Unit. 10, 52, 54, 75, 142, 148

PPG

Photoplethysmography. 9, 10, 30, 43, 45–48, 50–55, 58, 61, 63, 64, 66–70, 72–74, 109–112, 114–118, 120, 122, 123, 125, 142–145, 164, 165, 168–170, 172, 173

PPGi

Photoplethysmography Imaging. 10, 30, 46, 47, 51–61, 63–74, 109–120, 122–125, 142–146, 148, 149, 165, 166, 168–170, 172–175

PRD

root-mean-squared difference. 91, 92, 126, 127, 170

PTT

Pulse Travel Time. 45, 50, 65–67, 113, 114, 164

PVE

parameter vector error. 92, 93, 129–131, 171

RMSE

root-mean-square error. 64, 110, 173

ROI

Region-of-interest. 46, 47, 61, 63, 69, 70, 72, 144, 165, 174

SNR

Signal-to-noise ratio. 8, 46–48, 50, 52, 56, 57, 59, 61, 69–74, 90–94, 109, 110, 117, 118, 120, 121, 123–132, 142–144, 149, 165, 167, 170, 171, 173

UHF

Ultra-high-field. 8–10, 48, 49, 51–54, 60, 64, 67, 68, 75, 95, 107, 109, 112, 113, 116, 117, 119, 120, 125, 139, 141–143, 145, 146, 148, 149, 165, 168, 169, 172

List of Figures

2.1 Spatial quantization of spin angular momentum for a $s = \frac{1}{2}$ particle. . 12

2.2 Splitting of nuclei spin energies as a function of magnetic field strength. 13

2.3 Schematic representation (y-axis suppressed) of individual nuclear spins (thin arrows), aligning parallel or antiparallel to the z-axis within a static magnetic field $\overrightarrow{B0}$. As $N_{\uparrow\uparrow} > N_{\downarrow\uparrow}$, $\overrightarrow{M0}$ (bold arrow) precesses around $\overrightarrow{B0}$ with frequency ω_0. 14

2.4 Excitation of $\overrightarrow{M}(t)$ with $\|\overrightarrow{B0}\| = 3\,\mathrm{T}$, and $\|\overrightarrow{B1}\| = 50\,\mathrm{mT}$. 16

2.5 Relaxation of $\overrightarrow{M}(t)$ with $\mathrm{T}_1 = 1607\,\mathrm{ms}$ and $\mathrm{T}_2 = 85\,\mathrm{ms}$. 16

2.6 Relaxation using the T_1, T_2 values from Fig. 2.5 and $\|\overrightarrow{B0}\| = 3\,\mathrm{T}$. 17

2.7 $Lx(t) = \alpha x(\alpha\pi - t)$ with $\alpha = 0.5$ is applied to a signal $x(t) = e^{-t^2}\cos(5t)$. 19

2.8 Magnitudes $\hat{x}(\omega)$ and $\hat{y}(\omega)$ corresponding to the signals shown in Fig. 2.7. 20

2.9 Visualization of $x(t) \rightleftharpoons \hat{x}(\omega)$ which is here $1_{[-\tau,\tau]} \rightleftharpoons \frac{\sin(\tau\omega)}{\omega}$. The complex exponentials $e^{-j\omega t}$ as eigenfunctions of the Fourier Transform are visualized as sine waves in the surface spanned between ω- and t-axis. The transfer function $\hat{h}(\omega)$ of L allow to attenuate certain frequencies (dashed lines). $x(t)$ is discontinuous at $t = \pm\tau$ requiring to modify the integral limits of eq. (2.27) but concepts remain identical. 22

2.10 Spectrograms of a chirp signal with logarithmically increasing frequency and a short pulse at $t = 3$. A Hamming window $\phi(t) = 0.54 - 0.46\cos(2\pi n/N)$ is used with length of $N = 100$ (left) and $N = 50$ (right). Increasing pixel darkness denotes increasing amplitudes. . . . 23

2.11 Heisenberg boxes of a window function. Dimensions are not up to scale. 25

2.12 *Left:* "Mexican hat" wavelet $\Psi_{\mathrm{m}} = -(2/\pi)^{0.25}(1/\sqrt{3})(4t^2 - 2)e^{-t^2}$. *Right:* "Morlet" wavelet $\Psi_{\mathrm{M}} = e^{-t^2}\cos(5t)$ demonstrating the oscillatory nature of wavelets. 26

2.13 Heisenberg boxes of a Morlet wavelet (→ Fig. 2.12, right) with non-fixed lengths. Dimensions are not up to scale. 27
2.14 *Left:* Scalogram of the chirp signal shown in Fig. 2.10 for $t \in [0, 4]$ and $s \in [1, 30]$ *Right:* Segment $t \in [2.8, 3.2]$ for scales $s \in \{ 9,\ 18,\ 27 \}$. 28
2.15 Applying the Wavelet Transform according to eq. (2.43) allows detecting singularities in a signal $x(t)$, such as a unit pulse (→ Fig. 2.9). The convolution $x(t) \star \theta_s$ averages the signal, resulting in extrema in WT^1 and in extrema and zero-crossings in WT^2. Under certain conditions, those exist for all s (dotted line). 29
2.16 Schema of systematic circulation, the blood flow throughout the lower part of the body. Red indicates oxygenated blood and blue deoxygenated blood. In this figure, the heart connecting the aorta and vena cava is not shown (→ Fig. 2.17). 31
2.17 Schema of flow of blood throughout the body. Arrows indicate the direction of flow and text above arrows indicates the valves the blood is passing. The outlined area indicates the systemic circulation shown in Fig. 2.16. The remainder constitutes the circulation between the heart, consisting of atria, ventricles, and valves, and lungs termed pulmonary circulation. 32
2.18 Four states of a cardiac muscle cell (rectangle): ① polarized resting state, ② state of depolarization (gray area) initiated by an external stimulus (lightning symbol), ③ fully depolarized state, and ④ state of repolarization. After state ④ the cell returns to state ①. The arrow indicates the direction of depolarization. 34
2.19 Diagram showing the direction of electrical impulses indicated by arrows. Taken from: (Constanzo 2009) 35
2.20 Diagram showing time until an impulse arrives at a superimposed location. Taken from: (Constanzo 2009) 35
2.21 Anatomy of the human skin which consists of three layers denoted on the right. Veins and arteries are located in the fat layer called subcutis with capillaries rising into the dermis. Taken from: https://commons.wikimedia.org/wiki/File:Diagram_showing_the_structure_of_the_skin_CRUK_371.svg (Attribution: Cancer Research UK / CC BY-SA (https://creativecommons.org/licenses/by-sa/4.0) 36

2.22 Relationship between the cardiac vector $\vec{V}$ (bold arrow) and the measured ECG signal using leads I-III (thin arrows). $\oplus$ and $\ominus$ indicate the positive and negative electrodes, respectively. For the given $\vec{V}$, all leads result in a positive value. 37

2.23 Cardiac electrical activity and direction of $\vec{V}$ throughout a cardiac cycle. Propagation of cardiac impulses are shown as gray areas. The ECG is assumed to be acquired from a lead positioned at the $\vdash$ symbol therefore a lead similar to lead II shown in Fig. 2.22 is used. Taken from: (Sörnmo, Laguna 2005). 38

2.24 ECG signal (record id: `16483`) from the MIT-BIH Normal Sinus Rhythm Database with manual annotations of all P-/Q-/R-/S- and T-waves, and the QT interval (arrow). Each wave has an onset and offset point, which are shown here for the P- and T-wave as dotted lines. 40

2.25 Example signals from the QT database showing typical artifacts occurring during ECG acquisition: ① Atypical, fragmented QRS complex morphology (record: `sele0133`), ② Premature ventricular contraction (record: `sel221`), ③ Baseline wandering (record: `sel39`), ④ Bursts of high-frequency noise (record: `sele0129`). Further information on the QT database can be found in the appendix. 42

2.26 Light absorbance of hemoglobin & oxyhemoglobin with values taken from (Takatani, Graham 1979). The wavelength values on the x-axis have a color according to visible-light spectrum for humans, invisible wavelengths are shown in black. Dotted lines denote typical center wavelengths used for the light sources in pulse oximetry. 44

2.27 ECG and PPG (pulse oximeter) signal from the MIMIC II Waveform Database. The peak-to-peak distances of ECG signal (RR interval) and PPG signal (PP) are similar but there is a phase shift between both due to PTT. 45

2.28 Computation of the PPGi signal from a video. The image stack from the video of a subject's forehead is shown (left) with a suitable ROI covering the forehead indicated by red color. The grid lines are not part of the actual video. The averaged pixel values within the ROI constitute the PPGi signal for each frame. Computing the averaged value for a sequence of frames results in the one-dimensional PPGi signal (right) similar to the PPG signal but with lower SNR. 47

2.29 ECG signals acquired from a healthy volunteer with the patient table in home position ($0.3\,\mathrm{T}$) and imaging position ($7\,\mathrm{T}$). No imaging was performed, therefore the noise stems from the MHD effect only. The x-axes of both signals were manually adjusted. The signals are part of the dataset described in Chapter 3.1.1. 49

3.1 Experimental setup during stage ①: The patient is lying feet-first on the patient table and the camera (arrow) is pointed towards the forehead. The camera is mounted on a MR-compatible custom-built stand. During stages ② and ③ the setup remains identical but the patient table is located at the isocenter of the scanner. 55

3.2 Experimental setup with arrows indicating the camera and the dedicated LED illumination. The setup was placed in a portable sun shade which is not shown. 57

3.3 Schematic diagram of the setup for PPGi-based cardiac triggering. Dotted lines indicate room walls and arrows indicate cable connections. Providing illumination is optional but strongly advised for increasing the SNR of the PPGi signal. 59

3.4 Setup for PPGi acquisition during $7\,\mathrm{T}$ MRA. Arrows indicate from top to bottom: glass plate, dedicated LED illumination, UHF MRI-compatible camera. 60

3.5 The PPGi signal (black curve) is assumed be similar to a sine (dotted curve), allowing to calculate, at a given point in time (gray dot), the phase and computing the time Δ (arrow) until the next trigger ought to be sent (black dot). 60 cycles/minute are assumed, i.e. $\gamma_{\mathrm{HR}} = 1$ and therefore $\angle_{\mathrm{HR}} = -0.5\pi$ and $\Delta = 0.25\,\mathrm{s}$. 65

3.6 Synthesis of phase map: For each pixel in the video, demonstrated here for a single example pixel (black square), the surrounding 10×10 pixels (red squares) are averaged and the value is stored. This is done for all video frames, resulting in a one-dimensional signal $x(t)$. Subsequently, the Fourier Transform of the signal is computed and the phase $\angle\hat{x}(k_{\mathrm{HR}})$ is stored and visualized as a pseudo-colored image. 71

3.7 Synthesis of (selective) magnitude map: For each pixel in the video (palm of the hand), a PPGi signal $x(t)$ is computed by capturing the values of a single pixel over time. The Fourier Transform of the signal is computed and the magnitude $|\hat{x}(k_{\mathrm{HR}})|$ is stored in a pseudo-colored image if the magnitude belongs to the highest values of all pixels. Some pixels are saturated due to frontal LED illumination. 72

3.8 *Top row:* Two configurations of the 5-parameter model function defined by parameters $(A, \sigma, \tau, \mu, B)^T$ and one configuration of the 8-parameter model with the left half being identical to the first and the right half identical to the second configuration. Parameter sets are $\vec{P}_1 = (1, 1, 0, 0, 1)^T$, $\vec{P}_2 = (1, 1, 3, 0, 1)^T$, and for the piecewise model $\vec{P}_{\text{left}} = \vec{P}_1$ and $\vec{P}_{\text{right}} = \vec{P}_2$. *Bottom row:* Corresponding zero-crossings in the WT^1 (black lines) and WT^2 (gray lines) scalograms. Black lines are associated to local extrema of the input signals and gray lines are associated to inflection points. 76

3.9 Analytic framework for calculating parameters of signal $x(t)$. Zero-crossings of WT^1 and WT^2 are denoted by $u0^1$ and $u0^2$, respectively. The input function $x(t)$ follows the model function $G_{A,\sigma,\tau,\mu,B}(t)$ and the output values are a scalar for each parameter (A, σ, τ, μ, B) at scale s. Optionally, these values can be refined using non-analytical optimization (fitting) which will be denoted msPE$^{\text{fit}}$. 78

3.10 *Top left:* $x(t) = G_{A,\sigma,\tau,\mu,B}(t)$ (black curve). *Right:* $x(t)$ biased by uniformly distributed noise (red curve). *Bottom:* Zero-crossings in the time-scale plane associated with extrema (WT^1, black) and inflection points (WT^2, gray) are indicated. 79

3.11 Configurations of the piecewise model $G_{\mathrm{pw}}(t)$ described by eq. (3.45) with $A = \bar{A} = 1$, $\mu = 0$, $B_{\mathrm{L}} = B_{\mathrm{R}} = 0$ and remaining parameters given in the legend. 83

3.12 Same visualization as in Fig. 3.10 showing different combinations of lines of WT^1 (black) and WT^2 zero-crossings (gray) of the model $G_{A,\sigma,\tau,\mu,B}(t)$. Panel ⑩ shows all lines and panels ① to ⑨ depict subsets. The lines shown in panel ① are equivalent to the Gaussian model (→ Fig. 3.8, left) and do not allow to compute parameter τ. 84

3.13 Numerical counterpart to the analytic framework. Discrete signals are denoted by square brackets and discrete versions of parameters (e.g. u, s) by subscripts. The input signal $x[t_i]$ is processed numerically to obtain zero-crossing lines with the individual zero-crossings at a certain scale are substituted into the expressions stemming from the analytical framework resulting in model parameters. 85

3.14 Example signals from experiment 1. Gaussian signals $x[t_i]$ (black curves) are generated which are superposed by noise signals $\eta[t_i]$ drawn from a normal distribution, resulting in $\tilde{x}[t_i]$ signals (red curves). Model parameters are $A = 1$, $\mu = 0.08$, $\sigma = 0.51$ and SNR increases from -10 (left), 0 (center), to 10dB (right). 90

3.15 Example signals from experiment 2. Signals $x[t_i]$ (black curves) are generated with parameters ($A = \sigma = \tau = 2$, $\mu = B = -2$) which are superposed by noise signals $\eta[t_i]$ which are drawn from a normal distribution, resulting in $\tilde{x}[t_i]$ signals (red curves). SNR increases from -10 (left), 0 (center), to 10 dB (right). 91

3.16 Example signals from experiment 3 (SNR 10 dB). $\tilde{x}[t_i]$ signals (red curves) are generated by using signals $x[t_i]$ (black curves) following the piecewise model eq. (3.45) which are superposed by noise signals $\eta[t_i]$ drawn from a normal distribution. 93

3.17 *Left:* Normal, lognormal, and uniform distribution *Right:* Example spectra of correlated noise generated using the method proposed in (Kasdin 1995). 94

3.18 Example signals from experiment 4 (SNR 10 dB). $x[t_i]$ signals (black curves) follow the symmetric model eq. (3.22) and noise $\eta[t_i]$ is drawn from correlated noise with $\alpha = 0$ (left, no correlation), $\alpha = 1$ (center, pink noise), $\alpha = 2$ (right, brown noise), resulting in $\tilde{x}[t_i]$ signals (red curves). 94

3.19 Flowchart of the proposed method for ECG delineation with the individual steps (white/gray boxes) being performed from top to bottom in seven stages, denotes by numbers in circles. Input and output data is visualized as arrows. Stage ① is performed once while stages ② to ⑦ (dashed region) are performed once for each ECG wave (P, QRS, T). . 96

3.20 ① Visualization of segmentation of ECG signal $\tilde{x}[t_i]$. *Top:* The input signal is split into three segments for the P-wave (gray), QRS complex (red), and T-wave (blue). *Bottom:* Segmentation of the time-scale plane of the QRS complex. 98

3.21 ② Visualization of time-scale plane funnel with the lines of the model ($u0^1_{\{-1,+1\}}$, $u0^2_{\{-2,-1,+1,+2\}}$) associated to a given funnel are indicated above it. Hatched regions indicate the valid intervals in which zero-crossing lines are kept. *Bottom:* Application of the $u0^2_{\{-1,+1\}}$ funnel to the time-scale plane shown in Fig. 3.20. 100

3.22 ④ Visualization of method for computing the error measure for a given noisy signal (red curve). Zero-crossings at scale 1 of the input signal without noise (black curve) are indicated by black and gray dots. For each possible combination of available zero-crossings lines, one E_n value can be computed which is demonstrated here for a single combination at a single scale (bold circles). They are substituted into equations for parameter estimation which are then used to predict the positions at $s + k$ (thin circles). The mismatch between predicted/extrapolated position and actual occurrence is then stored for each zero-crossing individually (red letters). In the shown case, the lines $u0^1_{-1}$ and $u0^2_{+2}$ show a high error. Therefore, it would be favorable to use the the remaining lines for parameter estimation only. 103

3.23 $G_{\text{pw}}(t)$ with $\sigma_{\text{L}} = \sigma_{\text{R}} = 1$ and $\tau = 0$ (left) and $\tau = 2$ (right). $c_{\text{on}} = c_{\text{off}} \in \{1, 1.5, 2\}$ with X_{on} and X_{off} indicated by gray (1), blue (1.5), and red (2) dots. 105

3.24 Three example segments $\tilde{x}[t_i]$ of ECG signals acquired within a 7 T UHF MRI bore (black curve) and with the patient table in home position (0.3 T, dashed). 107

4.1 HR estimates obtained from ECG, PPG, and PPGi signals of subject seven during stage ① (→ Table 4.1: S7). 111

4.2 HR results for subject four during stage ② (→ Table 4.2: S4). As the ECG signal is biased severely due to MHD artifacts, resulting in HR values larger than 100 cycles per minute, they can not be seen. 111

4.3 *Left*: Real PPGi signals acquired during UHF MRI study. *Right*: Synthetic PPGi signal computed using concatenated cosine waves with cardiac cycle lengths acquired from the Normal Sinus Rhythm RR Interval Database and noise estimated from real PPGi signals. The bottom plots depict the first 20 seconds of both signals. 113

4.4 Results of application of Alg. 2 to synthetic PPGi signals w.r.t. different combinations of M and N. Absolute differences between estimated and ground truth trigger points in time were computed for each cardiac cycle within a signal and averaged over the whole signal. Subsequently, $\mathrm{m}(\cdot)$ (left) and $\mathrm{sd}(\cdot)$ (right) of all errors were computed and stored in the corresponding coordinate with values being displayed in unit samples. A minimum error valley is highlighted in red color. 114

4.5 Histograms of trigger-to-trigger durations of PPG (gray) and PPGi (black) signals. Data is from the same experiment, therefore the PPG histograms are identical. PPGi triggers were obtained with N set to 50 (left), 125 (center), and 300 (right). 115

4.6 Error of Alg. 2 w.r.t. parameter T ($M = 50$ and $N = 125$). For each experiment, the $\mathrm{m}(\cdot)$ and $\mathrm{sd}(\cdot)$ of PPGi trigger-to-trigger durations were computed. The boxplots show the differences between these values and $\mathrm{m}(\cdot)$ (left) and $\mathrm{sd}(\cdot)$ (right) of trigger-to-trigger durations computed from the ground truth PPG signals. 115

4.7 Comparison of trigger-to-trigger durations in PPG, ECG and PPGi signals with the latter being obtained by using Alg. 2 with optimized parameters ($M = 50$, $N = 125$, $T = 0.2$ s). Stage ① was conducted at 0.3 T and stages ② ③ at 7 T. During stage ③ MR imaging was performed. The raw data of the experiment marked with an asterisk (first subject, first stage) is shown in Fig. 4.8. 116

4.8 ECG, PPG, and PPGi trigger-to-trigger durations. 117

4.9 MIP images obtained using PPG (left) and PPGi triggering (right). A) shows a vessel only visible in the PPG-gated MIP image and B) a vertical radio-frequency artifact visible in both images. Gray areas shows regions that were blended. 118

4.10 *Left:* Chart of cardiac signal strength w.r.t. camera channel. *Right:* Peak wavelengths of the camera channels obtained from the camera's datasheet. 119

4.11 *Left:* Magnitude maps *Right:* Phase maps. Both were computed for all three stages ① - ③ and color values were normalized with regard to the min/max values within a type of map. In the magnitude maps, a "hot spot" of SNR can be observed in all three stages and is marked by a circle. In the phase map of stage ③, two regions are indicated that are used in Fig. 4.13 and magnified here. 121

4.12 Averaged values of all pixels of the raw PPGi data of the three stages and as ground truth the PPG signal is given. 122

4.13 Same visualization of PPGi data as shown in Fig. 4.12, but using only the two pixels indicated in the phase map of stage ③ shown in Fig. 4.11. 122

4.14 *Left:* Example magnitude map of a palm of the hand with pixels showing the highest portion of cardiac signal being pseudo-colored from low (blue) to high (yellow). *Right:* PPGi signal obtained from all pixel within the video and PPG signal. 123

4.15 Log-log error plot showing mean PRD values resulting from applying Alg. 3 and the reference methods proposed by (Caruana et al. 1986), (Guo 2011), (Roonizi 2013) to 150 synthetic signals w.r.t. SNR. Adding an assumption regarding signal shape to Alg. 3 allows improving PRD values considerably. Raw data of SNR$= 20\,$dB (asterisk) is shown in Fig. 4.16. 127

4.16 *Panels* ① to ③: Error in estimation of true parameters μ, A, σ (gray) by Alg. 3 (blue) and the Roonizi algorithm (red). A dashed region indicates particular high errors in σ estimation. *Panel:* ④ Results after modifying Alg. 3 by eq. (4.1). 128

4.17 PVE distribution of experiment 2. At each SNR level, 1024 random signals of the 5-parameter model $G_{A,\sigma,\tau,\mu,B}(t)$ were generated and corrupted by Gaussian noise. Each signal was processed by three implementations of msPE. The red ellipse is used to underline the difference in accuracy of the three methods with regards to outliers. A dashed line marks the 5% error level. 129

4.18 PVE distribution of experiment 3. At each SNR level, 1024 signals of the 8-parameter model $G_{\text{pw}}(t)$ were generated and corrupted by Gaussian noise. 130

4.19 PVE distribution of experiment 4. At each SNR level, 1024 random signals of the 5-parameter model $G_{A,\sigma,\tau,\mu,B}(t)$ were generated and corrupted by correlated (red boxplots) or non-Gaussian noise (gray boxplots). The boxplots from Fig. 4.17 for Gaussian noise are given as reference. All signals were processed by the same implementation of $\text{msPE}^{\text{fit}}_{\text{tsp}}$ ($\rightarrow$ Alg. 4 including step 7). 131

4.20 Exemplary results from experiments 2, 3, and 4 for SNR levels 20, 10, and 0 dB. In the first two columns, additive noise is drawn from a normal distribution while in the third column noise is drawn from correlated "brown" noise with $\alpha = 2$. 132

4.21 E values computed for each line combination of QRS complexes of the QT database (black) and the subset of the one line combination with minimum E value for each individual QRS complex (gray). The first distribution is bimodal with 97.3% of all minimum E values lying in the left term. Values $E > 2$ were clamped. 134

4.22 Three example delineation results that were randomly chosen out of 3194 P-waves, 3542 T-waves, and 3623 QRS complexes from the QT database. Computed fiducial points $\{\text{P, QRS, T}\}_{\{\text{on, peak, off}\}}$ are depicted as red lines to avoid overlapping with the dots used for the visualization of annotations of human experts. T_{on} was not defined by the human annotator within the first row. 136

4.23 QRS complexes with irregular shapes using the same visualization as used in Fig. 4.22. The first QRS complex as marked by the annotators as being "unclassifiable", the second shows a case of severe atrial fibrillation distorting the typical QRS waveform, and the third shows an indadequate configuration of the ECG measurement hardware as values above a certain limit are cropped. 138
4.24 Example results from the 7 T experiments for each subject. Due to the MHD noise the morphologies of the QRS complexes are abnormal, i.e. they are very similar to a Gaussian (left), or in proximity to a T-wave which shows high amplitude (center), or exhibit large undershoots (right). $G_{pw}(t)$ is plotted in blue color if the distance between QRS_{peak} and the ground truth value is ≤ 50 ms or in red color else. 140

5.1 Qualitative assessment of the feasibility of ECG, PPG, and PPGi for cardiac monitoring and triggering within clinical MRI (light gray) and UHF MRI (dark gray). For PPGi, results are identical for both environments. Each category is evaluated using a measure ranging from low (center) to high (border) and the assessment of categories reliability and accuracy (bold values) is backed by results presented in this work while the remaining categories are subjective evaluations. 145

List of Tables

2.1 Relaxation times for different tissues, taken from (McRobbie 2006). . . 17

3.1 Core parameters of the numerical part of the msPE framework. 88
3.2 Parameterization of the time-space plane funnel. 99
3.3 Parameterization of eqs. (3.61) and (3.62) 106

4.1 RMSE in HR of 8 subjects during stage ① at 0.3 T. Ground Truth: ECG 110
4.2 RMSE in HR of 8 subjects during stage ② at 7 T. Ground Truth: PPG . 110
4.3 Results of comparing PPGi measurements from the hand to the foot. Each row represents a subject and columns $1-5$ and $7-11$ display SNR values using different metrics for the hand and foot, respectively. The last row shows $\mathrm{ma}(\cdot)$ values. 124
4.4 Delineation of ECG signals from the QT database [Sensitivity, $\mathrm{m} \pm \mathrm{sd}$] . 137
4.5 Results of $\mathrm{QRS}_{\mathrm{peak}}$ detection in ECG data obtained at 0.3 T and 7 T. . . . 140

Appendix

Open Source Software During this work, a software demonstrating the research activites was made publicly-available (https://github.com/nspi/vbcg). The software is published under an open-source license, written in Python 2.7 and provides soft realtime feasibility as well as an interactive graphical user interface. The software is able to read video frames from a video camera or from hard disk and offers a tool for definition of a ROI or the Viola-Jones algorithm for face detection (Viola, Jones 2001). The acquired PPGi signal can be processed by the algorithms described in chapters 3.2.1 and 3.2.2 and can be connected to the trigger device, described in the next section, for MRI cardiac triggering.

Trigger device A low-cost device was custom-built for sending triggers to the MR-scanner on basis of an open source development board (Arduino Nano, Arduino, Turin, Italy). The schematics are depicted below: The device is connected to a computer via USB and to the MR scanner via BNC connection. Once a signal is invoked from the laptop, a 5 V trigger is sent to the scanner which activates image acquisition.

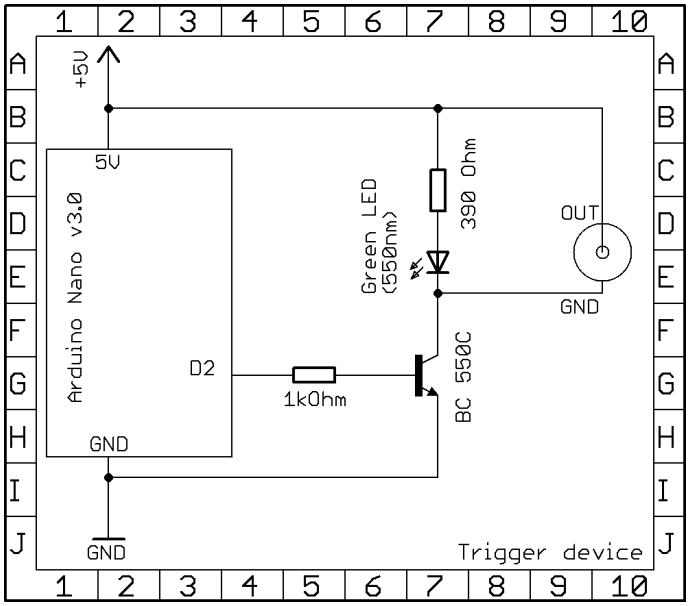

Benchmark datasets In this work, two publicly-available benchmark datasets were used. Both datasets were obtained from Physionet (https://www.physionet.org) (Goldberger et al. 2000) using the provided WFDB Software Package. The Normal Sinus Rhythm RR Interval Database was used for generation of synthetic PPGi signals while the QT database was used for evaluation of ECG delineation algorithms.

The Normal Sinus Rhythm RR Interval Database is based on long-term ECG recordings from 54 healthy subjects (sex: $24/30$ f/m, age range: $28-76$ years). ECG signals were acquired with a sampling rate of 128 Hz and an automated algorithm was used for detecting QRS complexes. Incorrect detections were manually corrected and based upon the corrected R positions, RR intervals ($\rightarrow$ chapter 2.3.2) were computed and published.

The QT database is the de-facto standard database for quantitative evaluation of ECG delineation algorithms (Laguna, Mark, et al. 1997), i.e. algorithms which compute ECG fiducial points ($\rightarrow$ Fig. 2.24). It provides 105 two-channel ECG recordings (250 Hz) with a duration of 15min each that were measured using Holter devices. The recordings were chosen to represent a wide bandwidth of different ECG morphologies and include recordings from patients suffering from cardiac diseases, such as arrhythmia or changes in the ST-segment. Two expert cardiologists annotated the onset, peak, and offset points for at least 30 cardiac cycles per record, resulting in annotations for 3194 P-waves, 3542 T-waves, and 3623 QRS complexes. Furthermore, fiducial points computed by an automatic algorithm (Laguna, Jané, et al. 1994) are available.

Acknowledgement

This work summarizes the research I conducted between 2015 and 2020 in a close collaboration between the Erwin L. Hahn Institute for Magnetic Resonance Imaging (ELH) and the Department of Computer Science of the University of Applied Science and Arts Dortmund (UAS). During this exciting time, I have benefited greatly from the guidance of Prof. Dr. Markus Kukuk (UAS), Prof. Dr. Mark E. Ladd (German Cancer Research Center, Heidelberg & Medical Faculty, University of Duisburg-Essen), and Dr. Stefan Maderwald (ELH).

The collaboration with Prof. Dr. Markus Kukuk goes back to him supervising my B.Sc. Thesis in 2011 which culminated in the msPE framework. During this long and intense quest he always provided motivation and working with him improved my scientific thinking, writing style, and sense of taste for coffee significantly. I would like to thank Prof. Dr. Mark E. Ladd for his continued support during the last years and giving me the freedom to shape this dissertation at my own choice. Despite the long distance to Heidelberg and his responsibilities there, he was always available and provided valuable advice immediately. I am thankful to Dr. Stefan Maderwald for being my contact at the ELH. He supervised all experiments and provided valuable insight into MRI at the beginning of this work. Moreover, I will always keep our trips to the ISMRM meetings in good memory.

Additionally, I would like to thank Prof. Dr. Dr. Hans-Gerd Lipinski who aroused my interest in signal processing and Dr. Birger Jettkant who introduced me to the world of wavelets. Without their motivation during my studies, this work would not certainly exist.

I am grateful for a PhD grant from the Promotionskolleg of the UAS which was essential for this work. Furthermore, I thank Prof. Dr. Britta Böckmann for offering me a position in her group when the Wissenschaftszeitvertragsgesetz posed a problem in 2018. I thank the DAAD for funding a conference attendance and a RISE summer internship in 2017. I thank the ISMRM for granting me stipends for attending their meetings from 2014 to 2016.

I had the pleasure to meet many passionate and talented colleagues. As they are far too many to list here – a huge thanks to everyone from both sites I had the opportunity to collaborate with. You made the last five years with all ups and downs very enjoyable and I wish each of you collectively all the best for your future endeavors.

Finally, I thank my family and friends for their everlasting support. Mum & Dad, thank you for trusting me that this project is worth it and not lamenting the many hours we missed. Sarah, thank you for your unlimited support in the last decade despite the cons of having a partner who pursues a scientific career.

Curriculum Vitae

Der Lebenslauf ist in der Online-Version aus Gründen des Datenschutzes nicht enthalten.